Thin-Film Transistors for Large Area Opto/Electronics

Dissertation

for the award of the academic degree of

Doctor of Philosophy (Ph.D.)

from the

Department of Physics (Blackett Laboratory)

Imperial College London

submitted by

Paul Henrich Wöbkenberg

London, 2009

External examiner: Dr. Hagen Klauk (Max Planck Institute for Solid State Research, Stuttgart, Germany)

Internal examiner: Prof. Jenny Nelson (Imperial College London, UK)

Supervisors: Dr. Thomas D. Anthopoulos, Prof. Donal D. C. Bradley (Imperial College London, UK)

Abstract

The present work addresses several issues in the field of organic and transparent electronics. One of them is the prevailing high power consumption in state-of-the-art organic field-effect transistors (OFETs). A possible solution could be the implementation of complementary, rather than unipolar logic, but this development is currently inhibited by a distinct lack of high performance electron transporting (n-channel) OFETs. Here, the issue is addressed by investigating a series of solution processable n-channel fullerene molecules in combination with optimized transistor architectures. Furthermore, the trend towards complementary circuit design could be facilitated by employing ambipolar organic semiconductors, such as squaraine molecules or polymer/fullerene blends. These materials can fill the role of p- or n-channel semiconductors and enable the facile implementation of power saving complementary-like logic, eliminating the cost-intensive patterned deposition of discrete p-and n-channel transistors. Alternatively, a patterning method for organic materials adapted from standard photolithography is discussed. Furthermore, ambipolar FETs are found to be capable of light sensing at wavelength of 400-1000 nm. Hence their use in low-cost, organic based optical sensor arrays can be envisioned.

Another strategy to reduce the power consumption and operating voltages of OFETs is the use of ultra-thin, self-assembled molecular gate dielectrics, such as alkyl-phosphonic acid molecules. Based on this approach solution processed n- and p-channel OFETs and a complementary organic inverter circuit are demonstrated, which operate at less than 2 Volts.

Finally, transparent oxide semiconductors are investigated for use in thin-film transistors. Titanium dioxide (TiO_2) and zinc oxide (ZnO) films are deposited by means of a low-cost large area compatible spray pyrolysis technique. ZnO transistors exhibit high electron mobility of the order of 10 cm^2/Vs and stable operation in air at less than 2 Volts. These results are considered significant steps towards the development of organic and transparent large-area optoelectronics.

Except where specific reference is made to the involvement of others, the work presented herein is my own and contains nothing which is the result of collaboration. This dissertation has not been submitted in whole or in part for the award of a degree at this, or any other University.

Paul Henrich Wöbkenberg

London, August 2009

Acknowledgements

This thesis describes work undertaken at the Blackett Physics Laboratory at Imperial College London during the period September 2006 to August 2009. The work was funded by a PhD scholarship from the Engineering and Physical Sciences Research Council in the UK, grant No. EP/C539524/1.

My thanks go first of all to my supervisors Dr. Thomas Anthopoulos and Prof. Donal Bradley for continuously providing insight, encouragement and support throughout the course of my PhD. Their positive attitude made this work very enjoyable.

I am grateful for all the fruitful discussions with other members of the Experimental Solid State Physics group and our collaborators, who provided me with support and advice. These were in particular Dr. Xuhua Wang, Dr. Justin Dane, Dr. Monika Voigt, Thilini Ishwara, Stephen Cussel, David Bowler, Jeremy Smith, James Ball, John Labram, Florian Colleaux, Aneeqa Bashir, Dr. Georges Adamopoulos, Dr. Peter Hotchkiss, Dr. Leem Dong Seok, Dr. Floris Kooistra, Prof. Jan C. Hummelen and Dr. Jean-Pierre Djukic.

At this point I would also like to thank several people who have motivated me and sparked my interest to pursue science at different stages of my life, namely Dr. Martin Pfahl, Prof. Veit Wagner and Dr. Jörg Seekamp.

My deepest thanks go to my parents and my sister for always supporting and encouraging me. None of my endeavours would be possible without them. I would also like to thank Lauren Raghoo for her support, inspiration and for believing in me.

Contents

Abstract **3**

Acknowledgements **5**

Table of Contents **7**

List of Figures and Tables **13**

Figures 13

Tables 18

Chapter 1: Introduction **19**

Chapter 2: Background **29**

2.1. Introduction to Organic Semiconductors 30

2.1.1. Electronic structure and covalent bonds 30

2.1.2. Energy levels 31

2.1.3. Polarons 33

2.1.4. Excitons 33

2.1.5. Electronic transitions 34

2.2. Electronic Transport in Organic Semiconductors 35

2.2.1. Bandlike transport 35

2.2.2. Multiple trapping and release model 36

2.2.3. Polar transport 37

2.2.4. Variable range hopping model 37

2.2.5. Bässler disorder model 39

2.2.6. Vissenberg-Matters model 40

2.2.7. Metal - organic semiconductor interfaces 42
2.3. Field-Effect Transistors 43
2.3.1. Operating principles 43
2.3.2. Charge carrier injection in FETs 50
2.3.3. The dielectric layer 51
2.4. Organic Semiconductors 53
2.4.1. Hole transporting organic semiconductors 53
2.4.1.1. Small molecules 53
2.4.1.2. Polymers 55
2.4.2. Electron transporting organic semiconductors 57
2.5. Ambipolar Field-Effect Transistors 59
2.5.1. Ambipolar OFET characteristics 59
2.5.2. Ambipolar FETs based on organic heterostructures 61
2.5.3. Ambipolar FETs based on organic blend 62
2.5.4. Ambipolar OFETs based on a single material 63
2.6. Logic Circuits 65
2.7. Photoresponsive Organic Field-Effect Transistors 68
2.8. Surface Free Energy 71
2.8.1. Pendant drops and contact angle 71
2.8.2. Interfacial free energy and work of adhesion 73
2.9. Transparent Oxide Semiconductors 75
2.9.1. Introduction 75
2.9.2. Charge transport in oxide semiconductors 76
2.9.3. Photoinduced conductivity in TOS 78
Reference List 79

Chapter 3: Materials and Experimental Methods 93
3.1. Material Characterization 94
3.1.1. X-Ray Diffraction 94
3.1.2. Differential Scanning Calorimetry 95
3.1.3. Optical Polarized Microscopy 95
3.1.4. Atomic Force Microscopy 96
3.1.5. Surface Energy Analysis 96

3.1.6. UV-Vis-near IR optical absorption measurements 98
3.1.7. Cyclic Voltammetry 99
3.2. Device Fabrication 100
3.2.1. Spin coating 100
3.2.2. Evaporation 102
3.2.3. Curing of polymer layers 102
3.2.4. Photolithography 103
3.2.5. Fabrication of ring oscillators 103
3.2.6. Self-assembly of organic molecules on metal oxides 104
3.2.7. Spray pyrolysis 105
3.3. Device Characterization 107
3.3.1. Impedance spectroscopy 107
3.3.2. I(V) characteristics 107
3.3.3. Static and dynamic characterization of integrated circuits 108
3.3.4. Static and dynamic characterization of light sensing devices 109
Reference List 110

Chapter 4: Electron-transporting Organic Field-Effect Transistors 113
4.1. Introduction 114
4.2. The model n-channel organic semiconductor 115
4.3. The role of the gate dielectric 116
4.3.1. Benzocyclobutene gate dielectric 117
4.3.2. Electrical stressing 121
4.3.3. Top gate transistor architecture 122
4.4. Metal contact electrodes 124
4.4.1. Electron injection 124
4.4.2. Parasitic contact resistance in organic transistors 126
4.5. Film morphology of [60]PCBM 128
4.6. Charge transport mechanism in [60]PCBM 130
4.7. Other fullerenes and derivatives 134
4.7.1. C_{70} Methanofullerene 134
4.7.2. Fluorinated fullerene derivatives 137
4.8. Integrated circuits 142

4.8.1. Unipolar inverters 143
4.8.2. Unipolar ring oscillators 144
4.8.3. Complementary inverters 145
4.9. Outlook 147
Reference List 148

Chapter 5: Ambipolar organic field-effect transistors for opto/electronic applications 155
5.1. Introduction 156
5.2. Chemical characterization of Squarylium dye 157
5.3. Ambipolar organic field-effect transistors 160
5.3.1. Squarylium as organic semiconductor 160
5.3.2. [60]PCBM - OC_1C_{10}-PPV blend as organic ambipolar semiconductor 162
5.4. Ambipolar transistor applications 164
5.4.1. UV-Vis and near-IR absorption measurements 164
5.4.2. Light-sensing OFETs 165
5.4.3. Complementary-like integrated circuits 172
5.5. Outlook 173
Reference List 174

Chapter 6: Fabrication of Organic Transistors by Interlayer Lithography 177
6.1. Introduction 178
6.2. Electrode patterning by Interlayer Lithography 179
6.3. OFETs and their integrated circuits 181
6.4. Outlook 185
Reference List 187

Chapter 7: Low-Voltage Organic Transistors and Circuits based on Self-Assembled Monolayer Dielectrics 191
7.1. Introduction 192
7.2. SAM based gate dielectrics 193
7.3. Surface energy and solution processing 194

7.3.1. Surface energy of hybrid dielectric 195
7.3.2. Liquid surface energy of organic semiconductor solutions 196
7.4. Low-voltage, high mobility n-type OFETs 199
7.5. Low-voltage complementary inverters 201
7.6. Outlook 203
Reference List 204

Chapter 8: Thin-Film Transistors based on Transparent Oxide Semiconductors deposited by Spray Pyrolysis 207
8.1. Introduction 208
8.2. Air-stable TFTs based on transparent oxide semiconductors 208
8.2.1. TiO_2 semiconductor layers 209
8.2.2. ZnO semiconductor layers 212
8.3. Spray Pyrolysis on Self-Assembled Monolayer gate dielectrics 214
8.3.1. Low voltage, high mobility ZnO transistors 214
8.3.2. Low voltage ZnO based unipolar inverters 217
8.4. UV-induced doping in ZnO transistors 218
8.5. Outlook 219
Reference List 220

Chapter 9: Conclusion 223

Appendix A: List of patents and publications 227
A.1. Patents 227
A.2. Journal Publications 227
A.2.1. Articles in preparation or submitted 227
A.2.2. Published Articles 228
A.2.3. Conference Proceedings 230

Appendix B: Abbreviations, Symbols and Constants 231
Abbreviations 231
Symbols 233
Constants 233

List of Figures and Tables

Figures

		p.
1.1	Crystalline silicon and fluorescent organic semiconductors under UV illumination	20
1.2	Flexible, organic based radio frequency identification tags	21
1.3	Examples of organic based display technology	23
2.1	Electronic configuration in Carbon atoms	30
2.2	σ- and π-bond in Ethene molecule	31
2.3	Energy levels resulting from a π-bond in Ethene	32
2.4	Peierls Distortion in Polyacetylene	32
2.5	Intersystem crossing between singlet and triplet states	34
2.6	Multiple Trapping and Release model	37
2.7	Bässler model accounts for energy disorder in form of a gaussian-distributed DOS	39
2.8	Energy levels in a metal-semiconductor interface without and with a dipole layer	42
2.9	Schematic representation of a typical FET structure in the cross-section and from the top	43
2.10	Operation regimes of FETs	44
2.11	Schematic representation of transfer and output characteristics of unipolar field-effect transistors	47
2.12	The most common FET configurations	49
2.13	Charge injection in top gate FETs	50
2.14	Density of states broadening at the interface induced by disordered dipoles in dielectrics with high ε	52

2.15	Chemical structure of unsubstituted and alkyl end-substituted oligothiophenes, Pentacene	54
2.16	Crystal packing arrangements found for many acene and thiophene based molecules	55
2.17	Chemical structure of poly(3-hexylthiophene)	56
2.18	Chemical structure of [60]PCBM	57
2.19	Charge accumulation in an ambipolar OFET	60
2.20	Calculated transfer and output characteristics of an ambipolar transistor	61
2.21	Schematic representations of various inverter circuits	66
2.22	Schematic output characteristics and power consumption of unipolar and complementary voltage inverters and the determination of their noise margins	67
2.23	Simplified schematic of exciton dissociation at junction between donor and acceptor	71
2.24	Droplets of water on hydrophilic and hydrophobic surfaces	71
2.25	Definition of contact angle and surface energy components in a liquid drop on a solid surface	72
2.26	ZnO energy band diagram	77
3.1	Bragg diffraction	94
3.2	Bonding of hexamethyldisilazane molecules on SiO_2 surface	104
3.3	Step-wise bonding of phosphonic acid molecules to Al-oxide surface	105
3.4	Ti isopropoxide, acetyl acetone, Zn acetate dihydrate, schematic of spray pyrolysis setup	106
3.5	Experimental setup for characterization of field-effect transistors	108
4.1	Transfer and output curves of a bottom gate transistor employing [60]PCBM as n-channel semiconductor and Au bottom contact S-D electrodes	115
4.2	Chemical structure of BCB before (monomer) and after curing (polymer network). Atomic force microscopy image of cured BCB surface	117
4.3	Capacitance measurements of dielectric Benzocyclobutene layers of different thicknesses and theoretical fit	118
4.4	Transfer and output characteristics of [60]PCBM – based top contact	119

	OFET on SiO_2/BCB dielectric layer system	
4.5	Transfer characteristics of [60]PCBM based bottom contact and top contact OFETs on BCB dielectric	120
4.6	Transfer characteristics of [60]PCBM based top contact OFET on BCB dielectric before and after stressing	121
4.7	Chemical structure of Cytop dielectric. Schematic representation of device architectures compared by their transfer curves. Output characteristics of a BC-TG device.	123
4.8	Transfer and output curves of [60]PCBM based transistors with top gold and top calcium S-D electrodes	125
4.9	Schematic representation of metal work functions relative to LUMO and HOMO energies of [60]PCBM. Effect of different work function metals on n-channel OFET performance	126
4.10	Contact resistance in [60]PCBM based top contact FETs with Au and Ca S-D electrodes	127
4.11	Analysis of [60]PCBM films by optical polarized microscopy, atomic force microscopy, differential scanning calorimetry and X-ray diffraction measurements	129
4.12	Analysis of [60]PCBM based transistor with Ca S-D top contacts on BCB dielectric at temperatures between 180 K and 430 K.	131
4.13	Molecular structures of [60]PCBM and [70]PCBM. Extinction coefficient of films on quartz substrates	135
4.14	Transfer and output characteristics of [70]PCBM based OFET with aluminium top contacts	136
4.15	Transfer and output characteristics of [70]PCBM based OFET with Al coated calcium top contacts	136
4.16	Molecular structures of perfluorinated methanofullerenes and their absorbance spectra	138
4.17	Transfer and output curves of F17-DOPF based FETs	139
4.18	Wetting envelopes of SiO_2-HMDS and BCB dielectric surfaces	140
4.19	Evolution of on and off currents over time in [60]PCBM and F17-DOPF based transistors in air	142
4.20	Circuitry and performance characteristics of unipolar voltage inverter constructed of [60]PCBM transistors	143
4.21	Circuitry and output characteristics of a 7-stage ring oscillator	145
4.22	Circuitry and performance characteristics of complementary voltage	146

	inverter constructed of n-type [60]PCBM and p-type PTAA transistors	
5.1	Molecular formula of SQ1. CSD Mercury ellipsoid diagram and numbering scheme of the structure of *trans*-SQ1. View of the packing scheme in the crystal lattice.	157
5.2	Cyclic voltammetry of SQ1	158
5.3	Lowest unoccupied molecular orbital (LUMO) and highest occupied molecular orbital (HOMO) of SQ1 obtained from density functional theory calculations	159
5.4	Polarized optical reflection microscopy of crystalline SQ1 films. Transfer and output characteristics of ambipolar SQ1 transistor	161
5.5	Schematic representation of LUMO and HOMO energies in SQ1 and PCBM:OC_1C_{10}-PPV blend	162
5.6	Molecular structures of OC_1C_{10}-PPV and [60]PCBM. Architecture of bottom gate-bottom contact ambipolar OFET. Transfer and output characteristics of the ambipolar blend transistor	163
5.7	Absorbance characteristics of thin films of SQ1 and PCBM:OC_1C_{10}-PPV blend	164
5.8	Ambipolar SQ1 transistor measured in dark and under illumination. Analysis of photosensitivity, external quantum efficiency and dynamic photo-modulation	166
5.9	Photo-modulation of ambipolar transfer characteristics of [60]PCBM:OC_1C_{10}-PPV blend transistor by fluorescent white light and a pulsed LED	170
5.10	Output curves of a complementary-like voltage inverter based on two ambipolar SQ1 transistors	173
6.1	Interlayer lithography process. Photograph of patterned PEDOT:PSS fields on glass	180
6.2	Array of PEDOT:PSS source and drain electrodes patterned on glass and PET	181
6.3	Schematic representation of transistor architecture and optical micrograph of crystalline diF-TESADT:PTAA film on PEDOT:PSS contact and glass substrate	182
6.4	Chemical structures of diF-TESADT, PTAA and [60]PCBM	182

semiconductors
6.5 Transfer and output characteristics of field-effect transistors with PEDOT:PSS source-drain electrodes patterned on glass by interlayer lithography 183
6.6 Schematic representation of complementary inverter circuit and its output characteristics in quasi-static operation 185

7.1 Molecular structure of octadecylphosphonic acid (ODPA). Water contact angle on Al-AlO_X electrode before and after treatment with ODPA 193
7.2 Schematic representation of metal-insulator-metal structures employed to measure the leakage currents at different stages of Al-AlO_X-SAM dielectric fabrication 194
7.3 Contact angles of water, diiodomethane and ethylene glycol on Al-AlO_X-ODPA 195
7.4 Pendant drops of F17-DOPF and [60]PCBM in chlorobenzene solutions used to measure liquid surface tension 196
7.5 Wetting envelopes for the AlOx-ODPA surface with coordinates of liquid surface energy components of various semiconductor solutions 197
7.6 Transfer and output characteristics of F17-DOPF based n-channel transistor fabricated on SAM dielectric 200
7.7 Transfer and output characteristics of P3HT based p-channel transistor fabricated on SAM dielectric 200
7.8 Output characteristics of complementary low-voltage inverter 202

8.1 Absorbance and transmission characteristics of TiO_2 films deposited by spray pyrolysis 209
8.2 Transfer and output characteristics of BG-BC TiO_2 transistor. Schematic representation of TiO_2 band gap and energy offsets to fermi levels of Au and Al injecting electrodes 210
8.3 Transfer and output characteristics of BG-TC TiO_2 transistor with Al S-D electrodes 211
8.4 Arrhenius-type dependence of saturation field-effect mobility in TiO_2 transistor on temperature 211
8.5 Evolution of electron mobility and current on/off ratio in a TiO_2 transistor stored and operated in air 212

8.6	Absorbance characteristics and close contact AFM images of ZnO films deposited by spray pyrolysis	213
8.7	Transfer and output characteristics obtained from a BG-TC TFT employing semiconducting ZnO films deposited by spray pyrolysis	214
8.8	Images of water droplets on the surfaces of Al-AlOx, Al-AlOx-SAM and Al-AlOx-SAM after annealing at 400°C in N_2	215
8.9	Transfer and output characteristics measured from low-voltage ODPA-based ZnO transistor and unipolar inverter	217
8.10	UV-induced shift of transfer characteristics of low voltage ZnO transistor	219

Tables

		p.
2.1	Truth table for an inverter	65
3.1	Information on chemical structures, material purity, solvent and concentration of the solutions, highest occupied (HOMO) and lowest unoccupied (LUMO) molecular orbitals of organic semiconductors employed in this work	101
4.1	Summary of performance parameters of transistors based on various fullerene derivatives and their liquid surface tension components in chlorobenzene solutions	140
5.1	Electrochemical data measured on Squaraine molecules by cyclic voltammetry and rotating disk voltammetry	158
6.1	Summary of performance parameters of [60]PCBM and diF-TESADT:PTAA based transistors	184
7.1	Summary of material properties of a range of soluble fullerene derivatives and performance characteristics of low-voltage transistors	197
8.1	Performance parameters of low-voltage BG-TC ZnO transistors based on AlOx-SAM dielectrics	216

Chapter 1: Introduction

Most people, when I introduce them to my research area, “Organic Electronics”, still wonder whether that means making bio-degradable, or ecologically friendly electronic devices. I then explain that these properties may apply to some outcomes of organic electronics, but that the notion of “organic” generally refers to “carbon based” materials, which often do not occur naturally, but which have been developed with the help of sophisticated chemical synthesis. More recently during the course of my PhD some people have started to react differently by asking about organic light-emitting diodes (OLEDs) and foldable displays, which they read or heard about.

While the first commercially available organic electronic components have been emerging on the market over the last few years, the research on organic electronic materials and devices has been flourishing everywhere in the world for decades.[3-8] Organic materials have been recommended for use in a wide range of applications, including organic photo-voltaics (OPVs),[10,11] OLEDs,[13] chemical or optical organic sensors,[14,15] organic memory elements and organic field-effect transistors (OFETs).[16-18] OFETs have been the focus of my work for this PhD thesis.

The microelectronics industry has been heavily relying on inorganic components, e.g. semiconductors such as Silicon (Si) [Fig. 1.1] and gallium arsenide (GaAs). So called metal-oxide-semiconductor field-effect transistor (MOSFET) technology is very well established and the large scale fabrication is cheap. The cost of a single MOSFET today is of the order of 10^{-7} US$.[19] Despite great research

progress in the area of organic devices it is unlikely that their performance will ever reach that of their inorganic analogues. The reasons for that lie in the inherently more disordered morphology and chemical bonding properties of the organic materials, as will be discussed in chapter 2. Nevertheless, for some emerging applications the well known inorganic materials are experiencing strong competition from organic materials [Fig. 1.1].

The development of organic electronics is driven by several technological advantages, which are in particular the availability of a wide range of materials, the ease of low cost processing, often from solution at room temperature and ambient pressure, and the facility of chemically tailoring the materials to suit particular purposes.[5,18,20] For example it is possible to alter the emission wavelength in OLEDs, maximise the orbital overlap to improve the charge carrier mobility, or change the surface energy to manage the behaviour of solutions on a surface. Furthermore, their light weight, in some cases optical transparency and compatibility with deposition onto mechanically flexible substrates[21] make organic materials interesting candidates for novel specialized applications. While the development, synthesis and purification of organic materials can be quite expensive, organic-based devices are expected to benefit from the advantages of low cost processing.[8] For example from solution, which, in principle, enables the deposition by low cost roll-to-roll, i.e. continuous, patterning techniques such as inkjet or gravure printing.[5,22] Eventually the cost of organic electronic components is therefore expected to fall below that of inorganic elements.[5,8]



Fig. 1.1: Crystalline silicon (left) and fluorescent organic semiconductors under UV illumination (right).

Organic field-effect transistors already comply with the performance requirements for use in some low-end, large area microelectronic applications, such as radio frequency identification (RFID) tags[23] or the driving circuitry in electrophoretic[24] or active matrix OLED (AMOLED) optical displays.[25] RFID technology based on silicon has been successfully implemented for, for example, tracking of high value items. Mass production, however, for lower cost articles could be greatly enhanced by introducing printed organic circuitry [Fig. 1.2].[23] The use of organic electronics for visual displays potentially enables the fabrication of very large area screens and flexible electronic paper, possibly fabricated using a printing technique.[24,25] Electrophoretic displays [Fig. 1.3(a)] with organic driving circuitry are already becoming commercially available since here the OFET performance is less critical than for AMOLED displays [Fig. 1.3(b-c)], which require large driving currents.[26] In the latter high charge carrier mobility (e.g. > 1 cm^2/Vs desirable) is needed to keep the transistor size to a minimum and to achieve a large pixel fill factor.

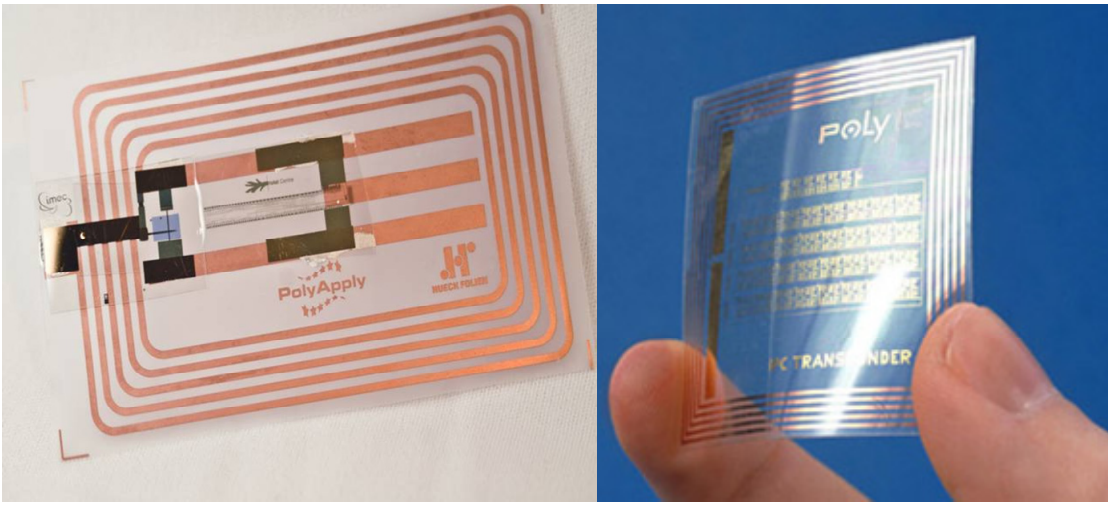


Fig. 1.2: Flexible, organic based radio frequency identification tags (left: *Holst Centre*[1], right: *Poly-IC*[9]).

The performance of some hole conducting organic semiconductors is nowadays comparable to that of amorphous silicon (α-Si),[27] a popular material for large-area, high volume applications in the electronics industry. But the prevailing problems, which are currently restricting the large scale implementation of organic electronics, are the following:[8,26,28]

- poor air stability of organic semiconductors, i.e. problems with unintentional doping, charge trapping and chemical instability

- relatively low charge carrier mobility, i.e. insufficient performance for fast switching applications
- high power consumption, due to lack of high performance electron transporting organic semiconductors for use in complementary circuits and the relatively high operating voltages

Furthermore, the challenge of patterning the organic materials efficiently and without performance loss has to be addressed before the production of organic integrated circuits can be moved to an industrial scale.

The work presented in this thesis addresses these problems and challenges and aims to demonstrate strategies to solve or circumvent them. First, the focus lies on the development of high mobility solution processed electron transporting OFETs. This is considered a major step towards the implementation of low-cost complementary integrated circuit design, which comprises both hole and electron transporting devices. Complementary logic[29] has proven to significantly reduce the power consumption, while improving the gain and noise margins compared to unipolar logic based on high performance hole transporting transistors.[30] Soluble fullerene derivatives were chosen as a promising class of materials to simultaneously fulfil the requirements of high electron mobility and facile processing from solution.[31]

Complementary logic circuits are normally constructed employing discrete hole and electron transporting transistors that require patterning of the respective materials at a high resolution without performance degradation, which still represents the most difficult production step. To address this issue another strategy is investigated, namely the use of ambipolar semiconductors, which can transport both, holes and electrons.[32,33] These rather versatile materials enable the fabrication of complementary-like circuits without the need for patterning of two separate semiconductors (i.e. p- and n-channel). Two different material systems are proposed: i) ambipolar Squaraine derivatives and ii) polymer:fullerene material blends. In this context it is also worth emphasizing the suitability of organic materials for optoelectronic devices. An interesting example is light sensing transistors, which respond to electrical as well as optical signals.[34-36] Since the electronic properties are strongly dependent on their chemical structure and morphology, organic materials can be tuned to a virtually infinite variety of optical absorption and emission spectra [Fig.

1.1]. This makes them interesting candidates for application in colour sensitive optical sensing arrays.[37] In this work ambipolar OFETs are investigated as ultraviolet (≈ 400 nm) and infrared (≈ 900 nm) light-sensing devices.

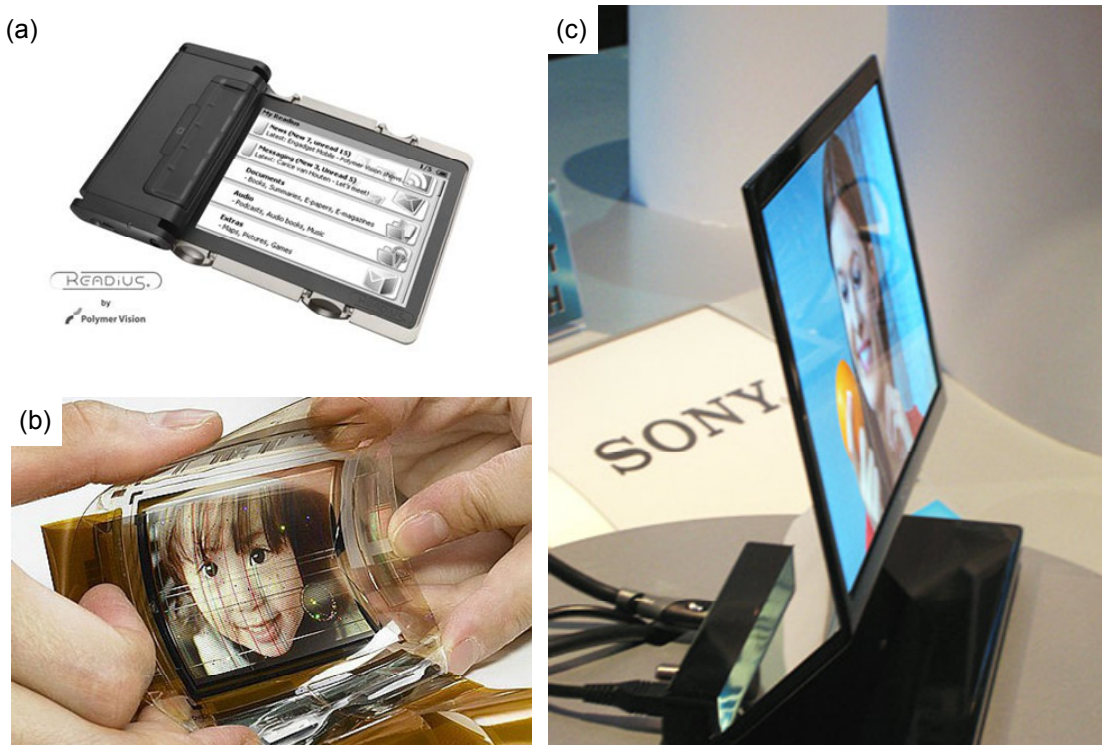


Fig. 1.3: Examples of organic based display technology: (a) flexible electrophoretic field-driven display (*Polymer Vision*),[2] (b) flexible current driven AM-OLED display (*Sony*), (c) first commercial 11 inch OLED TV (*Sony*).[12]

Another strategy in tackling the problem of patterning organic materials is to develop patterning methods that can provide high resolution with minimal material degradation as a result of the processing. Photolithography is most commonly employed in MOSFET technology and is thus also available to organic electronics. However the chemical bath and lift-off processes involved in this patterning method are sometimes complex and have been shown to affect the conducting or semiconducting properties of the patterned material.[38] A simplified lithography technique has been presented[39] and is here proposed also for the fabrication of short channel ($L \leq 20$ μm) OFETs.[40]

Besides the use of complementary logic, low operating voltages are also critical to ensure a low power consumption of organic electronic circuits. Currently most OFETs produced in research laboratories operate at 20-100 V.[25] These rather high operating voltages render conventional OFET technology incompatible with battery

powered applications. Since organic materials are expected to be most competitive in portable, light weight, mechanically flexible devices, OFET operation at < 5 V is essential for their implementation.[41] Lower operating voltages can be achieved through the use of either high-k or ultra-thin gate dielectrics.[42-45] Here the use of ultra-thin gate dielectrics based on self-assembled monolayers of alkylphosphonic acid molecules is investigated as a mean of reducing the operating voltages in solution processed OFETs and circuits.

In recent years the family of transparent oxide semiconductors (TOS) has drawn considerable attention in regard to their application in field-effect transistors and can be regarded as a serious competition to organic semiconductors.[46-49] Oxide based semiconductor materials combine several features that are absent or underdeveloped in traditional inorganic (i.e. α-Si) or organic semiconductors. For example they

- are hardly affected by ambient air or moisture,
- exhibit high charge carrier mobility, superior to that of amorphous silicon or organic semiconductors
- are compatible with a wide range of deposition techniques, including solution processing, and
- are highly transparent to the visible part of the electromagnetic spectrum.

Oxide semiconductors offer a promising route to reach the goals which research on organic electronics has been striving to achieve over the last few decades. A major drawback is currently the lack of facile deposition methods and the absence of a hole transporting metal oxide semiconductor, which in turn prevents the development and implementation of complementary logic. Furthermore, when deposited from solution, the films often require sintering at temperatures of 200 – 700 °C.[50-52] This is a problem when flexible, light weight substrates such as plastic foils are considered. Here TiO_2 and ZnO are investigated for use in high performance electron transporting field-effect transistors. The films are deposited employing a very simple solution deposition technique, namely spray pyrolysis.[53,54]

In summary, this work addresses several current challenges in the development of thin-film transistors for low-cost, light weight and flexible (opto-) electronics. First,

an introduction to the research on organic electronics is given in the following chapter as background to the work presented subsequently.

Reference list:

1 HolstCentre. http://www.holstcentre.com/ (2008).

2 PolymerVision. *The worlds first pocket eReader employing rollable display technology*, http://www.readius.com/ (2008).

3 Sun, Y., Liu, Y. & Zhu, D. Advances in organic field-effect transistors. *Journal of materials chemistry* **15**, 53-65 (2005).

4 Dimitrakopoulos, C. D. & Malenfant, P. R. L. Organic Thin Film Transistors for Large Area Electronics. *Adv. Mater.* **14**, 99-117 (2002).

5 Forrest, S. R. The path to ubiquitous and low-cost organic electronic appliances on plastic. *Nature* **428**, 911-918 (2004).

6 Kudo, K., Yamashina, M. & Moriizumi, T. Field-Effect Measurement of Organic-Dye Films. *Japanese Journal of Applied Physics* **23**, 130 (1984).

7 Koezuka, H., Tsumura, A. & Ando, T. Field-effect transistor with polythiophene thin film. *Synthetic Metals* **18**, 699-704 (1987).

8 Sheats, J. R. Manufacturing and commercialization issues in organic electronics. *J. Mater. Res.* **19**, 1974-1989 (2004).

9 PolyIC. http://www.polyic.com/en/index.php (2008).

10 C. J. Brabec, N. S. Sariciftci & J. C. Hummelen. Plastic Solar Cells. *Adv. Funct. Mater.* **11**, 15-26 (2001).

11 Gunes, S., Neugebauer, H. & Sariciftci, N. S. Conjugated Polymer-Based Organic Solar Cells. *Chem. Rev.* **107**, 1324-1338 (2007).

12 Sony. *First commercial organic light-emitting diode TV: Sony XEL-1*, http://www.sony.co.uk/product/tvp-oled-tv/xel-1 (2008).

13 Friend, R. H. *et al.* Electroluminescence in conjugated polymers. *Nature* **397**, 121-128 (1999).

14 Torsi, L. & Dodabalapur, A. Organic Thin-Film Transistors as Plastic Analytical Sensors. *Anal. Chem.* **77**, 380 A-387 A (2005).

15 Mabeck, J. & Malliaras, G. Chemical and biological sensors based on organic thin-film transistors. *Anal. Bioanal. Chem.* **384**, 343-353 (2006).

16 Sirringhaus, H. Device Physics of Solution-Processed Organic Field-Effect Transistors. *Adv. Mater.* **17**, 2411-2425 (2005).

17 Horowitz, G. Organic Field-Effect Transistors. *Adv. Mater.* **10**, 365-377 (1999).

18 Facchetti, A. Semiconductors for organic transistors. *Materials Today* **10**, 28-37 (2007).

19 Kumar, R. *Fabless Semiconductor Implementation*. (McGraw-Hill Professional, 2008).

20 Mas-Torrent, M. & Rovira, C. Novel small molecules for organic field-effect transistors: towards processability and high performance. *Chem. Soc. Rev.* **37**, 827-838 (2008).

21 Sheraw, C. D. *et al.* Organic thin-film transistor-driven polymer-dispersed liquid crystal displays on flexible polymeric substrates. *Appl. Phys. Lett.* **80**, 1088-1090 (2002).

22 Noh, Y.-Y., Zhao, N., Caironi, M. & Sirringhaus, H. Downscaling of self-aligned, all-printed polymer thin-film transistors. *Nat Nano* **2**, 784-789 (2007).

23 Subramanian, V. *et al.* Progress Toward Development of All-Printed RFID Tags: Materials, Processes, and Devices. *Proceedings of the IEEE* **93**, 1330-1338 (2005).

24 Jang, J. Displays develop a new flexibility. *Materials Today* **9**, 46-52 (2006).

25 Martin, S., Hamilton, M. & Kanicki, J. Organic-polymer thin-film transistors for active-matrix flat-panel displays? *Journal of the society for Information Display* **11**, 543-549 (2003).

26 Loo, Y.-L. & McCulloch, I. Progress and Challenges in Commercialization of Organic Electronics. *MRS Bulletin* **33**, 653-662 (2008).

27 Payne, M. M., Parkin, S. R., Anthony, J. E., Kuo, C.-C. & Jackson, T. N. Organic Field-Effect Transistors from Solution-Deposited Functionalized Acenes with Mobilities as High as 1 cm2/V.s. *Journal of the American Chemical Society* **127**, 4986-4987 (2005).

28 Sirringhaus, H. & Ando, M. Materials Challenges and Applications of Solution-Processed Organic Field-Effect Transistors. *MRS Bulletin* **33**, 676-682 (2008).

29 Crone, B. *et al.* Large-scale complementary integrated circuits based on organic transistors. *Nature* **403**, 521-523 (2000).

30 Smith, J. *et al.* High-performance organic integrated circuits based on solution processable polymer-small molecule blends. *Appl. Phys. Lett.* **93**, 253301-253303 (2008).

31 Anthopoulos, T. D. *et al.* Ambipolar Organic Field-Effect Transistors Based on a Solution-Processed Methanofullerene. *Adv. Mater.* **16**, 2174-2179 (2004).

32 Anthopoulos, T. D., Anyfantis, G. C., Papavassiliou, G. C. & de Leeuw, D. M. Air-stable ambipolar organic transistors. *Appl. Phys. Lett.* **90**, 122105 (2007).

33 Zaumseil, J. & Sirringhaus, H. Electron and ambipolar transport in organic field-effect transistors. *Chem.Rev.* **107**, 1296-1323 (2007).

34 Anthopoulos, T. D. Electro-optical circuits based on light-sensing ambipolar organic field-effect transistors. *Appl. Phys. Lett.* **91**, 113513-113513 (2007).

35 Hamilton, M. C., Martin, S. & Kanicki, J. Thin-film organic polymer phototransistors. *Electron Devices, IEEE Transactions on* **51**, 877-885 (2004).

36 Noh, Y.-Y. & Kim, D.-Y. Organic phototransistor based on pentacene as an efficient red light sensor. *Solid-State Electronics* **51**, 1052-1055 (2007).

37 Street, R. A. *et al.* Image capture array with an organic light sensor. *Appl. Phys. Lett.* **78**, 4193-4195 (2001).

38 Priscilla G. Taylor *et al.* Orthogonal Patterning of PEDOT:PSS for Organic Electronics using Hydrofluoroether Solvents. *Adv. Mater.* **21**, 2314-2317 (2009).

39 Huang, J. *et al.* Patterning of organic devices by interlayer lithography. *Journal of materials chemistry* **17**, 1043-1049 (2007).

40 Dong-Seok, L. *et al.* Interlayer lithographic patterning of high conductivity PEDOT:PSS for organic field-effect transistors. *submitted*.

41 Klauk, H., Zschieschang, U., Pflaum, J. & Halik, M. Ultralow-power organic complementary circuits. *Nature* **445**, 745-748 (2007).

42 Halik, M. *et al.* Low-voltage organic transistors with an amorphous molecular gate dielectric. *Nature* **431**, 963-966 (2004).

43 Yoon, M.-H., Facchetti, A. & Marks, T. J. Sigma-pi molecular dielectric multilayers for low-voltage organic thin-film transistors. *Proc. Natl. Acad. Sci. U. S. A.* **102**, 4678-4682 (2005).

44 Park, Y. D. *et al.* Low-voltage polymer thin-film transistors with a self-assembled monolayer as the gate dielectric. *Appl. Phys. Lett.* **87**, 243509 (2005).

45 Collet, J. & Vuillaume, D. Nano-field effect transistor with an organic self-assembled monolayer as gate insulator. *Appl. Phys. Lett.* **73**, 2681-2683 (1998).

46 Wager, J. F., Keszler, D. A. & Presley, R. E. *Transparent Electronics*. (Springer, 2008).

47 Fortunato, E. *et al.* Recent advances in ZnO transparent thin film transistors. *Thin Solid Films* **487**, 205-211 (2005).

48 Nomura, K. *et al.* Room-temperature fabrication of transparent flexible thin-film transistors using amorphous oxide semiconductors. *Nature* **432**, 488-492 (2004).

49 Ohta, H. *et al.* Frontier of transparent oxide semiconductors. *Solid-State Electronics* **47**, 2261-2267 (2003).

50 Aneeqa Bashir, P. H. W., Jeremy Smith, James M. Ball, George Adamopoulos, Donal D. C. Bradley, Thomas D. Anthopoulos,. High-Performance Zinc Oxide Transistors and Circuits Fabricated by Spray Pyrolysis in Ambient Atmosphere. *Adv. Mater.* **9999**, NA (2009).

51 Chang, Y.-J., Lee, D.-H., Herman, G. S. & Chang, C.-H. High-performance, spin-coated zinc tin oxide thin-film transistors. *Electrochemical and solid-state letters* **10**, H135-H138 (2007).

52 Norris, B., Anderson, J., Wager, J. F. & Keszler, D. A. Spin-coated zinc oxide transparent transistors. *Journal of physics.D, applied physics* **36**, L105-L107 (2003).

53 Perednis, D. & Gauckler, L. J. Thin film deposition using spray pyrolysis. *Journal of electroceramics* **14**, 103-111 (2005).

54 Studenikin, S. A., Golego, N. & Cocivera, M. Optical and electrical properties of undoped ZnO films grown by spray pyrolysis of zinc nitrate solution. *J. Appl. Phys.* **83**, 2104-2111 (1998).

Chapter 2: Background

The field of organic optoelectronics has captured a lot of attention over the past three decades. Tremendous progress has been made since the first optoelectronic devices based on organic materials were demonstrated in the 1980s. Understanding the principles of electronic processes (i.e. conduction, optical absorption and emission, etc.) in organic materials and the physics of organic semiconductor devices is critical to further improving their performance. Furthermore, the properties of transparent metal-oxides are discussed, which have recently been emerging as promising semiconductors for microelectronic applications.

2.1. Introduction to Organic Semiconductors

The semiconducting properties of some organic materials are intimately related to the atomic structure of carbon and its capability of engaging in molecular bonds. Furthermore the nature of interaction and resulting bond strength between organic molecules compared to that of inorganic crystalline materials helps us to understand their very different charge transport behaviour. Numerous attempts have been made to model charge transport in organic solids accurately, yet it has to be accepted that the mechanisms always depend on the particular material in question and its morphology, which in turn depends on a wide range of processing parameters and often also the ambient conditions. This chapter will concentrate on presenting the most important aspects of organic semiconductors, as background to the analysis of the work carried out in the general field of organic field-effect transistors in following chapters. An introduction to the theoretical background of the work on transparent oxide semiconductors is also presented.

2.1.1. Electronic structure and covalent bonds

Organic molecules and polymers mostly contain carbon atoms, which contain six electrons in a $1s^2 2s^2 2p^2$ configuration. Two electrons of opposite spins are in each, the 1s and in the 2s orbitals closest to the nucleus. The remaining two electrons separate into the degenerate $2p_x$ and $2p_y$ orbitals [Fig. 2.1].

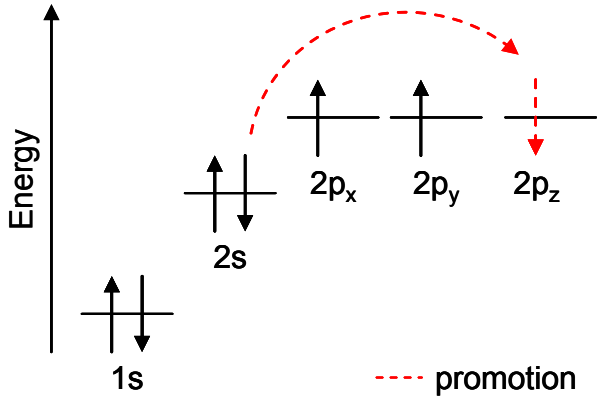


Fig. 2.1: Electronic configuration in Carbon atoms. In order to form energetically favourable double bonds, one of the 2s electrons can be promoted to the $2p_z$ orbital.

By promoting one of the 2s electrons into the $2p_z$ orbital, three sp^2 orbitals are created by hybridization of the 2s, $2p_x$ and $2p_y$ orbits. These hybrids can form σ-bonds with sp^2 electrons from neighbouring Carbon atoms or with 1s electrons from surrounding hydrogen atoms by spin pairing. The remaining 2p electron ($2p_z$) cannot participate in

the hybridization because its orbital axis is perpendicular to the plane in which the s, p_x and p_y orbits hybridize. However, p_z orbitals can approach side-by-side to form spin pairs and build a π-bond. The total binding energy brings the molecule into a much lower energy state and compensates for the promotion of one of the electrons. Bonds consisting of σ- and π- orbitals are referred to as double bonds (for example Ethene: C=C, see Fig. 2.2). A long chain of alternating double and single bonded carbon atoms is called a conjugated polymer, in which the p_z electrons are delocalized over the entire length of the polymer, due to the overlap of π-electron clouds.

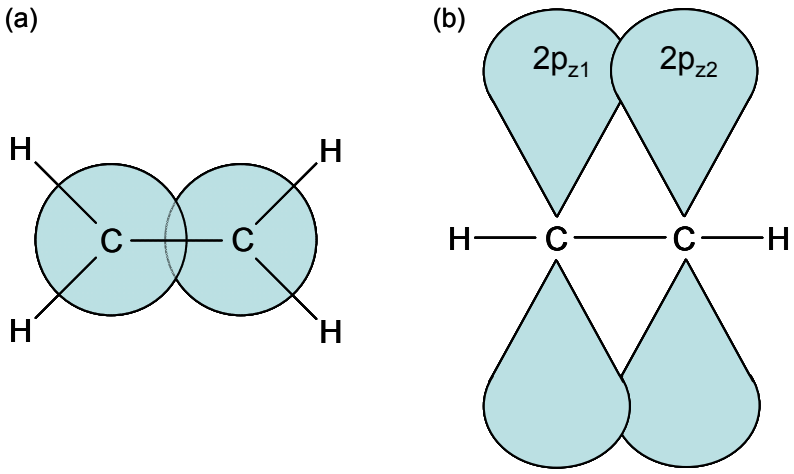


Fig. 2.2: σ- and π-bond in Ethene molecule. π-bond forms from overlap of the 2pz orbitals. (a) top view, (b) side view.

2.1.2. Energy levels

Using the Hückel[1] approximation, the molecular orbital energy level diagrams of conjugated molecules can be constructed. Erich Hückel suggested in 1931 that the σ- and π- orbitals could be treated separately. Assuming that the σ- orbitals form a rigid framework that determines the general shape of the molecule, he concentrated on finding the energies of the π- bonds. In the approximation all electron – electron interactions are neglected and only nearest neighbours are considered. For each π-bond, two energy levels are created due to different relative spin orientations, which separate into bonding (π) and antibonding (π*) states [Fig. 2.3]. Filling the molecular orbitals according to the Pauli- principle, the highest occupied molecular orbital (HOMO) - and the lowest unoccupied molecular orbital (LUMO) energy levels can be determined. With the number of pi-electron contributing atoms in the chain, the number of energy levels increases and the energy difference between the LUMO and

the HOMO level decreases. In an ideal infinite conjugated polymer, the very dense energy states can be described by a continuous energy band, which is filled with electrons up to the HOMO level.

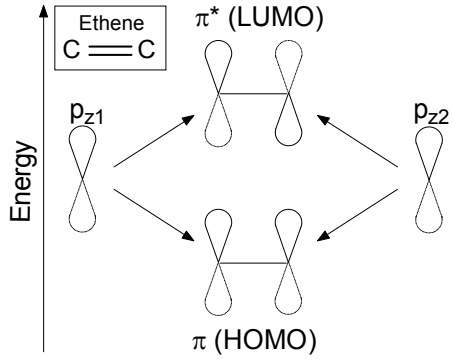


Fig. 2.3: Energy levels resulting from a π-bond in Ethene. In the ground state, the bonding levels are occupied by the two p_z electrons (HOMO), whereas the antibonding states are unoccupied (LUMO).

Often, a polymer can lower its energy by doubling its period, i.e. by assuming a configuration where single bonds alternate with double bonds [Fig. 2.4]. This so called Peierls-effect opens up a gap at the Fermi level, separating the HOMO and LUMO level by E_{gap}. It is therefore associated with the transition between a metallic phase and a semiconducting/insulating phase of materials.

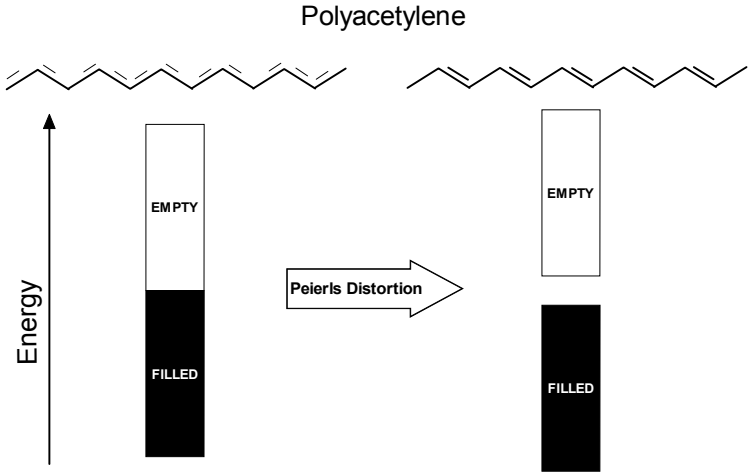


Fig. 2.4: Peierls Distortion in Polyacetylene: due to the regular alternation of double and single bonds, an energy gap opens between the HOMO and the LUMO level.

The electron delocalization in polymers is limited when parts of the chain of carbon atoms are out of plane or contain kinks, defects etc. These disturbances prevent the p_z orbitals from overlapping and cause localization of electrons.[2] The distance over which the electrons are delocalized in the polymer is referred to as conjugation length and is typically of the order of several nanometers. Due to defects, kinks etc. the conjugation length varies across the polymer material. The distribution of different conjugation lengths causes the separation of electronic states to vary across the polymer material and affects also the gap between HOMO and LUMO

levels. As a result, transition energies are not clearly defined, which is reflected in Gaussian shaped absorption peaks. Shortening the conjugation length leads to a wider separation of energy levels and thus to shorter absorption wavelengths, whereas less disturbances in the polymer facilitate absorption of longer wavelength. Consequently, by altering the carbon backbones or influential side groups of polymers, their electronic and optical properties can be tailored to specific applications. For example, polythiophenes have been optimized to be air stable while still providing high hole mobilities in FETs.[3-5]

2.1.3. Polarons

When an electron (hole) is injected into the conduction (valence) band in organic semiconductor films, the electrostatic interaction with its environment leads to a polarized region and deformation of the polymer chain. This distortion is referred to as polaron. Due to the alteration of the nuclear geometry and resulting attenuation of nearby bonds, polarons can create new excited energy states within the energy gap between the HOMO and the LUMO level. Single polarons possess spin, two nearby polarons forming a so called bipolaron however are spinless and create energy levels even deeper into the bandgap.[6-8] The spreading over one or several polymer chains of the polaron wavefunction indicates the extent of delocalization of charge carriers in polymers. A localized polaron wavefunction means that injected charges are trapped.

2.1.4. Excitons

Electrons can be optically or thermally excited across the gap between HOMO and LUMO level. Transitions require an amount of energy larger or equal to the gap energy. However, if the electron and the remaining hole stay spatially correlated due to Coulomb interaction, an exciton is formed, which requires slightly less energy due to the binding. Excitons therefore provide energy states within the HOMO-LUMO bandgap.[9,10]

There are two kinds of excited electronic states: singlet states, if the spins of the bound electron and hole are aligned anti-parallel, and triplet states if the spins are parallel. The energy of triplet states is slightly lower than that of singlets. Generally

spins cannot change orientation relative to each other during transitions and since photons do not carry angular momentum, optical transitions between singlet and triplet states are forbidden.[11]

However, the coupling between the electron's spin magnetic moment and the magnetic field arising from its orbital angular momentum (spin-orbit coupling) may allow for triplet-singlet transitions to occur. The coupling is particularly large when heavy atoms are present.[12]

2.1.5. Electronic transitions

According to the Franck-Condon principle,[13] electronic transitions take place on a faster time scale than the nuclear motions that are necessary to bring a molecule to its new vibrational ground state. Transitions which are compatible with the current geometry of the nuclei are more likely to happen than transitions requiring changes in the nuclei' positions. In a dispersion diagram *E(k)*, electrons are therefore likely to undergo predominantly vertical transitions to energy states above the LUMO level and then relax radiationless to the lowest vibrational level of the excited electronic state. From there they can decay to vibrational levels of the lower electronic state via photon emission [Fig. 2.5].

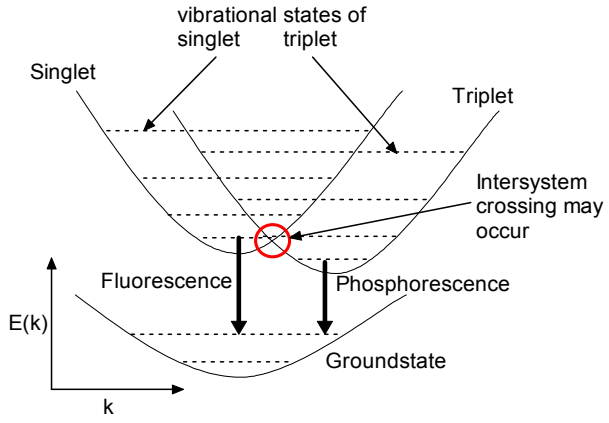


Fig. 2.5: A molecule can relax radiationless to lower vibrational states. Intersystem crossing may occur where singlet and triplet energy dispersion intersect. Vertical transitions occur under the emission of radiation from the singlet state (fluorescence) or the triplet state (phosphorescence).

It is important to note that the experimentally obtained absorption spectra usually reflect the vibrational characteristics of the excited state, whereas the emission spectra yield information about the lower electronic state. Due to the loss in energy during relaxation, the emitted radiation is generally of lower energy than the absorbed light (Stokes Shift[1,12]). This chain of events is referred to as fluorescence. The absorbed radiation is converted very fast into re-emitted energy.

In some cases, the presence of a triplet excited state plays a decisive role. Under particular circumstances excitons can undergo intersystem crossing[12] and occupy triplet states, where the potential energy curves of singlet and triplet states intersect. If an exciton crosses into a triplet state, it continues relaxing into lower vibrational levels. At the lowest level of the excited triplet state however, the exciton is trapped because the lowest triplet state is lower than the excited singlet state minimum. The environment can not take up the significantly larger energy quantum that would result from further relaxation and the radiative transition into the singlet groundstate is forbidden due to spin conservation. However, spin-orbit coupling allows for slow leakage of the energy via emission of radiation and for the molecules to slowly return to their groundstates. This process called Phosphorescence takes significantly longer (μs to ms) than Fluorescence (ns) and radiation is still emitted long after the original excited state was formed.[1]

2.2. Electronic Transport in Organic Semiconductors

The solid state description of amorphous or crystalline inorganic semiconductors is in most cases not suitable for the description of organic semiconductors. Their morphologies are dominated by disorder, defects and impurities. For electronic transport, localization of charge carriers is a big issue and various models have been developed to simulate and understand the processes involved in the conduction of charges in organic semiconductors. The applicability of each model strongly depends on the morphology of the particular material in question.

2.2.1. Bandlike transport

In an ideal semiconducting crystal, the electronic states describing the valence and the conduction band are separated by an energy gap, the so-called bandgap (E_{gap}) energy. At zero temperature the valence band is completely filled, whereas there are no electrons in the conduction band. By thermal excitation or through doping, charge carriers can be transferred to the conduction band, where they are ideally delocalized over the whole crystal. Their movement is limited by phonon scattering due to lattice vibrations, thus their mobility decreases with increasing temperature.

In inorganic semiconductors, the coupling between atoms is significantly stronger than in molecular crystals, which rely on van-der-Waals forces and π - π interactions. Hence, the bandwidth is smaller and the effective mass is larger in organic crystals, inflicting intrinsically lower charge carrier mobility.[14] Also, the weaker bonds in organic crystals are broken easily by phonons and lattice disorder, which lead to a higher density of localised states.

Band-like transport, indicated by an increase of mobility with decreasing temperature, has been reported only for high purity organic single crystals at low temperatures, such as naphthalene,[15] anthracene,[16] rubrene[17] and pentacene[18]. Yet most organic semiconductors are dominated by high degrees of disorder, grain boundaries and impurities, which prevent band-like transport.

2.2.2. Multiple trapping and release model

The multiple trapping and release (MTR) model was initially developed for amorphous silicon films.[19] G. Horowitz used it to explain charge transport in organic semiconductors with the help of a high concentration of localized trap states.[20,21] In this model it is assumed that moderate disorder allows for the density of states in a certain energy range to become sufficiently high, so that electronic states above a certain energy level are extended. Electronic states below that mobility level remain localized. Charges are trapped in the localized states and released back to the transport level, before they are trapped again [Fig. 2.6]. Assuming that carriers are trapped instantaneously when they arrive at a trap and that they can be released by a thermally activated process, the drift mobility μ_D is related to the mobility μ_0 in the perfectly delocalized band by an expression of the form:

$$\mu_D = \mu_0 \cdot \alpha \exp\left(-\frac{E_t}{k_B T}\right) \tag{2.1}$$

If the energy level of all traps is the same, E_t corresponds to the energy difference between the trap level and the delocalized conduction band edge, and α is the ratio of the effective density of states at the delocalized band edge to the concentration of traps. In the case of energy-distributed traps, effective values of N_t and α have to be calculated.

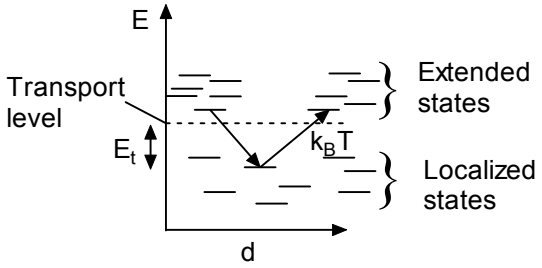


Fig. 2.6: In the MTR model charge carriers are traped in localized states at E_t below the transport level and can be released back into extended states by thermally activated processes.

2.2.3. Polaron transport

Charges that are localized in a lattice deformation caused by their own potential (polarons) can hop to a different location when the molecular configuration of the final site allows for a similar deformation as the original site. The polaron needs to have the same energy on either site. This transfer process can be explained using Marcus theory,[22-24] according to which the thermally activated transfer between neighbouring sites happens at a rate k_{CT} of:

$$k_{CT} = \frac{4\pi^2}{h} t^2 \frac{1}{\sqrt{4\pi\lambda k_B T}} \cdot e^{-\frac{(\lambda-\Delta E)^2}{4\lambda k_B T}} \qquad (2.2)$$

where t stands for the transfer integral or interaction energy between the two sites, ΔE is the charge's free energy difference after the transfer and λ is the total reorganization energy, which represents the thermal activation for polaron hopping and is given by $\lambda \approx 2E_P$ (the polaron binding energy). Accordingly, for high transfer rates and hence high charge carrier mobilities, high transfer integrals and full compensation between ΔE and λ are required. However, in most organic semiconductors variations of the backbone conformation, presence of impurities, structural defects and dipolar disorder cause the energy of polaronic charge carriers to vary across the polymer network.[4] Also, Marcus theory often leads to activation energies which are small compared to experimentally observed activation energies in organic semiconductors.[25,26]

2.2.4. Variable range hopping model

Conventionally, charge transport in metals and semiconductors is possible because of delocalized states, being limited by the scattering of the carriers with thermally induced lattice vibrations (phonons). In amorphous or organic semiconductors, this model becomes invalid because the mean free path of carriers is often lower than the mean atomic distance. In these materials one has to model

hopping between localized states, the main difference being that the transport is not anymore limited by phonon scattering, but phonon assisted. Hence, the charge carrier mobility increases with rising temperature and in most hopping models it follows a temperature dependence of the form:

$$\mu = \mu_0 \cdot e^{-\left(\frac{T_0}{T}\right)^{1/\alpha}} \tag{2.3}$$

where α is an integer ranging from 1 to 4.

One can usually distinguish between localized and delocalized transport phenomena when the mobility reaches values between 0.1 and 1 cm^2/Vs. For example, Miller and Abrahams[27] established a model which could explain the temperature dependence of the mobility by evaluating a hopping rate ν_{ij} from site *i* to site *j* with an energy difference of E_{ij} and spatial distance R_{ij}:

$$\nu_{ij} = \nu_0 \cdot e^{\left(-\frac{E_{ij}}{k_B T}\right)} \cdot e^{\left(-2\alpha R_{ij}\right)} \qquad \text{for } E_{ij} > 0 \tag{2.4}$$

$$\nu_{ij} = \nu_0 \cdot e^{\left(-2\alpha R_{ij}\right)} \qquad \text{for } E_{ij} < 0 \tag{2.5}$$

where α is the inverse of the decay length of the wavefunction and ν_0 is the attempt frequency. The two exponential terms account for the temperature dependency and the tunnelling probability, respectively. The model as such does not allow for jumps to sites further than the nearest neighbours, due to the exponential form of the tunnelling probability.

The model was modified by Mott,[28] who developed the variable range hopping model (VRH) to allow for hops over long distances with low activation energy or short distances with high activation energy. In his model the temperature dependence follows:

$$\mu_{VRH} \propto e^{\left(-\frac{T_0}{T}\right)^{1/(n+1)}} \tag{2.6}$$

where T_0 is a parameter inversely proportional to the density of states at the Fermi level and *n* is the dimensionality of the system (*n = 1, 2, 3*). The problem with the Mott analysis is that it assumes a constant density of states (DOS) thus making long distance hops disproportionately important.

2.2.5. Bässler disorder model

In order to account for the numerous sources of disorder in organic semiconductors, Bässler[29] developed a model based on a non-constant, disorder-broadened Gaussian density of transport states with a width σ [Fig. 2.7]. The model includes fluctuation of site energy and inter-site distance disorder. Using statistical Monte-Carlo simulations Bässler obtained a universal law relating the mobility to the degree of energetic and positional disorder as well as temperature T and electric field F:

$$\mu_{disorder} = \mu_0 \cdot e^{\left(-\frac{2\sigma}{3k_BT}\right)^2} \cdot e^{C\left[\left(\frac{\sigma}{k_BT}\right)^2 - \Sigma^2\right]\sqrt{F}} \tag{2.7}$$

μ_0 is the mobility limit at $T \rightarrow \infty$ and C is a constant that depends on the site spacing. The temperature dependence of the mobility thus follows $\ln \mu \propto T^{-2}$.

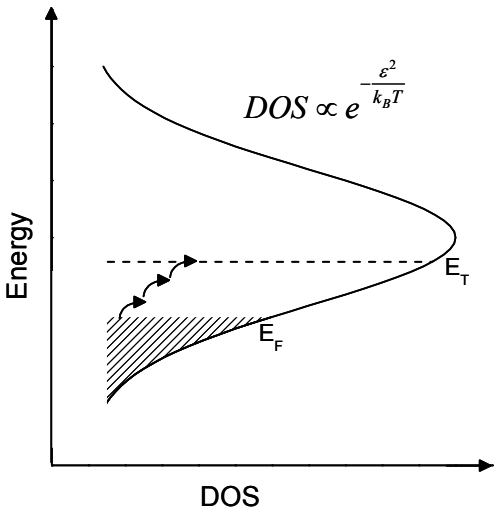


Fig. 2.7: The Bässler model accounts for energy disorder in form of a Gaussian-distributed DOS. The states are filled up to the fermi energy and higher energy levels, e.g. above the energy required for delocalized transport, can be reached by thermal excitation.

The Bässler model fits temperature and field-dependence of mobility well in conjugated polymers at very high fields, but cannot explain the field dependence at lower field strength (below 10^8 V/m). Novikov *et al.* improved the model by taking into account spatial correlations such as long-range charge-dipole interactions, which arise due to the random orientations of dipole moments of nearby molecules.[30,31] The result was the so called correlated disorder model (CDM), which suggests that the mobility is given by:

$$\mu_{CDM} = \mu_0 \cdot e^{\left(-\frac{3\sigma}{5k_BT}\right)^2} \cdot e^{C_0\left[\left(\frac{\sigma}{k_BT}\right)^{3/2} - 2\right]\sqrt{\frac{q_e aF}{\sigma}}} \tag{2.8}$$

where C_0 is 0.78 and a is the intersite separation.[32,33] This formula bears a better agreement with the observed mobility at low field strength. Both models however consider only single charges and are in principle not suited for situations of high carrier densities as is the case in some semiconductor devices such as FETs. In long channel FETs, the effect of the typically small lateral fields is negligible.

2.2.6. Vissenberg - Matters model

In order to fit the charge carrier density dependent mobility in FETs, Vissenberg and Matters refined the VRH model by taking into account the accumulation of charge in particular regions of the semiconducting layer.[34] Accumulated charge carriers fill the lower lying states and additional charges will occupy states at relatively high energies. Those charges will require comparatively less energy to tunnel to a different site. As a result, the mobility increases with accumulation of more charge carriers at increasing gate voltages. At low carrier densities and low temperature, the transport properties are dominated by the tail of a Gaussian density of localized states distribution. This can be approximated by an exponential DOS of the form:

$$g(\varepsilon) = \frac{N_t}{k_B T_0} \cdot e^{\left(\frac{\varepsilon}{k_B T_0}\right)} \qquad \text{for } -\infty < \varepsilon \leq 0 \tag{2.9}$$

where N_t is the number of states per unit volume, T_0 is the width of the exponential distribution and ε is the level energy. Using percolation theory an expression for the local field-effect mobility in a transistor can be derived as a function of the carrier concentration p:

$$\mu(V_{eff}) = \frac{\sigma_0}{e} \cdot \left(\frac{\left(\frac{T_0}{T}\right)^4 \sin\left(\pi \frac{T}{T_0}\right)}{(2\alpha)^3 B_c} \right)^{T_0/T} \cdot p^{\frac{T_0}{T}-1} \quad \text{with} \tag{2.10}$$

$$p = \frac{(C_i V_{eff})^2}{2 k_B T_0 \varepsilon_S \varepsilon_0} \tag{2.11}$$

where σ_0 is a conductivity pre-factor from percolation theory, α is the effective overlap parameter between the wave functions of localized states, B_c is the critical number of bonds for the onset of percolation (B_c = 2.8 for 3-dimensional amorphous systems), ε_s is the dielectric constant of the semiconductor, C_i is the geometrical capacitance of the gate dielectric and V_{eff} is the effective potential that determines the amount of induced charges at a given position within the transistor channel. The temperature dependence of the mobility follows an Arrhenius type behaviour, $\mu \propto e^{\frac{E_A}{k_B T}}$, where the activation energy E_A decreases with increasing gate voltage, in agreement with experimental results in disordered semiconductors.

For the source-drain current (I_D) in the saturation regime in FETs one can derive:

$$I_{D,sat} = \frac{\sigma_0}{e} \cdot \left(\frac{\left(\frac{T_0}{T}\right)^4 \sin\left(\pi \frac{T}{T_0}\right)}{(2\alpha)^3 B_c} \right)^{T_0/T} \cdot \left(\frac{1}{2k_B T_0 \varepsilon_S \varepsilon_0} \right)^{\frac{T_0}{T}-1} \cdot C_i^{\frac{2T_0}{T}-1} \cdot \frac{WT^2}{L2T_0(2T_0 - T)} \left(V_{eff}\right)^{\frac{2T_0}{T}} \tag{2.12}$$

where L and W are the length and width of the transistor channel. In systems where the mobility is independent of the gate voltage, T equals T_0 and the equation collapses to the classical saturated transistor equation.

The Vissenberg-Matters model has been successfully employed to model field effect mobility in disordered systems.[35,36] Differences in charge carrier mobility amongst a variety of device structures based on the same material were explained by differences in carrier concentrations.[36-39]

In some cases results have shown that several concepts (e.g. polaron hopping and disorder) are required to explain experimentally observed transport properties accurately.[25] This happens when the expected activation energy for polaronic transport starts to become comparable to the observed activation energy of the field-effect mobility near room temperature for high mobility devices.[26]

2.2.7. Metal – organic semiconductor interfaces

In many applications, charge carrier injection from metals into organic semiconductors plays an important role. Often the work function of the electrode material does not match the HOMO or LUMO level of the semiconductor in use. The charge carriers to be injected therefore have to overcome a potential Mott-Schottky barrier at the metal-semiconductor interface, which is equal to the difference between HOMO/LUMO level (more precisely the positive or negative polaron level) and the Fermi level in the metal [Fig. 2.8(a)].[40] Depending on which level is closer to the work function of the electrode, HOMO or LUMO, holes or electrons are easier to inject into the valence or conduction band, respectively. In particular cases the barrier height can be influenced by introducing dipoles at the metal surface, for example by using self-assembled monolayers [Fig. 2.8(b)].[41] The presence of dipoles changes the metal work function Φ_{metal} (i.e. shift in vacuum level by Δ) and if employed correctly, can lead to an improvement of charge injection into organic semiconductors.[42,43]

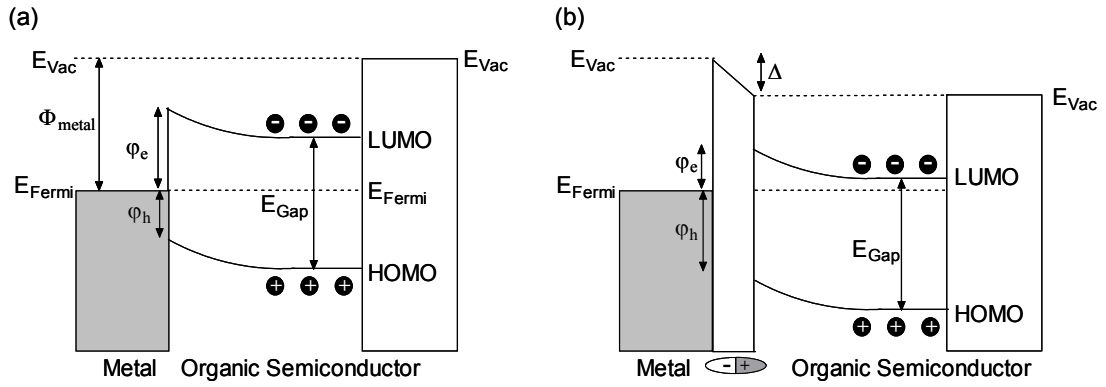


Fig. 2.8: Energy levels in a metal-semiconductor interface (a) without and (b) with a dipole layer. Alignment of the Fermi level in metal and semiconductor causes bending of the HOMO and LUMO levels. The barrier heights for injection of electrons (φ_e) and holes (φ_h) can be modified by introducing a dipole layer at the interface (b).

For a better understanding of charge injection, the Mott-Schottky barrier model has been complemented by a variety of models, such as thermally assisted tunnelling from the metal to localized states,[44] tunnelling into polaron levels in polymers,[45] thermally assisted injection into an energetically disordered dielectric[46,47] or diffusion-limited thermionic emission.[48]

2.3. Field-Effect Transistors

2.3.1. Operating principles

A field-effect transistor consists of several basic components [Fig. 2.9]. A semiconducting layer is in contact with a source and a drain electrode of width *W*, which are situated at a distance *L* of each other. The semiconducting layer is separated from a third electrode, the gate electrode, by an insulating layer, the gate dielectric. The semiconducting layer can be sputtered, vacuum sublimed, spin coated or drop-cast depending on the material. The gate electrode is highly conductive and can be made using doped inorganic semiconductors, metals or conductive polymers/oxides. For the dielectric it is common to use inorganic insulators such as SiO_2 (thermally grown or sputtered), Al_2O_3 and SiN_x or polymeric insulators, such as poly(methyl methacrylate) (PMMA), poly(4-vinylphenol) (PVP) or benzocyclobutene (BCB) amongst others (see section 2.3.3.). The drain and source electrodes can also be metals or conducting polymers, such as PEDOT:PSS, which are used to exploit the advantages of inkjet printing.[49]

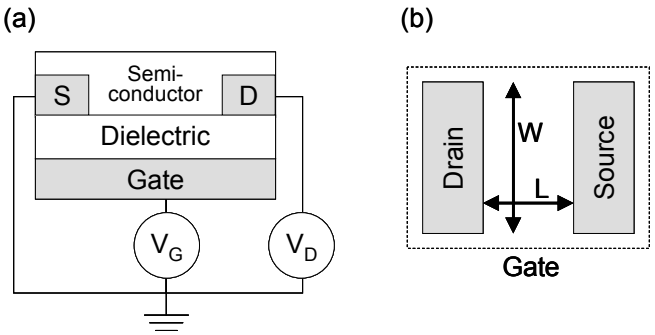


Fig. 2.9: Schematic representation of a typical FET structure (a) in the cross-section and (b) from the top.

Assuming that the drain and source electrodes are both grounded and that a voltage is applied to the gate electrode, a simple metal insulator semiconductor (MIS-) diode forms between the drain/source and the gate electrode. For a positive gate voltage, negative charge carriers (electrons) are injected into the semiconductor and accumulate at the semiconductor-insulator interface. At negative gate bias, positive charge carriers (holes) accumulate. The amount of accumulated charge is directly proportional to the gate voltage and to the capacitance of the insulator. The first injected charges are likely to be trapped in localized states in the semiconductor or at the dielectric surface and only additional charges which are injected at a gate voltage

above a certain threshold voltage V_T will be mobile. The effective gate voltage is therefore given by V_G - V_T and the transistor operates in the accumulation mode. At the same time, impurities can act as dopants and provide free charges even at zero gate bias, so that an opposite gate voltage has to be applied to completely deplete the interface of free charges and to turn the transistor off. The transistor then operates in the depletion mode.

At zero drain-source voltage (V_D) and a given gate potential, a homogeneous channel of accumulated charges forms at the semiconductor/insulator interface between the drain and the source electrodes [Fig. 2.10(a)]. The charge carrier density decreases exponentially with increasing distance from the interface.[37]

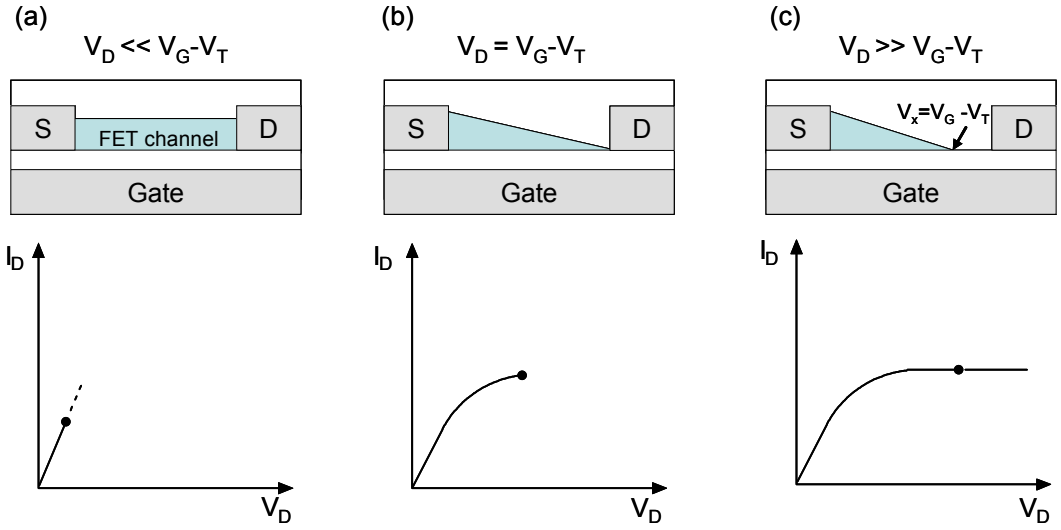


Fig. 2.10: Operation regimes of FETs: (a) Linear regime, (b) Pinch-Off Point, (c) Saturation regime.

When a small drain voltage ($V_D < V_G - V_T$) is applied, the charges migrate along the semiconductor-insulator interface towards the drain electrode, where they are absorbed. A linear gradient of the charge density is established and a current flows, which is proportional to V_D (linear regime) [Fig. 2.10(b)]. When the drain voltage is increased further and reaches $V_D = V_G$ - V_T, the difference between the local potential $V(x)$ and the gate voltage falls below the threshold voltage and a depletion region forms at the drain electrode. The channel is "pinched off" at $V_D = V_G$ - V_T and the drain current is now independent of V_D [Fig. 2.10(c)]. Only a limited amount of charges can be swept across the depletion region by the comparatively high electric field between the pinch-off point and the drain electrode. Further increasing V_D mostly leads to an expansion of the depletion region and thus a shortening of the

channel, which however is small compared to the channel length L. I_D is saturated (saturation regime) for the given gate bias and can only increase significantly when the number of charge carriers is increased in the channel region by means of a higher gate voltage.

Since the first OFET demonstration in 1984,[50] great research effort has been directed towards the description of charge transport within the channel. In many cases, a relatively simple approximation is used, which originates from studies on the first inorganic field-effect transistors. In the gradual channel approximation it is assumed that the field perpendicular to the current flow generated by the gate voltage is much larger than the lateral electric field parallel to the current flow. The model describes the different operating regimes of FETs quite well for long channel transistors, but starts to fail for very short channel lengths, in which case the depleted portion of the channel in saturation becomes comparable to the channel length.

In accordance with the gradual channel approximation, the current-voltage characteristics of FETs can be derived as follows. For gate voltages above the threshold voltage, the density of accumulated mobile charge at the semiconductor/insulator interface is

$$Q_{mob} = C_i \cdot (V_G - V_T) \tag{2.13}$$

where C_i is the capacitance per unit area (geometrical capacitance) of the gate dielectric. When the drain-source voltage is turned on and the channel potential $V(x)$ drops linearly between drain and source, the induced mobile charge in dependence on the position in the channel is given by:

$$Q_{mob} = C_i \cdot (V_G - V_T - V(x)) \tag{2.14}$$

Neglecting diffusion, the drain current I_D is proportional to the channel width W, the charge carrier mobility μ, the mobile charge density Q_{mob} and the electric field $F(x) = \frac{dV}{dx}$ at the position x:

$$I_D = W \mu Q_{mob} F(x) \tag{2.15}$$

In this model μ is assumed to be gate voltage independent.

Substitution gives:

$$I_D dx = W\mu C_i \cdot (V_G - V_T - V(x))dV \tag{2.16}$$

Integration over the entire transistor channel, i.e. over the entire potential range between the electrodes, gives the gradual channel approximation:

$$I_D = \frac{WC_i}{L} \cdot \mu \cdot \left((V_G - V_T) \cdot V_D - \frac{V_D^2}{2} \right) \tag{2.17}$$

Approximating $V_D << V_G$ results in a simplified formula for the linear regime:

$$I_{D,lin} = \frac{WC_i}{L} \cdot \mu \cdot (V_G - V_T) \cdot V_D \tag{2.18}$$

The field-effect mobility can be extracted directly from the slope of experimentally obtained transfer characteristics of a transistor (I_D vs. V_G):

$$\mu_{lin} = \frac{\partial I_D}{\partial V_G} \cdot \frac{L}{WC_i V_D} \tag{2.19}$$

In the saturation regime, $V_D = V_G - V_T$ can be substituted into the gradual channel approximation to obtain:

$$I_{D,sat} = \frac{WC_i}{2L} \cdot \mu \cdot (V_G - V_T)^2 \tag{2.20}$$

The saturation mobility is obtained as:

$$\mu_{sat} = \frac{\partial^2 I_{D,sat}}{\partial V_G^2} \cdot \frac{L}{WC_i} \tag{2.21}$$

The independence of the mobility from the gate voltage is, in reality, inaccurate in many solution processed organic semiconductor systems.[51,52] To circumvent this discrepancy, often models are used that presuppose a particular transport theory commonly exhibiting power-law dependence of the form $\mu = \mu_0 (V_G - V_T)^{\alpha}$.[53,54] Here, μ_0 is the mobility prefactor defined as the mobility at $V_G - V_T = 1$ V and α is a constant that can be extracted from experimental data. Although there is a physical basis for this approach, it is unsatisfactory as a stand-alone measure without experimental evidence further supporting the use of a particular transport model. Other models have also been used but, again, invoke a transport model before the mobility is extracted.[39] Attempts at re-formulating equations (2.18) and (2.20) using a mobility of the form of a polynomial of n^{th} degree dependence on the gate voltage can determine an accurate

fit of the mobility without presupposition of a transport model.[55] Such empirical fitting techniques, where the degree of precision is somewhat arbitrary, can leave physical interpretation with a lot to be desired. In this report the threshold voltage and mobility will generally be extracted by extrapolation of $I_{D,lin}$ and $I_{D,sat}^{1/2}$ vs. V_G [Fig. 2.11(a)].

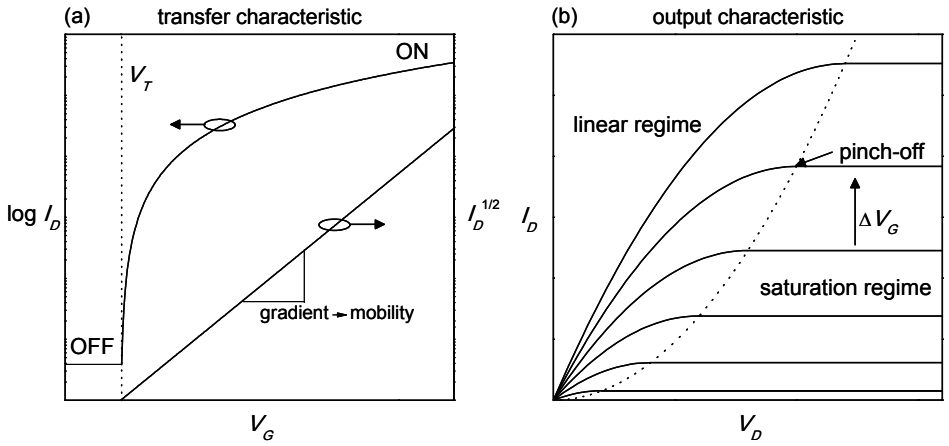


Fig. 2.11: Schematic representation of (a) transfer (in saturation) and (b) output characteristics of unipolar field-effect transistors.

The exact origin of the threshold voltage (indicated in Fig. 2.11(a)) is most often unknown, but it can be assumed that built-in dipoles,[56] impurities, interface states and charge traps contribute.[57] The number density of trapped charges is typically related to the threshold voltage or a shift therein by:

$$n_{trap} = \frac{V_T \cdot C_i}{e} \tag{2.22}$$

V_T can be reduced by using gate insulators with higher dielectric constants[58] or by reducing the thickness of the dielectric,[59] i.e. the induction of more charges at lower applied gate voltages. The threshold voltage of a device can change over time, for example, if it increases due to bias stress. During measurements this can lead to large hysteresis, i.e. current differences between forward and backward scanning of bias voltages.[60-64] Also stressing the device by continuous operation over prolonged periods of time can lead to threshold voltage shifts, which are generally associated with the charging of deep trap states in the transistor channel. Trapping of charge can occur through different mechanisms and in different locations, including trapping in near-surface defects of the dielectric, trapping in localized states at the dielectric/semiconductor interface, trapping in the semiconductor, ion migration in the

dielectric or the semiconductor and trapping due to structural changes of the semiconductor.[61] The influence of various surface treatments and self-assembled mono layers on the interface quality and the threshold voltage has been investigated.[65]

The most important parameters for characterizing and comparing field-effect transistors are the charge carrier mobility, the on/off current ratio, the threshold or switch-on voltage and the subthreshold slope. All these parameters can be extracted from the transfer (I_D vs. V_G) and the output (I_D vs. V_D) curves, schematic representations of which are shown in Fig. 2.11. The subthreshold slope is calculated as

$$S = \frac{\partial V_G}{\partial(\log_{10} I_D)} \tag{2.23}$$

and is expressed in V/dec, i.e. the change in gate voltage that induces a drain current increase by one order of magnitude. In MOSFET theory the subthreshold swing is approximated by:[66]

$$S \approx \frac{k_B T}{e} \ln 10 \cdot \left(1 + \frac{C_D + C_{it}}{C_i}\right) \tag{2.24}$$

where k_B is the Boltzmann constant, C_D is the depletion layer capacitance, $C_{it} = en_{trap}$ is the capacitance due to the interface trap density n_{trap} and e is the elementary charge. This method gives an estimation for the upper limit of the trap density, which is hence denoted $n_{trap}^{\max}$.[67] Assuming that the transistor channel is entirely depleted (i.e. $C_D \approx 0$), the interfacial trap density is obtained by rewriting equation 2.24 as:[68]

$$n_{trap}^{\max} \approx C_i \left(\frac{S}{k_B T \ln 10} - \frac{1}{e}\right) \tag{2.25}$$

For a fully depleted transistor and in the absence of interface traps one finds the room temperature limit for the subthreshold slope to be[69]

$$S \to \frac{k_B T}{e} \ln 10 \approx 60 mV / dec \tag{2.26}$$

A small subthreshold slope indicates efficient formation of a conductive channel and is associated with a low density of traps in the channel. It is therefore considered an important figure of merit for good dielectric-semiconductor interfaces.

The current on/off ratio is often limited by non-negligible bulk conductivity of the semiconductor, particularly in short channel devices. This can in some cases be controlled by reducing the semiconductor film thickness. In such a case efficient patterning of the semiconductor is also needed to control the cross talk between different transistors on the same substrate and to reduce leakage currents to the gate.

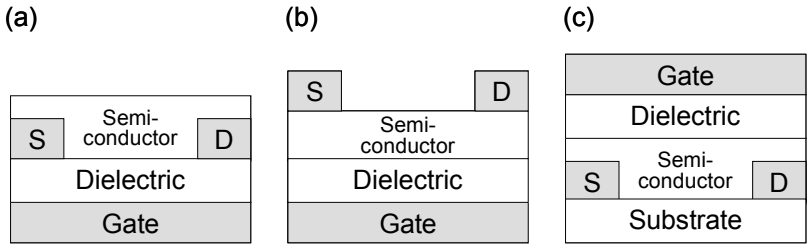


Fig. 2.12: The most common FET configurations: (a) planar bottom contact/bottom gate, (b) staggered top contact/bottom gate, (c) staggered top gate.

Field-effect transistors can be built in a variety of configurations, depending on the processability of the semiconductor and the dielectric material. The most common structures are bottom contact - bottom gate (BC-BG), top contact-bottom gate (TC-BG), and bottom contact-top gate (BC-TG) devices [Fig. 2.12]. The various geometries often lead to different device characteristics. For example, in BC-BG devices, charges are directly injected into the channel at the semiconductor/insulator interface, whereas in the other structures they have to travel through a layer of bulk semiconductor in order to reach the interface. However, in these devices charges are not only injected from the edges of the electrodes, but also from those parts of the electrode that overlap with the gate [Fig. 2.13], allowing for lower contact resistance.[70] Additional advantages of a top gate architecture include the encapsulating effect of the gate dielectric and gate electrode on top of the semiconducting channel, as well as the possibility of employing high resolution patterning methods for structuring the drain and source electrodes without the risk of degrading the other TFT component layers.[71] In addition, the different structures may yield different morphologies at the interface between semiconductor/insulator and semiconductor/electrodes.[70] Known phenomena include the formation of trap states during metal evaporation on organic semiconductors.[72] For comparison of different semiconductors, it is therefore important to bear in mind which device geometry was employed.

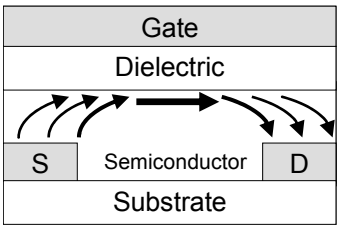


Fig. 2.13: Charge injection in top gate FETs. Charges are not only injected and extracted through the edges, but also through the surface of the electrodes, where there is an overlap with the overlying gate electrode.

2.3.2. Charge carrier injection in FETs

Depending on what kind of semiconductor is used, the choice of electrode material is crucial to ensure sufficient charge carrier injection at reasonable gate voltages.[73] Only if the barrier height (ϕ_h , ϕ_e) for one type of charge carrier is very small, one can consider the contact to be ohmic [Fig. 2.8]. Otherwise, contact resistance has to be taken into account in the modelling of the device characteristics. In the output characteristic, high non-ohmic contact resistance is usually observed in form of initially suppressed and then super-linearly increasing current in the otherwise linear region.[74]

Contact resistance can be measured by non-contact scanning probe potentiometry (e.g. Kelvin probe) as a voltage drop at the electrodes[73,75] or by four-point probe measurements.[76] Another way to determine the contact resistance is by extracting the channel resistances of identical transistors with different channel lengths from the linear regime. Extrapolation to zero channel length gives an estimate of the contact resistance (scaling method).[77-79] Recently, Natali *et al.* described a method that allows to extract contact resistance from the current-voltage characteristics of a transistor by differential analysis.[53] It exploits a variety of functional dependencies of the current on the gate voltage, which are induced by contact resistances. Particularly for small channel length, the contact resistance can be comparable to the channel resistance and affect the transistor's performance, most strongly in the linear regime.[80,81] A large portion of the source-drain voltage then already drops at the contacts and not across the channel.

The temperature dependence of contact resistance is often expressed in terms of the thermionic emission model, which predicts an injection current density of:[46,48,76]

$$J = A^* T^2 \exp\left(-\frac{e\phi_b}{kT}\right) \tag{2.27}$$

where A^* is the effective Richardson constant, e the elementary charge and ϕ_b is the energy barrier height at the interface.[82] At high fields the injection is enhanced by carrier tunnelling, which is enabled by energy band-bending at the interface. In disordered semiconductors a less thermally activated injection process has been observed. This is because in a Gaussian DOS the equilibrium energy, to which the charge carriers have to be injected is located at an energy σ^2/kT from the centre of the DOS, which facilitates the hopping of charges from the metal fermi level into the disordered energy levels in the semiconductor at low temperatures.[82]

Furthermore in low mobility materials a space charge region was observed to form in the semiconductor close to the metal contact. This charge will lower the injecting electric field and hence attenuate the injection of additional charges, causing a diffusion limited current.[48]

2.3.3. The dielectric layer

For the operation of a FET, the interface between dielectric and semiconductor plays a crucial role. It is within a distance from the interface of few nm that the charge carriers accumulate to form the conducting channel between source and drain contacts.[37] Therefore the quality of the interface is most important for the performance of the device. It is easily influenced by the presence of trap states, impurities, and interface roughness.[70]

The important characteristics of good gate dielectrics include very high dielectric breakdown strength, extremely low concentration of impurities that could act as traps, environmental stability, easy processability and compatibility with preceding and subsequent processing steps. The performance of a gate dielectric is also often characterized by its dielectric constant, which determines the geometrical capacitance $C_i = \frac{\varepsilon_r \varepsilon_0}{d}$ for a dielectric of thickness d and hence the amount of induced charges at the interface per unit gate voltage applied.

SiO_2 is currently the most frequently used gate dielectric due to the good availability of very smooth thermally grown dioxide layers on highly doped Silicon substrates. Typical SiO_2 thicknesses of 200-300 nm, i.e. $C_i \approx 10^{-8}$ F/cm^2, lead to operating voltages of the transistor of > 10 V. Usually however, the surface has to be

passivated due to the presence of a large number of –OH groups which may act as trapping sites or otherwise change the transport behaviour.[83] This is typically done by applying a self-assembled monolayer, the most common being hexamethyl disilazane (HMDS) and octadecyl trichlorosilane (OTS).[84] Other metal oxides, such as Al_2O_3, have also been used to produce very thin dielectric layers.[85]

Another option, which is becoming more and more attractive, is the use of insulating polymers. They are compatible with a fully solution processed methodology and with flexible, i.e. bendable, devices. Furthermore they can easily be optimized chemically to suit particular device requirements. Using solvents for semiconductor and dielectric that do not dissolve underlying layers (orthogonal solvents), the polymers can also be spin coated on top of the semiconductor to make top gate devices.[56,86] Alternatively, some organic dielectric materials can be cured by UV radiation- or heat- initiated cross linking processes to provide stability against solvents in subsequent processing steps.[87]

Besides the simple assumptions on amounts of induced charges and breakdown strength, it was shown by Veres *et al.*[56,57] that the mobility in devices depended strongly on the dielectric constant of the dielectrics. In brief, it was shown that a lower dielectric constant led to higher mobilities. This trend was argued to be due to additional energetical disorder at the interface, introduced by dipoles in higher ε materials. As illustrated in Fig. 2.14 the disorder leads to a broadened Gaussian density of states in Bässler's disorder model, which decreases the effective mobility (see section 2.2.5).[29] In the meantime, some groups have successfully employed high-ε_r dielectrics in order to reduce the operating voltages of OFETs.[57,88]

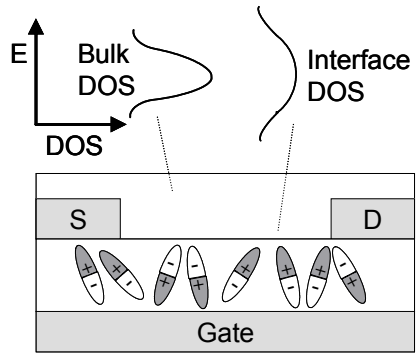


Fig. 2.14: Density of states broadening at the interface induced by disordered dipoles in dielectrics with high ε.

Reducing the thickness of the gate dielectric has been considered as a viable strategy to increase the capacitance and thereby achieve FET operation at low voltages. Low operating voltages in the range of 1-5 V can typically be achieved with

a gate dielectric geometrical capacitance of the order of 10^{-7} F/cm^2. Thin inorganic dielectrics often suffer from high current leakage, which renders them incompatible with low mobility semiconductors. Thin (10-20 nm), cross linkable polymer dielectrics have been employed by Yoon *et al.* to achieve FET operation at < 4 V.[89] Another very successful approach has been the use of insulating self-assembled monolayers (SAMs)[90-94] and multilayers[95] in gate dielectrics. The SAM molecules employed usually consist of a functional group which bonds to the gate and an alkyl chain which presents a large tunnelling barrier for charge carriers. Like polymers, SAMs can be chemically tailored to optimize material compatibility and device performance. In this way transistors operating at < 2 V have been demonstrated.[93]

2.4. Organic Semiconductors

Organic semiconductors can broadly be divided into conjugated polymers and small molecules. While organic materials should in principle be capable of electron and hole transport, the materials are often classified as either n-type or p-type. Note however that doping, as known from inorganic materials, is rarely employed in the case of organics. In practice it is much harder to observe n-type behaviour due to the challenges of charge injection and interfacial transport of electrons in OFETs.[96] Since the discovery of conduction in polymers there has been steady progress in the development of new conjugated materials for use in organic electronics and a few selected benchmark materials will be introduced in the following sections.

2.4.1. Hole transporting organic semiconductors

2.4.1.1. Small molecules

In 1984, the first OFET based on small conjugated molecules (merocyanine dye) was reported by Kudo *et al.*[50] A frequently studied group of small molecules for use in OFETs are the Oligothiophenes (*nT*, where *n* stands for the number of thiophene units, see Fig. 2.15(a)), which are usually non-substituted or substituted at both ends by a linear alkyl group.[97] Later on it was shown that the end-substitution with appropriate (for example dimethyl- or dihexyl-) groups can lead to significant increase of the mobility.[98,99] X-ray diffraction measurements showed that the film

consisted of a superposition of layers, in which the molecules were packed parallel to each other and almost perpendicular to the plane of the film. This very regular pi-stacking arrangement [Fig. 2.16(a)] is maintained for film thicknesses up to several micrometers and makes the material a two-dimensional medium, in which charges can move very quickly in direction perpendicular to the axis of the molecules. Mobilities ranging from 0.095 to 0.13 cm^2/Vs were measured using dihexyl substituted 6T (DH6T) on optimized gate insulator materials.[100] It was also found that the field-effect mobility is almost identical in all oligothiophenes.[100-102] The growth of single 6T crystals led to a five fold increase of charge mobility (0.1 cm^2/Vs instead of 0.02 cm^2/Vs on PMMA dielectric).[103] As a comparison, in polycrystalline silicon, the mobility is approximately 100 times lower than in a single-crystal, due to the effect of grain boundaries. The surprisingly low improvement in the mobility for 6T leads to the question whether higher performance is prevented by flaws in the device (such as high contact resistance or a poor dielectric/semiconductor interface) or whether the upper limit for charge carrier mobility in this material has been reached.

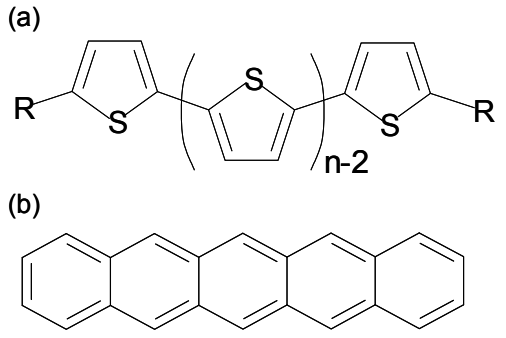


Fig. 2.15: Chemical structure of
(a) unsubstituted (R = H) and alkyl end-substituted ($R = C_n H_{2n+1}$) oligothiophenes
(b) Pentacene

Pentacene is another small molecule that has been studied extensively because of its high charge carrier mobility. It consists of five aligned condensed benzene rings [Fig. 2.15(b)]. In most reported devices pentacene films are evaporated in vacuum and give high field-effect mobilities of 1-5 cm^2/Vs, which are generally attributed to highly ordered film morphologies exhibiting a typical "herringbone" pattern [Fig. 2.16(b)].[104-106] Solution-processed devices have also been reported based on a soluble precursor molecule. The films are converted into the fully conjugated form by thermal (150 – 250 °C)[107] or irradiative[108] annealing.

Small molecules can often be rendered solution processible by attaching solubilizing side-chains. However, the growth conditions need to be monitored carefully as the molecules often crystallize while still in solution, which leads to poor

connectivity and disorder of the grains in the film. Very recently there have also been reports on soluble acene derivatives, which exhibit excellent hole mobility of the order of 1 cm^2/Vs in solution processed transistor devices without high temperature annealing.[109-111]

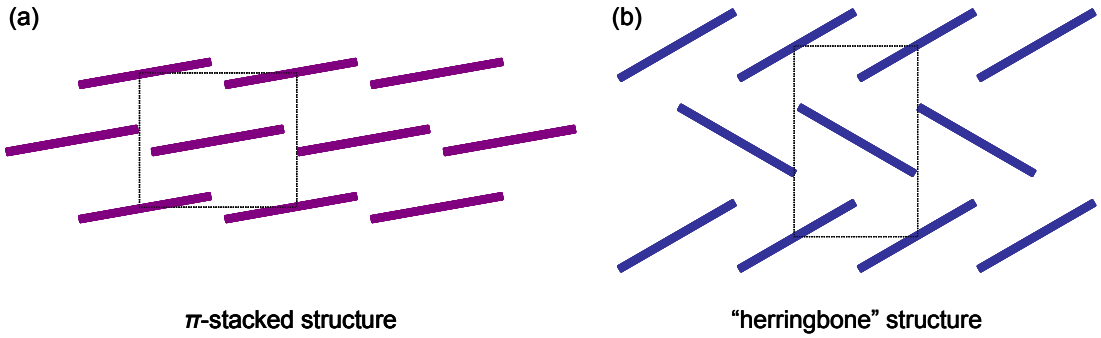


Fig. 2.16: Crystal packing arrangements found for many thiophene and acene based molecules. Dashed boxes represent a typical unit cell.

2.4.1.2 Polymers

The charge mobility in polymers is typically one order of magnitude lower than in small molecules, due to the poorer ordering in solution processed films. For example, mobilities in the range of 10^{-2} cm^2/Vs have been reached using a regioregular polythiophene.[112,113] Initially it was found that amorphous, disordered, conjugated polymers such as regioirregular polythiophene[114] or polyacetylene[115] produced very low mobilities in field-effect devices, in the range of 10^{-3} to 10^{-4} cm^2/Vs. However, more recently higher field-effect mobilities in the range of 10^{-2} cm^2/Vs were achieved using amorphous polymers based on triarylamine. The devices showed good operating characteristics and were environmentally stable.[56,57] Higher field-effect mobilities of 0.1 - 0.3 cm^2/Vs can be achieved with microcrystalline polymers, such as regioregular poly(3-hexylthiophene) (P3HT) [Fig. 2.17].[116] In thin films, the P3HT polymers form an anisotropic lamellar microstructure consisting of two-dimensional conjugated layers characterized by strong π-π interchain interactions, separated by layers of solubilising, insulating side chains. The structure allows for fast in-plane charge transport.[117]

The mobility in P3HT has been found to increase with higher degrees of crystallinity, which can be manipulated by varying the boiling point of the solvent.[118] Slower evaporation of the solvent facilitates the crystal growth during spin coating or

drop casting. Also, there is evidence that the mobility increases with increasing molecular weight of the polymer. There are several explanations for this effect. For example Kline *et al.* attributed the decrease in mobility for lower molecular weight samples to the higher effect of grain boundaries, which limit the transport.[119] Zen *et al.*, however, argued that the lower mobility was due to the less planar polymer backbone in the amorphous regions of the film for low-molecular weight material.[120] More recently, Chang *et al.*[121] and Ballantyne *et al.*[122] observed saturation and even decrease of the charge carrier mobility with molecular weight in high molecular weight P3HT. This trend was attributed to the occurrence of entanglements between long molecular chains, which increases the risk of kinks and twists, limiting the intrachain charge transport.

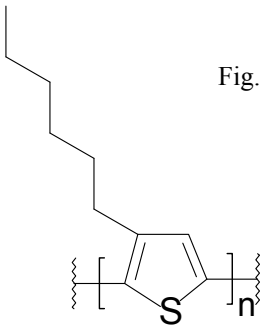


Fig. 2.17: Chemical structure of poly(3-hexylthiophene).

A major problem with semiconducting polymers with low ionization potential, such as regioregular P3HT, is their low stability upon exposure to air and ultraviolet sunlight. This is expressed in large positive threshold voltage shifts, which are presumably due to doping of the polymer. In top-gate configurations, the active material is encapsulated below the other layers (dielectric, gate etc.). In this way shelf-life stability of P3HT OFETs has been achieved, however at low ON/OFF current ratios of 10^3.[123] UV-light exposure in the presence of oxygen leads to the formation of carbonyl defects, which entails loss of conjugation and mobility degradation.[124] In order to improve the stability of P3HT, its fully planar conformation can be disrupted by altering its side-chain substitution pattern[5] or partially conjugated co-monomers can be incorporated into the main chain.[3] In these ways the beneficial microcrystallinity and the good field-effect mobility (intermolecular transport) are preserved, while the environmental stability is greatly improved.

2.4.2. Electron transporting organic semiconductors

P-channel conduction has been achieved with a number of organic semiconductors by using conventional SiO_2 as gate dielectric and gold drain-/source electrodes. Evidence of n-type conductivity, however, has only been reported for few materials. Electron trapping and difficult electron injection are most often the cause for suppressed electron transport in organic devices. Nevertheless, n-channel devices are needed for complementary logic circuits.[125]

Organic semiconductors with high electron affinity (EA) (above 3 eV) were generally found to be less susceptible to the presence of electron-trapping impurities and therefore more likely to exhibit n-type behaviour. In these materials the LUMO states are below the typical trap states, hence withdrawal and trapping of mobile electrons is less likely to occur.[96,126] Importantly, in most cases a higher EA also allows for a better alignment between the LUMO level of the semiconductor and the work function of the metal electrodes, which results in a lower electron injection barrier.

For example, n-channel field-effect mobilities in the range of 10^{-3} – 10^{-1} cm^2/Vs have been achieved with soluble fullerenes derivatives (such as [6,6]-phenyl C_{61}-butyric acid methyl ester ([60]PCBM)), which have particularly high EA [Fig. 2.18].[74,80,127-129] In films deposited in vacuum and at elevated temperature maximum electron mobility of the order of 6 cm^2/Vs was achieved.[130,131] Recently it has been shown that electron conduction is possible in materials with lower EA, when particular dielectrics are used.[83] Chua *et al.* demonstrated n-type behaviour of normally only hole conducting materials on a hydroxyl-free benzocyclobutene (BCB) gate dielectric.

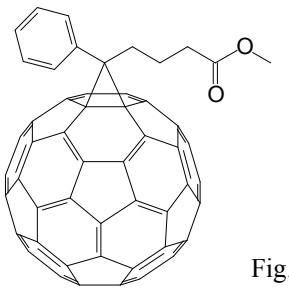


Fig. 2.18: Chemical structure of [60]PCBM.

A major problem of electron conducting materials is their strong instability with respect to oxygen and water, which is also related to low electron affinity.[132]

Anthopoulos *et al.* found that materials with LUMO energies higher than approximately 4 eV are far less sensitive to atmospheric air than molecules characterised by a lower LUMO.[133] The latter study reported air-stable electron transport in the dithiolene derivative diphenylethylenedithiolate 1,3-dithiol-2-thione-4,5-dithiolate [Ni(dpedt)(dmit)], which has a LUMO level of 4.4 eV. In accordance with this observation, Yan *et al.*[134] recently reported a polymer with a low LUMO of 4 eV, which exhibited air stable electron transport with unprecedented mobilities of 0.45 - 0.85 cm^2/Vs when deposited from solution. The air-stability was ascribed to the polymer's electronic configuration as well as to the encapsulating top gate architecture employed in their devices. Another polymer with very high EA of 4.0 - 4.4 eV is poly(benzobisimidazobenzophenanthroline) (BBL), which can be solution-processed into microcrystalline thin films.[135] High electron mobilities of 0.03-0.1 cm^2/Vs were achieved in bottom-gate FETs with SiO_2 gate dielectric, measured without encapsulation in air.

The EA of a particular molecule can be increased by adding strong electron withdrawing groups such as fluorine, cyano or diimide moieties.[96] Even though a high EA helps to improve the environmental stability, the radical anions, as present in the channel region when a positive gate voltage is applied, remain thermodynamically unstable especially towards oxygen in the presence of water. The most effective way of producing truly stable devices is by implementing a kinetic barrier against diffusion of water and air into the channel. This can be achieved by designing molecules which pack very closely, such as fluorinated copper phthalocyanine ($F_{16}CuPc$).[136,137] Recently Chikamatsu *et al.* reported air stable electron transport in solution processable perfluoroalkyl-substituted C_{60} derivatives.[138] The stability in their devices was attributed to a densely packed and ordered layer of the fluorinated side chains, acting as a shield against atmospheric oxidants. Finally, improved air-stability in fullerene based devices has also been achieved by implementing strongly hydrophobic bottom gate dielectrics such as parylene.[139] The prolonged device operation compared to devices on SiO_2 dielectric was attributed to the highly water repellent nature of this hydrophobic dielectric. Other air-stable n-channel OFETs were reported based on dicyanoperylene-3,4:9,10-bis(dicarboximide PDI-8CN2)[140,141] and α,ω-diperfluoro-hexylsexithiophene (DHF-6T).[142]

Further organic materials which are known to exhibit n-channel transport in FETs include N,N'ditridecylperylene- 3,4,9.10-tetracarboxylic diimide (PTCDI-$C_{13}H_{27}$),[143] and a number of thiophenes with electron withdrawing groups like tricyanovinyl,[144] perfluoroalkyl,[142] perfluoroarene,[145] carbonyl[146] and dicyanomethyl.[147,148]

2.5. Ambipolar Field-Effect Transistors

From inorganic microelectronics it is known that complementary logic can address the issues of power dissipation, noise margin, and hence circuit robustness, in large scale integrated circuits (ICs).[125] However, the integration of both p- and n-channel devices, as required in CMOS, on one substrate demands significant fabrication effort for organic electronics. An alternative approach is the development of ambipolar organic semiconductor materials, which can conduct both, electrons and holes, depending on the biasing conditions. Ambipolar FETs have been constructed in a variety of architectures, some of which will be described in the following section.

2.5.1. Ambipolar OFET characteristics

The basic operation of an ambipolar FET can be described in three regimes: the unipolar linear regime, the reversed unipolar regime and ambipolar regime.[39] For $|V_D| < |V_G - V_T|$ and both, V_D and V_G, positive (negative), electrons (holes) accumulate at the source electrode and the current is given by:

$$|I_D| = \frac{WC_i}{L} \cdot \mu_e \cdot \left((V_G - V_{T,e}) \cdot V_D - \frac{V_D^2}{2} \right) \tag{2.28}$$

where $V_{T,e}$ ($V_{T,h}$) and μ_e (μ_h) are the threshold voltage and mobility for electrons (holes), respectively. The transistor operates in a unipolar linear regime. For the case where V_D is negative and $V_G - V_{T,e}$ is positive, the effective gate potential is positive throughout the channel, so that electrons accumulate at the drain electrode and the transistor operates as a unipolar *n*-type transistor with reversed current direction. Similarly, when V_D is positive and $V_G - V_{T,h}$ is negative, the effective gate potential in the channel is negative, so that holes accumulate at the drain electrode.

For $V_D \leq V_G - V_{T,h} < 0$ and $V_D \geq V_G - V_{T,e} > 0$ a normal unipolar transistor is pinched off and enters the saturation regime. In ambipolar transistors, the effective gate potential in the pinched-off part of the channel changes sign and allows for injection of the opposite charge carrier from the drain electrode. The transistor enters the ambipolar regime, where both types of charge carriers accumulate at opposite ends in the channel. In this regime the channel consists of an electron- and a hole accumulation layer of length L_e and L_h respectively [Fig. 2.19]. At the point between drain and source electrode where the accumulation layers meet, an infinite recombination rate of holes with electrons is assumed. In electroluminescent materials light is emitted from within the channel.[149] Under the assumption that the two accumulation layers together make up the total length of the channel ($L = L_e + L_h$), and that the total current equals the hole and the electron current ($I_D = I_e = I_h$), one can derive:

$$|I_D| = \frac{WC_i}{2L} \cdot \left\{ \mu_e \cdot \left(V_G - V_{T,e}\right)^2 + \mu_h \cdot \left(V_D - \left(V_G - V_{T,h}\right)\right)^2 \right\} \tag{2.29}$$

The transfer curves of ambipolar transistors are typically V-shaped, with the current rising to both sides for either electron (positive V_G) or hole (negative V_G) accumulation [Fig. 2.20(a)]. The curve shape is also dependent on the drain-source voltage, since it changes the effective gate voltage for hole and electron accumulation.

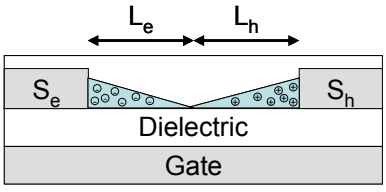


Fig. 2.19: Charge accumulation in an ambipolar OFET. Both types of charges are injected through their respective source electrodes.

The output curves [Fig. 2.20(b)] show the normal saturated behaviour of one charge carrier a at $V_D > V_G - V_{T,a}$ and superlinear current increase for small gate voltages and large drain-source voltages when the opposite charge carrier is injected.

From these considerations the location of the recombination zone $x_0 = L_e$ in the channel can be obtained:

$$x_0 = \frac{L \cdot \left(V_G - V_{T,e}\right)^2}{\left(V_G - V_{T,e}\right)^2 + \frac{\mu_h}{\mu_e} \cdot \left(V_D - \left(V_G - V_{T,h}\right)\right)^2} \tag{2.30}$$

This rather simple model can be used to predict basic behaviour of the recombination zone in ambipolar transistors. It reflects a strong dependence on the ratio between hole and electron mobility and on V_G, V_D and V_T. However, the assumption of an infinite recombination rate is rarely realistic, which means that holes and electrons usually penetrate into each other's accumulation layers before recombining. The recombination zone is then a space charge limited region. Refining the model by including Langevin recombination and contact effects, the general shape of current-voltage characteristics in ambipolar transistors can be reproduced very well.[150,151]

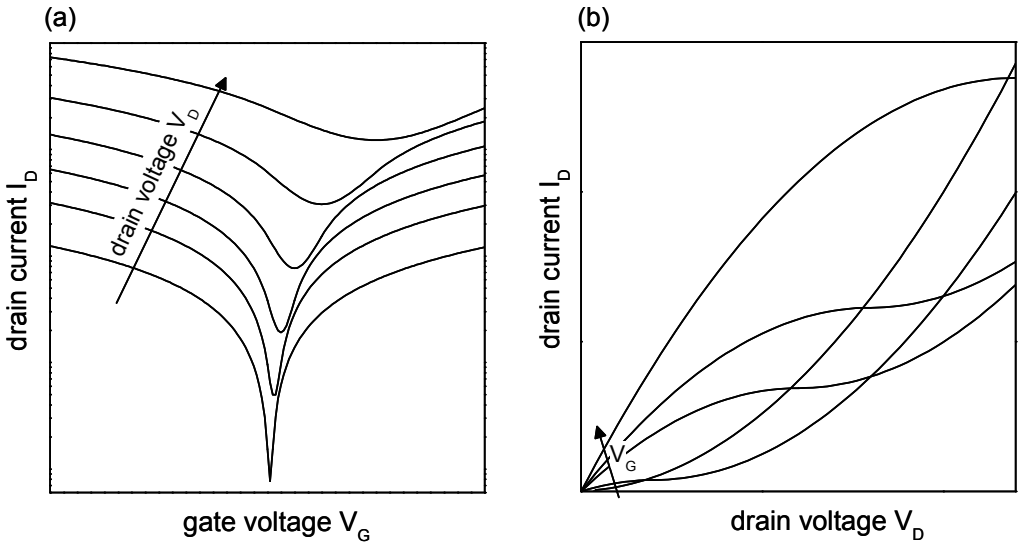


Fig. 2.20: Calculated transfer (a) and output (b) characteristics of an ambipolar transistor with balanced hole and electron mobility and $V_{T,e} = V_{T,h} = 0$.

2.5.2. Ambipolar FETs based on organic heterostructures

Ambipolar charge transport can be achieved by stacking an n-channel and a p-channel organic material on top of each other, in a bilayer structure. An energy barrier prevents charge carriers from crossing into the other material, so that charge transport occurs in two separate channels, one of which is located at the interface between the two semiconducting materials and one at the semiconductor / insulator interface.

The first ambipolar heterostructured OFET was reported by Dodabalapur *et al.* [152,153] In the latter study they combined layers of α-hexathienylene (α-6T) and C_{60}. The devices showed both, hole and electron accumulation, but with lower mobilities than those obtained from the pristine materials. They concluded that the careful choice of materials according to the relative positions of their HOMO and LUMO levels as

well as the deposition order were important in order to obtain ambipolar characteristics. Later on, ambipolar transport was achieved with a variety of material combinations, such as pentacene/PTCDI-$C_{13}H_{27}$,[143,154] pentacene/C_{60}[155] and CuPc/F_{16}CuPc.[136,156,157]

2.5.3. Ambipolar FETs based on organic blends

Another way of achieving ambipolar transport is by depositing films based on blends of n-type and p-type organic semiconductors. Such devices are in principle easily processable and thus well suited for applications in integrated circuit (IC) technology.

A film consisting of a mix of two materials can be deposited either from solution or from simultaneous evaporation (co-evaporation). First results by Tada *et al.* were obtained by mixing an electron conducting dye N,N'-bis(2,5-di-tert-butylphenyl)-3,4,9,10-perylene dicarboximide with hole conducting poly(3-dodecylthiophene).[158] The mobilities were very low and in the range of 10^{-7} cm^2/Vs for holes and 10^{-9} cm^2/Vs for electrons.

Meijer *et al.* were the first to achieve mobilities of $7 \cdot 10^{-4} cm^2/Vs$ and $3 \cdot 10^{-5} cm^2/Vs$ for holes and electrons, respectively, in films of blended poly[2-methoxy-5-(3′,7′-dimethyloctyloxy)]-p-phenylene vinylene (OC_1C_{10}-PPV) with [60]PCBM.[159] Singh *et al.* found a strong influence of the dielectric and the resulting morphology of the films on the resuls.[160] Similar to their experiments with bilayer structures, Rost *et al.* showed ambipolar transport in equal fraction blends of PTCDI-$C_{13}H_{27}$ / α-quinquethiophene (α-5T) with hole and electron mobilities of 10^{-4} cm^2/Vs and 10^{-3} cm^2/Vs, respectively. These results were again lower than the mobilities in the pristine materials.[161]

With respect to the decrease in mobility, it was argued that due to the mixing only a fraction of the material can conduct each type of charge carrier, so that the effective mobility of both types in such a percolating network is lowered compared to a neat film. This assumption was confirmed when Loi *et al.* found an increase of hole or electron mobility when the fraction of α-5T or PTCDI-$C_{13}H_{27}$ was increased, respectively.[162]

Other ambipolar blends were achieved by coevaporating pentacene/PTCDI-$C_{13}H_{27}$[163] and pentacene/fluorinated pentacene.[164] More recently, blends of MEH-PPV/C_{60},[165] MEH-PPV/[60]PCBM,[166] CuPc/poly(benzobisimidazo-nezophenanthroline),[167] regio-regular P3HT/[60]PCBM[168] and thieno[2,3-b]thiophene terthiophene polymer/[60]PCBM were fabricated, leading to mobilities in the range of 10^{-4} to 10^{-3} cm^2/Vs.

2.5.4. Ambipolar OFETs based on a single material

The bandgap of organic semiconductors is usually in the range of 2-3 eV. The work function of a metal can therefore only be aligned with either the LUMO (electron injection) or the HOMO (hole injection), the opposite charge carriers facing injection barriers larger than 1 eV. Despite this limitation, in recent years ambipolar OFETs based on a number of organic molecules have been demonstrated.

A particular example are the fullerenes and their derivatives, which were first known only as n-channel semiconductors. Anthopoulos *et al.* fabricated transistors from solution processable [60]PCBM with gold electrodes on HMDS treated SiO_2, which exhibited p-channel as well as n-channel behaviour, with similar mobilities ($10^{-2} cm^2/Vs$) for holes and electrons.[35,169] Ambipolar transport was also demonstrated in higher fullerene analogues such as C_{70} and C_{84}, for which more reproducible and less air-sensitive results were obtained.[74,80] Ambipolar transport was also recently reported for single crystal materials, such as rubrene ($\mu_e \cong 0.01\ cm^2/Vs$),[170] copper phthalocyanine (CuPc) ($\mu_e \cong 0.001\ cm^2/Vs$)[171] and iron phthalocyanine (FePc) ($\mu_e \cong 0.03\ cm^2/Vs$).[171] However the electron transport was strongly limited by injection barriers and the high hole mobilities in these materials were not achieved with electrons.

Pentacene, which has one of the highest hole mobilities amongst all organic semiconductors, has also been shown to exhibit n-type conduction. The first to produce an ambipolar transistor from pentacene were Meijer *et al.* on HMDS treated SiO_2 dielectrics and with gold bottom contact electrodes.[159] The electron mobilities were extremely low ($\mu_e \cong 10^{-6} cm^2/Vs$) and were only observable in vacuum. The n-type performance was improved using calcium electrodes for a lower electron

injection barrier on poly(chloro-p-xylylene) as gate dielectric ($\mu_e \cong 2.7 \cdot 10^{-5} cm^2/Vs$), which however resulted in low hole mobilities due to an increased hole injection barrier ($\mu_h \cong 4.5 \cdot 10^{-4} cm^2/Vs$).[172,173] Singh *et al.* reported much higher mobilities for OFETs based on poly(vinyl alcohol) (PVA) as dielectric and gold top electrodes.[174,175] Hole and electron mobilities reached values of $\mu_h \cong 0.5\ cm^2/Vs$ and $\mu_e \cong 0.2\ cm^2/Vs$, respectively. These results were strongly dependent on the type of gate dielectric, since replacing the PVA with poly(4-vinyl phenol) PVP led to the disappearance of electron transport. Schmechel *et al.* avoided the problem of high injection barriers by using electrodes with asymmetric work functions.[176] They achieved ambipolar transport in pentacene by doping the semiconductor/insulator interface with Ca atoms and using a calcium electrode for electron injection and a gold electrode for hole injection. Hole and electron mobilities in the order of $\mu \cong 0.1\ cm^2/Vs$ were reported.

Using different materials for the injection of opposite charge carriers can lead to ambipolar behaviour even in wide band-gap semiconductors. Electron injection has been achieved in what are normally p-type materials using calcium[177] and aluminium[178] electrodes.

Ambipolar transport is generally easier to achieve in materials with a low band gap. Meijer *et al.* demonstrated this with poly(3,9-di-t-butylindeno[1,2-b] fluorine) (PIF), which has a bandgap energy of 1.55 eV.[159,179] They obtained mobilites of $\mu_h \cong 4 \cdot 10^{-5} cm^2/Vs$ and $\mu_e \cong 5 \cdot 10^{-5} cm^2/Vs$. Anthopoulos *et al.* reported air stable ambipolar OFETs based on soluble dithiolene derivatives.[133] The devices exhibited similar mobilities (10^{-4} cm^2/Vs) for holes and electrons with shelf life times exceeding three months. In the latter study, air stability was predicted for n-type organic semiconductors with electron affinities above 4 eV, in accordance with previous findings on the influence of atmospheric oxidants (see section 2.4.2.). This was the first example of air stable ambipolar transport in a single component based OFET. Another interesting class of low-band gap molecules for which ambipolar charge transport with balanced hole and electron mobilities of the order of 10^{-4} cm^2/Vs was reported using a single electrode material are the squaraines.[180] Devices based on these materials were shown to emit light in the near-infrared spectrum.

Since devices with one type of electrode material require less processing steps, narrow bandgap materials are a promising route towards ambipolar devices in organic electronics.

2.6. Logic Circuits

Ultimately the performance of OFETs in performing logic operations as part of integrated circuits (ICs) will determine their suitability for implementation into real device applications.[125] Therefore the transistors are often tested in simple logic circuits to demonstrate the feasibility of organic ICs. Furthermore it is interesting to study the effects of particular features in the transistor characteristics on the outcome of the logic circuit element under investigation. A simple case is the voltage inverter, which is an important building block for standard logic gates. It is a two transistor device and operates as a NOT-gate:

IN	OUT
1	0
0	1

Table 2.1.: Truth table for an inverter

The inverter circuit can generally be considered as a potential divider [Fig. 2.21(a-b)].[181] At a low input voltage ($V_{IN} \approx 0$ V) the driving transistor (FET_D) is switched off while the load transistor (FET_L) has a finite resistance (i.e. $R_D >> R_L$), so that the supply voltage (V_{DD}) drops over R_D and $V_{OUT} \approx V_{DD}$ (LOW state) [Fig. 2.21(a)]. At increasing input voltages the driving transistor gradually switches on and eventually $R_D << R_L$, hence the supply voltage drops over R_L and $V_{OUT} \approx 0$ (HIGH state) [Fig. 2.21(b)]. While there are many different circuit arrangements for an inverter, there are generally two families of logic to be considered, *unipolar*[182] and *complementary logic*.[181] State-of-the-art inorganic electronics is dominated by complementary metal oxide semiconductor (CMOS) circuits employing both, p- and n-type transistors. With regard to organic electronics, both types of logic are associated with advantages and disadvantages.[183] Typical circuit diagrams for complementary and unipolar inverters are displayed in [Fig. 2.21(c-e)]. In the unipolar case, there must either be a difference in I_{ON} or in V_T between the load and the drive

transistor. A common approach is the so called ratio logic, where a different channel width W is employed to alter I_{ON}. The load transistor is then gated to the supply voltage [Fig. 2.21(c)], operating like a diode, or has its gate and source connected, in the so called "$V_G = 0$" logic [Fig. 2.21(d)]. The diode configuration has been shown to exhibit a faster operating speed due to higher circuit currents, at the cost of increased static power consumption.[184] In either case the load transistor is never completely switched off and hence power is continuously dissipated for one half of the range of input signals [Fig. 2.22(a)].[185] This problem does not occur in complementary logic [Fig. 2.21(e)], in which p- and n-type transistors share the same gate bias, which implies that one of the transistors is always in the off state, preventing current leakage in quasi-static operation. Power is only dissipated during the switching process [Fig. 2.22(b)].[181]

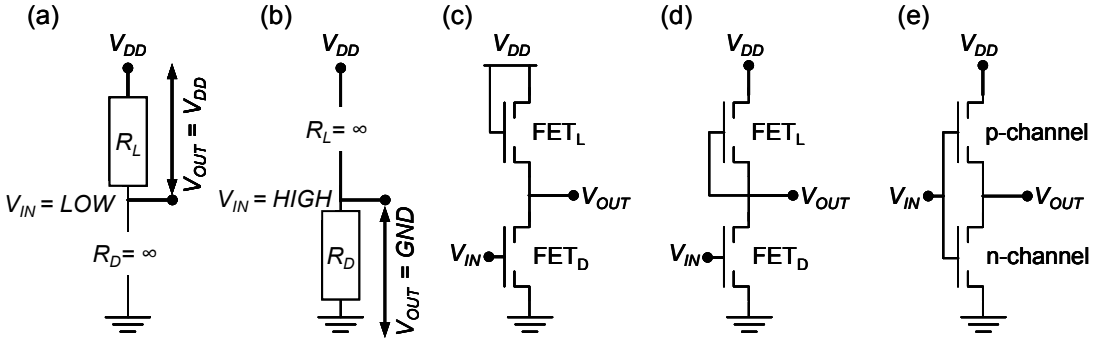


Fig. 2.21: Circuit diagrams of schematic representation of inverter as voltage divider in (a) LOW and (b) HIGH state, of a unipolar inverter in (c) "diode" and (d) "$V_G = 0$" configuration, (e) of a complementary inverter.

There are two more important parameters that characterize an inverter, namely the gain, defined as the maximum value of $\partial V_{OUT}/\partial V_{IN}$, and the noise margin. A gain >1 is needed for a signal to propagate without attenuation through a circuit with several stages. The noise margin represents the range of voltages that will be recognized as the HIGH and LOW state by the inverter. It is typically determined by plotting the output characteristics of the inverter twice with V_{IN} and V_{OUT} on exchanged axes in the same graph [Fig. 2.22(c-d)]. The noise margin determines the reliability of the circuit and its tolerance to signal fluctuations and noise. Gains and noise margins can be significantly enhanced by implementing complementary circuit design, as shown in Fig. 2.22. This is because of the insufficient "pull-up" and "pull-down" in unipolar inverters, which is caused by the higher circuit currents.

Furthermore, an asymmetric position of the trip point in unipolar inverters often decreases their noise margins.

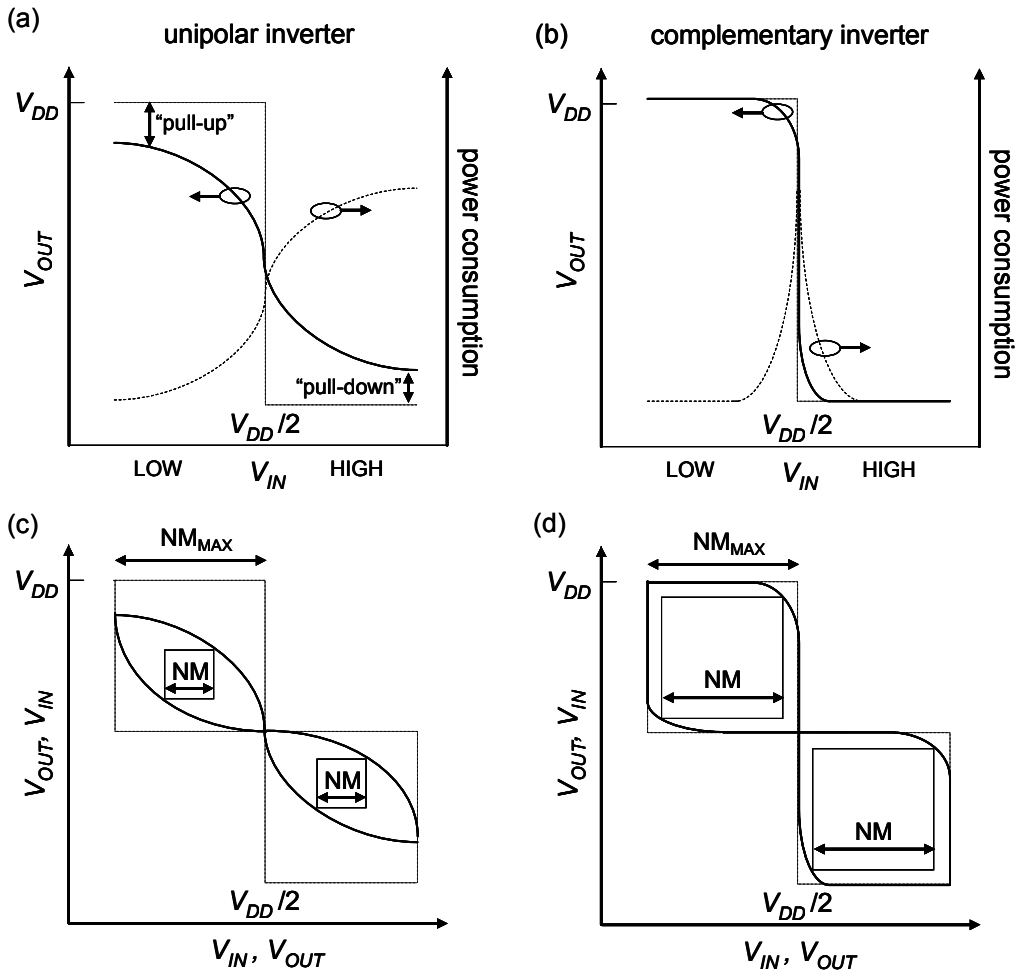


Fig. 2.22: Schematic output characteristics (solid, left axes) and power consumption (dashed, right axes) of (a) unipolar and (b) complementary voltage inverters and the determination of their noise margins in (c) and (d), respectively. The dotted lines indicate the ideal inverter step function. Complementary inverters exhibit lower power consumption, higher gain, better pull up and pull down characteristics and wider noise margins than unipolar inverters.

While complementary logic exhibits clearly superior performance characteristics, it has not yet been widely employed in organic electronics because of two hindrances. First, high performance electron transporting organic semiconductors are less well investigated compared to p-channel materials. Second, the patterning of p- and n- channel materials in close proximity on the same substrate imposes significant experimental challenges. Complementary-like logic has been suggested as a viable strategy to circumvent this problem.[159] It employs ambipolar OFETs based on a single material or blend, which operate in either hole or electron accumulation depending on the biasing conditions. The operating characteristics are determined by the relative positions of $V_{T,e}$ and $V_{T,h}$, as well as by the electron and hole mobility. A

dependence of V_{OUT} on V_{IN} is often observed in the HIGH and the LOW states due to the narrow range of gate biases in which the transistors are OFF. Due to their capability of ambipolar transport, the drive and load devices can be regarded as parallel circuits of p- and n-channel transistors. As a result the circuit current is higher than in truly complementary logic, and the inverters may suffer from insufficient "pull-up" and "pull-down". Nevertheless, their characteristics are still superior to those of unipolar voltage inverters and CMOS-like gain, noise-margins and power consumption can be obtained, while saving the costly patterning steps of separate p- and n-channel OFETs.

Another key feature of an organic circuit element is the speed at which it can operate. This will critically influence the dynamic response of the digital circuit in which it is used. For this purpose ring oscillators are fabricated by connecting an odd number of inverter stages in series, with the output of the last inverter looped back to the input of the first.[186] This produces an unstable system which will begin to oscillate between high and low voltages at a frequency dependent on the inverter stage delay, τ_d. For n stages this delay can be calculated using equation 2.31:

$$\tau_d = \frac{1}{2nf_{osc}} \tag{2.31}$$

where f_{osc} is the frequency at which the oscillator operates. The stage delay and thus the operating frequency is determined by the current at V_{OUT}, the capacitance at the output node and the voltage needed to drive the next inverter stage. The exact dependence on transistor performance parameters is difficult to obtain, however it can be said that higher mobilities, shorter channel lengths and larger transistor operating voltages lead to higher currents and faster charging of the subsequent inverter input.[186]

2.7. Photoresponsive Organic Field-Effect Transistors

Upon illumination the current-voltage characteristics of OFETs often change. This is due to mainly two processes occurring in the organic semiconductor layer, namely *photoconductivity* and the *photovoltaic effect*.[187,188] The photovoltaic effect, together with a shift of the threshold voltage towards the off state is caused by a large number of trapped charge carriers near the source contact.[189] It dominates the photocurrent in the ON state of the transistor and is described by equation 2.32:[187,190]

$$I_{ph,pv} = G_M \cdot \Delta V_T = \frac{BkT}{q} \ln\left(1 + \frac{\eta e \lambda P_{opt}}{I_{pd} hc}\right) \tag{2.32}$$

where η is the quantum efficiency (i.e. the number of charge carriers generated per incident photon), e is the elementary charge, P_{opt} is the incident optical power, I_{pd} is the dark current, hc/λ is the photon energy (E_γ), G_M is the transconductance, ΔV_T is the threshold voltage shift and B is a fitting parameter.

When the transistor is in the OFF state, the photocurrent is dominated by photoconductivity as described by equation 2.33:[66]

$$I_{ph,pc} = (e\mu nE)Wd = BP_{opt} \tag{2.33}$$

where μ is the charge carrier mobility, n is the carrier density, E is the lateral electric field in the channel, W is the channel width and d the thickness of the active layer. $I_{ph,pc}$ is therefore directly proportional to P_{opt}.

Useful figures-of-merit for phototransistors are:

- The photosensitivity, PS or signal (photocurrent) to background (dark current) ratio of the device, which is calculated as:

$$PS = \frac{I_{ill} - I_{dark}}{I_{dark}} \tag{2.34}$$

- The photoresponsivity, R (expressed in A/W) of the device, which is defined as:

$$R = \frac{I_{ph}}{P_{opt}} = \frac{(I_{ill} - I_{dark})}{P_{inc} A} \tag{2.35}$$

  Where P_{inc} is the incident optical power density, or irradiance, and A is the active area, given by the width and length of the transistor channel as $A = L \cdot W$.

- The external quantum efficiency η_{EQE}, defined as the ratio of the number of photo-generated charge carriers N_e that contribute to I_D per unit time t

$$N_e = \frac{I_{ph} \cdot t}{e} \tag{2.36}$$

to the number of photons N_γ incident on the transistor channel area per unit time t

$$N_\gamma = \frac{P_{opt} \cdot t}{E_\gamma} = \frac{P_{opt} \cdot t \cdot \lambda}{h \cdot c}. \tag{2.37}$$

Consequently the external quantum efficiency is given by equation 2.38:[191]

$$\eta_{EQE} = \frac{N_e}{N_\gamma} = \frac{I_{ph} \cdot h \cdot c}{e \cdot P_{opt} \cdot \lambda} \tag{2.38}$$

The physical phenomena responsible for the photogeneration of charge carriers in the organic semiconductors can be understood in terms of the absorption of photons and formation of excitons upon illumination. Organic semiconductor molecules will absorb photons with energy greater than their band gap energy, i.e. the LUMO – HOMO difference. The absorbed energy sets the molecule into an excited state, where a spatially correlated electron-hole pair (i.e. exciton) is formed. Under the influence of an externally applied electric field excitons can diffuse through the material for a short time, before they are likely to recombine. Depending on the chemical composition of the material the exciton may encounter a so called dissociation site. This is typically a chemical group with high electron affinity, which allows the exciton to lower its energy state by separating into a hole and an electron. The electron will then transfer to the accepting molecule, while the hole resides on the donating molecule and both may contribute to the observed photocurrent [Fig. 2.23]. Dissociation sites can be implemented by carefully designing the organic semiconducting molecule so that it incorporates electron donating and accepting chemical groups.[192] Another strategy is to blend donating and accepting molecules to form a bulk heterojunction film. This has been successfully demonstrated employing polymers, e.g. poly-thiophene or poly-phenylenevinylene based, as donors and soluble fullerene derivatives, e.g. [6,6]-phenyl-C61-butyric acid ester, as acceptors.[193,194] The essence of the bulk heterojunction is to intimately mix the donor and acceptor components in the bulk film so that each absorbing site is within a distance less than the exciton diffusion length of the closest donor-acceptor interface.

Illumination can also induce direct band-to-band excitation of electrons, for example of charges trapped in localized gap states.[189] By absorbing incident photon

energy these charges may reach the transport level and become mobile charge carriers, contributing to the photocurrent.

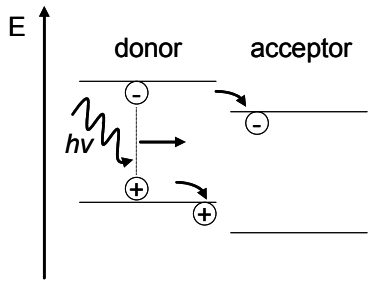


Fig. 2.23: Simplified schematic of exciton dissociation at junction between donor and acceptor.

2.8. Surface Free Energy

Surface free energy plays an important role in the deposition of semiconducting materials. For example, an adequate surface energy configuration of the dielectric surface can improve crystal formation and lead to larger grain sizes of vacuum deposited organic semiconductors in bottom gate OFETs.[195] For solution processing the surface energy interplay between solid surface and the liquid determines whether a particular solution will wet a surface well [Fig. 2.24(a)] or not [Fig. 2.24(b)]. A good film formation of the organic semiconductor is particularly important at the interface to the dielectric, where a conducting channel has to form for OFET operation. Hence the investigation of surface energy properties of liquid semiconductor solutions and the relevant solid surfaces is crucial to the successful processing of OFETs from solution.

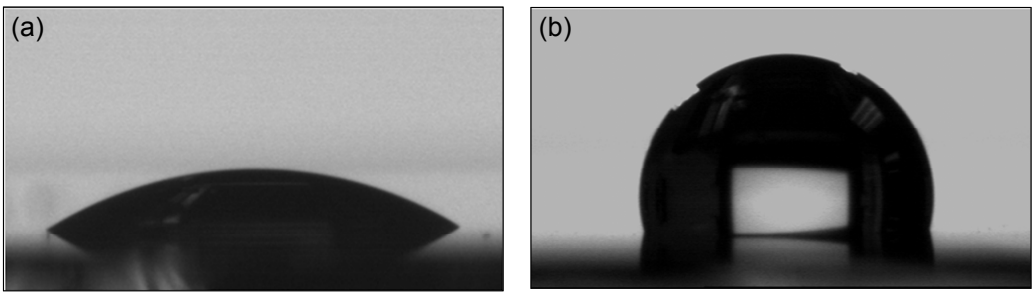


Fig. 2.24: Droplets of water on (a) a hydrophilic and (b) a hydrophobic surface.

2.8.1. Pendant drops and contact angle

The shape of a drop is normally dependent on the interfacial surface tension between the drop and the medium around it. Besides the interfacial tension, gravity acts on the drop and distorts its shape. According to the Laplace-Young equation for a

pendant drop of liquid L in its vapour V, the drop curvature plotted against elevation gives a straight line with slope a:[196]

$$a = -\Delta\rho \frac{g}{\gamma_{LV}} \tag{2.39}$$

where Δρ is the difference in density of the two media, g is the gravitational acceleration and γ_{LV} is the interfacial surface energy of the liquid and its vapour. The latter can therefore be obtained from geometrical analysis of a pendant drop shape.

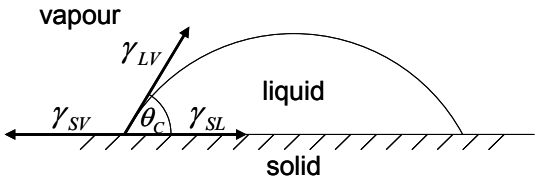


Fig. 2.25: Definition of contact angle and surface energy components in a liquid drop on a solid surface.

The wetting of a particular liquid on a solid surface is generally measured in terms of its macroscopic contact angle (θ_C) on that surface. The equilibrium contact angle is reached when a force balance is achieved at the intersection between solid, liquid and vapour of the liquid under investigation. Young described this situation assuming a perfectly smooth solid surface:[197-200]

$$\gamma_{sv} = \gamma_{lv} \cos\theta_C + \gamma_{sl} \tag{2.40}$$

where the terms γ_{sv}, γ_{lv} and γ_{sl} denote the free energy per unit area (force per unit length) of the solid-vapour, solid-liquid and liquid-vapour interfaces respectively. From Fig. 2.25 it is evident that wetting is favoured by low interfacial free energy, high solid surface free energy and low liquid surface free energy.[200] Normally, an atmosphere of saturated vapour of the liquid is unlikely to be achieved under laboratory measurement conditions. Therefore the energies of the vapour interfaces are considered to differ from their pure solid and liquid phases by π_e:[199]

$$\gamma_S - \gamma_{SV} = \pi_{eSV} \tag{2.41}$$

$$\gamma_L - \gamma_{LV} = \pi_{eLV} \tag{2.42}$$

π_e is the equilibrium pressure of adsorbed vapour. De Gennes has suggested, based on experimental results, that $\pi_e \approx 0$ for low volatility organic liquids on molecular solids.[197] Furthermore, we assume that the experiment is performed in an extremely clean and dry environment, avoiding the formation of any possible adsorbate from the

atmosphere on the solid or the liquid. Therefore γ_S and γ_L will be used henceforth to denote the measured solid and liquid surface energy.

2.8.2. Interfacial free energy and work of adhesion

In order to describe the behaviour of liquids on solids we examine the interactions at this interface. Before the liquid is in contact with the solid the total free energy per unit area of the interface is simply the sum of that of the solid and that of the liquid. Upon contact the attractive forces between the two media lower the interfacial free energy density by an amount W_{SL}:[199]

$$\gamma_{SL} = \gamma_L + \gamma_S - W_{SL} \tag{2.43}$$

W_{SL} is known as the work of *adhesion* and is defined as the work required to separate a unit area of solid-liquid interface. Similarly, the work of *cohesion* can be defined as the work required to separate a unit area of solid-solid or liquid-liquid interface (i.e. create a clean separation between two parts of the same material), denoted as W_{SS} and W_{LL}, respectively. Taking into account that the interfacial free energy density of like-like phases in contact is 0, it is shown that the works of cohesion are given by:

$$0 = 2\gamma_S - W_{SS} \tag{2.44}$$

$$0 = 2\gamma_L - W_{LL} \tag{2.45}$$

Fowkes suggested that the total free energy at a surface is the sum of contributions from the different types of intermolecular forces at the surface.[201] These are in particular London dispersion forces and quasi-chemical forces resulting from hydrogen bonds and dipole-dipole interactions. The idea was extended by Owens, Wendt[200] and Kaelble[202], who formulated:

$$\gamma_i = \gamma_i^D + \gamma_i^P \tag{2.46}$$

where the superscripts D and P refer to the dispersion force and polar hydrogen bonding components, respectively. Hence the works of adhesion and cohesion can be formulated as

$$W_{ij} = W_{ij}^P + W_{ij}^D \tag{2.47}$$

where *i* and *j* can be any phase/material. In order to evaluate the interactions between unlike pairs, i.e. the interaction between molecules of the liquid and the solid, combining rules are applied as an approximation. One such method is Berthelot's rule, which expresses a general potential energy parameter of unlike pair interactions as the geometric mean of like pair interactions:[203]

$$\varepsilon_{ij} = \sqrt{\varepsilon_{ii}\varepsilon_{jj}} \tag{2.48}$$

This approximation is found to overestimate the interaction energy when the two species differ,[203] hence the function should be modified to take arising discrepancies into account. Numerous functions have been proposed, all of which are normalized such that they revert to the Berthelot geometric mean when like pairs are considered.[203] However, when dealing with common organic solids and liquids interactions should in general be quite similar, as confirmed by the observation of low contact angles. For simplicity the error will therefore be neglected in further discussion.

Since the work of adhesion is directly proportional to the energy parameter, i.e. $W \propto \varepsilon$, the Berthelot geometric mean approximation can directly be applied to give:

$$W_{SL} = \sqrt{W_{SS}^{P} W_{LL}^{P}} + \sqrt{W_{SS}^{D} W_{LL}^{D}} = 2\sqrt{\gamma_S^{P}\gamma_L^{P}} + 2\sqrt{\gamma_S^{D}\gamma_L^{D}} \tag{2.49}$$

Substitution into 2.43 yields:[200]

$$\gamma_{SL} = \gamma_S + \gamma_L - 2\sqrt{\gamma_S^{P}\gamma_L^{P}} - 2\sqrt{\gamma_S^{D}\gamma_L^{D}} \tag{2.50}$$

This expression for γ_{SL} can be substituted into Young's equation 2.40 to give the so called Owens-Wendt-Kaelble equation:

$$\gamma_L(\cos\theta_C + 1) = 2\sqrt{\gamma_S^{P}\gamma_L^{P}} + 2\sqrt{\gamma_S^{D}\gamma_L^{D}} \tag{2.51}$$

Comparison with equation 2.49 gives an alternative expression for the work of adhesion between solid and liquid:

$$W_{SL} = \gamma_L(\cos\theta_C + 1) \tag{2.52}$$

The latter two equations are the most important tools for the analysis and extraction of surface energy parameters, as discussed in section 3.1.5.

Finally, the difference between the work of cohesion of the liquid-liquid interface and the work of adhesion to the solid is called the spreading parameter ΔW:[197]

$$\Delta W = W_{SL} - W_{LL} = \gamma_L(\cos\theta_C - 1) \tag{2.53}$$

It measures the relative strength of interaction at the solid-liquid interface compared to that of the liquid-liquid interface and indicates whether a particular liquid is likely to adhere to the solid or not. Hence it is a useful quantification of the quality of the solid-liquid interface for film formation during solution processing. In the special case of complete wetting, $\theta_C = 0$, $\Delta W = 0$ and the liquid is shown to adhere equally well to the solid surface as it would to itself.

2.9. Transparent Oxide Semiconductors

2.9.1. Introduction

The extinction coefficient of most materials is coupled to their electrical conductivity. Materials that are highly conductive, like metals, will not normally transmit visible light, while highly transparent media, like oxide glasses, behave as insulators.[204] Only when considering the role of chemical structure, bonding and film morphology for charge transport it can be understood why high optical transparency is retained in most high mobility oxide semiconductors and transparent conducting oxides (TCO). These materials typically exhibit high carrier concentrations $>10^{18}$ cm^{-3}, charge mobility > 1 cm^2/Vs and a sufficiently large energy gap to be transparent to visible light.[205] Tin doped indium oxide (ITO) is the most widely used TCO in optoelectronics and was first shown in 1954 by Rupprecht.[206] ITO exhibits high optical transparency (85-90%) and high electrical conductivity ($\approx 10^4$ $cm^{-1}\Omega^{-1}$).[207] Other TOS, such as SnO_2, In_2O_3, ZnO and Cu_2O, as well as their doped analogues or binary, ternary or quaternary metal oxide systems, are also heavily investigated for their properties and potential applications as semiconductors or conducting electrodes.[204,208]

The electronic and optical properties of TOS are strongly dependent on their morphology and defects. The atomic arrangement of metal cations, their number and nature play an important role. Most of the useful TOS are degenerate electron

transporters (i.e. n-type), because of their high electron density (e.g. for ZnO, $n > 10^{21}$ cm^{-3}). Hole transporting (i.e. p-type) TOS (although they are strongly desired for optoelectronic applications based on p-n junctions) are relatively new and scarce. The problem with p-type oxides is the poor performance due to very low hole mobilities ($<< 1$ cm^2/Vs) and difficulties in reproducibility.[209] $CuAlO_2$ is the most studied p-type TOS, both from a theoretical as well as the experimental point of view.[209,210] Durability, work function, toxicity and deposition temperatures may also influence the choice of TOS for any particular application.

The method chosen for fabrication has an important influence on the TOS properties. To date a variety of processing techniques have been developed, each with their own advantages and disadvantages. These techniques are either based on vacuum deposition methods, e.g. radio frequency (RF) sputtering,[211-213] pulsed laser deposition[214], metal-organic chemical vapour deposition (MOCVD)[215] etc., or on solution processing methods such as chemical bath deposition,[216] spin coating[217-220] and spray pyrolysis.[221-223]

2.9.2. Charge transport in oxide semiconductors

In common oxide semiconductors such as In_2O_3, SnO_2 and ZnO, the conduction band (CB) is generally attributed to the ns metallic orbital and the valence band (VB) to oxygen anion energy levels. For example, the electronic band structure of ZnO is displayed in Fig. 2.26 (taken from the article by Ivanov *et al.*[224]). The valence band structure of ZnO consists of six bands, which originate from the O^{2-}: 2p states.[224] Two conduction bands are localized on zinc and correspond to the unoccupied Zn^{2+}: 4s levels. Electronic activity in these materials is a result of large spatial spreading of ns orbitals as compared to light metal oxides such as MgO and Al_2O_3, which are insulators.[207] In fact the strong overlap of adjacent ns orbitals allows delocalization of charges even in systems with highly distorted and disordered metal-oxygen-metal bonds, i.e. in amorphous-like metal oxides. The metal ion radius, metal and oxygen bond length and angle are among the defining factors for mobility in these materials.[225] Jin *et al.* reported that the main drive for conductivity is the cations' orbital overlap if they are large in comparison to the counter anion (oxygen).[226]

The n type conduction in ZnO is attributed to deviations from the stoichiometry. In undoped ZnO, it is donating defects, such as oxygen vacancies and/or Zn interstitials, which release free carriers into the conduction band; otherwise foreign atoms can provide the donor levels near the conduction band edge to enhance the conductivity.[227,228]

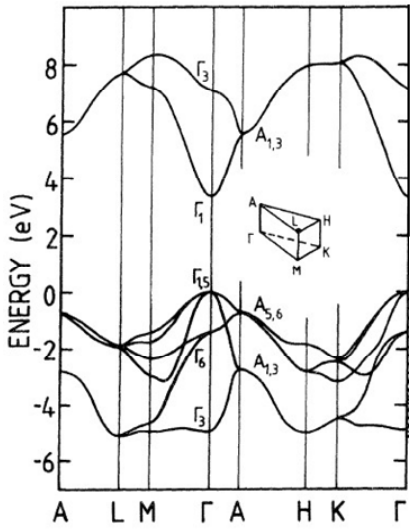


Fig. 2.26: ZnO energy band diagram, taken from reference 224 by Ivanov *et al*.

Concepts of carrier scattering mechanisms such as grain boundary scattering (GBS), ionised impurity scattering (IIS), and lattice vibration scattering (LVB) are commonly employed to describe the mobility variations in TOS. However, no consistent picture of prevailing scattering mechanisms exists because the operation of each, to a certain extent, is dependent upon morphology, carrier concentration and temperature. In their reviews Minami[208] and Ellmer[229] concluded that IIS limits the mobility for $n \geq 10^{20}$ cm^{-3}. But due to the high degeneracy in TOS like ITO and F:SnO_2, IIS was found to cause no change to mobility down to 100 K temperature. Only at high temperatures the charge carrier mobility in these systems decreases due to lattice vibration scatterings, exhibiting a T^{-1} dependence.[230] In polycrystalline films, the nano/microstructure of the film complicates the analysis of mobility data. Grain boundary scattering comes into play when the crystallite size of the material (with low carrier concentration $<10^{18}$ cm^{-3}) is comparable or less than the electronic mean free path (~few nm).[230] In addition, grain size uniformity and grain boundary angles are crucial factors in controlling the mobility. Grain boundaries between crystallites tend to contain chemisorbed oxygen molecules, which can capture electrons from the conduction band and hence act as electron traps. Trapping of electrons can also occur at other point defects, such as metal-vacancies. Furthermore the negative charge on

the grain boundaries builds up a potential barrier for cross boundary electron transport, hence limiting the mobility.[231] The competing mechanisms of electron trapping (i.e. leading to temperature activated transport) and electron scattering (i.e. temperature limited transport) in TOS often cause ambiguous and temperature specific dependencies of the charge carrier mobility on temperature, which are difficult to accurately interpret.[230]

2.9.3. Photoinduced conductivity in TOS

Due to their wide band gap, TOS are interesting candidates for application as UV-sensitive photoconductors. For example, a photoresponse in ZnO was first found by Mollwo *et al.* in the late 1940s.[232] Lateron it was observed that the ZnO surface strongly adorbs oxygen from ambient gases.[231] Adsorbed oxygen molecules can capture electrons from the conduction band and thereby negatively charge the surface. The resulting depletion layer beneath the surface causes a decrease in conductivity of the film. Under UV illumination, photogenerated holes will be attracted to the negatively charged surface and neutralize the adsorbed oxygen. This process is called photodesorption and increases the surface conductivity significantly.[231] When the UV illumination is terminated, adsorption of oxygen leads to renewed trapping of electrons and a reduced conductivity. If the measurements are performed in vacuum, the adsorption process is expected to be extremely slow due to the lack of oxygen, hence the photocurrent will decay very slowly.[231]

Zhang *et al.* also showed that this explanation can be extended to oxygen located at the grain boundaries in polycrystalline ZnO films. Here the potential barriers at the grain boundary caused by trapped electron charge are lowered upon illumination due to the temporary neutralization of the oxygen molecules. Hence a bulk-photoconductivity effect is observed.[231] The phenomenon was confirmed in observations made by several other groups.[233-236]

Reference list:

1 Atkins, P. W. & Locke, J. W. (Oxford University Press, 1987).
2 Sirringhaus, H. Device Physics of Solution-Processed Organic Field-Effect Transistors. *Adv. Mater.* **17**, 2411-2425 (2005).
3 Heeney, M. *et al.* Stable polythiophene semiconductors incorporating thieno[2,3-b]thiophene. *J.Am.Chem.Soc.* **127**, 1078-1079 (2005).
4 Setayesh, S. *et al.* Polyfluorenes with polyphenylene dendron side chains: toward non-aggregating, light-emitting polymers. *J.Am.Chem.Soc.* **123**, 946-953 (2001).
5 Ong, B. S., Wu, Y., Liu, P. & Gardner, S. High-performance semiconducting polythiophenes for organic thin-film transistors. *J.Am.Chem.Soc.* **126**, 3378-3379 (2004).
6 Brown, P. J., Sirringhaus, H., Harrison, M., Shkunov, M. & Friend, R. H. Optical spectroscopy of field-induced charge in self-organized high mobility poly(3-hexylthiophene). *Phys. Rev. B* **63**, 125204 (2001).
7 D. Beljonne *et al.* Optical Signature of Delocalized Polarons in Conjugated Polymers. *Adv. Funct. Mater.* **11**, 229-234 (2001).
8 Lefrant, S., Perrin, E., Buisson, J. P., Eckhardt, H. & Han, C. C. Vibrational studies of polyparaphenylene-vinylene (PPV). *Synthetic Metals* **29**, 91-96 (1989).
9 Rauscher, U., Bassler, H., Bradley, D. D. & Hennecke, M. Exciton versus band description of the absorption and luminescence spectra in poly(p-phenylenevinylene). *Phys. Rev. B* **42**, 9830-9836 (1990).
10 Alvarado, S. F., Seidler, P. F., Lidzey, D. G. & Bradley, D. D. Direct Determination of the Exciton Binding Energy of Conjugated Polymers Using a Scanning Tunneling Microscope. *Phys. Rev. Lett.* **81**, 1082-1085 (1998).
11 Beljonne, D., Ye, A., Shuai, Z. & Bredas, J. L. Chain-length dependence of Singlet and Triplet Exciton Formation Rates in Organic Light Emitting Diodes. *Adv. Funct. Mater.* **14**, 684-692 (2004).
12 Kasha, M. Characterization of electronic transitions in complex molecules. *Discuss.Faraday Soc.* **9**, 14-19 (1950).
13 Ashcroft, N. W. & Mermin, N. D. - (Brooks Cole, 1976).
14 Haddon, R. C. *et al.* Band Electronic Structure of One- and Two-Dimensional Pentacene Molecular Crystals. *Journal of Physical Chemistry B* **106**, 8288-8292 (2002).
15 Schein, L. B., Duke, C. B. & McGhie, A. R. Observation of the Band-Hopping Transition for Electrons in Naphthalene. *Phys. Rev. Lett.* **40**, 197-200 (1978).
16 Karl, N. *et al.* Fast electronic transport in organic molecular solids? *The Journal of vacuum science and technology* **17**, 2318-2328 (1999).
17 Podzorov, V., Menard, E., Rogers, J. A. & Gershenson, M. E. Hall effect in the accumulation layers on the surface of organic semiconductors. *Phys.Rev.Lett.* **95**, 226601 (2005).
18 Ostroverkhova, O. *et al.* Ultrafast carrier dynamics in pentacene, functionalized pentacene, tetracene, and rubrene single crystals. *Appl. Phys. Lett.* **88**, 162101 (2006).
19 Le Comber, P. G. & Spear, W. E. Electronic Transport in Amorphous Silicon Films. *Phys. Rev. Lett.* **25**, 509-511 (1970).

20 Horowitz, G., Hajlaoui, R. & Delannoy, P. Temperature Dependence of the Field-Effect Mobility of Sexithiophene. Determination of the Density of Traps. *Journal de Physique III* **5**, 355-371 (1995).

21 Horowitz, G. Organic Field-Effect Transistors. *Adv. Mater.* **10**, 365-377 (1999).

22 Marcus, R. A. Electron transfer reactions in chemistry. Theory and experiment. *Reviews of modern physics* **65**, 599-610 (1993).

23 Bredas, J. L., Beljonne, D., Coropceanu, V. & Cornil, J. Charge-transfer and energy-transfer processes in pi-conjugated oligomers and polymers: a molecular picture. *Chem. Rev.* **104**, 4971-5004 (2004).

24 Barbara, P. F., Meyer, T. J. & Ratner, M. A. Contemporary Issues in Electron Transfer Research. *Journal of Physical Chemistry* **100**, 13148-13168 (1996).

25 Fishchuk, I. I., Kadashchuk, A., Bassler, H. & Nespurek, S. Nondispersive polaron transport in disordered organic solids. *Phys. Rev. B* **67**, 224-303 (2003).

26 Fishchuk, I. I., Kadashchuk, A., Bässler, H. & Abkowitz, M. A. Low-field charge-carrier hopping transport in energetically and positionally disordered organic materials. *Phys. Rev. B* **70**, 245212 (2004).

27 Miller, A. & Abrahams, E. Impurity Conduction at Low Concentrations. *Physical review* **120**, 745-755 (1960).

28 Mott, N. F. & Davis, E. A. *Electronic Processes in Non-Crystalline Materials*. 2nd edn, 590 (Oxford University Press, 1979).

29 H. Bässler. Charge Transport in Disordered Organic Photoconductors a Monte Carlo Simulation Study. *physica status solidi (b)* **175**, 15-56 (1993).

30 Novikov, S. V. & Vannikov, A. V. Cluster Structure in the Distribution of the Electrostatic Potential in a Lattice of Randomly Oriented Dipoles. *The Journal of physical chemistry* **99**, 14573 (1995).

31 Gartstein, Y. N. & Conwell, E. M. High-field hopping mobility in molecular systems with spatially correlated energetic disorder. *Chemical Physics Letters* **245**, 351-358 (1995).

32 Dunlap, D. H., Parris, P. E. & Kenkre, V. M. Charge-Dipole Model for the Universal Field Dependence of Mobilities in Molecularly Doped Polymers. *Phys. Rev. Lett.* **77**, 542-545 (1996).

33 Novikov, S. V., Dunlap, D. H., Kenkre, V. M., Parris, P. E. & Vannikov, A. V. Essential Role of Correlations in Governing Charge Transport in Disordered Organic Materials. *Phys. Rev. Lett.* **81**, 4472 (1998).

34 Vissenberg, M. J. C. M. & Matters, M. Theory of the field-effect mobility in amorphous organic transistors. *APS Physical Review B* **67**, 12964-12967 (1998).

35 Anthopoulos, T. D. *et al.* Ambipolar Organic Field-Effect Transistors Based on a Solution-Processed Methanofullerene. *Adv. Mater.* **16**, 2174-2179 (2004).

36 Tanase, C., Meijer, E. J., Blom, P. W. M. & de Leeuw, D. M. Unification of the Hole Transport in Polymeric Field-Effect Transistors and Light-Emitting Diodes. *Phys. Rev. Lett.* **91**, 216601 (2003).

37 Tanase, C., Meijer, E. J., Blom, P. W. M. & De Leeuw, D. M. Local charge carrier mobility in disordered organic field-effect transistors. *Organic electronics* **4**, 33-37 (2003).

38 Meijer, E. J. *et al.* Switch-on voltage in disordered organic field-effect transistors. *Appl. Phys. Lett.* **80**, 3838 (2002).

39 Smits, E. C. P. *et al.* Ambipolar charge transport in organic field-effect transistors. *Phys. Rev. B* **73**, 205316-205319 (2006).

40 Ishii, H., Sugiyama, K., Ito, E. & Seki, K. Energy Level Alignment and Interfacial Electronic Structures at Organic/Metal and Organic/Organic Interfaces. *Adv. Mater.* **11**, 605-625 (1999).

41 Kahn, A., Koch, N. & Gao, W. Electronic Structure and Electrical Properties of Interfaces between Metals and pi-Conjugated Molecular Films. *Journal of polymer science B* **41**, 2529-2548 (2003).

42 de Boer, B., Hadipour, A., Mandoc, M. M., van Woudenbergh, T. & Blom, P. W. M. Tuning of Metal Work Functions with Self-Assembled Monolayers. *Adv. Mater.* **17**, 621-625 (2005).

43 Hamadani, B. H., Corley, D. A., Ciszek, J. W., Tour, J. M. & Natelson, D. Controlling Charge Injection in Organic Field-Effect Transistors Using Self-Assembled Monolayers. *Nano letters* **6**, 1303 (2006).

44 Abkowitz, M. A., Mizes, H. A. & Facci, J. S. Emission limited injection by thermally assisted tunneling into a trap-free transport polymer. *Appl. Phys. Lett.* **66**, 1288 (1995).

45 Conwell, E. M. & Wu, M. W. Contact injection into polymer light-emitting diodes. *Appl. Phys. Lett.* **70**, 1867 (1997).

46 Arkhipov, V. I., Emelianova, E. V., Tak, Y. H. & Bassler, H. Charge injection into light-emitting diodes: Theory and experiment. *J. Appl. Phys.* **84**, 848-856 (1998).

47 Novikov, S. V. & Malliaras, G. G. Roughness-induced energetic disorder at the metal/organic interface. *Physical review* **73**, 33302 (2006).

48 Scott, J. C. & Malliaras, G. G. Charge injection and recombination at the metal-organic interface. *Chemical Physics Letters* **299**, 115-119 (1999).

49 Kawase, T., Shimoda, T., Newsome, C., Sirringhaus, H. & Friend, R. H. Inkjet printing of polymer thin film transistors. *Thin Solid Films* **438**, 279-287 (2003).

50 Kudo, K., Yamashina, M. & Moriizumi, T. Field-Effect Measurement of Organic-Dye Films. *Japanese Journal of Applied Physics* **23**, 130 (1984).

51 Horowitz, G. *et al.* Organic Field-Effect Transistors with Self-Assembled Monolayers. *Proc. Int. Symp. Super-Functionality Organic Devices* **6**, 125-129 (series 6).

52 Mottaghi, M. & Horowitz, G. Field-induced mobility degradation in pentacene thin-film transistors. *Organic electronics* **7**, 528-536 (2006).

53 Natali, D., Fumagalli, L. & Sampietro, M. Modeling of organic thin film transistors: Effect of contact resistances. *J. Appl. Phys.* **101**, 014501 (2007).

54 Horowitz, G., Hajlaoui, M. E. & Hajlaoui, R. Temperature and gate voltage dependence of hole mobility in polycrystalline oligothiophene thin film transistors. *J. Appl. Phys.* **87**, 4456-4463 (2000).

55 Katz, O., Roichman, Y., Bahir, G., Tessler, N. & Salzman, J. Charge carrier mobility in field effect transistors: analysis of capacitance-conductance measurements. *Semicond. Sci. Technol.*, 90 (2005).

56 Veres, J. Low-k Insulators as the Choice of Dielectrics in Organic Field-Effect Transistors. *Adv. Funct. Mater.* **13**, 199-204 (2003).

57 Veres, J., Ogier, S., Lloyd, G. & De Leeuw, D. M. Gate insulators in organic field-effect transistors. *Chemistry of materials* **16**, 4543-4555 (2004).

58 Dimitrakopoulos, C. D., Purushothaman, S., Kymissis, J., Callegari, A. & Shaw, J. M. Low-voltage organic transistors on plastic comprising high-dielectric constant gate insulators. *Science* **283**, 822-824 (1999).

59 Collet, J., Tharaud, O., Chapoton, A. & Vuillaume, D. Low-voltage, 30 nm channel length, organic transistors with a self-assembled monolayer as gate insulating films. *Appl. Phys. Lett.* **76**, 1941-1943 (2000).
60 Salleo, A. *et al.* Intrinsic hole mobility and trapping in a regioregular poly (thiophene). *Physical review* **70**, 115311 (2004).
61 Salleo, A. & Street, R. A. Light-induced bias stress reversal in polyfluorene thin-film transistors. *J. Appl. Phys.* **94**, 471-479 (2003).
62 Street, R. A., Salleo, A., Chabinyc, M. & Paul, K. Localized state effects in polymer thin film transistors. *Journal of Non-Crystalline Solids* **338-340**, 607-611 (2004).
63 Rep, D. B. A., Mopurgo, A. F., Sloof, W. G. & Klapwijk, T. M. Mobile ionic impurities in organic semiconductors. *J. Appl. Phys.* **93**, 2082-2090 (2003).
64 Kagan, C. R., Afzali, A. & Graham, T. O. Operational and environmental stability of pentacene thin-film transistors. *Appl. Phys. Lett.* **86**, 193505 (2005).
65 Ng, T. N., Marohn, J. A. & Chabinyc, M. L. Comparing the kinetics of bias stress in organic field-effect transistors with different dielectric interfaces. *J. Appl. Phys.* **100**, 084505 (2006).
66 Sze, S. M. *Physics of Semiconductor Devices*. (Wiley, 1981).
67 McDowell, M., Hill, I. G., McDermott, J. E., Bernasek, S. L. & Schwartz, J. Improved organic thin-film transistor performance using novel self-assembled monolayers. *Appl. Phys. Lett.* **88**, 073505 (2006).
68 Klauk, H., Zschieschang, U. & Halik, M. Low-voltage organic thin-film transistors with large transconductance. *J. Appl. Phys.* **102**, 074514 (2007).
69 Wouters, D. J., Colinge, J. P. & Maes, H. E. Subthreshold slope in thin-film SOI MOSFETs. *Electron Devices, IEEE Transactions on* **37**, 2022-2033 (1990).
70 Newman, C. R., Chesterfield, R. J., Panzer, M. J. & Frisbie, C. D. High mobility top-gated pentacene thin-film transistors. *J. Appl. Phys.* **98**, 084506 (2005).
71 Noh, Y.-Y. & Sirringhaus, H. Ultra-thin polymer gate dielectrics for top-gate polymer field-effect transistors. *Organic electronics* **10**, 174-180 (2009).
72 Lei, C. H., Das, A., Elliott, M., MacDonald, J. E. & Turner, M. L. Au-poly (3-hexylthiophene) contact behaviour at high resolution. *Synthetic Metals* **145**, 217-220 (2004).
73 Burgi, L., Richards, T. J., Friend, R. H. & Sirringhaus, H. Close look at charge carrier injection in polymer field-effect transistors. *J. Appl. Phys.* **94**, 6129-6137 (2003).
74 Anthopoulos, T. D. *et al.* Air-Stable n-Channel Organic Transistors Based on a Soluble C84 Fullerene Derivative. *Adv. Mater.* **18**, 1679-1684 (2006).
75 Burgi, L., Sirringhaus, H. & Friend, R. H. Noncontact potentiometry of polymer field-effect transistors. *Appl. Phys. Lett.* **80**, 2913-2915 (2002).
76 Pesavento, P. V., Chesterfield, R. J., Newman, C. R. & Frisbie, C. D. Gated four-probe measurements on pentacene thin-film transistors: Contact resistance as a function of gate voltage and temperature. *J. Appl. Phys.* **96**, 7312-7324 (2004).
77 Kanicki, J., Libsch, F. R., Griffith, J. & Polastre, R. Performance of thin hydrogenated amorphous silicon thin-film transistors. *J. Appl. Phys.* **69**, 2339-2345 (1991).
78 Zaumseil, J., Baldwin, K. W. & Rogers, J. A. Contact resistance in organic transistors that use source and drain electrodes formed by soft contact lamination. *J. Appl. Phys.* **93**, 6117-6124 (2003).

79 Klauk, H. *et al.* Contact resistance in organic thin film transistors. *Solid-State Electronics* **47**, 297-301 (2003).
80 Anthopoulos, T. D. *et al.* Solution processible organic transistors and circuits based on a C70 methanofullerene. *J. Appl. Phys.* **98**, 054503 (2005).
81 Hamadani, B. H. & Natelson, D. Temperature-dependent contact resistances in high-quality polymer field-effect transistors. *Appl. Phys. Lett.* **84**, 443-445 (2004).
82 Woudenbergh, T. v., Blom, P. W. M., Vissenberg, M. C. J. M. & Huiberts, J. N. Temperature dependence of the charge injection in poly-dialkoxy-p-phenylene vinylene. *Appl. Phys. Lett.* **79**, 1697-1699 (2001).
83 Chua, L. L. *et al.* General observation of n-type field-effect behaviour in organic semiconductors. *Nature* **434**, 194-199 (2005).
84 Scavia, G. *et al.* Effect of the silanization and annealing on the morphology of thin poly(3-hexylthiophene) (P3HT) layer on silicon oxide. *Surf. Sci.* **602**, 3106-3115 (2008).
85 Kim, K. D. & Song, C. K. Low voltage pentacene thin film transistors employing a self-grown metal-oxide as a gate dielectric. *Appl. Phys. Lett.* **88**, 233508 (2006).
86 Sirringhaus, H. *et al.* High-Resolution Inkjet Printing of All-Polymer Transistor Circuits. *Science* **290**, 2123-2126 (2000).
87 Chua, L. L., Ho, P. K., Sirringhaus, H. & Friend, R. H. High-stability ultrathin spin-on benzocyclobutene gate dielectric for polymer field-effect transistors. *Appl. Phys. Lett.* **84**, 3400-3402 (2004).
88 Jeong, Y. T. & Dodabalapur, A. Pentacene-based low voltage organic field-effect transistors with anodized Ta2O5 gate dielectric. *Appl. Phys. Lett.* **91**, 193509 (2007).
89 Yoon, M.-H., Yan, H., Facchetti, A. & Marks, T. J. Low-Voltage Organic Field-Effect Transistors and Inverters Enabled by Ultrathin Cross-Linked Polymers as Gate Dielectrics. *Journal of the American Chemical Society* **127**, 10388-10395 (2005).
90 Collet, J. & Vuillaume, D. Nano-field effect transistor with an organic self-assembled monolayer as gate insulator. *Appl. Phys. Lett.* **73**, 2681-2683 (1998).
91 Halik, M. *et al.* Low-voltage organic transistors with an amorphous molecular gate dielectric. *Nature* **431**, 963-966 (2004).
92 Klauk, H., Zschieschang, U., Pflaum, J. & Halik, M. Ultralow-power organic complementary circuits. *Nature* **445**, 745-748 (2007).
93 Wöbkenberg, P. H. *et al.* Low-voltage organic transistors based on solution processed semiconductors and self-assembled monolayer gate dielectrics. *Appl. Phys. Lett.* **93**, 013303-013303 (2008).
94 Park, Y. D. *et al.* Low-voltage polymer thin-film transistors with a self-assembled monolayer as the gate dielectric. *Appl. Phys. Lett.* **87**, 243509 (2005).
95 Yoon, M.-H., Facchetti, A. & Marks, T. J. Sigma-pi molecular dielectric multilayers for low-voltage organic thin-film transistors. *Proc. Natl. Acad. Sci. U. S. A.* **102**, 4678-4682 (2005).
96 Newman, C. R. *et al.* Introduction to organic thin film transistors and design of n-channel organic semiconductors. *Chemistry of materials* **16**, 4436-4451 (2004).
97 Horowitz, G., Fichou, D., Peng, X., Xu, Z. & Garnier, F. A field-effect transistor based on conjugated alpha-sexithienyl. *Solid State Communications* **72**, 381 (1989).

98 Akimichi, H., Waragai, K., Hotta, S., Kano, H. & Sakaki, H. Field-effect transistors using alkyl substituted oligothiophenes. *Appl. Phys. Lett.* **58**, 1500-1502 (1991).
99 Garnier, F. *et al.* Molecular engineering of organic semiconductors: design of self-assembly properties in conjugated thiophene oligomers. *Journal of the American Chemical Society* **115**, 8716 (1993).
100 Katz, H. E., Dodabalapur, A., Torsi, L. & Elder, D. Precursor Synthesis, Coupling, and TFT Evaluation of End-Substituted Thiophene Hexamers. *Chemistry of materials* **7**, 2238 (1995).
101 Hajlaoui, R. *et al.* Organic transistors using -octithiophene and , -dihexyl--octithiophene: Influence of oligomer length versus molecular ordering on mobility. *Adv. Mater.* **9** (1997).
102 Hajlaoui, R. *et al.* Improved field-effect mobility in short oligothiophenes: Quaterthiophene and quinquethiophene. *Adv. Mater.* **9**, 389-391 (1997).
103 Horowitz, G. *et al.* Growth and Characterization of Sexithiophene Single Crystals. *Chemistry of materials* **7**, 1337 (1995).
104 Dimitrakopoulos, C. D., Brown, A. R. & Pomp, A. Molecular beam deposited thin films of pentacene for organic field effect transistor applications. *J. Appl. Phys.* **80**, 2501 (1996).
105 Gundlach, D. J., Lin, Y. Y., Jackson, T. N., Nelson, S. F. & Schlom, D. G. Pentacene organic thin-film transistors - molecular ordering and mobility. *IEEE electron device letters* **18**, 87-89 (1997).
106 Klauk, H. *et al.* High-mobility polymer gate dielectric pentacene thin film transistors. *J. Appl. Phys.* **92**, 5259-5263 (2002).
107 Herwig, P. T. & Mullen, K. A Soluble Pentacene Precursor: Synthesis, Solid-State Conversion into Pentacene and Application in a Field-Effect Transistor. *Adv. Mater.* **11**, 480 (1999).
108 Afzali, A., Dimitrakopoulos, C. D. & Breen, T. L. High-performance, solution-processed organic thin film transistors from a novel pentacene precursor. *Journal of the American Chemical Society* **124**, 8812-8813 (2002).
109 Park, S. K., Jackson, T. N., Anthony, J. E. & Mourey, D. A. High mobility solution processed 6,13-bis(triisopropyl-silylethynyl) pentacene organic thin film transistors. *Appl. Phys. Lett.* **91**, 063514 (2007).
110 Park, S. K., Mourey, D. A., Subramanian, S., Anthony, J. E. & Jackson, T. N. High-mobility spin-cast organic thin film transistors. *Appl. Phys. Lett.* **93**, 043301 (2008).
111 Hamilton, R. *et al.* High-Performance Polymer-Small Molecule Blend Organic Transistors. *Adv. Mater.* **21**, 1166-1171 (2009).
112 Bao, Z., Feng, Y., Dodabalapur, A., Raju, V. R. & Lovinger, A. J. High-performance plastic transistors fabricated by printing techniques. *Chemistry of materials* **9**, 1299-1301 (1997).
113 Bao, Z., Dodabalapur, A. & Lovinger, A. J. Soluble and processable regioregular poly (3-hexylthiophene) for thin film field-effect transistor applications with high mobility. *Appl. Phys. Lett.* **69**, 4108-4110 (1996).
114 Koezuka, H., Tsumura, A. & Ando, T. Field-effect transistor with polythiophene thin film. *Synthetic Metals* **18**, 699-704 (1987).
115 Burroughes, J. H., Friend, R. H. & Allen, P. C. Field-enhanced conductivity in polyacetylene-construction of a field-effect transistor. *Journal of Physics D: Applied Physics* **22**, 956-958 (1989).

116 Sirringhaus, H., Tessler, N. & Friend, R. H. Integrated optoelectronic devices based on conjugated polymers. *Science* **280**, 1741-1744 (1998).
117 Sirringhaus, H. *et al.* Two-dimensional charge transport in self-organized, high-mobility conjugated polymers. *Nature* **401**, 685-688 (1999).
118 Chang, J.-F. *et al.* Enhanced Mobility of Poly(3-hexylthiophene) Transistors by Spin-Coating from High-Boiling-Point Solvents. *Chemistry of materials* **16**, 4772-4776 (2004).
119 Kline, R. J., McGehee, M. D., Kadnikova, E. N., Liu, J. & Frechet, J. M. J. Controlling the Field-Effect Mobility of Regioregular Polythiophene by Changing the Molecular Weight. *Adv. Mater.* **15**, 1519-1522 (2003).
120 Zen, A. *et al.* Effect of Molecular Weight and Annealing of Poly (3-hexylthiophene) s on the Performance of Organic Field-Effect Transistors. *Adv. Funct. Mater.* **14**, 757-764 (2004).
121 Chang, J.-F. *et al.* Molecular-weight dependence of interchain polaron delocalization and exciton bandwidth in high-mobility conjugated polymers. *Physical Review B (Condensed Matter and Materials Physics)* **74**, 115318 (2006).
122 Amy M. Ballantyne *et al.* The Effect of Poly(3-hexylthiophene) Molecular Weight on Charge Transport and the Performance of Polymer:Fullerene Solar Cells. *Adv. Funct. Mater.* **18**, 2373-2380 (2008).
123 Flora, M. L., Yuri, V., Sarswati, K. & Arokia, N. *Photolithographically defined polythiophene organic thin-film transistors*, 2006).
124 Ficker, J. *et al.* Influence of intensive light exposure on polymer field-effect transistors. *Appl. Phys. Lett.* **85**, 1377 (2004).
125 Crone, B. *et al.* Large-scale complementary integrated circuits based on organic transistors. *Nature* **403**, 521-523 (2000).
126 Dimitrakopoulos, C. D. & Malenfant, P. R. L. Organic Thin Film Transistors for Large Area Electronics. *Adv. Mater.* **14**, 99-117 (2002).
127 Kobayashi, S. Fabrication and characterization of C60 thin-film transistors with high field-effect mobility. *Appl. Phys. Lett.* **82**, 4581 (2003).
128 Waldauf, C. Solution-Processed Organic n-Type Thin-Film Transistors. *Catal. Today* **67**, 369- (2001).
129 Chikamatsu, M. *et al.* Solution-processed n-type organic thin-film transistors with high field-effect mobility. *Appl. Phys. Lett.* **87**, 203504 (2005).
130 Singh, B. *et al.* Characterization of highly crystalline C60 thin films and their field-effect mobility. *Phys. Status Solidi B* **244**, 3845-3848 (2007).
131 Anthopoulos, T. D. *et al.* High performance n-channel organic field-effect transistors and ring oscillators based on C60 fullerene films. *Appl. Phys. Lett.* **89**, 213504-213503 (2006).
132 de Leeuw, D. M., Simenon, M. M. J., Brown, A. R. & Einerhand, R. E. F. Stability of n-type doped conducting polymers and consequences for polymeric microelectronic devices. *Synthetic Metals* **87**, 53-59 (1997).
133 Anthopoulos, T. D., Anyfantis, G. C., Papavassiliou, G. C. & de Leeuw, D. M. Air-stable ambipolar organic transistors. *Appl. Phys. Lett.* **90**, 122105 (2007).
134 Yan, H. *et al.* A high-mobility electron-transporting polymer for printed transistors. *Nature* **457**, 679-686 (2009).
135 Babel, A. & Jenekhe, S. A. High electron mobility in ladder polymer field-effect transistors. *Journal of the American Chemical Society* **125**, 13656-13657 (2003).

136 Bao, Z., Lovinger, A. J. & Brown, J. New air-stable n-channel organic thin film transistors. *Journal of the American Chemical Society* **120**, 207-208 (1998).
137 Ling, M.-M. & Bao, Z. Copper hexafluorophthalocyanine field-effect transistors with enhanced mobility by soft contact lamination. *Organic electronics* **7**, 568-575 (2006).
138 Chikamatsu, M., Itakura, A., Yoshida, Y., Azumi, R. & Yase, K. High-Performance n-Type Organic Thin-Film Transistors Based on Solution-Processable Perfluoroalkyl-Substituted C60 Derivatives. *Chemistry of materials* **20**, 7365-7367 (2008).
139 Kubozono, Y. *et al.* High-performance C60 thin-film field-effect transistors with parylene gate insulator. *Appl. Phys. Lett.* **93**, 033316 (2008).
140 Yoo, B. *et al.* High-mobility bottom-contact n-channel organic transistors and their use in complementary ring oscillators. *Appl. Phys. Lett.* **88**, 082104 (2006).
141 Jones, B. A. *et al.* High-mobility air-stable n-type semiconductors with processing versatility: dicyanoperylene-3,4:9,10-bis(dicarboximides). *Angewandte Chemie (International ed.)* **43**, 6363-6366 (2004).
142 Facchetti, A., Mushrush, M., Katz, H. E. & Marks, T. J. n-Type Building Blocks for Organic Electronics: A Homologous Family of Fluorocarbon-Substituted Thiophene Oligomers with High Carrier Mobility. *Adv. Mater.* **15**, 33-38 (2003).
143 Rost, C., Gundlach, D. J., Karg, S. & Riess, W. Ambipolar organic field-effect transistor based on an organic heterostructure. *J. Appl. Phys.* **95**, 5782-5787 (2004).
144 Cai, X. *et al.* N- and P-channel transport behavior in thin film transistors based on tricyanovinyl-capped oligothiophenes. *The Journal of Physical Chemistry B* **110**, 14590-14597 (2006).
145 Facchetti, A., Yoon, M. H., Stern, C. L., Katz, H. E. & Marks, T. J. Building blocks for n-type organic electronics: regiochemically modulated inversion of majority carrier sign in perfluoroarene-modified polythiophene semiconductors. *Angewandte Chemie (International ed.)* **42**, 3900-3903 (2003).
146 Yoon, M.-H., Dibenedetto, S. A., Facchetti, A. & Marks, T. J. Organic thin-film transistors based on carbonyl-functionalized quaterthiophenes: high mobility N-channel semiconductors and ambipolar transport. *Journal of the American Chemical Society* **127**, 1348-1349 (2005).
147 Pappenfus, T. M. A pi-Stacking Terthiophene-Based Quinodimethane Is an n-Channel Conductor in a Thin Film Transistor. *Journal of the American Chemical Society* **124**, 4184-4185 (2002).
148 Chesterfield, R. J. *et al.* High Electron Mobility and Ambipolar Transport in Organic Thin-Film Transistors Based on a pgr-Stacking Quinoidal Terthiophene. *Adv. Mater.* **15**, 1278-1282 (2003).
149 Zaumseil, J., Friend, R. H. & Sirringhaus, H. Spatial control of the recombination zone in an ambipolar light-emitting organic transistor. *Nature Materials* **5**, 69-74 (2006).
150 Verlaak, S., Cheyns, D., Debucquoy, M., Arkhipov, V. & Heremans, P. Numerical simulation of tetracene light-emitting transistors: A detailed balance of exciton processes. *Appl. Phys. Lett.* **85**, 2405-2407 (2004).
151 Paasch, G. *et al.* Operation and properties of ambipolar organic field-effect transistors. *J. Appl. Phys.* **98**, 084505 (2005).
152 Dodabalapur, A., Katz, H. E., Torsi, L. & Haddon, R. C. Organic Heterostructure Field-Effect Transistors. *Science* **269**, 1560-1562 (1995).

153 Dodabalapur, A., Katz, H. E. & Torsi, L. Molecular orbital energy level engineering in organic transistors. *Adv. Mater.* **8**, 853-855 (1996).
154 Dinelli, F. *et al.* High-Mobility Ambipolar Transport in Organic Light-Emitting Transistors. *Adv. Mater.* **18**, 1416-1420 (2006).
155 Kang, S. J. *et al.* Ambipolar organic thin-film transistors using C60/pentacene structure: Characterization of electronic structure and device property. *Appl. Phys. Lett.* **87**, 233502 (2005).
156 Wang, J., Wang, H., Yan, X., Huang, H. & Yan, D. Organic heterojunction and its application for double channel field-effect transistors. *Appl. Phys. Lett.* **87**, 093507 (2005).
157 Ye, R., Baba, M., Oishi, Y., Mori, K. & Suzuki, K. Air-stable ambipolar organic thin-film transistors based on an organic homostructure. *Appl. Phys. Lett.* **86**, 253505 (2005).
158 Tada, K., Harada, H. & Yoshino, K. Polymeric bipolar thin-film transistor utilizing conducting polymer containing electron transport dye. *Japanese Journal of Applied Physics* **35**, 944-946 (1996).
159 Meijer, E. J. *et al.* Solution-processed ambipolar organic field-effect transistors and inverters. *Nat.Mater.* **2**, 678-682 (2003).
160 Singh, T. B., Marjanovic, N., Sariciftci, N. S. & Menon, R. Correlation between morphology and ambipolar transport in organic field-effect transistors. *J. Appl. Phys.* **97**, 114508 (2005).
161 Rost, C. *et al.* Ambipolar light-emitting organic field-effect transistor. *Appl. Phys. Lett.* **85**, 1613-1615 (2004).
162 Loi, M. A. *et al.* Tuning Optoelectronic Properties of Ambipolar Organic Light-Emitting Transistors Using a Bulk-Heterojunction Approach. *Adv. Funct. Mater.* **16**, 41-47 (2006).
163 Narayan Unni, K. N., Pandey, A. K., Alem, S. & Nunzi, J. M. Ambipolar organic field-effect transistor fabricated by co-evaporation of pentacene and N, N'-ditridecylperylene-3, 4, 9, 10-tetracarboxylic diimide. *Chemical Physics Letters* **421**, 554-557 (2006).
164 Inoue, Y. Organic Thin-Film Transistors with High Electron Mobility Based on Perfluoropentacene. *Japanese Journal of Applied Physics* **44**, 3663-3668 (2005).
165 Hayashi, Y. *et al.* Facile fabrication method for p/n-type and ambipolar transport polyphenylenevinylene-based thin-film field-effect transistors by blending C[sub 60] fullerene. *Appl. Phys. Lett.* **86**, 052104 (2005).
166 R. C. G. Naber, P. W. M. Blom, G. H. Gelinck, A. W. Marsman & D. M. de Leeuw. An Organic Field-Effect Transistor with Programmable Polarity. *Adv. Mater.* **17**, 2692-2695 (2005).
167 A. Babel, J. D. Wind & S. A. Jenekhe. Ambipolar Charge Transport in Air-Stable Polymer Blend Thin-Film Transistors. *Adv. Funct. Mater.* **14**, 891-898 (2004).
168 Cho, S., Yuen, J., Kim, J. Y., Lee, K. & Heeger, A. J. Ambipolar organic field-effect transistors fabricated using a composite of semiconducting polymer and soluble fullerene. *Appl. Phys. Lett.* **89**, 153505 (2006).
169 Anthopoulos, T. D. *et al.* Organic complementary-like inverters employing methanofullerene-based ambipolar field-effect transistors. *Appl. Phys. Lett.* **85**, 4205-4207 (2004).
170 Takahashi, T., Takenobu, T., Takeya, J. & Iwasa, Y. Ambipolar organic field-effect transistors based on rubrene single crystals. *Appl. Phys. Lett.* **88**, 033505 (2006).

171 de Boer, R. W. I. *et al.* Ambipolar Cu-and Fe-phthalocyanine single-crystal field-effect transistors. *Appl. Phys. Lett.* **86**, 262109 (2005).
172 Yasuda, T., Goto, T., Fujita, K. & Tsutsui, T. Ambipolar Carrier Transport in Polycrystalline Pentacene Thin-Film Transistors. *Molecular Crystals and Liquid Crystals* **444**, 219-224 (2006).
173 Yasuda, T., Goto, T., Fujita, K. & Tsutsui, T. Ambipolar pentacene field-effect transistors with calcium source-drain electrodes. *Appl. Phys. Lett.* **85**, 2098-2100 (2004).
174 Singh, T. B. *et al.* High-Performance Ambipolar Pentacene Organic Field-Effect Transistors on Poly(vinyl alcohol) Organic Gate Dielectric. *Adv. Mater.* **17**, 2315-2320 (2005).
175 Singh, T. B. *et al.* Organic inverter circuits employing ambipolar pentacene field-effect transistors. *Appl. Phys. Lett.* **89**, 033512 (2006).
176 Schmechel, R., Ahles, M. & von Seggern, H. A pentacene ambipolar transistor: Experiment and theory. *J. Appl. Phys.* **98**, 084511 (2005).
177 Ahles, M., Schmechel, R. & Seggern, H. v. n-type organic field-effect transistor based on interface-doped pentacene. *Appl. Phys. Lett.* **85**, 4499-4501 (2004).
178 Yamamoto, T., Yasuda, T., Sakai, Y., Aramaki, S. & Ramaw, A. Ambipolar Field-Effect Transistor (FET) and Redox Characteristics of a pi-Conjugated Thiophene/1,3,4-Thiadiazole CT-Type Copolymer. *Macromolecular Rapid Communications* **26**, 1214-1217 (2005).
179 Reisch, H., Wiesler, U., Scherf, U. & Tuytuylkov, N. Poly (indenofluorene)(PIF), a novel low band gap polyhydrocarbon. *Macromolecules* **29**, 8204-8210 (1996).
180 Smits, E. C. P. *et al.* Near-infrared light-emitting ambipolar organic field-effect transistors. *Adv. Mater.* **19**, 734-738 (2007).
181 Dodabalapur, A., Laquindanum, J., Katz, H. E. & Bao, Z. Complementary circuits with organic transistors. *Appl. Phys. Lett.* **69**, 4227-4229 (1996).
182 Gelinck, G. H., Geuns, T. C. T. & de Leeuw, D. M. High-performance all-polymer integrated circuits. *Appl. Phys. Lett.* **77**, 1487- (2000).
183 Anthopoulos, T. D. *et al.* Air-stable complementary-like circuits based on organic ambipolar transistors. *Adv. Mater.* **18**, 1900- (2006).
184 Cantatore, E. & Meijer, E. J. in *Solid-State Circuits Conference, 2003. ESSCIRC '03. Proceedings of the 29th European.* 29-36.
185 Smits, E. C. P. *et al.* Bottom-up organic integrated circuits. *Nature* **455**, 956-959 (2008).
186 Fix, W., Ullmann, A., Ficker, J. & Clemens, W. Fast polymer integrated circuits. *Appl. Phys. Lett.* **81**, 1735-1737 (2002).
187 Kang, H.-S., Choi, C.-S., Choi, W.-Y., Kim, D.-H. & Seo, K.-S. Characterization of phototransistor internal gain in metamorphic high-electron-mobility transistors. *Appl. Phys. Lett.* **84**, 3780-3782 (2004).
188 Saragi, T. P. I., Londenberg, J. & Salbeck, J. Photovoltaic and photoconductivity effect in thin-film phototransistors based on a heterocyclic spiro-type molecule. *J. Appl. Phys.* **102**, 046104 (2007).
189 Hamilton, M. C., Martin, S. & Kanicki, J. Thin-film organic polymer phototransistors. *Electron Devices, IEEE Transactions on* **51**, 877-885 (2004).
190 Takanashi, Y., Takahata, K. & Muramoto, Y. Characteristics of InAlAs/InGaAs high-electron-mobility transistors under illumination with modulated light. *Electron Devices, IEEE Transactions on* **46**, 2271-2277 (1999).

191 Rauch, T. *et al.* Near-infrared imaging with quantum-dot-sensitized organic photodiodes. *Nat Photon* **3**, 332-336 (2009).
192 Saragi, T. P. I., Onken, K., Suske, I., Fuhrmann-Lieker, T. & Salbeck, J. Ambipolar organic phototransistor. *Optical Materials* **29**, 1332-1337 (2007).
193 Anthopoulos, T. D. Electro-optical circuits based on light-sensing ambipolar organic field-effect transistors. *Appl. Phys. Lett.* **91**, 113513-113513 (2007).
194 Marjanovic, N. *et al.* Photoresponse of organic field-effect transistors based on conjugated polymer/fullerene blends. *Organic electronics* **7**, 188-194 (2006).
195 S. Y. Yang, K. Shin & C. E. Park. The Effect of Gate-Dielectric Surface Energy on Pentacene Morphology and Organic Field-Effect Transistor Characteristics. *Adv. Funct. Mater.* **15**, 1806-1814 (2005).
196 Lopez de Ramos, A., Redner, R. A. & Cerro, R. L. Surface tension from pendant drop curvature. *Langmuir* **9**, 3691-3694 (2002).
197 de Gennes, P. G. Wetting: statics and dynamics. *Reviews of modern physics* **57**, 827 (1985).
198 Kwok, D. Y. & Neumann, A. W. Contact angle measurement and contact angle interpretation. *Adv. Colloid Interface Sci.* **81**, 167-249 (1999).
199 Good, R. J. Contact angle, wetting, and adhesion: a critical review. *J. Adhes. Sci. Technol.* **6**, 1269-1302 (1992).
200 D. K. Owens, R. C. W. Estimation of the surface free energy of polymers. *Journal of Applied Polymer Science* **13**, 1741-1747 (1969).
201 Fowkes, F. M. Attractive forces at interfaces. *Industrial & Engineering Chemistry* **56**, 40-52 (1964).
202 Kaelble, D. H. Dispersion-Polar Surface Tension Properties of Organic Solids. *The Journal of Adhesion* **2**, 66 - 81 (1970).
203 Zhang, J. & Kwok, D. Y. Calculation of Solid-Liquid Work of Adhesion Patterns from Combining Rules for Intermolecular Potentials. *The Journal of Physical Chemistry B* **106**, 12594-12599 (2002).
204 Exarhos, G. J. & Zhou, X.-D. Discovery-based design of transparent conducting oxide films. *Thin Solid Films* **515**, 7025-7052 (2007).
205 Wager, J. F. Applied physics. Transparent electronics. *Science* **300**, 1245-1246 (2003).
206 Rupprecht, G. Untersuchungen der elektrischen und lichtelektrischen Leitfähigkeit dünner Indiumoxydschichten. *Zeitschrift für Physik A Hadrons and Nuclei* **139**, 504-517 (1954).
207 Edwards, P. P., Porch, A., Jones, M. O., Morgan, D. V. & Perks, R. M. Basic materials physics of transparent conducting oxides. *Dalton Trans.*, 2995-3002 (2004).
208 Minami, T. New n-type transparent conducting oxides. *MRS Bulletin* **25**, 38 (2000).
209 Yanagi, H. *et al.* Electronic structure and optoelectronic properties of transparent p-type conducting CuAlO2. *J. Appl. Phys.* **88**, 4159-4163 (2000).
210 Robertson, J., Peacock, P. W., Towler, M. D. & Needs, R. Electronic structure of p-type conducting transparent oxides. *Thin Solid Films* **411**, 96-100 (2002).
211 Carcia, P. F., McLean, R. S., Reilly, M. H. & Nunes, J. G. Transparent ZnO thin-film transistor fabricated by rf magnetron sputtering. *Appl. Phys. Lett.* **82**, 1117-1119 (2003).
212 Fortunato, E. *et al.* High field-effect mobility zinc oxide thin film transistors produced at room temperature. *Journal of Non-Crystalline Solids* **338**, 806-809 (2004).

213 Chiang, H. Q., Wager, J. F., Hoffman, R. L., Jeong, J. & Keszler, D. A. High mobility transparent thin-film transistors with amorphous zinc tin oxide channel layer. *Appl. Phys. Lett.* **86**, 013503 (2005).
214 Nishii, J. *et al.* High Mobility thin film transistors with transparent ZnO channels. *Japanese journal of applied physics.Supplement* **42**, 347-349 (2003).
215 Jo, J., Seo, O. & Jeong, E. Effect of hydrogen in zinc oxide thin-film transistor grown by metal organic chemical vapor deposition. *Japanese journal of applied physics.Supplement* **46**, 2493-2495 (2007).
216 Ohya, Y., Niwa, T., Ban, T. & Takahashi, Y. Thin film transistor of ZnO fabricated by chemical solution deposition. *Japanese journal of applied physics.Supplement* **40**, 297-298 (2001).
217 Chang, Y.-J., Lee, D.-H., Herman, G. S. & Chang, C.-H. High-performance, spin-coated zinc tin oxide thin-film transistors. *Electrochemical and solid-state letters* **10**, H135-H138 (2007).
218 Norris, B., Anderson, J., Wager, J. F. & Keszler, D. A. Spin-coated zinc oxide transparent transistors. *Journal of physics.D, applied physics* **36**, L105-L107 (2003).
219 Volkmann, S. K. *et al.* A novel transparent air-stable printable n-type semiconductor technology using ZnO nanoparticles. *Proceedings of the IEEE*, 769-772 (2004).
220 Ong, B. S., Li, C. S., Li, Y. N., Wu, Y. L. & Loutfy, R. J. Stable, solution-processed, high-mobility ZnO thin-film transistors. *Journal of the American Chemical Society* **129**, 2750-2751 (2007).
221 Paraguay, D., Estrada, L., Acosta, N., Andrade, E. & Miki-Yoshida, M. Growth, structure and optical characterization of high quality ZnO thin films obtained by spray pyrolysis. *Thin Solid Films* **350**, 192-202 (1999).
222 Studenikin, S. A., Golego, N. & Cocivera, M. Optical and electrical properties of undoped ZnO films grown by spray pyrolysis of zinc nitrate solution. *J. Appl. Phys.* **83**, 2104-2111 (1998).
223 Krunks, M. & Mellinkov, E. Zinc oxide thin films by the spray pyrolysis method. *Thin Solid Films* **270**, 33-36 (1995).
224 Ivanov, I. & Pollmann, J. Electronic structure of ideal and relaxed surfaces of ZnO: A prototype ionic wurtzite semiconductor and its surface properties. *Phys. Rev. B* **24**, 7275 (1981).
225 Shimakawa, K., Narushima, S., Hosono, H. & Kawazoe, H. Electronic transport in degenerate amorphous oxide semiconductors. *Philos. Mag. Lett.* **79**, 755-761 (1999).
226 Jin, S. *et al.* Tuning the Properties of Transparent Oxide Conductors. Dopant Ion Size and Electronic Structure Effects on CdO-Based Transparent Conducting Oxides. Ga- and In-Doped CdO Thin Films Grown by MOCVD. *Chemistry of materials* **20**, 220-230 (2007).
227 Minami, T., Sato, H., Nanto, H. & Takata, S. Group III Impurity Doped Zinc Oxide Thin Films Prepared by RF Magnetron Sputtering. *Japanese Journal of Applied Physics* **24**, 781-784 (1985).
228 Hagemark, K. I. Defect structure of Zn-doped ZnO. *J. Solid State Chem.* **16**, 293-299 (1976).
229 Ellmer, K. Resistivity of polycrystalline zinc oxide films: current status and physical limit. *Journal of physics. D, Applied physics* **34**, 3097 (2001).

230 Zhang, D. H. & Ma, H. L. Scattering mechanisms of charge carriers in transparent conducting oxide films. *Appl. Phys. A: Mater. Sci. Process.* **62**, 487-492 (1996).
231 Zhang, D. H. Fast photoresponse and the related change of crystallite barriers for ZnO films deposited by RF sputtering. *Journal of physics. D, Applied physics* **28**, 12731277 (1995).
232 Mollwo, E. Die Wirkung von Wasserstoff auf die Leitfähigkeit und Lumineszenz von Zinkoxydkristallen. *Zeitschrift für Physik A Hadrons and Nuclei* **138**, 478-488 (1954).
233 Bae, H. S., Yoon, M. H., Kim, J. H. & Im, S. Photodetecting properties of ZnO-based thin-film transistors. *Appl. Phys. Lett.* **83**, 5313-5315 (2003).
234 Collins, R. J. & Thomas, D. G. Photoconduction and Surface Effects with Zinc Oxide Crystals. *Physical review* **112**, 388 (1958).
235 H. Kind, H. Yan, B. Messer, M. Law & P. Yang. Nanowire Ultraviolet Photodetectors and Optical Switches. *Adv. Mater.* **14**, 158-160 (2002).
236 Takahashi, Y., Kanamori, M., Kondoh, A., Minoura, H. & Ohya, Y. Photoconductivity of Ultrathin Zinc Oxide Films. *Japanese Journal of Applied Physics* **33**, 6611-6615 (1994).

Chapter 3: Materials and Experimental Methods

The successful fabrication of a functional electronic device based on organic materials depends crucially on the methodology and choice of parameters employed in the process. Furthermore, the successful reproduction and validation of results depends on the sincerity in reproducing the processing conditions. Here the fabrication and characterization methodologies employed in this work are explained.

3.1. Material Characterization

3.1.1. X-Ray Diffraction

The structural properties of thin films of organic semiconductors were examined using x-ray diffraction (XRD) measurements. In this method an incoming beam of very short wavelength radiation (≈ 1 Å) is refracted at the lattice planes of molecularly ordered films [Fig. 3.1]. Using Bragg's law:

$$n \cdot \lambda = 2d \cdot \sin\theta \tag{3.1}$$

where the plane distances d can be determined from the angular distribution of minima and maxima in the interference pattern of outgoing radiation. The distances can be compared to chain lengths of polymers and their side chains to obtain some understanding of the structural composition of the film on a molecular level.

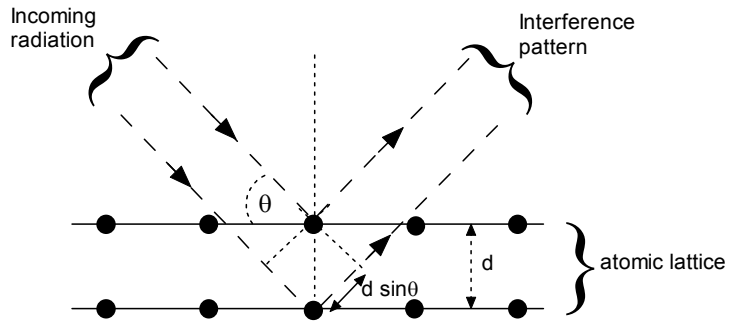


Fig. 3.1: Bragg diffraction: from the interference pattern of refracted short wavelength radiation the distances between lattice planes can be determined.

Here wide-angle X-ray diffraction (WAXD) measurements were performed on an *Oxford Diffraction Xcalibur^{TM} XP (Abingdon, Uk)* instrument using Mo Kα graphite-monochromated radiation (λ = 0.71073 Å).

Normally the morphology of molecular solids or thin films exhibits a certain degree of disorder, which means that the XRD spectrum shows a broadening of the diffraction peaks. The disorder arises from a distribution of lattice spacings, crystal domain size and orientation. As analogy it is useful to remember effects observed with optical gratings, where the position of the diffraction maximum depends only on the groove spacing, while the width of the peak decreases as the number of diffracting grooves increases. For X-ray studies the Scherrer equation correlates the peak width at half maximum (β_w) to the average size of the crystallites (R_0), i.e. the number of

refracting lattice planes, assuming that the film consists of sub-micrometer crystal domains.[1]

$$R_0 = \frac{K\lambda}{\beta_w \cos\theta} \tag{3.2}$$

K is the so called Scherrer constant, which varies with the shape of the crystallites and is typically taken as 0.9. λ is the X-ray wavelength and θ is the Bragg angle.

3.1.2. Differential Scanning Calorimetry

The exotherms and endotherms of materials were recorded using a *Mettler DSC822e* differential scanning calorimeter (DSC), calibrated with indium and zinc. The technique consists of measuring the difference in heat required to increase the temperature of a sample and a reference material. Sample and reference are kept at nearly the same temperature throughout the experiment. This method allows detecting heat flow into the sample material (endotherms) and heat release (exotherms) by the material when phase transitions occur, such as melting, glass transitions or decompositions. These transitions normally involve changes in energy or heat capacity. Here, samples of 1-10 mg sealed in aluminium crucibles were heated under nitrogen at a scanning rate of 10 °C/min from 25 °C to a temperature of around 25 °C above the melting temperature of the material in question.

3.1.3. Optical Polarized Microscopy

Optical polarized microscopy (Nikon Eclipse LV100) was employed to study the morphology of thin films. Linearly polarized light was used to illuminate the film, which was observed either in reflection or transmission through an analyzer oriented at 90° relative to the polarizer. Any refractive index anisotropy (e.g. crystalline domains) in the film causes birefringence, which leads to bright features in the microscopy image. Isotropic films (e.g. amorphous regions) do not change the light's polarization and will appear in a homogeneously dark colour due to the crossed polarizer.

3.1.4. Atomic Force Microscopy

Atomic force microscopy (AFM) is used to examine the surface profile of substrates and thin films. In this technique a nanoscale probe is mounted on a cantilever. Upon vertical movement of the tip, due to height variations of the sample surface, the bending angle of the cantilever changes and it reflects an incoming laser beam to a slightly different location on a distant high resolution photodetector. This displacement is translated to height variations to create an image of the surface profile. An important piece of information extracted of such measurements is the root mean square (rms) surface roughness.

There are several operation modes of AFM, used here were the contact mode and the close-contact mode. In the former the tip is in continual contact with the surface. In the latter the tip oscillates back and forth in close proximity to the surface, maintaining a constant low force level between tip and surface. The forces involved in this interaction can be manifold, e.g. mechanical, van-der-Waals, electrostatic, magnetic, capillary etc. The close-contact mode is often considered more appropriate for soft, organic materials. It also allows recording the phase of oscillation of the tip to detect surface regions of different composition. The AFM employed in this work (*Pacific Nanotechnology Nano-R2*) allows a scanning region of up to approximately 60 x 60 μm^2 with a vertical resolution of 1 nm.

3.1.5. Surface Energy Analysis

Pendant and sessile drop shapes were recorded and analyzed on a *Kruess DSA1000* drop shape analysis system. For the determination of solid surface energy components, the contact angles of three reference liquids (de-ionized water (γ^P = 46.4 mN/m, γ^D = 26.4 mN/m), diiodomethane (γ^P = 0 mN/m, γ^D = 50.8 mN/m) and ethylene glycol (γ^P = 21.3 mN/m, γ^D = 26.4 mN/m)) were measured.[2] Then the Owens-Wendt-Kaelble method (see section 2.8.2.) was used to fit a line to these three data points in a plot of equation 3.3:

$$\frac{\gamma_L\left(\cos\theta_C+1\right)}{2\left(\gamma_L^D\right)^{1/2}}=\left(\gamma_S^P\right)^{1/2}\left(\frac{\gamma_L^P}{\gamma_L^D}\right)^{1/2}+\left(\gamma_S^D\right)^{1/2} \tag{3.3}$$

In this plot the solid polar and dispersive surface energy components can be directly extracted from the slope and the intercept.

A useful graphical representation of the properties of the surface with respect to any liquid is given by its wetting envelopes. These are lines of constant contact angle plotted on the coordinate axes of the liquid polar and dispersive surface energy components. The wetting envelopes are calculated from solving the Owens-Wendt-Kaelble equation 2.51 for γ_L^P, using the substitution (2.46) $\gamma_L = \gamma_L^P + \gamma_L^D$:

$$\gamma_L^P = \left(\frac{\left(\gamma_S^P\right)^{1/2} + \sqrt{\gamma_S^P - (\cos\theta_C + 1)[\gamma_L^D(\cos\theta_C + 1) - 2\left(\gamma_L^D \gamma_S^D\right)^{1/2}]}}{(\cos\theta_C + 1)} \right)^2 \tag{3.4}$$

From these plots the wetting behaviour of any liquid can be predicted whose polar and dispersive surface energy components are known. These components can be determined from the contact angle of the liquid on an apolar surface, i.e. a surface which is incapable of polar interactions. This eliminates the polar liquid surface energy component from equation 3.3 and yields:

$$\gamma_L^D = \left(\frac{\gamma_L(\cos\theta_C + 1)}{2\left(\gamma_S^D\right)^{1/2}} \right)^2 \tag{3.5}$$

The polar component is then obtained from the relation $\gamma_L^P = \gamma_L - \gamma_L^D$, using γ_L as obtained from the geometric analysis of a static pendant drop of the liquid (section 2.8.1.). Commonly Teflon (PTFE, $\gamma_S^P \approx 0$) is used for this experiment. However, it was found that the PTFE surface exhibits a strong tendency to become charged. The electrostatic interaction with the liquid drop distorts the drop shape and was found to give no reproducible results. Careful discharge of the surface can be undertaken, but the method still yields significant experimental error. It is noted that in other studies, meticulous chemical and heat treatments were performed on the PTFE surfaces to yield accurate contact angle measurements.[3]

An alternative approach was developed,[4] which departs from the idea that the liquid surface tension is independent of the solid it contacts. Rearranging equation 3.3 gives:

$$\left(\gamma_L^P\right)^{1/2} = \frac{\gamma_L\left(\cos\theta_C + 1\right) - 2\left(\gamma_{Si}^D \gamma_L^D\right)^{1/2}}{2\left(\gamma_{Si}^P\right)^{1/2}} \tag{3.6}$$

where *i* stands for any surface. Equating 3.6 for two different surfaces and rearranging for γ_L^D yields:

$$\gamma_L^D = \left(\frac{\gamma_L\left(\cos\theta_1 + 1\right)\left(\gamma_{S2}^P\right)^{1/2} - \gamma_L\left(\cos\theta_2 + 1\right)\left(\gamma_{S1}^P\right)^{1/2}}{2[\left(\gamma_{S1}^D \gamma_{S2}^P\right)^{1/2} - \left(\gamma_{S2}^D \gamma_{S1}^P\right)^{1/2}]} \right)^2 \tag{3.7}$$

Using this expression the dispersive liquid surface energy component of a liquid can be calculated once its contact angles on two surfaces of known surface energy components have been measured. As mentioned in section 2.8.2 in the discussion of Berthelot's approximation, large differences between the liquid and solid surface energies can produce inaccurate results. Hence it has to be taken into account that the assumption of solid-independent liquid surface energy components is only valid for surfaces that are capable of similar interactions to those of the liquid. As for the standard method, γ_L^P is obtained from $\gamma_L^P = \gamma_L - \gamma_L^D$.

3.1.6. UV-Vis-near IR optical absorption measurements

Absorption spectra were measured in the ultraviolet-visible to near-infrared spectrum using a *Varian Cary 05E* spectrophotometer. The material of interest was spin coated from solution onto a quartz substrate and the film thickness was determined using a *Dektak* profilometer. After calibrating the UV-Vis to the spectral lamp intensity, the absorbance of the sample was measured in reference to a second, blank quartz substrate. From the absorbance spectra expressed as

$$A = \log\frac{I_0}{I} \tag{3.8}$$

the extinction coefficient was obtained using the relations

$$I = I_0 \cdot e^{-\alpha z} \tag{3.9}$$

$$K = \frac{\alpha\lambda}{4\pi} \tag{3.10}$$

where I/I_0 is the ratio of intensities behind the sample and the reference substrate, α is the absorption coefficient, z is the film thickness, λ is the light's wavelength in vacuum and K is the extinction coefficient. Substitution results in:

$$K = \frac{A\lambda}{4\pi \cdot z \cdot b} \tag{3.11}$$

where b is the ratio between log_{10} and ln, i.e. $b \approx 0.43429$. From the onset of absorption, the minimum energy for electronic transitions in the film materials was determined. This energy is likely to be the material's optical band gap (or lowest exciton) energy.

3.1.7. Cyclic Voltammetry

In cyclic voltammetry the analyte in solution is oxidized or reduced by applying a voltage between a working and a counter electrode.[5] The loss or gain of electrons by the analyte molecules is recorded as an electrical current between the working electrode and a third, the reference electrode. When the potential at the working electrode reaches an oxidation or reduction potential of the analyte (depending on the scan direction) a current peak is observed. The current then decays due to the diffusion limited concentration of pristine, uncharged analyte molecules around the electrode. The scan direction is reversed once the highest set potential is reached and inverse current peaks are observed if the red-ox reactions of the analyte are reversible. Normally a supporting electrolyte is added to the analyte solution in order to ensure that the electric field is homogeneous and near zero and is not perturbed by the oxidation and reduction of the analyte.[6]

In this work electrochemical measurements were carried out in dichloromethane containing 0.1 M Bu_4NPF_6 (Fluka-electrochemical grade) as supporting electrolyte in a classical three-electrode cell by cyclic voltammetry (CV) at scan rates ranging from 0.1 to 10 V/s. The working electrode was a glassy C disk (3 mm in diameter), the auxiliary electrode a Pt wire, and the pseudo reference electrode a Pt wire. The cell was connected to an *Autolab PGSTAT30* potentiostat (Eco Chemie, Holland). All potentials are given *vs*. Fc^+/Fc used as internal reference and are uncorrected for ohmic drop.

3.2. Device Fabrication

As a general rule, any contamination of organic compounds, substrate surfaces and interfaces by adsorbates from ambient air is to be avoided. Therefore devices and solutions were generally prepared in a clean room or glove box (i.e. in inert nitrogen atmosphere). Substrates were always cleaned before use, normally by exposure to ultra sound in acetone and isopropanol (IPA).

3.2.1. Spin Coating

For organic field-effect transistors (OFETs) the control over grain size, crystallinity and crystallographic orientation of molecules in the film with respect to the channel is critical to obtaining good device performance. Many polymers and small molecules are soluble in standard organic solvents, such as chlorobenzene, chloroform, toluene and several others. Often very homogeneous films can be obtained from spin coating. The factors affecting the above mentioned parameters in the solution processed films are the rate of solvent evaporation, the nature of the semiconductor and its concentration in solution, the temperature of the substrate/solution and the properties of the substrate surface. In addition, post-fabrication annealing steps are sometimes used to remove residual solvent or change the microstructure. Information on the organic semiconductor solutions employed in this report is shown in Table 3.1, together with information on the HOMO and LUMO levels of these materials.

During spin coating the sample is held in position on the chuck of the spin coater by vacuum pressure. The parameters spin speed, acceleration and spin duration are set on the instrument, which is immediately set in motion after the solution is dispensed on the sample surface. Typically an amount of ≈ 100 µl was sufficient to cover a 2 x 2 cm^2 substrate. In this work all solutions were spin coated at room temperature in N_2 ambient. For small organic molecules, concentrations of ≈ 10-20 mg/ml, and for higher molecular weight polymers concentrations of ≈ 2 mg/ml were used. The resulting film thickness depends on a number of parameters, such as viscosity of the solution, spinning speed, surface energy of the substrate and temperature.

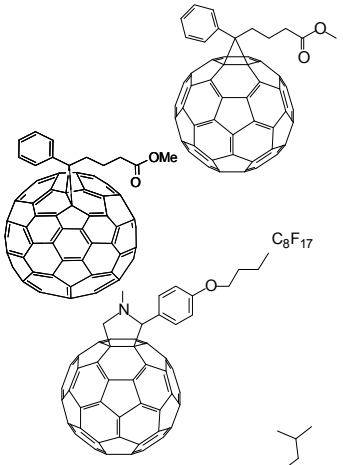
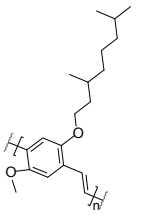
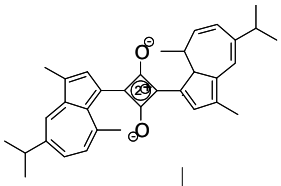
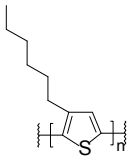
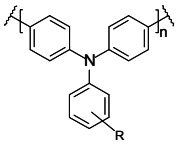
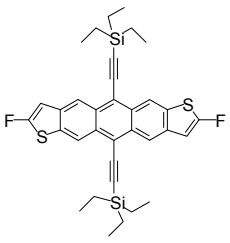
Chemical Structure	Abbreviated name (purity)	typical solvent (concentration (mg/ml)) / post deposition treatment	HOMO / LUMO (eV)	Reference
	[60]PCBM (99.5%)	Chlorobenzene (10-20) /-	5.7-6.1 / 3.5-3.8	Wöbkenberg *et al.* Synth. Metals 158, p.468 (2008)
	[70]PCBM (99%)	Chlorobenzene (10-20) /-	5.7-6.1 / 3.5-3.8	Wöbkenberg *et al.* Synth. Metals 158, p.468 (2008)
	F17-DOPF	Chlorobenzene (10) / -	5.7-6.1 / 3.5-3.8	Wöbkenberg *et al.* Appl. Phys. Lett. 92, p.143310 (2008)
	OC1C10-PPV	Chlorobenzene (2) / -	5.0 / 2.8	Meijer *et al.* Nat. Mater. 2, p.678 (2003)
	Squaraine SQ1	Chlorobenzene (10) / -	4.5-4.9 / 3.3-3.6	Wöbkenberg *et al.* in preparation
	P3HT	Chlorobenzene (20) / annealed at 90°C for 1 h	4.8-5.1 / 2.7-3.0	Koster *et al.* Appl. Phys. Lett. 88, p.093511 (2006)
	PTAA	Toluene (10) / -	5.1 / 1.8	Schols *et al.* Adv. Fun. Mater. 18, p.136 (2007)
	diF-TESADT	Tetralin (20) / annealed at 90 °C for 5 min	5.4 / 3.1	Day *et al.* Appl. Phys. Lett. 94, p.013306 (2009)

Table 3.1: Molecular structures and abbreviated names of organic semiconductors, as well as information on the material purity, solvent and concentration of the solutions employed in this work. Information on the highest occupied (HOMO) and lowest unoccupied (LUMO) molecular orbitals is also given.

Typical spin speeds and durations used in this work for most semiconductors and dielectrics ranged from 1000 rpm to 2000 rpm for 30 – 60 s, at an acceleration of ≈100-300 rpm/s. When wetting of the solution on the substrate was problematic, drop casting in combination with heating and slow spinning was employed to achieve film formation.

For a single type of material system (e.g. same material, same solvent, same substrate), in most cases a reproducible relationship between the spin speed, solution concentration and the film thickness can be established.

3.2.2. Evaporation

A vacuum evaporator was used to deposit different metal electrodes. For transistor fabrication different shadow masks were designed to pattern gate, and source-drain (S-D) electrodes. Dimensions of the S-D contacts were chosen to create devices with channel lengths and width of L = 20 - 100 μm and W = 0.5 – 2 mm, respectively. The evaporator is integrated with a glove box under nitrogen atmosphere. The masks and samples are placed above the shutters in the upper part of the evaporation chamber and a coil or boat type crucible with the electrode material (e.g. aluminium, gold, calcium, etc.) is installed between two electrodes of the evaporator. The evaporation chamber is then evacuated to pressures of approximately $6 \cdot 10^{-6} mbar$. The evaporation is started by slowly increasing the current flow across the evaporation coil/boat, until the deposition rate stabilizes at ≈0.1 nm/sec. The shutters are then opened and metal starts to deposit on the sample substrate above. The metal thickness depends on the rate and duration of evaporation and was typically in the range of 20 - 100 nm.

3.2.3. Curing of polymer layers

Some solution processed polymer films can be cured in order to stabilize them against solvents used in subsequent processing steps. In many cases cross linking agents are blended into the solution. Such linking agents accelerate the curing process for the respective material. In particular, the Benzocyclobutene (BCB) dielectric used for many transistors in this work is cured using a combination of UV exposure and

thermal curing on the hot plate. For UV curing the samples are placed at approximately 10 cm below a UV lamp (*Hoenle*, 250 mW/cm^2 UVA) in nitrogen atmosphere and exposure varied between a few seconds and 45 minutes, depending on the material and type of cross linking agent employed. Thermal curing is performed on a hotplate, also in nitrogen. During the latter samples are covered with a Petri dish to minimize the vertical temperature gradient.

3.2.4. Photolithography

Bottom contact FETs were fabricated on highly p-doped silicon wafers, with a thermally grown 200 nm thick oxide layer as gate dielectric. Gold S-D contacts were patterned using standard photolithography procedures described earlier.[7,8] In brief, a layer of photo sensitive resist is spin coated and exposed to UV light through a mask that is UV transparent at the S-D electrodes. Exposed areas of the resist are removed using specialized solvents, thus leaving blanks for the S-D electrodes. Prior to the evaporation of gold, a 10 nm layer of titanium is deposited to improve adhesion on the SiO_2. A final lift-off step removes the excess metal and leaves defined S-D electrodes. Finally, the SiO_2 dielectric surface is passivated using hexamethyldisilazane prior to semiconductor deposition.[9]

3.2.5. Fabrication of ring oscillators

For the fabrication of ring oscillators bottom gate-bottom contact transistors were employed on a SiO_2 substrate. Gate electrodes and first level interconnect lines were made by patterning a gold layer using standard photolithography techniques. The gate dielectric was a 300 nm thick photoimageable polymer (polyvinylphenol), which was spin coated and subsequently exposed to ultraviolet light to define contact holes (vias). S-D electrodes and second level interconnects were defined in the second gold layer. Finally, circuit fabrication was completed by spin coating the semiconductor solutions.

3.2.6. Self-assembly of organic molecules on metal oxides

The purposes of self-assembled molecular layers found in organic electronics are manifold and include workfunction modification for charge carrier extraction or injection,[10] surface energy modification[9] and surface passivation in interface transport devices.[11] Lately self-assembled monolayers (SAMs) have also been employed as dielectrics[12-14] and as organic semiconductors in OFETs.[15]

SAMs are typically deposited from solution, i.e. by spin coating, dip coating or drop casting, or by adsorption from the vapour phase. The SAM molecules always comprise a functional group which bonds to a metal or metal-oxide surface. Here we are concerned with two particular SAMs, hexamethyldisilazane (HMDS) for passivation of otherwise hydroxyl-rich SiO_2 dielectric surfaces and phosphonic-acid SAMs as part of ultra-thin dielectrics on Al gates. In order to maximize the monolayer coverage the surface must be as free from adsorbed impurities as possible and have sufficient reactive groups exposed. This is achieved by exposing the sample to oxygen plasma immediately prior to the SAM deposition. The process involves the creation of plasma in a low pressure oxygen atmosphere using radio frequency electromagnetic energy. The power and duration of the plasma exposure are typically chosen to be 80 – 100 W and 30 s – 5 min, respectively.

In the case of HMDS the bonding occurs under the release of NH_3, leaving a methylterminated SiO_2 surface behind [Fig. 3.2]. The samples are exposed to saturated HMDS vapour for several hours at room temperature and then rinsed in isopropanol (IPA).

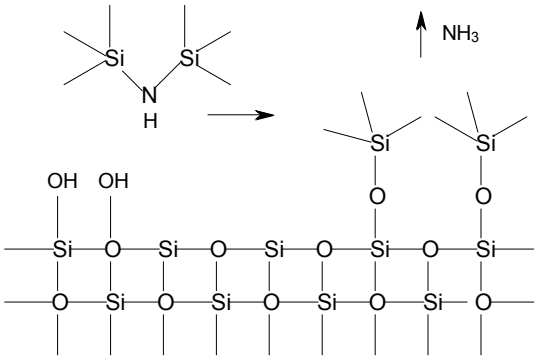


Fig. 3.2: Bonding of hexamethyldisilazane (HMDS) molecules on SiO_2 surface under release of NH_3.

For the fabrication of ultra-thin SAM based gate dielectrics, Al gate electrodes are evaporated onto glass substrates. Their surface is oxidized by exposure to oxygen plasma or thermal annealing on a hotplate in air, prior to deposition of the phosphonic

acid SAM solution (typically 5 mM, i.e. ≈ 17 mg/ml in IPA) by drop casting. Subsequent baking of the sample at 140°C for several hours ensures optimal bonding of the phosphonic acid groups to the oxide surface. Luschtinetz *et al.* explained that the bonding of phosphonic acid functional groups to Al_2O_3 consists of several steps, which lead to monodentate, bidentate or tridentate bonds [Fig. 3.3].[16]

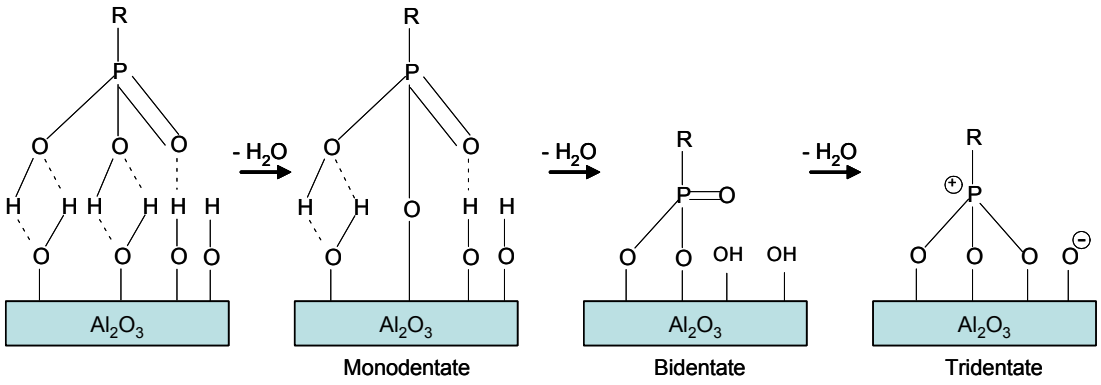


Fig. 3.3: Step-wise bonding of phosphonic acid molecules to Al-oxide surface under the release of water.

In this work further characterization of the SAM layer on a molecular level was not undertaken, but from reports in the literature it is expected that all three bond types occur.[16] Finally, rinsing in pure IPA and exposure to ultrasound in IPA ensures the removal of adsorbed residues of non-bonded organic molecules.

3.2.7. Spray Pyrolysis

Spray pyrolysis has been known as a very simple and low cost solution deposition method for films of any composition.[17] The method has been employed for the deposition of dense films, porous films and for powder production. Even multilayered films can easily be fabricated using this versatile technique. It has been used for several decades in the glass industry and in solar cell production.[18-21] The mechanisms involved in the spray pyrolysis process have been studied by several groups.[17,21,22] The basic principle is the conversion of a soluble precursor material into the target substance upon spraying of the precursor solution aerosols onto a heated substrate. Solubilizing organic ligands dissociate at the elevated temperature and are removed in the process together with the solvent due to their high volatility. The interplay between substrate temperature and dissociation temperature of the precursor is the most crucial factor in determining the resulting film quality. In the case of

metal-oxide deposition the temperature critically affects the film roughness, porosity, its crystallinity and cracking behaviour.[17]

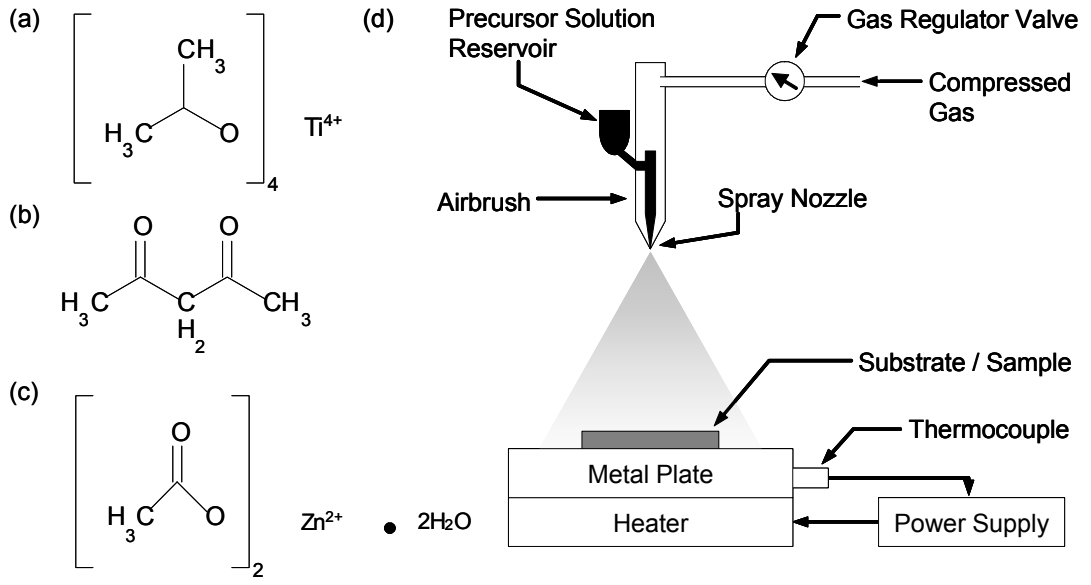


Fig. 3.4: (a) Ti isopropoxide, (b) acetyl acetone, (c) Zn acetate dihydrate, (d) schematic of spray pyrolysis setup.

The precursor material employed for the deposition of TiO_2 films by spray pyrolysis was titanium isopropoxide $Ti(OCH(CH_3)_2)_4$ [Fig. 3.4(a)]. The chelating agent acetyl-acetone[23] [Fig. 3.4(b)] was added to the Ti-isopropoxide liquid in a 5:7 proportion by weight, and the product was diluted in ethanol at a ratio 1:9 by volume.

In the case of ZnO, the solid powder zinc acetate dihydrate $[Zn(CH_3COO)_2].2H_2O$ (99.9%) precursor [Fig. 3.4(c)] was dissolved in methanol at a concentration of 0.2 M.

The substrates used for these transistors were typically highly doped Si wafers, serving as common gate electrode, with a 200-300 nm thick layer of thermally grown SiO_2 as gate dielectric. The S-D contacts were either patterned by photolithography prior to spray pyrolysis (bottom contact) or deposited afterwards via thermal metal evaporation through shadow masks (top contact).

The spray pyrolysis setup employed here is schematically shown in Fig. 3.4(d). Aerosols of the solution were sprayed vertically downwards onto the heated substrate (T = 200 – 500 °C) from a distance of 20-30 cm using a commercially available handheld airbrush (*Badger 100*). The carrier gas employed was nitrogen and the deposition was performed entirely in air under a fume hood without taking additional

precautions. When the aerosols reach the substrate surface the precursor solution decomposes into the metal oxide, water and various gases depending on the deposition temperature (normally CO_2 at $T_S > 400$ °C).[24,25]

Uniform, homogeneous and reproducible films were achieved by adopting the following procedure. The deposition sequence consisted of 5 spray cycles, during each of which solution was sprayed intermittently onto the heated substrates for 12 s. This was followed by a break of ca. 48 s to let the droplets adsorb to the surface. After the deposition was completed, the samples were allowed to cool down slowly to room temperature before device processing continued.

3.3. Device Characterization

3.3.1. Impedance spectroscopy

The capacitance of dielectric films sandwiched between two conducting electrodes of known area overlap was determined using a *Solatron 1260A Impedance Analyzer*. Measurements were performed between 10 Hz and 1 kHz, with a peak-to-peak voltage signal of 1 V. The capacitance value was extracted from the total impedance and divided by the overlap area of the two electrodes to give C_i, the geometrical capacitance:

$$C_i = \frac{\varepsilon_r \varepsilon_0}{d} \tag{3.12}$$

where ε_0 is the vacuum permittivity, ε_r and d are the relative permittivity and the thickness of the dielectric film, respectively.

3.3.2. I(V) characteristics

The quality of field-effect transistors can be assessed through analysis of their current-voltage characteristics. Transfer and output curves were measured using an *Agilent 4156C* or a *Keithley SCS4200* semiconductor parameter analyzer. Electrical connections were provided using fine probe tips. The instrument applies gate-source and drain-source bias, while measuring drain, source and gate currents [Fig. 3.5].

Measurements can be performed in nitrogen atmosphere ($H_2O \approx 2.5$ ppm, $O_2 < 0.1$ ppm), under high vacuum (10^{-5} mbar) or in ambient air.

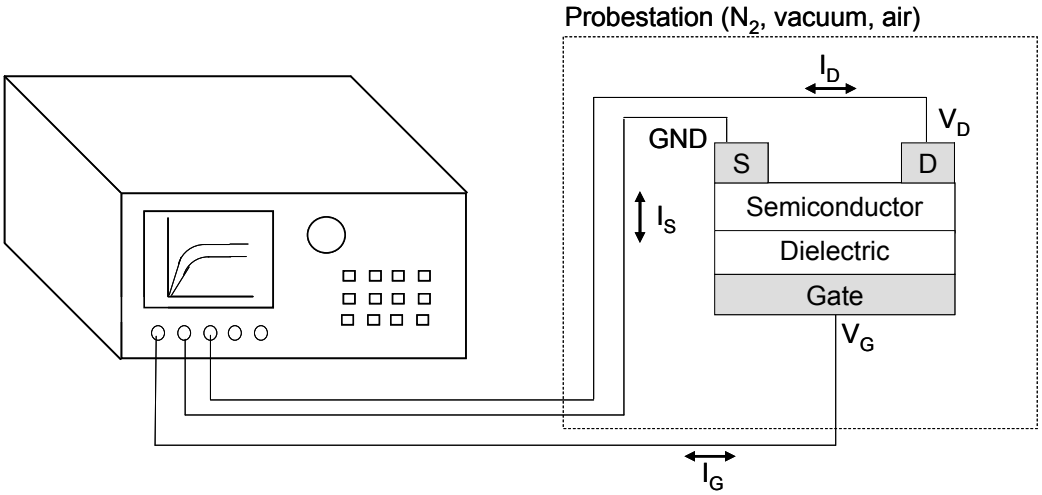


Fig. 3.5: Experimental setup for characterization of field-effect transistors.

The samples can also be cooled or heated to any temperature between 80 and 573 K. An external temperature controller monitors and adjusts the temperature of the sample holder by flow of liquid nitrogen and coil heating. The background (leakage) current when the needles are suspended in air or nitrogen is roughly a few pA. Currents below 1 pA can therefore not be detected with high degree of accuracy.

3.3.3. Static and dynamic characterization of integrated circuits

In quasi static operation inverter circuits were tested using the parameter analyzers. In a similar fashion to the characterization of single transistors, probe needles were used to contact the input, output and supply electrodes and voltages and currents were applied and measured through the various source measurement units (SMUs) of the analyzer.

The ring oscillators were supplied using *Keithley Sourcemeters* that were connected to the supply (V_{DD}) and ground electrodes in the probe station. The ground signal was fed to a *Stanford SR 570* current preamplifier, the output of which was connected to a *Tektronix TPS2024* oscilloscope. This setup allowed monitoring the oscillation trace and extracting the operational frequency at various supply voltages. Long operation times of the ring oscillators were avoided especially at high voltages in order to prevent deterioration of the device performance due to stressing effects.

Most circuit designs included a buffer inverter and transistor after the oscillator to prevent the capacitive load of the probe needle from limiting the operational frequency. The current amplifier provided the oscilloscope with a high impedance output, hence limiting the effect of parasitic capacitances.

3.3.4. Static and dynamic characterization of light sensing devices

Since the light sensing OFETs studied in chapter 5 were not air stable enough to perform the measurements in ambient atmosphere, the light sensing measurements were done in the glovebox in N_2 atmosphere. The light emitting diodes (LEDs) were installed in close proximity (≈ 0.5-1 cm) above the sample. For illumination we used a high power IR-LED from *Osram* with peak intensity at 880 nm, a blue InGaN LED (λ_{peak} = 469 nm) or white fluorescent light. The optical power density was recorded using an optical powermeter and a photocell (*Newport 1935-C*). Electrical characterization of the transistors in quasistatic operation was performed using a *Keithley SCS4200* parameter analyzer. For pulsed measurements the transistor was biased using two *Keithley Sourcemeters*. The source-drain current was amplified using a *Stanford SR570* current amplifier, the output of which was displayed on a *Tektronix TPS2024* oscilloscope. The LED was pulsed using the square wave function of a signal generator (*Thurlby Thandar TG4001*).

Reference list:

1 Guinier, A. *X-Ray Diffraction In Crystals, Imperfect Crystals, and Amorphous Bodies*. (Dover Publications, 1994).

2 Kruss. *Selected literature values for surface tension of liquids*, http://www.kruss.de/en/theory/substance-properties/liquids.html (2009).

3 Li, D. & Neumann, A. W. Contact angles on hydrophobic solid surfaces and their interpretation. *J. Colloid Interface Sci.* **148**, 190-200 (1992).

4 Wöbkenberg, P. H. *et al.* Low-voltage organic transistors based on solution processed semiconductors and self-assembled monolayer gate dielectrics. *Appl. Phys. Lett.* **93**, 013303-013303 (2008).

5 Nicholson, R. S. Theory and Application of Cyclic Voltammetry for Measurement of Electrode Reaction Kinetics. *Anal. Chem.* **37**, 1351-1355 (1965).

6 Dickinson, E. J. F., Limon-Petersen, J. G., Rees, N. V. & Compton, R. G. How Much Supporting Electrolyte Is Required to Make a Cyclic Voltammetry Experiment Quantitatively Diffusional? A Theoretical and Experimental Investigation. *The Journal of Physical Chemistry C* **113**, 11157-11171 (2009).

7 Anthopoulos, T. D. *et al.* Solution processible organic transistors and circuits based on a C70 methanofullerene. *J. Appl. Phys.* **98**, 054503 (2005).

8 Anthopoulos, T. D. *et al.* Air-Stable n-Channel Organic Transistors Based on a Soluble C84 Fullerene Derivative. *Adv. Mater.* **18**, 1679-1684 (2006).

9 Lim, S. C. *et al.* Surface-treatment effects on organic thin-film transistors. *Synthetic Metals* **148**, 75-79 (2005).

10 de Boer, B., Hadipour, A., Mandoc, M. M., van Woudenbergh, T. & Blom, P. W. M. Tuning of Metal Work Functions with Self-Assembled Monolayers. *Adv. Mater.* **17**, 621-625 (2005).

11 Yoo, B. *et al.* High-mobility bottom-contact n-channel organic transistors and their use in complementary ring oscillators. *Appl. Phys. Lett.* **88**, 082104 (2006).

12 Fontaine, P. *et al.* Octadecyltrichlorosilane monolayers as ultrathin gate insulating films in metal-insulator-semiconductor devices. *Appl. Phys. Lett.* **62**, 2256-2258 (1993).

13 Collet, J. & Vuillaume, D. Nano-field effect transistor with an organic self-assembled monolayer as gate insulator. *Appl. Phys. Lett.* **73**, 2681-2683 (1998).

14 Klauk, H., Zschieschang, U., Pflaum, J. & Halik, M. Ultralow-power organic complementary circuits. *Nature* **445**, 745-748 (2007).

15 Smits, E. C. P. *et al.* Bottom-up organic integrated circuits. *Nature* **455**, 956-959 (2008).

16 Luschtinetz, R. *et al.* Adsorption of phosphonic and ethylphosphonic acid on aluminum oxide surfaces. *Surf. Sci.* **602**, 1347-1359 (2008).

17 Perednis, D. & Gauckler, L. J. Thin film deposition using spray pyrolysis. *Journal of electroceramics* **14**, 103-111 (2005).

18 Hill, J. E., Chamberlin, Rhodes R. Process for making conductive film. United States patent (1964).

19 Mochel, J. M. Method of producing electrically conducting coatings on glass and mica sheets. United States patent (1950).

20 Kavan, L. & Grätzel, M. Highly efficient semiconducting TiO2 photoelectrodes prepared by aerosol pyrolysis. *Electrochimica Acta* **40**, 643-652 (1995).

21 Mooney, J. B. & Radding, S. B. Spray Pyrolysis Processing. *Annual Review of Materials Science* **12**, 81-101 (1982).

22 Viguie, J. C. & Spitz, J. Chemical Vapor Deposition at Low Temperatures. *J. Electrochem. Soc.* **122**, 585-588 (1975).

23 Hung, K., Hsieh, C., Yang, W. & Tsai, H. Synthesis of Nanometric-Sized Barium Titanate Powders Using Acetylacetone as the Chelating Agent in a Sol-Precipitation Process. *J. Electron. Mater.* **36**, 245-252 (2007).

24 Tonto, P., Mekasuwandumrong, O., Phatanasri, S., Pavarajarn, V. & Praserthdam, P. Preparation of ZnO nanorod by solvothermal reaction of zinc acetate in various alcohols. *Ceram. Int.* **34**, 57-62 (2008).

25 Krunks, M. *et al.* Thermoanalytical study of acetylacetonate-modified titanium(IV) isopropoxide as a precursor for TiO2 films. *J. Therm. Anal. Calorim.* **80**, 483-488 (2005).

Chapter 4: Electron transporting organic Field-Effect Transistors

The prevailing lack of high performance electron transporting organic semiconductors is often seen as a major hurdle for the large scale implementation of complementary logic into organic electronics. However, the development of organic complementary logic is crucial for the next generation of low power organic integrated circuits. Furthermore, it is desirable to develop soluble and air stable materials to enable the patterning by conventional solution deposition techniques, such as printing. Soluble Fullerene derivatives are investigated as promising electron transporting organic semiconductors that combine high mobility with facile solution processing. In optimized transistor architectures using a polymer dielectric and low-work function injection electrodes, transistors with very high electron field-effect mobility of 0.2 cm^2/Vs are demonstrated.

4.1. Introduction

Organic semiconductors have received increasing attention during the last two decades with regard to a range of electronic applications, such as solar cells, light emitting diodes, light detectors, memory devices, organic field-effect transistors (OFETs) and integrated circuits (ICs).[1] OFETs in particular offer a huge potential in a number of applications including pixel drivers in flexible displays and RFID tags. Recent research has developed a number of hole transporting organic semiconductors, which have been studied extensively and are readily employed in organic unipolar integrated circuitry.[2] In the meantime it has been shown that complementary logic, comprising both n-type and p-type devices, allows for lower power consumption, better noise margins and improved noise immunity compared to unipolar logic.[3] A significant technological challenge, however, associated with organic complementary circuits is the deposition and patterning of the p- and n-channel semiconductors with high resolution. The vast majority of organic complementary circuits reported in the literature to date are based on thermally evaporated p-channel/n-channel semiconductors.[3-6] Although an excellent proof of concept, practical implementation of the technology in large-scale ICs is limited due to design constraints imposed by the shadow masking utilised for semiconductor patterning. In this context, alternative deposition techniques (i.e. ink-jet printing, gravure printing, etc.) could potentially provide a long-term solution. In an effort to address this issue, significant research has focused on the synthesis of organic semiconductors with useful solubility.[7] As a result, a number of soluble p-channel semiconductors with carrier mobilities comparable to amorphous silicon (a-Si) have been demonstrated and utilised in unipolar ICs.[8-10] On the other hand, progress in the area of soluble n-channel semiconductors has been much slower with relatively few successful demonstrations.[11-16] This distinct lack of soluble n-channel semiconductors has, to a large extent, hindered the development of large-scale organic complementary ICs. Therefore the study and development of existing and new electron conducting organic materials is of high importance and a necessary step towards the next generation of high performance organic integrated circuits.

The major problems with most electron transporting organic semiconductors are their often poor processability and their low environmental stability against oxidization in the presence of ambient air. Also, electron transport at the

semiconductor-dielectric interface is very sensitive to the presence of charge trapping radical anions, which introduce localized electronic states within the semiconductor's energy gap. This problem has been discussed in detail by Chua *et al.*[17] Another issue with n-type semiconductors in field-effect transistors is the injection of electrons into the materials.

In this chapter some of these issues are addressed for the case of electron transporting fullerene materials and results of optimized devices are presented as benchmark for future work.

4.2. The model n-channel organic semiconductor

As a reference for further development of n-channel organic field effect transistors, [6,6]-phenyl-C61-butyric acid ester ([60]PCBM) was employed in a typical bottom contact configuration of gold electrodes on highly doped silicon substrates with a hexamethyldisilazane (HMDS) passivated layer of SiO_2 as gate dielectric. [60]PCBM (see Fig. 4.1(a) inset for molecular structure) is known for its electron transport properties[18] and is easily soluble in standard solvents, such as Chlorobenzene (CB).

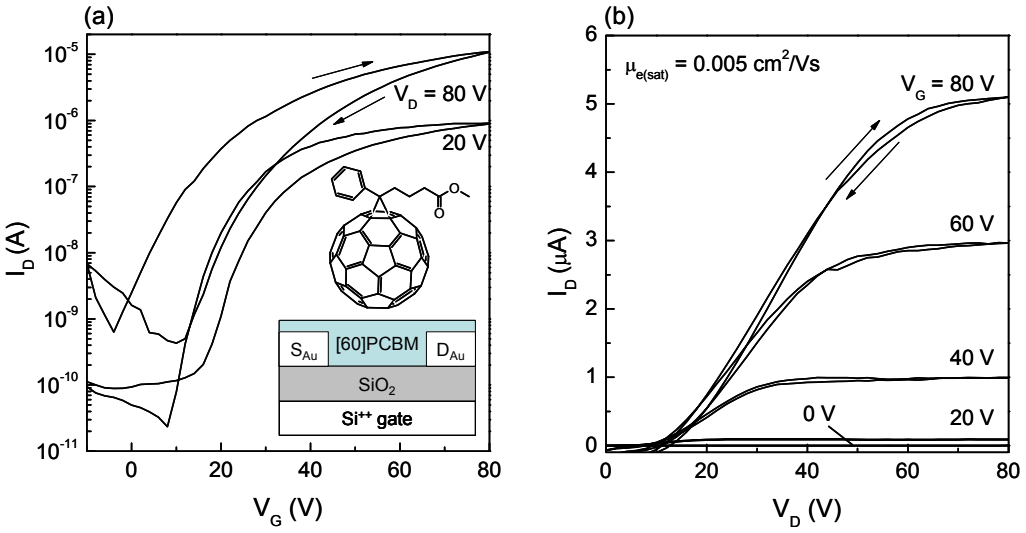


Fig. 4.1: Transfer (a) and output (b) curves of a bottom gate transistor employing [60]PCBM as n-channel semiconductor and Au bottom contact S-D electrodes. L = 30 μm, W = 10 mm, C_i = 17 nF/cm^2.

For the fabrication of FETs, the semiconductor is spin-coated and the samples are tested in nitrogen in order to minimize the effect of atmospheric oxidants. From a typical transfer characteristic [Fig. 4.1(a)] the field-effect mobility of the electrons in the device channel was determined in the saturation regime using the equation 2.21:

$$\mu_{sat} = \frac{\partial^2 I_{D,sat}}{\partial V_G^2} \cdot \frac{L}{WC_i} \tag{2.21}$$

The extracted electron mobility was of the order of 10^{-3} cm^2/Vs. The device characteristic is dominated by large hysteresis, which is attributed to charging of trap states at the interface between inorganic SiO_2 and C_{60}. Presence of hydroxyl functional groups at the oxide surface could be the origin of these states.[17] A large threshold for onset of current modulation and the nonlinear behaviour of the drain current in the output curves at low drain voltages [Fig. 4.1(b)] also indicate bad injection properties due to non-ohmic metal-semiconductor contact. These problems will be addressed in the following sections.

4.3. The role of the gate dielectric

"All-organic" devices require organic dielectrics that are easy to process (e.g. solution processable) and that are compatible with other processing steps (e.g. insolubility in solvent used to dissolve the semiconductor). Besides these requirements, organic dielectrics are expected to bear advantages for interface transport devices, such as FETs. For example, Chua *et al.* achieved electron transport in OFETs using conventional polymer hole transporting materials when suitable organic dielectrics were employed.[17,19] The interface between the organic semiconductor and the organic dielectric often contains less trap states than conventional inorganic oxide layers, mainly due to the absence of dangling bonds. The latter often require a number of treatments (s.a. oxygen plasma treatment or application of self assembled monolayers (SAMs), such as HMDS) before deposition of the semiconductor in order to prepare a homogeneous surface free of radical anions. Furthermore, organic dielectrics enable the fabrication of other types of device architectures, such as the top-gate configuration, where the dielectric and then gate electrode are deposited after the semiconductor. In some cases this approach can lead

to significant performance increase due to a better interface morphology at the top-side of the semiconductor layer.[9,20]

4.3.1. Benzocyclobutene gate dielectric

As previously shown by Chua *et al.*[19] and other groups[21-23] divinyltetramethyldisiloxane-bis(benzocyclobutene) (BCB) [Fig. 4.2(a)] shows promising characteristics as organic gate dielectric material. It can easily be processed from solution and provides a flat, nearly pinhole and defect free surface, which is a prerequisite for high mobility charge transport at the interface to the organic semiconductor.

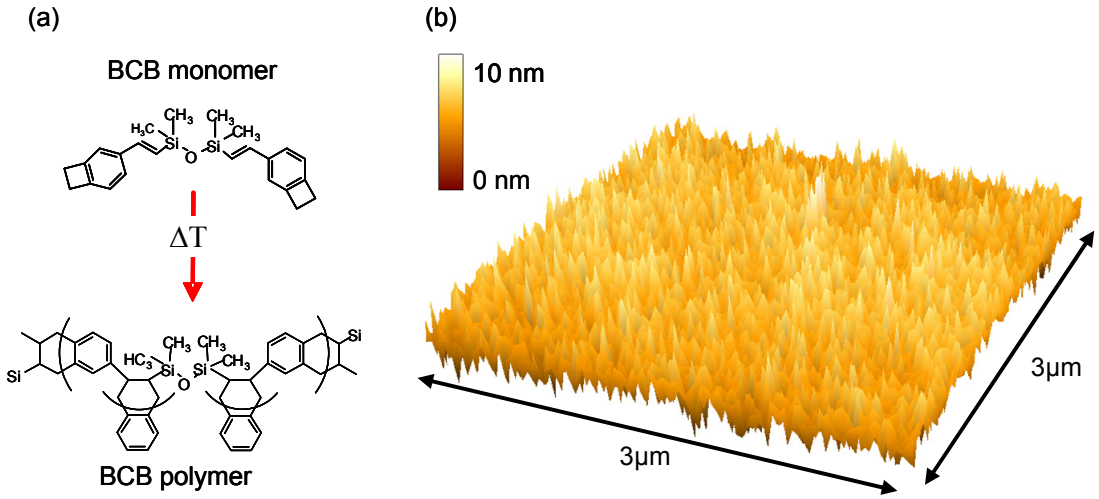


Fig. 4.2: (a) Chemical structure of the BCB before (monomer) and after curing (polymer network). (b) Atomic force microscopy image of cured BCB surface, rms roughness = 1.2 nm.

The surface roughness of cured BCB films on SiO_2 substrates was measured by atomic force microscopy (AFM) and was found to be approximately $rms_{BCB} \approx 1.2$ nm [Fig. 4.2(b)]. This value is very low, even compared to SiO_2 oxide surfaces ($rms_{SiO2} \approx 2.3$ nm), which are typically grown under precisely controlled conditions. The geometrical capacitance of BCB films of different thicknesses was measured on Indium Tin Oxide (ITO) coated glass substrates, using an evaporated Aluminium contact as top electrode [Fig. 4.3]. A clear correlation between the thickness and the capacitance of the films was established, in good agreement with the theoretical prediction based on a dielectric constant of $\varepsilon_{BCB} = 2.6$.[22] In a first attempt to improve the performance of the [60]PCBM based transistor, a 1 µm thick BCB layer was spin

coated and cured on highly doped silicon substrates with a thermally grown SiO_2 layer of 200 nm [Fig. 4.4(a) inset].

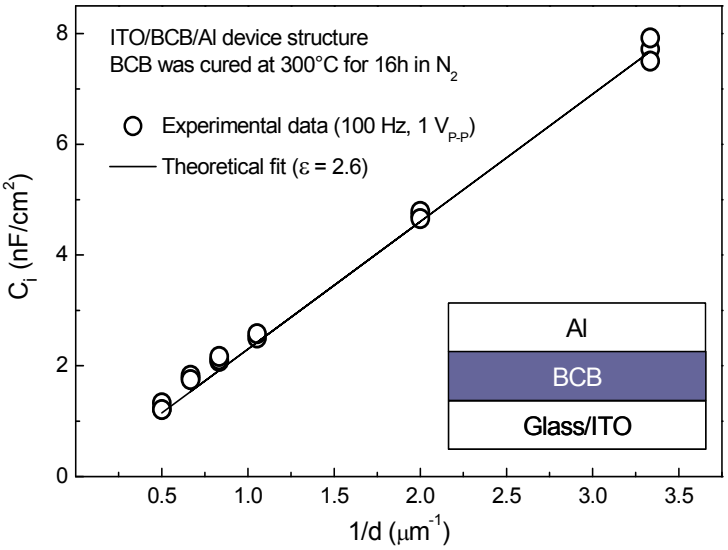


Fig. 4.3: Capacitance measurements of dielectric Benzocyclobutene layers of different thicknesses and fit using $\varepsilon_{BCB} = 2.6$.

[60]PCBM was then spin coated as the organic semiconductor followed by the top Al S-D electrode evaporation. The total gate-channel capacitance in this FET configuration is given by:

$$\frac{1}{C_i} = \frac{1}{C_{i,BCB}} + \frac{1}{C_{i,SiO_2}} \tag{4.1}$$

$$C_i = (2.3 \pm 0.1)\frac{nF}{cm^2} \tag{4.2}$$

where C_i is the total geometrical capacitance of the SiO_2 and BCB dielectric bilayer, while $C_{i,SiO2}$ and $C_{i,BCB}$ are the geometrical capacitances of the separate layers using $\varepsilon_{SiO_2} = 3.9$ and $\varepsilon_{BCB} = 2.6$, respectively. The error here accounts for thickness variation across the film. The transistors exhibit current on/off ratios of approximately 10^4. Using the data from the transfer characteristic in Fig. 4.4(a), the field effect mobility in the saturation regime was found to be of the order of 0.05 cm^2/Vs. The characteristics show negligible hysteresis and a switch on voltage close to 0 V. These are indications for the absence of charging effects of electron traps in the channel region. The linearly increasing drain current in the output curves [Fig. 4.4(b)] for low drain voltages implies that charge injection into the semiconductor is no longer dominated by non-ohmic contact resistance effects. Discussion of the improved electron injection properties with Al-top electrodes will follow.

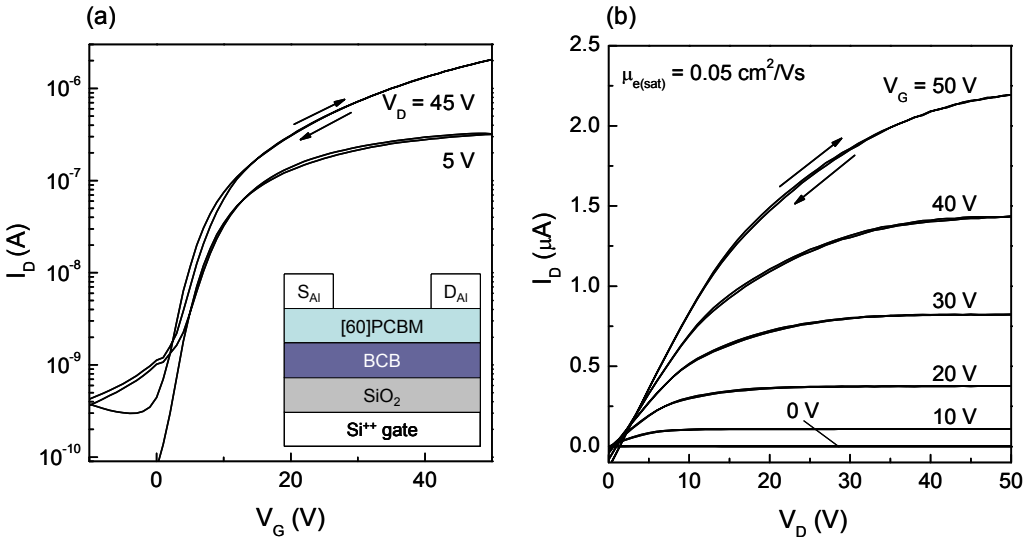


Fig. 4.4: Transfer (a) and output (b) characteristics of [60]PCBM – based top contact OFET on SiO_2/BCB dielectric layer system (inset a). W = 1.5 mm, L = 60 μm, C_i = 2.25 nF/cm^2.

The devices also exhibit a clear pinch off point ($V_D >> V_G$), which implies a constant conductance under an applied V_G. This kind of transistor characteristic is well described by the gradual channel formalism adopted from inorganic metal-oxide-semiconductor-FET (MOSFET) theory (see section 2.3.1).[24]

The same experiment was repeated with ITO coated glass substrates. The ITO served as gate electrode, onto which a 2 μm thick BCB film was spin coated and cured. The capacitance of the BCB dielectric layer is 1.2 (± 0.1) nF/cm^2. Two types of devices were prepared, Type I in a bottom gate - bottom contact (BG-BC) configuration, where the Al S-D contacts were evaporated before spin coating the [60]PCBM solution and Type II in a bottom gate - top contact (BG-TC) configuration, for which the contacts were evaporated onto the semiconductor film. Transfer characteristics of both types are shown in Fig. 4.5. It was found that devices with the top contact architecture [Fig. 4.5(b)] exhibited electron mobilities that were more than 20x higher than in the devices with bottom contacts [Fig. 4.5(a)]. Also the sub-threshold slope improved significantly in top contact (8 V/dec) compared to bottom contact (23 V/dec) devices, indicating a more efficient channel formation when a positive gate bias is applied. A lower sub-threshold slope also means a lower density of electron trap states at the interface between the dielectric and semiconductor (see 2.3.1.).

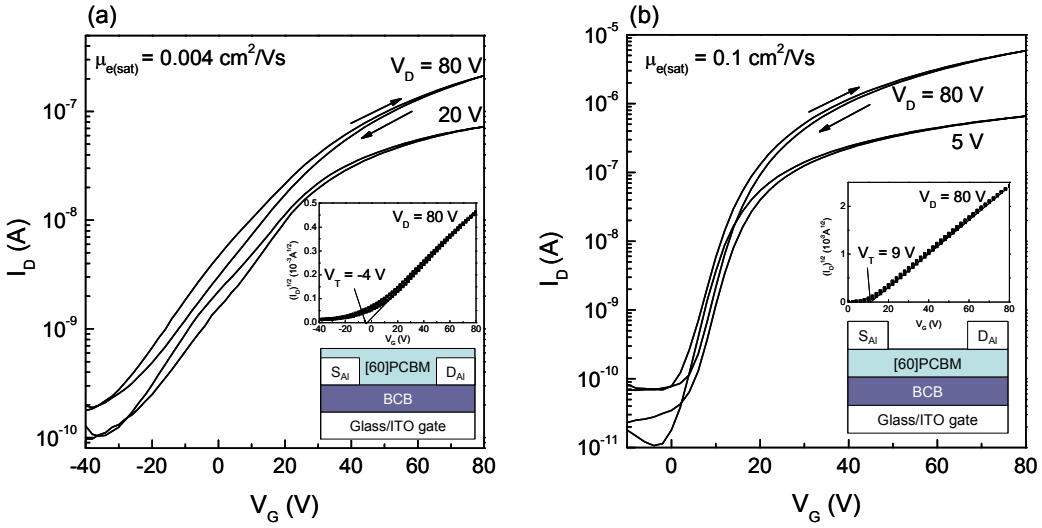


Fig. 4.5: Transfer characteristics of [60]PCBM based bottom contact (a) and top contact (b) OFET on BCB dielectric. W = 1.5 mm, L = 60 μm, C_i = 1.15 nF/cm^2. Insets: linear dependencies of $(I_D)^{1/2}$ on V_G and FET architectures.

The density of interfacial electron traps is estimated using equation 2.25, under the assumption that the transistor is switched on from a state where its channel is entirely depleted:

$$n_{trap}^{\max} \approx C_i \left(\frac{S}{k_B T \ln 10} - \frac{1}{e} \right) \tag{2.25}$$

Using T = 293 K and C_i = 1.2 nF/cm^2 an estimated upper limit for the trapped electron density was obtained for top and bottom contact devices to be $n_{trap,TC}^{\max} \approx 1 \cdot 10^{12} cm^{-2}$ and $n_{trap,BC}^{\max} \approx 3 \cdot 10^{12} cm^{-2}$. These trap densities are comparable to values previously reported for organic transistors[25-27] and reflect the better quality interface in the case of top contacts.

The lower performance in bottom contact devices is attributed to the disruption of the deposition process by the prefabricated S-D electrodes.[28] It is also expected that the surface energy discrepancy between the dielectric and the electrode metal may lead to a non-continuous film formation and hence a bad injection interface between the electrodes and the semiconductor.[28,29]

In top contact devices, electron mobilities of the order of 0.1 cm^2/Vs were obtained (in saturation), with current on/off ratios >10^4 and switch-on voltages around 0 V. From the straight line of $(I_D)^{1/2}$ vs. V_G [Fig. 4.5(b) inset] one can determine the

threshold voltage to be approximately 9 V. The gate leakage currents were always at least two orders of magnitude lower than the drain-source current. From these results it can be concluded that BG-TC OFETs with Al S-D electrodes and the organic dielectric yield significantly improved device characteristics. These results are comparable with state-of-the-art solution processed n-channel OFETs reported in the literature.[11,15,22,30]

4.3.2. Electrical Stressing

An important quality of a field-effect transistor is its response to continuous operation over prolonged periods of time. Similar to transistors based on amorphous silicon, organic FETs in the literature generally exhibit significant stressing effects, most often in the form of a shift of the threshold (or switch-on) voltage.[31]

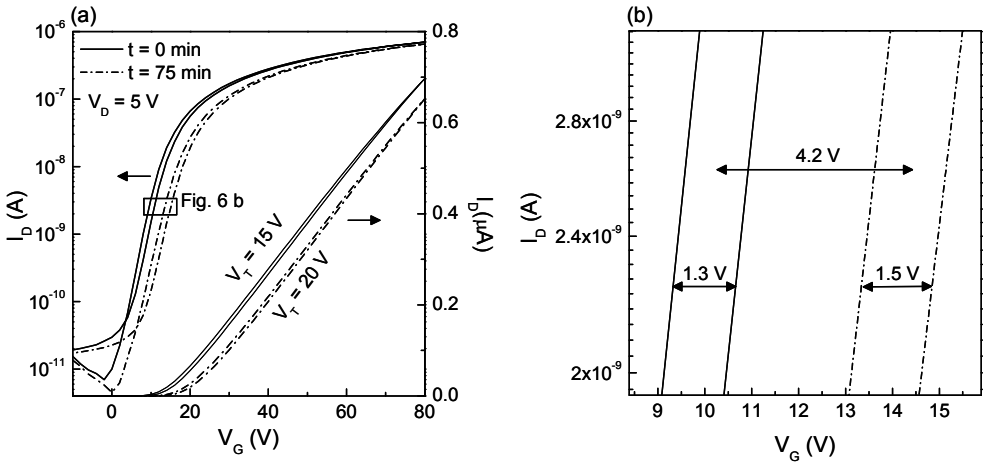


Fig. 4.6: (a) Transfer characteristics of [60]PCBM based top contact OFET on BCB dielectric before and after stressing at V_D = 5 V, V_G = 40 V for 75 min. (b) Enlarged extract from (a). W = 1.5 mm, L = 60 μm, C_i = 1.2 nF/cm^2.

In order to characterize the response to stressing a constant bias of V_D = 5 V and V_G = 40 V was applied to a BG-TC device using BCB as dielectric. Fig. 4.6(a) shows transfer curves (forward and backward sweep) at V_D = 5V before stressing and after 75 min of continuous operation. Both, the on and the off current levels remain unchanged after the stressing. The subthreshold slope, the mobility (represented in Fig. 4.6(a) by the slope of I_D vs. V_G on a linear scale) and the hysteresis between forward and backward scans do not change significantly either [Fig. 4.6(b)]. However, it is apparent from the plot that the transfer curve is shifted towards more positive gate voltages after the stress period. This corresponds to a shift in threshold (or switch-on)

voltage by approximately ΔV_T = 5 V. This observation is in good agreement with the stressing phenomena reported in literature.[32] The decrease in current at a particular gate bias without mobility degradation is explained by Salleo *et al.* as the removal of mobile charges from the channel during stressing. During continuous gate bias electrons will be drawn into the [60]PCBM film and accumulate in trap states at the dielectric-semiconductor interface, from where they partially screen the gate field. According to Salleo *et al.* [32] the density of additionally trapped electrons can be estimated using equation 2.22:

$$\Delta n = \frac{C_i \cdot \Delta V_T}{e} \approx 3 \cdot 10^{10} cm^{-2} \qquad (2.22)$$

Consequently a higher gate voltage is required to inject additional mobile charges that can contribute to the transistor current. Interestingly, Zhang *et al.* observed no bias stress effect on a BCB dielectric when they deposited purified C_{60} by standard physical vapour deposition.[21] The same was found for other hydroxyl-free polymer dielectrics. This comparison suggests that the stressing effect observed here is due to trapping in the semiconductor, rather than the dielectric. This is not unlikely taken into account that the [60]PCBM was deposited unpurified (99.5% , Solenne BV) from solution and no post-deposition treatment was performed. A possible remedy to improve the electrical stability of the solution processed transistors could be a post-fabrication annealing step in order to remove any remaining solvent molecules from the semiconductor film.

4.3.3. Top gate transistor architecture

In some cases the performance of organic semiconductors depends strongly on the device architecture and hence the order of processing of the transistor component layers.[20] For example, there may be strong differences between dielectric-semiconductor interfaces created by spin coating the semiconductor onto the dielectric compared to vice versa. A top gate (the dielectric is deposited onto the organic semiconductor) architecture allows to probe charge conduction at the top surface of the organic semiconductor film. A top-gate (TG) transistor was fabricated to be compared to the previously discussed bottom gate (BG) devices. In this case Cytop[33] (for chemical structure see Fig. 4.7(a)) was spin coated onto the [60]PCBM film as

the polymeric gate dielectric, followed by deposition of the gate electrode. The possible device geometries distinguished by the position of the S-D electrodes are depicted in Fig. 4.7(b).

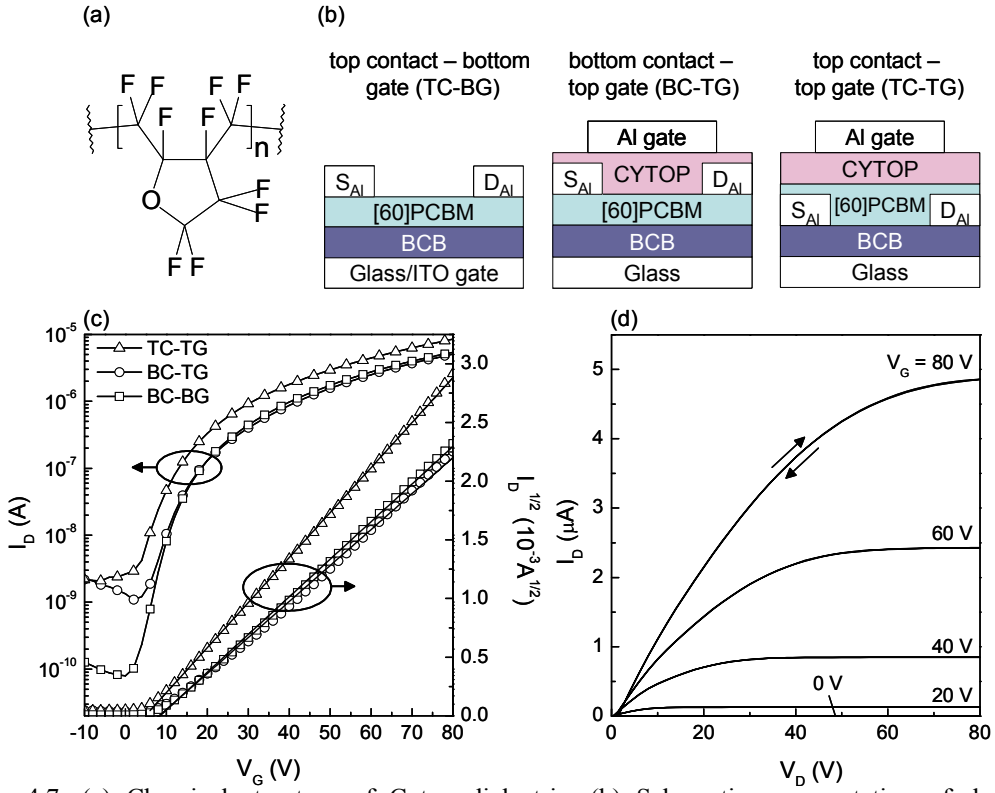


Fig. 4.7: (a) Chemical structure of Cytop dielectric. (b) Schematic representation of device architectures compared by their transfer curves in (c) (L = 60 μm, W = 1.5 mm, C_{iCytop}= 2 nF/cm^2, C_{iBCB} = 1.15 nF/cm^2). (d) output characteristics of a BC-TG device.

The output curves of a bottom contact (BC) - TG device are shown in Fig. 4.7(d). In similarity to the bottom gate devices on BCB dielectric there is no hysteresis between forward and backward scans and the drain current saturates for large V_D. Fig. 4.7(c) shows transfer curves in saturation of devices fabricated in the two different TG and the top contact (TC) - BG device architectures shown schematically in Fig. 4.7(b). The mobility and threshold voltage of the TC-TG transistor were 0.06 cm^2/Vs and 5 V, and the values extracted for both the BC-TG and the TC-BG devices were 0.04 cm^2/Vs and 8 V. The slight improvement in mobility and threshold voltage in the TC-TG configuration is attributed to a better quality interface between the dielectric and the undisturbed top surface of the amorphous-like [60]PCBM film. The lower threshold voltage signifies a reduced trap density. It could be reasoned that the spin coated [60]PCBM film provides a flatter surface for the formation of a conductive channel at the interface to the dielectric, compared to BCB as bottom gate dielectric.[34] However, AFM images of the surface of [60]PCBM films

(discussed later on) demonstrate that the surface roughness of these films is similar to the very smooth surface of BCB, with a roughness of rms ≈ 1 nm. The larger off current and hence the smaller on/off current ratio in the TG devices is due to a larger gate leakage current in the devices with Cytop dielectric. This leakage current is attributed to pinholes in the spin-coated dielectric film, possibly caused by rare spikes at the surface of the semiconductor film.[34] The different chemical composition (i.e. different charge trapping behaviour and different surface energy) of the two dielectric materials may also play a role in the observed differences in performance of the BG and TG devices. The good performance of the devices combined with the advantages related to the fabrication of the top gate device configuration (see section 2.3.1.) demonstrates the potential for further development of the transistor architecture.

4.4. Metal contact electrodes

4.4.1. Electron injection

Injection of charge carriers from the S-D electrodes into the organic semiconductor strongly depends on the position of the metal work function with respect to the energy bands in the semiconductor. Hole injection is generally facilitated by a high work function metal, where the Fermi level is aligned with the highest occupied molecular orbital (HOMO) in the semiconductor, whereas electron injection into the lowest unoccupied molecular orbital (LUMO) requires a low work function metal. Gold, which is often used for hole injection in p-channel devices has a high work function of approximately 5.1 eV. Since the LUMO level in [60]PCBM is approximately 3.7 eV (HOMO = 6.1 eV),[35] electrons in the gold have to overcome an energy barrier of roughly 1.4 eV in order to be injected into the organic material. Veenstra *et al.*[36] and van Duren *et al.*[37] showed that this energy gap decreases to 0.76 eV upon contact between gold and [60]PCBM due to the creation of electronic dipoles at the interface. Nevertheless, as a result of this energy offset fewer electrons are injected. Since a major part of the injected charges is localized in trap states (causing a positive threshold voltage and a high subthreshold swing), the lower concentration of charges at the semiconductor/insulator interface is reflected by smaller channel current, and hence a degradation in the device performance.

A typical device characteristic of a [60]PCBM transistor using BCB dielectric and top Au S-D electrodes is shown in Fig. 4.8(a-b). An electron mobility of 0.08 cm^2/Vs was obtained from the transfer curve measured at V_D = 80 V (saturation regime), shown in Fig. 4.8(a).

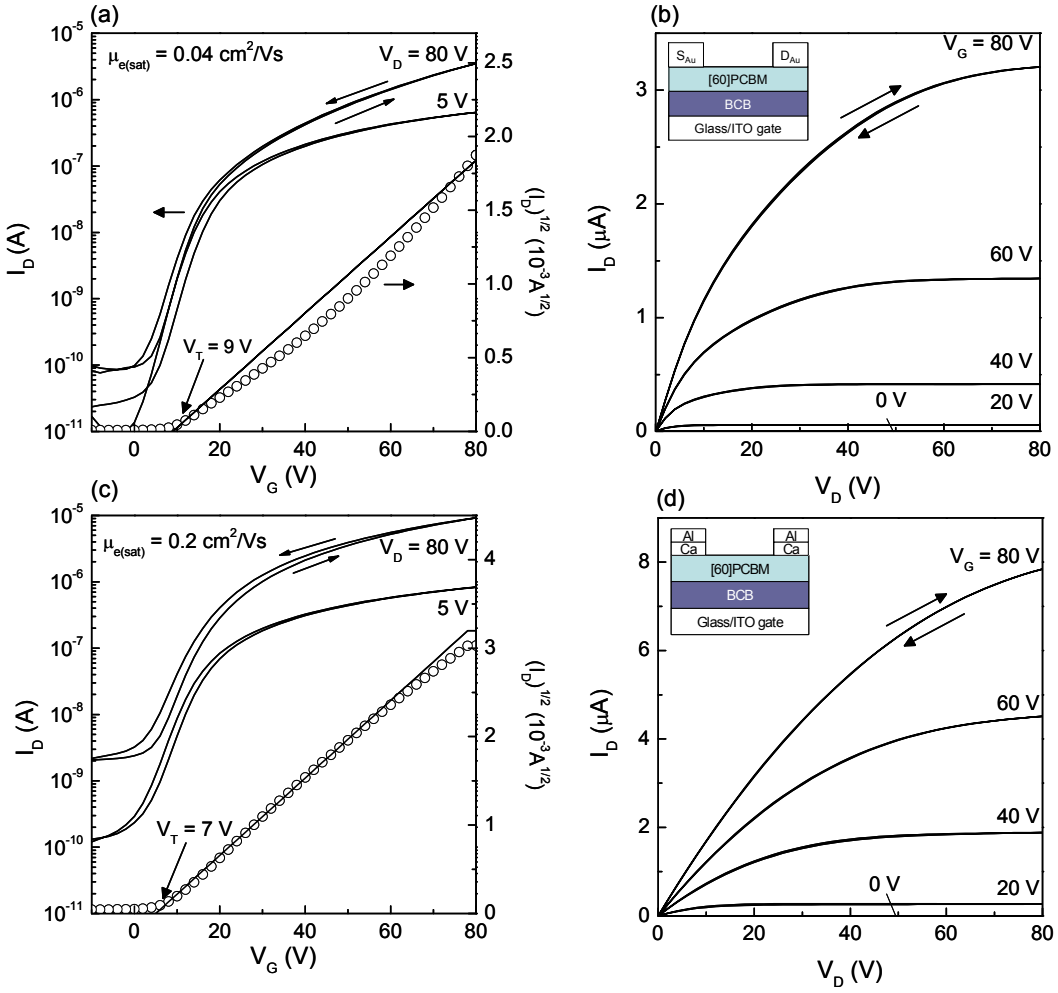


Fig. 4.8: Transfer and output curves of [60]PCBM based transistors with (a-b) top gold (W = 2 mm, L = 60 μm, C_i = 1.2 nF/cm^2) and (c-d) top calcium (W = 1 mm, L = 60 μm, C_i = 1.2 nF/cm^2) S-D electrodes. (a),(c) right axes: Comparison between experimental dependence of $I_D^{1/2}$ on V_G and theoretical fits according to the gradual channel approximation in case of (a) Au and (c) Ca electrodes. (b),(d) insets: device architectures employed.

Calcium (Ca) has a much lower work function (2.9 eV) than aluminium (4.08 eV) and gold (5.1 eV) [Fig. 4.9(a)] and is expected to improve the injection of electrons into the LUMO of [60]PCBM. Ca electrodes were evaporated onto the Glass/ITO/BCB/[60]PCBM layer system in a top contact configuration [Fig. 4.8(d) inset]. Since Ca reacts very easily with oxygen, the drain and source electrodes were coated with a top aluminium layer to prevent the formation of an insulating layer of natural calcium oxide.

Indeed, the use of Ca electrodes was found to improve the performance of [60]PCBM transistors significantly [Fig. 4.8(c-d)]. Maximum electron field-effect mobilities of 0.21 cm^2/Vs were achieved (in saturation), again with negligible switch-on voltage and on/off current ratio of 10^4. The superior injection quality of Ca electrodes is also evident from the plots of $(I_D)^{1/2}$ vs. V_G [Fig. 4.8(c)], for which theory predicts a linear relationship. Linear plots are obtained for aluminium and calcium electrodes [Fig. 4.5(b) inset and Fig. 4.8(c)]. For Au electrodes a super-linear current increase indicates injection difficulties at low V_G. The threshold voltage can be read off the plot to be approximately 7 V for devices with Ca S-D electrodes and several volts higher for devices with Au contacts. The relative performance of equivalent device structures with different electrode materials is summarized in Fig 4.9(b).

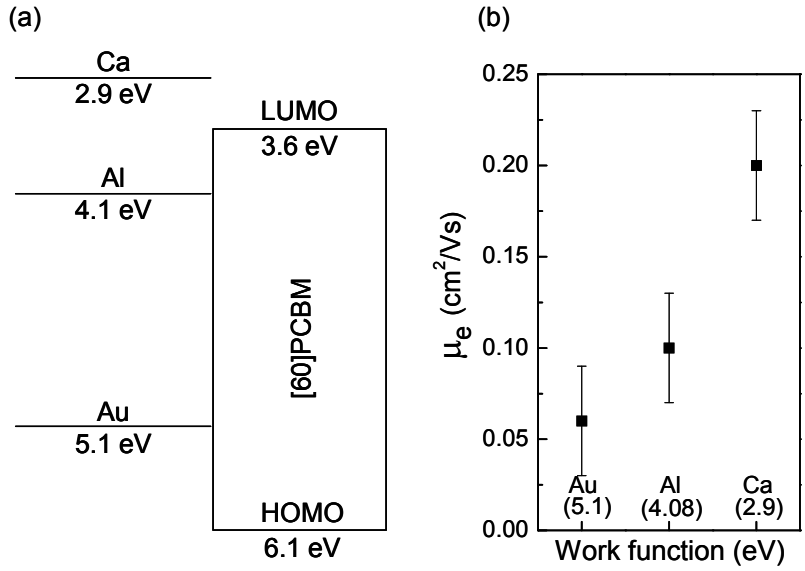


Fig. 4.9: (a) Schematic representation of metal work functions relative to LUMO and HOMO energies of [60]PCBM. (b) Effect of different work function metals on n-channel OFET performance.

4.4.2. Parasitic contact resistance in organic transistors

In order to estimate the magnitude of the parasitic contact resistance in the devices, the output curves of a large number of devices that were prepared under identical conditions with various channel lengths between 20 μm and 100 μm were recorded (the width was constant and equal to 1 mm in all devices). The ohmic resistance at different gate voltages was extracted as the slope of the linear output curves at low V_D and plotted against the channel length. As shown in Fig. 4.10(a) for

Au top contacts, the data points suggest a straight line fit for each gate voltage. Following the transmission line method mentioned in section 2.3.2.,[38-40] the total contact resistance is extracted by extrapolating the lines to the intercept at L = 0 µm. The slopes of the fitted lines represent the channel resistance per unit channel length, which decreases as the carrier concentration in the channel increases at higher gate voltages. In Fig. 4.10(b) the total channel resistance and the contact resistance are plotted vs. gate voltage for various channel lengths.

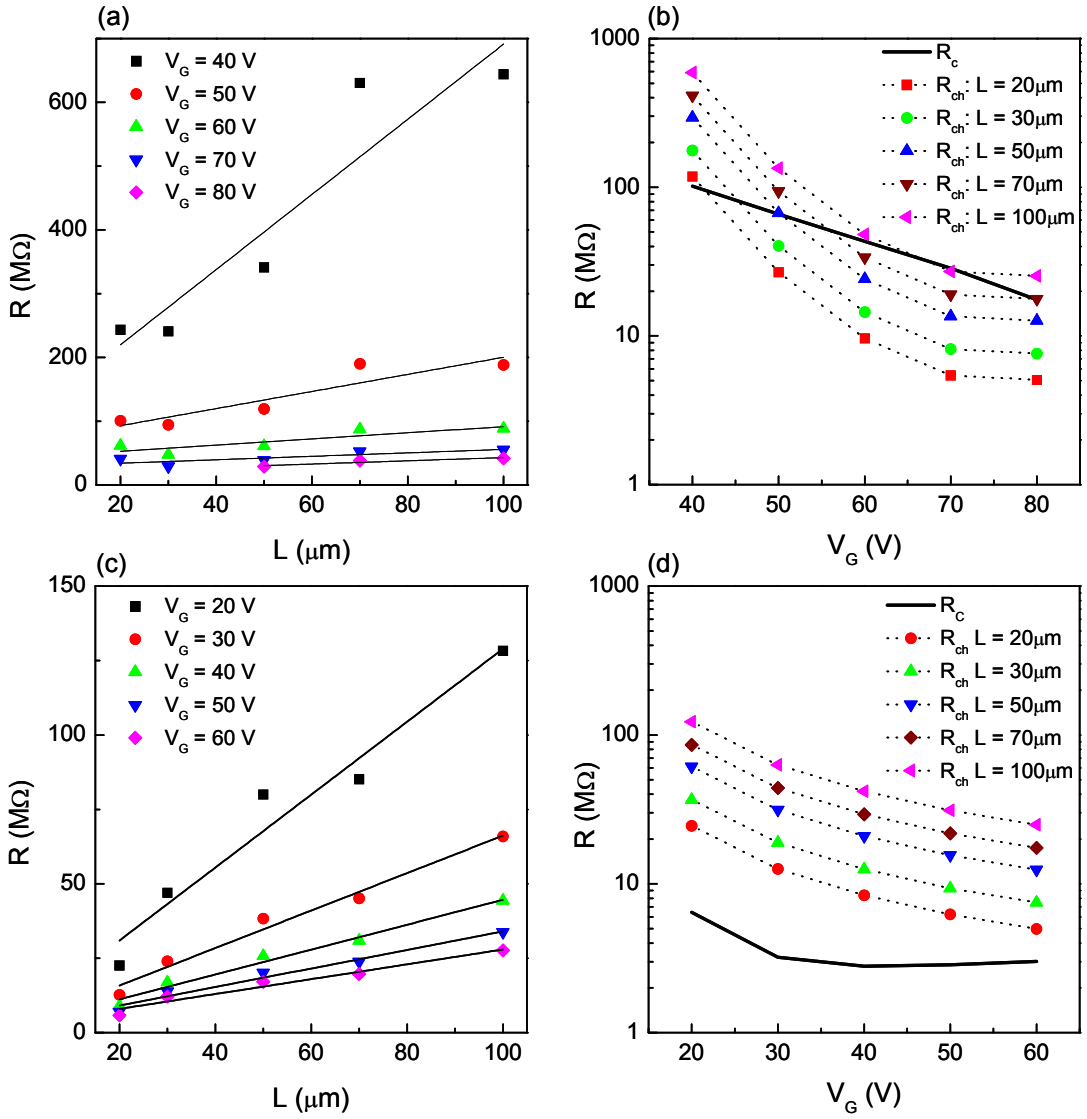


Fig. 4.10: Total resistance vs. channel length extracted from linear output curves of [60]PCBM based top contact FETs with (a) Au and (c) Ca S-D electrodes. Contact and channel resistance vs. gate voltage for the same devices with (b) Au and (d) Ca S-D electrodes. W = 1 mm, C_i = 1.2 nF/cm^2.

The same analysis was performed on devices with Ca top contacts [Fig. 4.10(c-d)]. The results suggest that for gold electrodes the contact resistance is similar or

higher than the channel resistance even for large channel lengths of 70 μm or more. The strong gate-voltage dependence of the contact resistance indicates that injection is limited by an energy barrier. An increasing electric field between gate and injecting electrode introduces a slope to the energy level configuration at the metal-semiconductor interface and the barrier for injection into the semiconductor, as seen by the electrons in the metal electrode, decreases. Therefore the performance of these devices is considered to be severely limited by carrier injection difficulties at the Au S-D contacts. For Ca S-D electrodes the contact resistance is ≈ 10 times lower than for Au and it is smaller than the channel resistance of all the devices [Fig. 4.10(d)]. Furthermore the contact resistance is relatively independent of gate voltage. This is a clear indication of the much enhanced electron injection through Ca electrodes compared to Au and confirms the observations made in previous subchapters.

From the results presented so far the Ca top-contact, bottom gate configuration employing a polymer dielectric has shown the best transistor performance in the case of [60]PCBM, and will be used as test-bed for further investigations.

4.5. Film Morphology of [60]PCBM

In order to gain insight into the structural properties of [60]PCBM, polarized optical transmission and reflection microscopy was performed on films deposited by spin coating. The image in Fig. 4.11(a) was taken of a film of [60]PCBM deposited on glass. It shows an entirely amorphous film of homogeneous colour in absence of any order or texture, independent of the relative position of polarizer and analyzer. AFM images of [60]PCBM films on BCB demonstrate the smoothness of the film surface [Fig. 4.11(b)]. The root-mean-square roughness of the film is measured to be < 1 nm. Under both, optical as well as atomic force microscopy, the film morphology does not appear to change upon annealing the film at 120 °C for 1 hour in air.

Differential scanning calorimetry of [60]PCBM dried in air from a chlorobenzene solution revealed a peak at approximately 150°C [Fig. 4.11(c)]. This is associated with a reorganization of the molecules in the film into a more ordered crystalline structure. Coinciding with this result, an irreversible degradation of electron mobility in [60]PCBM transistors measured at temperatures above 150°C was observed. The exact nature of this phenomenon is not clear at this point and could

be the focus of further investigations. This study focused on as deposited films without further treatment.

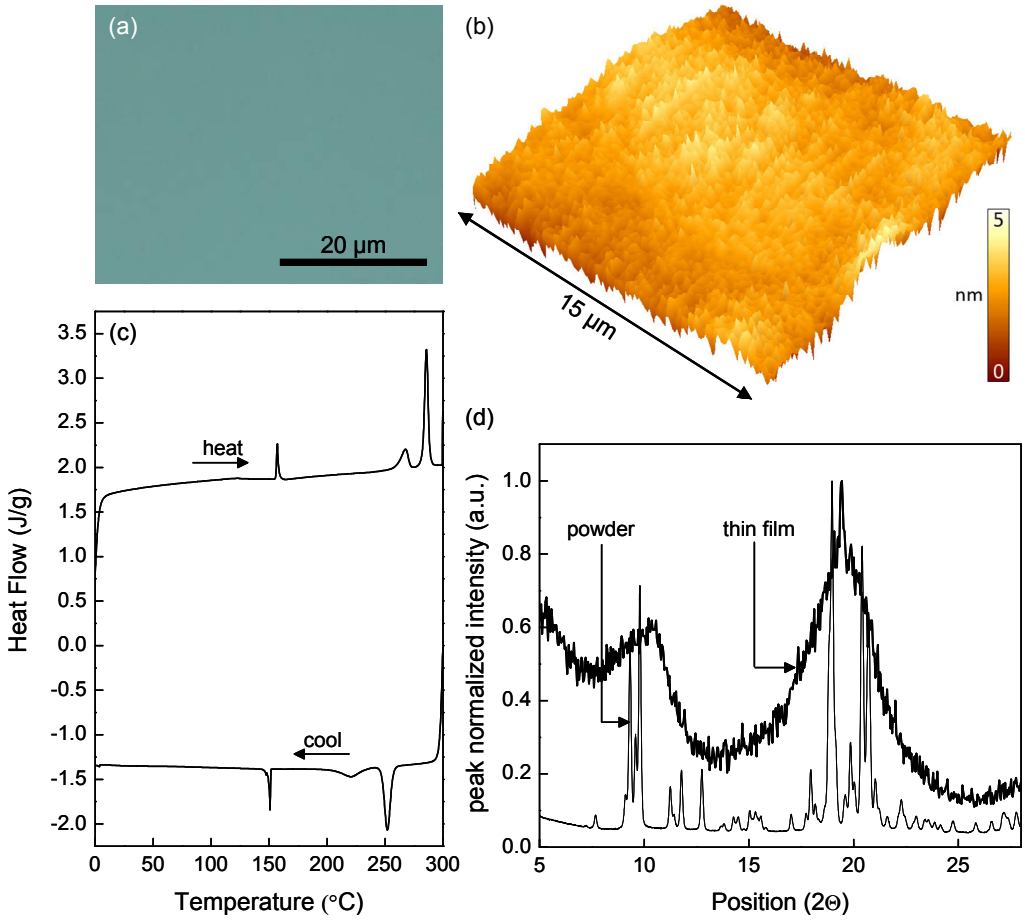


Fig. 4.11 (a) Optical polarized microscopy image of amorphous [60]PCBM film in transmission mode. (b) Atomic force microscopy image of [60]PCBM spin coated on BCB, roughness rms < 1 nm. (c) Differential scanning calorimetry of [60]PCBM dried from chlorobenzene solution. (d) X-ray diffraction pattern of amorphous [60]PCBM film spun on Si wafer compared to that of crystalline [60]PCBM powder.

Finally, wide angle x-ray diffraction (XRD) measurements were carried out in a reflection mode under ambient conditions. For this purpose fullerene films were spun on Silicon substrates. The resulting spectrum of scattered intensities is shown in Fig. 4.11(d). It shows two very broad peaks centred around $2\theta \approx 10°$ and $2\theta \approx 20°$. The peaks usually correspond to lattice spacings in the [60]PCBM film, suggesting a certain degree of order. However, the width of the peaks is very large compared to peaks observed in highly ordered crystalline films of other fullerene derivatives reported in literature.[41] In Fig. 4.11(d) the XRD spectrum of polycrystalline [60]PCBM powder is shown for comparison. The full width at half maximum (β_w) of

the peaks can be related to the average size of crystallites R_0 in the films using the Scherrer equation 3.2.[42]

$$R_0 = \frac{K\lambda}{\beta_w \cos\theta} \tag{3.2}$$

K is the Scherrer constant, which varies with the shape of the crystallites and is typically 0.9. Here R_0 is found to be of the order of 1 nm for the spin coated thin film and of the order of 10 nm for the crystalline powder. Hence the [60]PCBM films reported here are considered to be of a rather amorphous nature, consisting of a large number of randomly oriented nano-crystals. This is in good agreement with previous studies on [60]PCBM films spin coated from chlorobenzene solutions.[43]

From these results it can be concluded that the films are amorphous-like and do not bear any long range crystalline order. Taking this into consideration the electron transport could be ascribed to the molecular symmetry of the fullerene derivatives and strong π-π interactions between neighbouring C_{60} units even in the case of amorphous-like films. The nature of the charge transport mechanism will be investigated in the next subchapter.

4.6. Charge Transport Mechanism in [60]PCBM

In order to shed light on the nature of the electron transport mechanism in the [60]PCBM films, some of the high mobility transistors with Ca top S-D electrodes on BCB dielectric were characterized at various temperatures between 180K and 430K. The field-effect mobility was extracted in the linear regime (V_D = 5 V) and in the saturation regime (V_D = 60 V) at each temperature from the slope of I_D and $I_D^{1/2}$ vs. V_G, respectively. The perfect linearity of these plots (Fig. 4.12(a) for $I_D^{1/2}$ vs. V_G at 180 K, 293 K and 430 K) indicates gate field independent mobility above the threshold voltage. In this regime, and in accordance with the multiple trapping and release model discussed by Horowitz,[44,45] the mobility can be considered an intrinsic property of charges in the [60]PCBM film at a given temperature, independent of the charge carrier density induced by the gate field. Gate voltage independent mobility also suggests the absence of crystal defects and grain boundary effects typically observed in polycrystalline materials.[44] For lower gate voltages the majority of

induced charges are trapped in shallow or deep traps that are located within the energy gap between HOMO and LUMO level of the [60]PCBM molecules and the measured effective charge carrier mobility is low. In the following analysis, only the gate voltage independent mobility at $V_G >> V_T$ is considered.

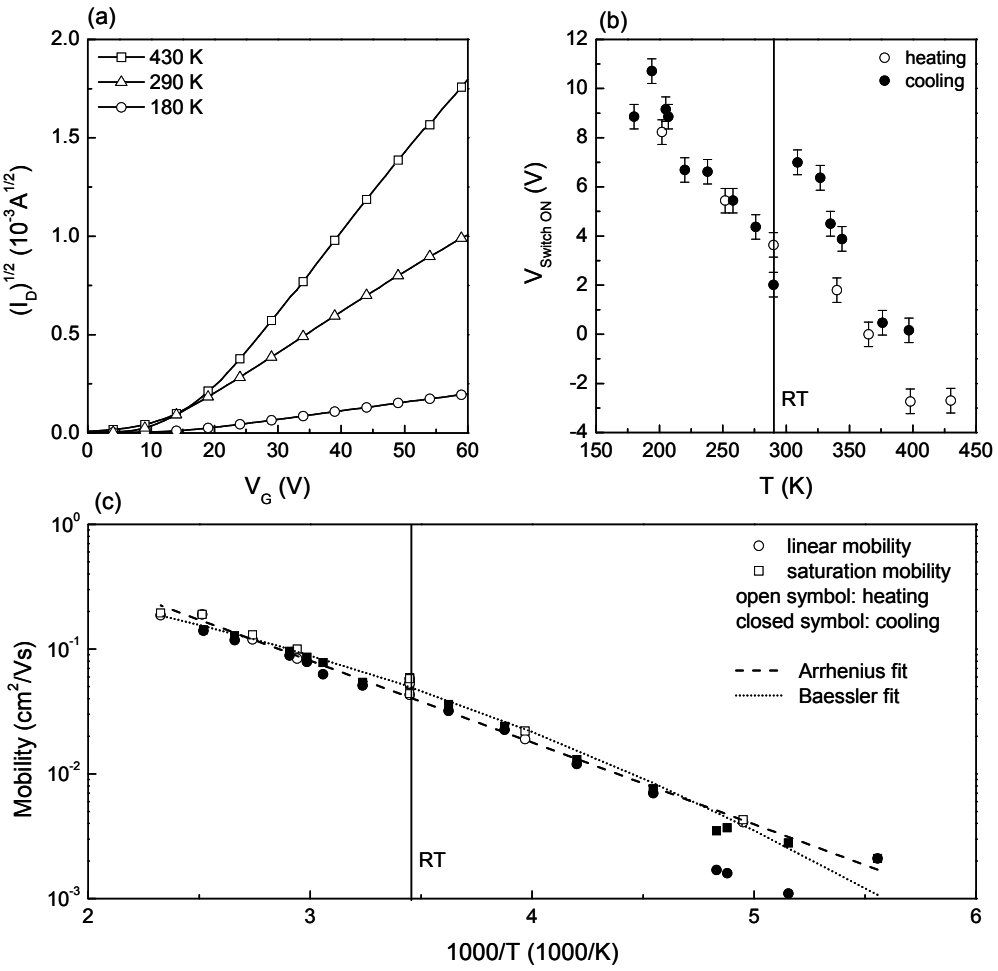


Fig. 4.12 (a) Linear $I_D^{1/2}$ vs. V_G dependence of [60]PCBM based transistor with Ca S-D top contacts on BCB dielectric measured at 180 K, 293 K and 430 K. (b) Monotonic decrease of switch-on voltage with increasing temperature. (c) Evolution of electron mobility of the device in the linear and saturation regime while cooling from RT to 180 K, then heating to 430 K and cooling back to RT. The data is described using an Arrhenius (dashed) and a Baessler (dotted) type fit. L = 70 μm, W = 1 mm, C_i = 1.15 nF/cm^2.

According to Meijer *et al.* the position of the threshold voltage in disordered organic semiconductors is considered a fitting parameter rather than a physically meaningful quantity.[46] Hence the switch-on voltage, defined as the gate voltage at which I_D starts to rise, is examined and is found to decrease monotonically from nearly 10 V at 180 K to -3 V at 430 K [Fig. 4.12(b)]. This trend is typically explained by an increase in the Fermi level with increasing temperature, and hence a decrease in

the effective depth of the trapping states.[44] As a result, at higher temperatures charges are more easily activated to the transport level and less injected charges are required to fill shallow traps near the LUMO level of [60]PCBM.[13]

Electron mobility readings were taken while cooling the device down to 180K, then while heating it to 430K and finally while cooling it down back to room temperature. The results [Fig. 4.12(c)] demonstrate that the device did not degrade irreversibly during the cooling or heating process, as the initial mobility at room temperature is reproduced after the cooling and heating cycle. The linear and saturation regime mobility were very similar in all measurements, which is a signature of an ideal device. The variation of mobility with drain voltage was found to be comparable in magnitude to the error associated with the extracted mobility values (e.g. determination of slope of $I_D^{1/2}$ vs. V_G). Therefore the lateral field-dependence of the mobility was neglected here and the mobility was extracted at the same drain voltages (V_D = 5 V in linear, V_D = 60 V in saturation regime) for all temperatures.

At first glance the results suggest a linear relationship between ln(μ) and 1/T, which corresponds to an Arrhenius type behaviour. This is often associated with thermally activated hopping transport of polarons in disordered organic semiconductor films (see section 2.2.2 and 2.2.3).[13,18,47] Fitting the data in Fig. 4.12(c) with equation 4.3

$$\mu_e = \mu_\infty \cdot e^{-\frac{E_A}{k_B T}} \tag{4.3}$$

an activation energy of E_A = 130 meV is extracted. k_B is the Boltzman constant and T is temperature. This value is comparable to activation energies that have been reported previously for fullerene films[13,22,23,48] and for other disordered molecular systems.[49,50] The theoretical mobility limit for very high temperatures is extracted as μ_∞ = 7.5 cm^2/Vs. A good fit is also obtained using the correlated disorder model based on Bässler's empirical model for Gaussian-type disorder in organic semiconductors, equation 2.8 (see section 2.2.5):

$$\mu_e = \mu_0 \cdot \exp\left[-\left(\frac{3\sigma}{5k_B T}\right)^2 + 0.78\left(\left(\frac{\sigma}{k_B T}\right)^{3/2} - 2\right)\sqrt{\frac{eaE}{\sigma}}\right] \tag{2.8}$$

A good match of the experimental data is obtained using μ_0 = 0.57 cm^2/Vs , σ = 68-71 meV and a = 3.4 nm. The effect of the lateral electric field E (= V_D/L) is negligible for the range of drain voltages and the uncertainty of σ considered here. μ_0 is the theoretical mobility limit in a disorder-free film. Values of the order μ_0 = 0.1 cm^2/Vs have previously been reported for other organic glasses.[51] The energy width σ of the Gaussian DOS and the average site separation of the [60]PCBM transport sites a found here are very similar to previously reported values for [60]PCBM.[52] It is noted that the spacing between transport sites on the [60]PCBM molecules is larger than the diameter of the fullerene molecule (typically d ≈ 1 nm).[52,53]

The energetic disorder in [60]PCBM is rather low when compared to energetic disorder obtained for amorphous polymers, such as polytriarylamines (PTAA)[50] or poly(p-phenylenevinylene) (PPV)[54,55], for example. Hole mobilities reported for these polymers are of the order of 10^{-4}-10^{-3} cm^2/Vs and the energetic disorder was found to be in the range σ = 68-90 meV for PTAA[50] and σ = 93-125 meV for PPV[54]. Hence the smaller energetic disorder here seems to correlate well with the higher mobility observed in the glassy [60]PCBM films. The energetic disorder in polymers such as PTAA or PPV is typically attributed to fluctuations in the length of the transporting conjugated chain segments.[52]

It was also attempted to fit the data using the variable range hopping model introduced by Vissenberg and Matters[56] for an exponential distribution of tail states. However, no set of parameters T_0, α^{-1}, σ_0 was found that reliably reproduced the data for different temperatures. As described above, the mobility in the transistors appears to be independent of the gate field. Hence the Vissenberg model may not be the best suited model to describe these devices.

Output curves were also recorded at each temperature in order to qualitatively monitor the electron injection from the Ca electrodes into the [60]PCBM film. The output curves are strictly linear at low V_D over the whole temperature range from 180 K to 430 K and no signature of injection limited transport was detected. This is in agreement with the previous observation that the contact resistance in these devices is low compared to channel resistance for the gate bias range examined here ($V_G > V_T$). Furthermore it has been reported that metal-organic interface phenomena causing injection limited current in disordered semiconductors often exhibit a smaller activation energy (are less temperature dependent) than space charge limited

conduction in the bulk semiconductor.[57] This is coherent with the predictions of the hopping model and a Gaussian DOS (see 2.3.2). Hence the injection properties of the metal-semiconductor interface in this device are not expected to change significantly over the studied temperature range.

Finally, it is noted that in the temperature range studied here, the differentiation between a 1/T and a $1/T^2$ dependency of $\ln\mu$ is rather difficult and hence no reliable conclusions on the exact nature of the charge transport mechanism can be drawn. Nevertheless, the results are in good agreement with the physical picture discussed previously in the literature.

4.7. Other fullerenes and derivatives

A number of other fullerenes, in particular pristine C_{70} and C_{84}, have been demonstrated in the literature to exhibit electron transporting properties.[13,38] In this section the results obtained from [70]PCBM as well as a number of side-chain perfluorinated C_{60} derivatives are presented. Aim of the work was to demonstrate high mobility electron transport as well as to study the effects of the different side groups in these C_{60} derivatives.

4.7.1. C_{70} Methanofullerene

Although [70]PCBM resembles [60]PCBM (see Fig. 4.13(a-b) for molecular structures), their electronic properties are expected to be different due to their slightly different physical and electronic structures.[58,59] For instance, in the case of unsubstituted C_{70}, the molecule is slightly larger in diameter and more asymmetric than C_{60}.[53] The larger dimensions of the carbon cage lead to a smaller electron-electron repulsion energy.[38,58] Moreover, pristine C_{70} is known to have a slightly lower ionization potential than C_{60} by approximately 100 meV.[60] For organic electronic devices and, in particular, transistors, this relatively small difference may have a large impact on the carrier injection efficiency. Indeed, earlier work[18,61-63] has demonstrated transistor and circuit operation with good performance characteristics. However, the large majority of these studies focussed on [60]PCBM transistors due to the availability of [60]PCBM whereas reports on [70]PCBM OFETs are very scarce.[38]

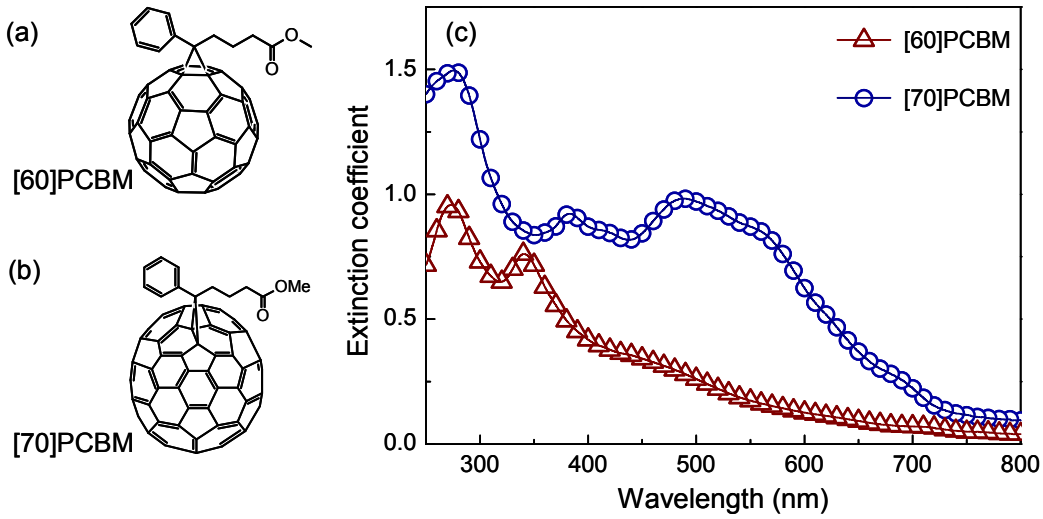


Fig. 4.13: Molecular structures of (a) [60]PCBM and (b) [70]PCBM. (c) Extinction coefficient of films on quartz substrates measured at wavelengths between 250 nm and 800 nm.

Fig. 4.13(c) shows the extinction coefficient of [60]PCBM and [70]PCBM films spin coated on quartz substrates. As can be seen, the onset of absorption is similar for both molecules with the [70]PCBM exhibiting a significantly stronger extinction coefficient. This observation is in agreement with measurements obtained from solutions.[64] By combining the optical data of Fig. 4.13(c) with electrochemical measurements reported by Anthopoulos *et al.*[13] and assuming an exciton binding energy of 0.3-0.4 eV, approximate values for the lower unoccupied molecular orbital (LUMO) and higher occupied molecular orbital (HOMO) levels were calculated yielding LUMOs in the range 3.5 - 3.8 eV and HOMOs in the range 5.7 - 6.1 eV.

Devices were fabricated on BCB gate dielectric with [70]PCBM, which was spin coated from a 2 % by weight solution in CB. For BG-TC transistors with top S-D Al electrodes electron mobilities were approximately 0.06 cm^2/Vs [Fig. 4.14(a-b)]. Current on/off ratios were about 10^4, with switch on voltages around 0 V. With Ca/Al electrodes the performance was improved significantly. As can be seen in Fig. 4.15(a), transistor operation exhibits negligible hysteresis with calculated electron mobility of the order of 0.1 cm^2/Vs. Moreover, the current on-off ratio is relatively high (>10^4) and the threshold voltage (V_T), obtained from a linear fit to $I_D^{1/2}$ versus V_G in saturation, is approximately 17 V. The subthreshold slope (S = 9.3 V/dec) is found to be similar to the slope in [60]PCBM transistors on BCB dielectric (see 4.3.1).

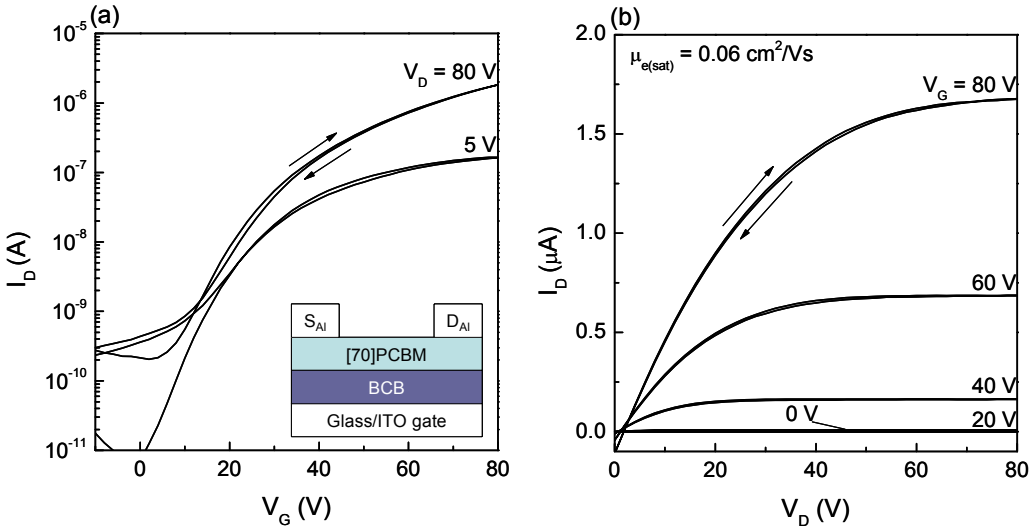


Fig. 4.14: (a) Transfer and (b) output characteristics of [70]PCBM based OFET with aluminium top contacts (inset a). W = 1.5 mm, L = 60 μm, C_i = 1.2 nF/cm^2.

Fig. 4.15(b) shows the output operating characteristics obtained from the same transistor. The Ca/Al electrodes exhibit ohmic injection behaviour, as is evident from the linearity of the characteristics at low V_D.

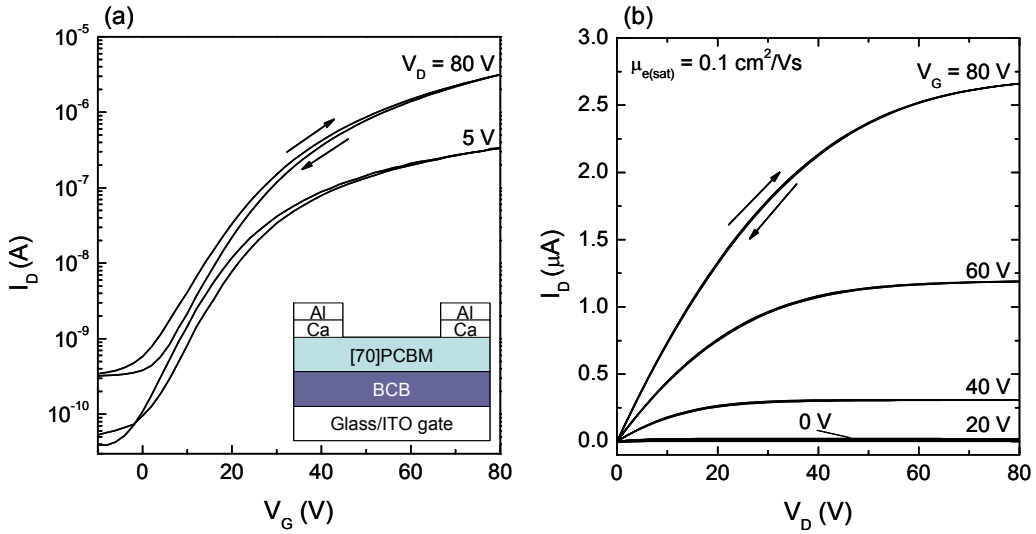


Fig. 4.15: (a) Transfer and (b) output characteristics of [70]PCBM based OFET with Al coated calcium top contacts (inset a). W = 1 mm, L = 60 μm, C_i = 1.2 nF/cm^2.

Early studies on OFETs based on pristine C_{70},[65,66] as well as [70]PCBM,[38] have consistently reported electron mobilities lower than values obtained from transistors based on C_{60} and its derivatives. It is evident from the present results that it can no longer be assumed that the electron mobility of [70]PCBM is significantly lower than that of [60]PCBM. One possible explanation for the observation of similar electron

mobility in [60] and [70]PCBM is that although the intrinsic mobility of the [60] derivative is higher, the solubility of [70]PCBM (80 mg/ml - chlorobenzene) is much higher than [60]PCBM (50 mg/ml - chlorobenzene).[67] The consequence of this could be that [70]PCBM forms a better interface with the dielectric layer when spin coated from solution, leading to enhanced mobilities. This finding could have significant implications not only for the use of [70]PCBM in organic ICs but also for its application in organic photo-voltaic devices (OPVs) where high absorption coefficients are required. This argument is inline with the recent demonstration of high performance OPVs based on polymer:[70]PCBM blends.[68,69]

4.7.2. Fluorinated Fullerene derivatives

A group of C_{60} derivatives with fluorinated substitutions (for molecular structures see Fig. 4.16(a)) was tested in BG-TC FETs using BCB as the gate dielectric. Different derivatives are expected to exhibit a different packing order and therefore potentially better charge transport characteristics. In addition, the hydrophobicity of Fluor groups could provide a better resistance against the intrusion of water and oxygen into the channel region.

Absorption characteristics of films spun from chlorobenzene solutions onto quartz substrates of all four molecules are shown in Fig. 4.16(b). As can be seen, the different non-conjugated side chain substitutions have a low impact on the electronic structure of C_{60} and hence its optical absorption characteristics.

To assess the suitability of these molecules as *n*-channel semiconductors in OFETs, two different device architectures were investigated. Type I transistors, with L = 60 μm and W = 1 mm, were fabricated in a BG-TC configuration employing glass substrates coated with indium tin oxide as the gate electrode. BCB was employed as gate dielectric with a geometrical capacitance of C_i = 1.2 nF/cm^2. The compounds were then spun from chlorobenzene solutions (10 mg/ml wt. %) at room temperature in N_2 ambient. Device fabrication was completed by the evaporation of Ca S-D electrodes through shadow masks. Type II transistors with L = 10 μm and W = 20 mm, were fabricated in a bottom-contact, bottom gate configuration using highly doped Si and SiO_2 as the gate electrode and gate dielectric (C_i = 17 nF/cm^2), respectively, and employing photolithographically defined gold S-D electrodes.

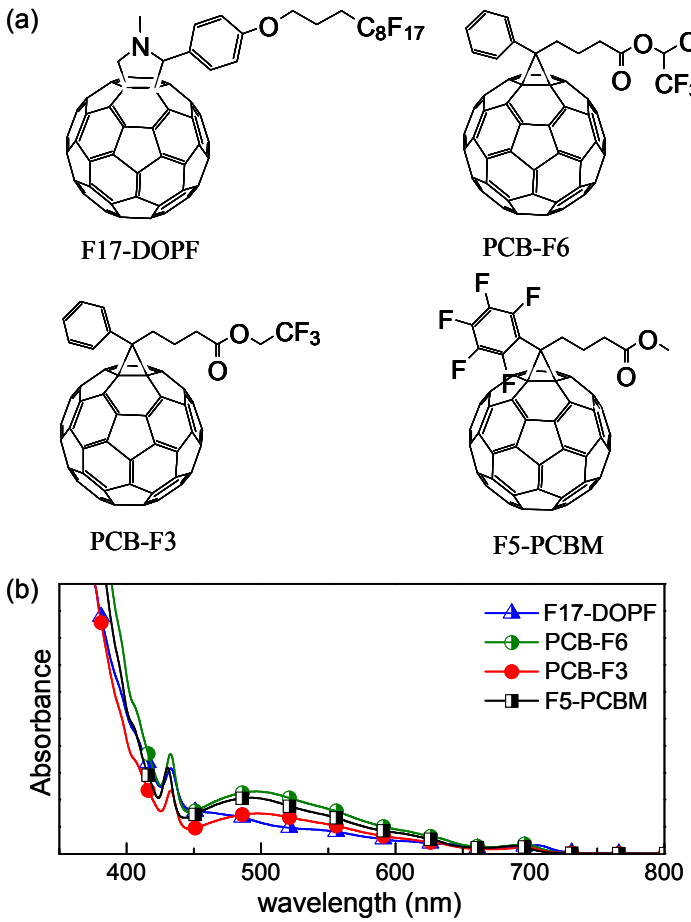


Fig. 4.16: (a) Molecular structures of perfluorinated methanofullerenes: F17-DOPF, PCB-F6, PCB-F3, F5-PCBM. (b) Absorbance spectra of films spun from chlorobenzene solution onto quartz substrates.

The SiO_2 layer was treated with the primer HMDS prior to semiconductor deposition [Fig. 3.2]. Fig. 4.17(a-b) illustrate the transfer and output curves for a type I OFET [Fig. 4.17(a) inset] based on F17-DOPF. The linearity of the output curves at low V_D indicates Ohmic-like injection behaviour. Moreover, the device exhibits negligible hysteresis, a sign of trap-free electron transport. Similar operating characteristics are observed for OFETs based on the other compounds. Fig. 4.17(c-d) display the transfer and output curves for a type II OFET [Fig. 4.17(c) inset] based on F17-DOPF. Unlike type I devices, the output curves show strongly injection-limited characteristics as evident from the superlinear dependence of I_D on V_D at low V_D. The latter is attributed to the significant energy offset (1.2–1.5 eV) between the Fermi level of Au and the LUMO energy of F17-DOPF (3.5 - 3.8 eV).[70] In addition, as discussed in 4.3.1, the bottom contact geometry of the device may reduce its performance. The characteristic performance parameters of type I and type II OFETs based on all compounds are summarized in Table 4.1.

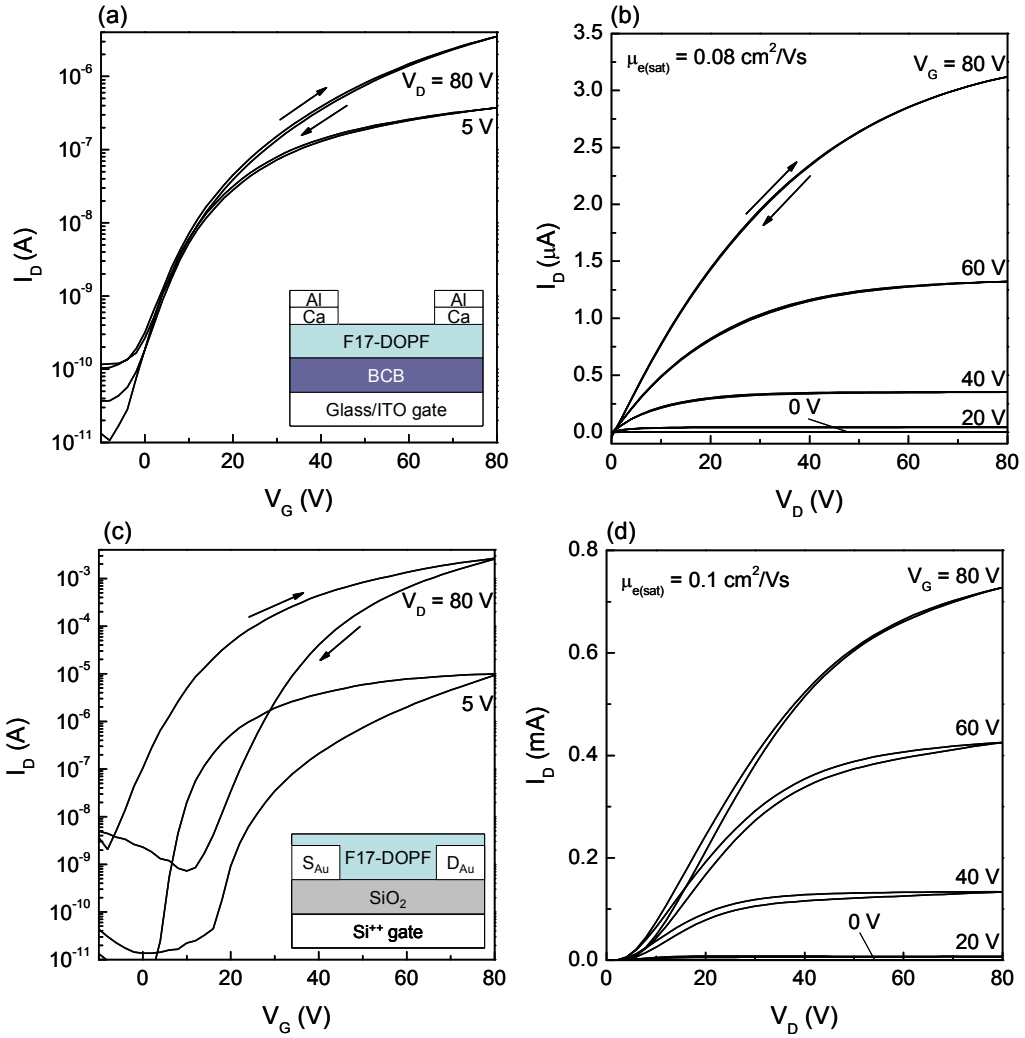


Fig. 4.17: Transfer (a,c) and output (b,d) curves of F17-DOPF based FETs. (a-b) Type I: Ca-top contacts on BCB dielectric (L = 35 μm, W = 1 mm, C_i = 1.15 nF/cm^2) and (c-d) Type II: Au-bottom contacts on SiO_2 dielectric (L = 10 μm, W = 20 mm, C_i = 17 nF/cm^2). Insets: device architectures employed.

Despite the significant barrier for injection, type II transistors based on F17-DOPF, PCB-F3 and F5-PCBM yield an electron mobility which is equivalent or superior to the mobility in the respective top contact devices with Ca electrodes. For comparison the results based on standard [60]PCBM are also given in Table 4.1. As described in the beginning of this chapter, the low performance of [60]PCBM on HMDS treated SiO_2 dielectric was attributed to the presence of radical anions and charge trapping. Now it appears that high mobility electron transport at such an interface is possible with fluorinated C_{60} derivatives. This observation could potentially be explained by better film forming properties of the fluorinated molecules on the SiO_2-HMDS dielectric compared to [60]PCBM.

Table 4.1: Summary of performance parameters of transistors in type I and type II device architectures based on various fullerene derivatives and their liquid surface tension components in chlorobenzene solutions.

		μ (cm^2/Vs)		on/off ratio (10^4)		V_T (V)		Liquid Surface Tension	
Nr.	Fullerene	I	II	I	II	I	II*	γ^P (mN/m)	γ^D (mN/m)
1	F17-DOPF	0.1	0.1	2.1	>100	21	12	3.5	19.9
2	PCB-F6	0.08	0.05	8.4	>10	27	30	1.8	25.9
3	PCB-F3	0.08	0.08	3.4	>10	10	10	3.3	21.4
4	F5-PCBM	0.02	0.03	1.3	>10	25	20	6.3	18.5
5	[60]PCBM	0.1	0.005	0.5	2	7	10	3.4	26.4

* Due to hysteresis in these transistors, V_T can only be an estimative value.

The wetting behaviour of the chlorobenzene solutions of all the C_{60} compounds on the SiO_2-HMDS and BCB surfaces was investigated by contact angle measurements and surface tension analysis. Contact angle measurements show that the BCB surface is characterized by a low polar component ($\gamma^P_{BCB} \approx 0.22$ mN/m) and a very high dispersive component ($\gamma^D_{BCB} \approx 36.54$ mN/m) as compared to SiO_2-HMDS ($\gamma^P_{SiO_2-HMDS} \approx 16.2$ mN/m and $\gamma^D_{SiO_2-HMDS} \approx 18.0$ mN/m, respectively). These results were used to plot the wetting envelopes, e.g. contour lines of $\theta_C = 0°$, in coordinates of polar and dispersive liquid surface tension components for both types of dielectric [Fig. 4.18].

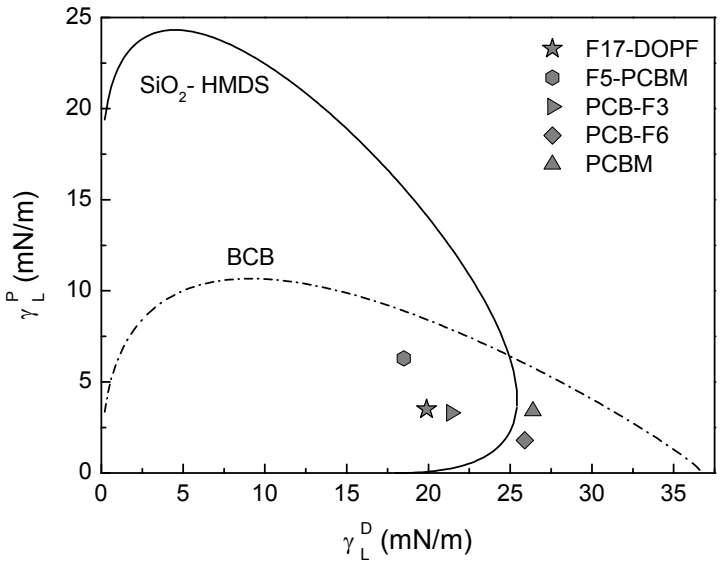


Fig. 4.18: Wetting envelopes of SiO_2-HMDS and BCB dielectric surfaces and polar and dispersive coordinates of liquid surface tension of various semiconductor solutions in chlorobenzene.

Furthermore, from surface tension measurements on pendant drops, the polar and dispersive components of the fullerene compounds in chlorobenzene solutions were calculated yielding the values presented in Table 4.1 and indicated on the graph in Fig. 4.18. Details of this analysis are discussed in section 2.8, 3.1.5 and chapter 7. All solutions lie within the wetting envelope of $\theta_C = 0°$ for BCB and are hence expected to wet this surface very well. However, the situation of the three compounds F17-DOPF, PCB-F3 and F5-PCBM within the wetting envelope of the SiO_2 – HMDS surface suggests that they wet this dielectric surface better than [60]PCBM and PCB-F6, which are situated outside the wetting envelope. A better film formation at the interface to the SiO_2-HMDS dielectric due to better wetting may explain the observations of higher charge carrier mobility.

The above results confirm the previous observation in [60]PCBM devices of a higher density of trap states at the SiO_2-HMDS interface, as demonstrated by the large hysteresis in type II devices. In addition, however, the same results illustrate the importance of wetting behaviour of semiconductor solutions on the dielectric surface as criterion for high charge carrier mobility at the dielectric-semiconductor interface in solution processed devices. Contact angle and pendant drop shape analysis prove to be powerful tools in the examination of surface tension characteristics and of the quality of film formation in such systems.

Finally, an additional advantage expected from the F containing derivatives is an improved stability towards atmospheric air. Very recently Chikamatsu *et al.* reported air stable electron transport in solution processable perfluoroalkyl-substituted C_{60} derivatives.[30] The stability in their devices was attributed to a densely packed and ordered layer of the fluorinated side chains, acting as a shield against atmospheric oxidants. Fig. 4.19 shows the evolution of the drain current in the on and the off state of TC-TG [60]PCBM and F17-DOPF transistors (using Cytop as gate dielectric) when the devices are exposed to ambient air at room temperature. The encapsulation by the dielectric in this device architecture slows down the intrusion of atmospheric oxidants into the film. In the case of [60]PCBM a steady decrease of the on-current is observed as soon as the device is exposed to air. In the case of F17-DOPF the current decay commences after roughly 100 minutes. Water molecules penetrating into the transistor channel are considered a likely cause for this decrease in the density of mobile charge. Anthopoulos *et al.* showed that organic molecules with a LUMO

energy higher than -4 eV have an electron affinity which is lower than that of H_2O.[71] Consequently electrons are withdrawn from the semiconductor molecules (i.e. H_2O molecules act as electron traps) and device degradation is observed. Therefore all the materials discussed here are not expected to be intrinsically stable against redox reactions in the presence of water molecules. However, the slightly delayed current decay in the case of F17-DOPF is attributed to the F atoms and their tendency to repel water.

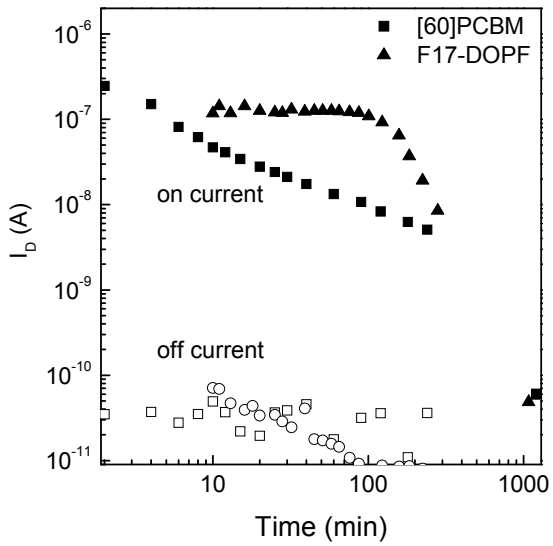


Fig. 4.19: Evolution of on and off currents over time in [60]PCBM and F17-DOPF based transistors in top gate configurations with Cytop as encapsulating dielectric.

The fluorinated molecules' side chains in the bulk semiconductor material could potentially provide a shield against the intrusion of water molecules into the channel region and hence protect the device from rapid degradation.[30,72] At this point however, the effect was found insufficient for stable device operation in air. After one day in air both devices had stopped working, i.e. no significant drain current was measured when a high gate bias was applied.

4.8. Integrated circuits

The applicability of organic transistors is generally assessed in integrated circuits. One of the most basic and fundamental integrated circuits is the voltage inverter and consists, typically, of two FETs [Fig. 4.20(a)]. As discussed earlier (section 2.6), there is a trend from unipolar logic (employing a single unipolar organic semiconductor) towards complementary logic (employing both p- and n-channel

transistors). In the next section the advantages of complementary over unipolar logic will be demonstrated using voltage inverters.

4.8.1. Unipolar inverters

Unipolar voltage inverters were constructed using two high mobility [60]PCBM devices according to the schematic in Fig. 4.20(a). The inverter's output characteristics measured in quasi-static mode are shown in Fig. 4.20(b). The hysteresis between forward and backward scans is found to be negligible and the maximum voltage gain (defined as dV_{OUT}/dV_{IN}) is ≈ 2 [Fig. 4.20(c)].

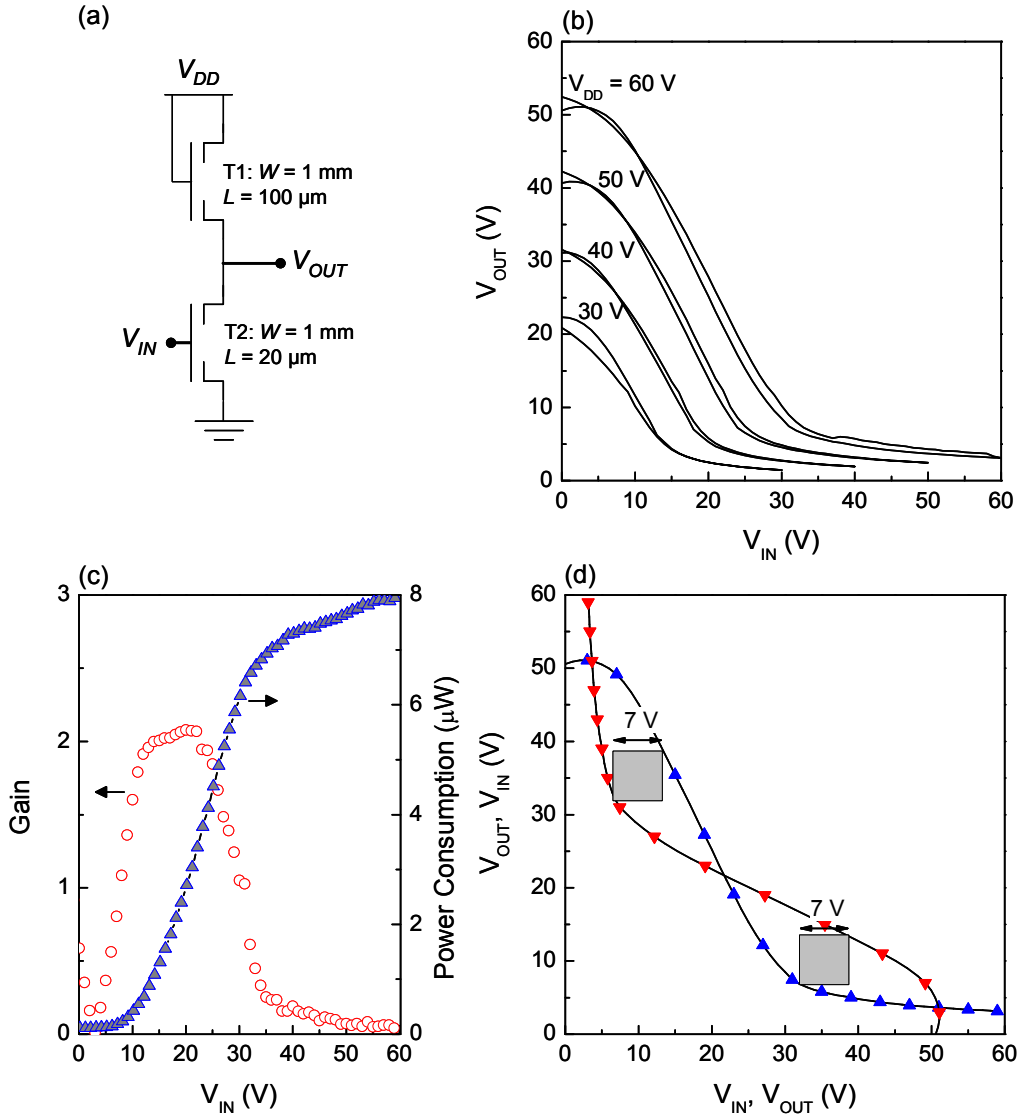


Fig. 4.20: (a) Schematic and (b) output characteristics of unipolar voltage inverter constructed of [60]PCBM transistors. (c) Gain and power consumption of the voltage inverter in quasi static operation. (d) Determination of noise margins.

The inverter's characteristic is dominated by a non-symmetric trip point and insufficient pull-up in the LOW input state. While typical for unipolar inverters consisting of devices which are both quite similar in terms of their threshold voltage and subthreshold swing, this result seriously affects the inverter's noise margin. The noise margin of the inverter was also calculated (at V_{DD} = 60 V) as the side of the largest square that can be ascribed between the transfer characteristics and the same curve re-plotted with exchanged input and output axes.[73] As demonstrated in Fig. 4.20(d) the noise margin (*NM*) of the inverter is rather small (7 V) and only 23% of its theoretical maximal value ($NM_{MAX} = V_{DD}/2$ = 30 V). A low noise margin entails a low tolerance to input signal fluctuations (i.e. noise). With regard to applications this could severely affect the reliability of the circuit and decrease the manufacturing yield and hence increase the production cost. The output characteristics of the unipolar inverter could potentially be improved by finding a better match of the driving and the load transistor. For example, a driving transistor with a slightly higher switch-on voltage would cause the trip point to be at a higher input voltage, and thereby improve the symmetry of the inverter's output characteristics. However, the necessity to adopt such an approach in order to obtain acceptable inverter characteristics demonstrates in itself the disadvantage of unipolar logic.

Another major problem of unipolar logic, which has been discussed earlier in this chapter, is the high power consumption. As evident from Fig. 4.20(c) the power consumption, measured as the product of the supply current and supply voltage, is low (≈ 0.2 μW) in one state of the inverter and high (≈ 8 μW) in the other. This is because the load transistor (T1) is continuously switched on, allowing current to flow to the ground when the driving transistor (T2) is turned on in the HIGH input state. This means that in quasi-static operation the circuit consumes power continuously in one out of two possible states. This situation is highly undesirable for portable applications where a limited power supply is available.

4.8.2. Unipolar ring oscillators

In order to quantify the dynamic response of such inverters, a number of multi-stage ring oscillators were fabricated according to the design shown in Fig. 4.21(a).[38] Fig. 4.21(b) displays a micrograph of a circuit based on type II transistors (see 4.7.2).

The specific circuit design employed is based on the ratio logic with the driver/ load transistor ratio set to 8. The widths of the driver, load, and buffer transistors were 2, 0.25, and 5 mm, respectively. The channel length for all transistors was kept constant and equal to 1.5 μm. The oscillation frequency (f_{OSC}) of a 7-stage ring oscillator based on F17-DOPF (section 4.7.2) as a function of applied voltage (V_{DD}) is displayed in Fig. 4.21(c). The inset shows the output signal at V_{DD} = 170 V. The maximum f_{OSC} measured is 10.4 kHz corresponding to a stage delay $\tau \approx 6.86$ μs ($\tau \approx 1/[2 \times n \times f_{OSC}]$ (equation 2.31), where n is the number of inverting stages). Despite the short channel dimensions (L = 1.5 μm) and the use of injection limiting gold electrodes the ring oscillator of Fig. 4.21 is amongst the fastest solution processed n-type circuits reported todate.[70]

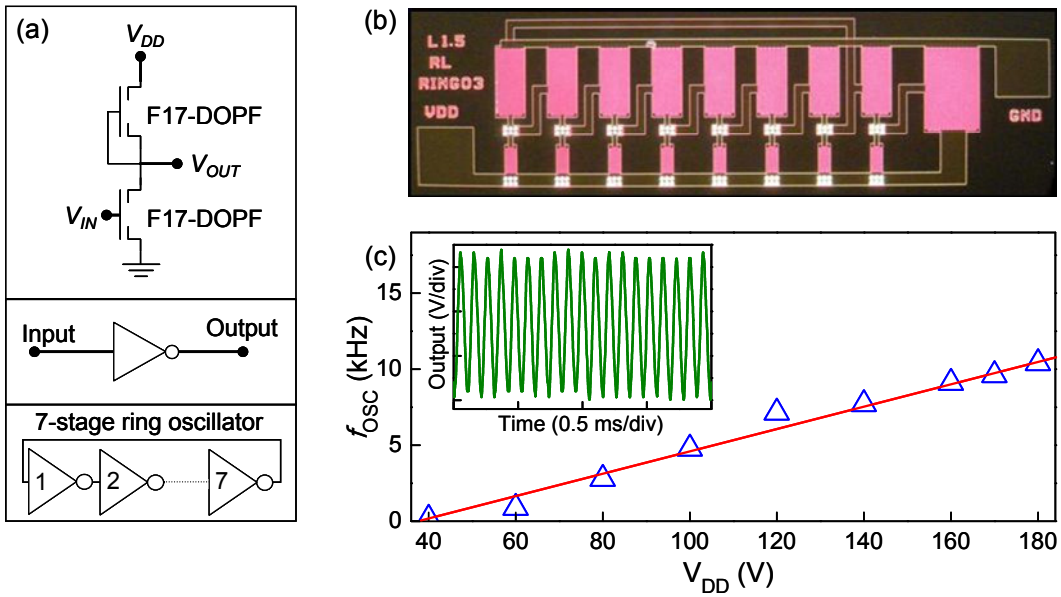


Fig. 4.21: (a) Circuitry and schematic representation of the inverter and 7-stage ring oscillator used. (b) Optical micrograph of a 7-stage unipolar ring oscillator. (c) Oscillation frequency vs. supply voltage characteristic and output signal at V_{DD} = 170 V (inset) of the ring oscillator.

4.8.3. Complementary inverters

In order to demonstrate the feasibility and the main advantages associated with organic complementary logic, voltage inverters have been fabricated from n-channel [60]PCBM transistors and p-channel OFETs based on polytriarylamines (PTAA) (see Table 3.1 for molecular structure) [Fig. 4.22(a-b)]. Despite the different carrier mobilities and the small W/L ratio between the two transistors, matching of the threshold voltage in the [60]PCBM and PTAA OFETs allows the design of inverters

with symmetric trip point. However, such an approach would be inappropriate for the design of truly complementary circuits since the dynamic response of the inverter would be severely limited by the transistor with the lowest mobility, i.e. the PTAA OFET ($\mu \approx 1\times10^{-2}$ cm^2/Vs). A p-channel semiconductor with hole mobility similar to the high electron mobility of [60]PCBM would have to be employed in order to maximize the inverter's dynamic performance.

The maximum voltage gain measured from Fig. 4.22(c) is ≈ 17 at a supply voltage V_{DD} = 80 V. From the plot in Fig. 4.22(d) the noise margin of 28 V can be estimated. The latter is approximately 70% of its maximum theoretical value NM_{MAX} = 40 V (at V_{DD} = 80 V) and is considered very high when compared to the unipolar organic inverter discussed earlier or to representative values from literature.[73]

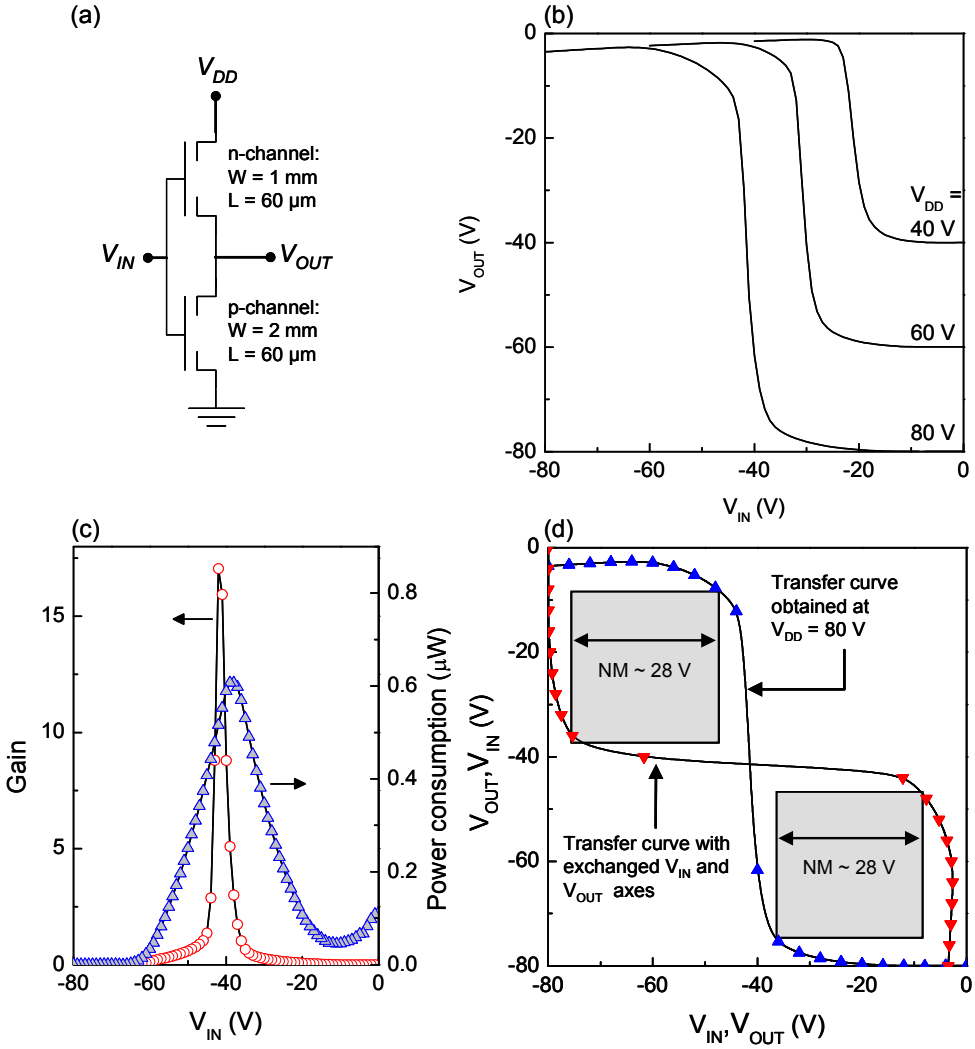


Fig. 4.22: (a) Schematic and (b) output characteristics of complementary voltage inverter constructed of n-type [60]PCBM and p-type PTAA transistors. (c) Gain and power consumption of the complementary voltage inverter in quasi static operation. (d) Determination of noise margins.

As evident from Fig. 4.22(c), the complementary voltage inverter only consumes significant power during the switching. In either HIGH or LOW input states at least one of the two transistors is completely turned off, limiting the current to the ground. Hence its power demand in quasi static operation at high or low input voltages is very low compared to the unipolar voltage inverter discussed in 4.8.1.

In summary, complementary logic, involving both n-channel and p-channel transistors, is shown to exhibit higher noise margins and lower power dissipation than unipolar logic.[3] Both parameters are of critical importance since a wide noise margin enables large-scale integration of OFETs with acceptable manufacturing yield while low power dissipation qualifies organic integrated circuits for battery-powered applications.

4.9. Outlook

In this chapter various phenomena related to the fabrication and development of electron transporting organic field-effect transistors are investigated. The study is driven by the need for soluble n-channel semiconductors for the development of complementary type logic in organic electronics. Soluble fullerene materials are found to be very promising candidates for application in solution processed organic circuits. The electron field-effect mobility of 0.2 cm^2/Vs measured in an optimized device configuration is amongst the highest values reported for solution processed organic n-channel transistors to date and is similar to the performance of state-of-the-art p-channel OFETs. The considerations regarding electron injection into organic materials, the trapping of electrons within the semiconductor bulk or at the dielectric surface, the importance of the film morphology and the role of surface energy for solution processing are generic and can be applied to most organic semiconductor systems and devices. It is expected that solving the problem of air stability and comparatively low electron mobility will be crucial to the further advancement of complementary, low power organic electronics.

Reference list:

1 Shaw, J. M. & Seidler, P. F. Organic Electronics: Introduction. *IBM J.Res.& Dev.* **45**, - (2001).

2 Sirringhaus, H. Device Physics of Solution-Processed Organic Field-Effect Transistors. *Adv. Mater.* **17**, 2411-2425 (2005).

3 Crone, B. *et al.* Large-scale complementary integrated circuits based on organic transistors. *Nature* **403**, 521-523 (2000).

4 Klauk, H., Zschieschang, U., Pflaum, J. & Halik, M. Ultralow-power organic complementary circuits. *Nature* **445**, 745-748 (2007).

5 Crone, B. K. *et al.* Design and fabrication of organic complementary circuits. *J. Appl. Phys.* **89**, 5125-5132 (2001).

6 Gundlach, D. J. *et al.* High mobility n-channel organic thin-film transistors and complementary inverters. *J. Appl. Phys.* **98**, 064502-064508 (2005).

7 Katz, H. E. Recent Advances in Semiconductor Performance and Printing Processes for Organic Transistor-Based Electronics. *Chemistry of materials* **16**, 4748-4756 (2004).

8 McCulloch, I. *et al.* Liquid-crystalline semiconducting polymers with high charge-carrier mobility. *Nat Mater* **5**, 328-333 (2006).

9 Smith, J. *et al.* High-performance organic integrated circuits based on solution processable polymer-small molecule blends. *Appl. Phys. Lett.* **93**, 253301-253303 (2008).

10 Gelinck, G. H. *et al.* Flexible active-matrix displays and shift registers based on solution-processed organic transistors. *Nat Mater* **3**, 106-110 (2004).

11 Newman, C. R. *et al.* Introduction to organic thin film transistors and design of n-channel organic semiconductors. *Chemistry of materials* **16**, 4436-4451 (2004).

12 Jones, B. A. *et al.* High-mobility air-stable n-type semiconductors with processing versatility: dicyanoperylene-3,4:9,10-bis(dicarboximides). *Angewandte Chemie (International ed.)* **43**, 6363-6366 (2004).

13 Anthopoulos, T. D. *et al.* Air-Stable n-Channel Organic Transistors Based on a Soluble C84 Fullerene Derivative. *Adv. Mater.* **18**, 1679-1684 (2006).

14 Chikamatsu, M. *et al.* Solution-processed n-type organic thin-film transistors with high field-effect mobility. *Appl. Phys. Lett.* **87**, 203504 (2005).

15 Yan, H. *et al.* A high-mobility electron-transporting polymer for printed transistors. *Nature* **457**, 679-686 (2009).

16 T.-W. Lee, Y. B., B.-W. Koo, I.-N. Kang, Y.-Y. Lyu, C. H. Lee, L. Pu, S. Y. Lee,. All-Solution-Processed n-Type Organic Transistors Using a Spinning Metal Process. *Adv. Mater.* **17**, 2180-2184 (2005).

17 Chua, L. L. *et al.* General observation of n-type field-effect behaviour in organic semiconductors. *Nature* **434**, 194-199 (2005).

18 Anthopoulos, T. D. *et al.* Ambipolar Organic Field-Effect Transistors Based on a Solution-Processed Methanofullerene. *Adv. Mater.* **16**, 2174-2179 (2004).

19 Chua, L. L., Ho, P. K., Sirringhaus, H. & Friend, R. H. High-stability ultrathin spin-on benzocyclobutene gate dielectric for polymer field-effect transistors. *Appl. Phys. Lett.* **84**, 3400-3402 (2004).

20 Hamilton, R. *et al.* High-Performance Polymer-Small Molecule Blend Organic Transistors. *Adv. Mater.* **21**, 1166-1171 (2009).

21 Zhang, X.-H., Domercq, B. & Kippelen, B. High-performance and electrically stable C60 organic field-effect transistors. *Appl. Phys. Lett.* **91**, 092114 (2007).

22 Singh, T. B. *et al.* Fabrication and characterization of solution-processed methanofullerene-based organic field-effect transistors. *J. Appl. Phys.* **97**, 083714 (2005).

23 Singh, T. B. *et al.* High-mobility n-channel organic field-effect transistors based on epitaxially grown C60 films. *Organic electronics* **6**, 105-110 (2005).

24 Sze, S. M. *Physics of Semiconductor Devices*. (Wiley, 1981).

25 Klauk, H., Zschieschang, U. & Halik, M. Low-voltage organic thin-film transistors with large transconductance. *J. Appl. Phys.* **102**, 074514 (2007).

26 Zan, H.-W. *et al.* Low-voltage organic thin film transistors with hydrophobic aluminum nitride film as gate insulator. *Organic electronics* **8**, 450-454 (2007).

27 McDowell, M., Hill, I. G., McDermott, J. E., Bernasek, S. L. & Schwartz, J. Improved organic thin-film transistor performance using novel self-assembled monolayers. *Appl. Phys. Lett.* **88**, 073505 (2006).

28 Sirringhaus, H., Tessler, N. & Friend, R. H. Integrated, high-mobility polymer field-effect transistors driving polymer light-emitting diodes. *Synthetic Metals* **102**, 857-860 (1999).

29 Dimitrakopoulos, C. D. & Malenfant, P. R. L. Organic Thin Film Transistors for Large Area Electronics. *Adv. Mater.* **14**, 99-117 (2002).

30 Chikamatsu, M., Itakura, A., Yoshida, Y., Azumi, R. & Yase, K. High-Performance n-Type Organic Thin-Film Transistors Based on Solution-Processable Perfluoroalkyl-Substituted C60 Derivatives. *Chemistry of materials* **20**, 7365-7367 (2008).

31 Kalb, W. L., Mathis, T., Haas, S., Stassen, A. F. & Batlogg, B. Organic small molecule field-effect transistors with Cytop gate dielectric: Eliminating gate bias stress effects. *Appl. Phys. Lett.* **90**, 092104 (2007).

32 Salleo, A. & Street, R. A. Light-induced bias stress reversal in polyfluorene thin-film transistors. *J. Appl. Phys.* **94**, 471-479 (2003).

33 Veres, J., Ogier, S., Lloyd, G. & De Leeuw, D. M. Gate insulators in organic field-effect transistors. *Chemistry of materials* **16**, 4543-4555 (2004).

34 Noh, Y.-Y. & Sirringhaus, H. Ultra-thin polymer gate dielectrics for top-gate polymer field-effect transistors. *Organic electronics* **10**, 174-180 (2009).

35 C. J. Brabec, N. S. Sariciftci & J. C. Hummelen. Plastic Solar Cells. *Adv. Funct. Mater.* **11**, 15-26 (2001).

36 Veenstra, S. C., Heeres, A., Hadziioannou, G., Sawatzky, G. A. & Jonkman, H. T. On interface dipole layers between C60 and Ag or Au. *Appl. Phys. A: Mater. Sci. Process.* **75**, 661-666 (2002).

37 Duren, J. K. J. v. *et al.* Injection-limited electron current in a methanofullerene. *J. Appl. Phys.* **94**, 4477-4479 (2003).

38 Anthopoulos, T. D. *et al.* Solution processible organic transistors and circuits based on a C70 methanofullerene. *J. Appl. Phys.* **98**, 054503 (2005).

39 Shockley, W. Research and investigation of inverse epitaxial UHF power transistors. *Air Force Atomic Laboratory, Wright-Patterson Air Force Base, Ohio* ***A1-TOR-64-20*** (1964).

40 Klauk, H. *et al.* Contact resistance in organic thin film transistors. *Solid-State Electronics* **47**, 297-301 (2003).

41 Chikamatsu, M. *et al.* Correlation of molecular structure, packing motif and thin-film transistor characteristics of solution-processed n-type organic semiconductors based on dodecyl-substituted C60 derivatives. *Journal of Photochemistry and Photobiology A: Chemistry* **182**, 245-249 (2006).

42 Guinier, A. *X-Ray Diffraction In Crystals, Imperfect Crystals, and Amorphous Bodies*. (Dover Publications, 1994).

43 X. Yang, J. K. J. van D., M. T. Rispens, J. C. Hummelen, R. A. J. Janssen, M. A. J. Michels, J. Loos,. Crystalline Organization of a Methanofullerene as Used for Plastic Solar-Cell Applications. *Adv. Mater.* **16**, 802-806 (2004).

44 Horowitz, G., Hajlaoui, M. E. & Hajlaoui, R. Temperature and gate voltage dependence of hole mobility in polycrystalline oligothiophene thin film transistors. *J. Appl. Phys.* **87**, 4456-4463 (2000).

45 Horowitz, G. Field-effect transistors based on short organic molecules. *Journal of materials chemistry* **9**, 2021 (1999).

46 Meijer, E. J. *et al.* Switch-on voltage in disordered organic field-effect transistors. *Appl. Phys. Lett.* **80**, 3838 (2002).

47 H. Bässler, P. M. B., R. J. Perry,. Charge transport in poly(methylphenylsilane): The case for superimposed disorder and polaron effects. *Journal of Polymer Science Part B: Polymer Physics* **32**, 1677-1685 (1994).

48 Tiwari, S. P., Namdas, E. B., Ramgopal Rao, V., Fichou, D. & Mhaisalkar, S. G. Solution-Processed n-Type Organic Field-Effect Transistors With High on /off Current Ratios Based on Fullerene Derivatives. *Electron Device Letters, IEEE* **28**, 880-883 (2007).

49 Coropceanu, V. *et al.* Charge transport in organic semiconductors. *Chem.Rev.* **107**, 926-952 (2007).

50 Veres, J. Low-k Insulators as the Choice of Dielectrics in Organic Field-Effect Transistors. *Adv. Funct. Mater.* **13**, 199-204 (2003).

51 Borsenberger, P. M. & Weiss, D. S. Organic photoreceptors for xerography. *CRC Press*, 491-506 (1998).

52 Mihailetchi, V. D., van Duren, J. K. J. & Blom, P. W. M. Electron Transport in a Methanofullerene. *Adv. Funct. Mater.* **13**, - (2003).

53 Tomiyama, T., Uchiyama, S. & Shinohara, H. Solubility and partial specific volumes of C60 and C70. *Chemical Physics Letters* **264**, 143-148 (1997).

54 Martens, H. C. F., Blom, P. W. M. & Schoo, H. F. M. Comparative study of hole transport in poly(p-phenylene vinylene) derivatives. *Phys. Rev. B* **61**, 7489 (2000).

55 Tanase, C., Meijer, E. J., Blom, P. W. M. & de Leeuw, D. M. Unification of the Hole Transport in Polymeric Field-Effect Transistors and Light-Emitting Diodes. *Phys. Rev. Lett.* **91**, 216601 (2003).

56 Vissenberg, M. J. C. M. & Matters, M. Theory of the field-effect mobility in amorphous organic transistors. *APS Physical Review B* **67**, 12964-12967 (1998).

57 Woudenbergh, T. v., Blom, P. W. M., Vissenberg, M. C. J. M. & Huiberts, J. N. Temperature dependence of the charge injection in poly-dialkoxy-p-phenylene vinylene. *Appl. Phys. Lett.* **79**, 1697-1699 (2001).

58 Shuai, Z. & Brédas, J. L. Electronic structure and nonlinear optical properties of the fullerenes C60 and C70: A valence-effective-Hamiltonian study. *Phys. Rev. B* **46**, 16135 (1992).

59 Kazaoui, S. & Minami, N. Intermolecular charge transfer excitons in C70 as compared with C60 films. *Synthetic Metals* **86**, 2345-2346 (1997).

60 Hertel, I. V. *et al.* Giant plasmon excitation in free C60 and C70 molecules studied by photoionization. *Phys. Rev. Lett.* **68**, 784 (1992).

61 Anthopoulos, T. D. *et al.* Organic complementary-like inverters employing methanofullerene-based ambipolar field-effect transistors. *Applied physics letters* **85**, 4205- (2004).

62 Waldauf, C. Solution-Processed Organic n-Type Thin-Film Transistors. *Catal. Today* **67**, 369- (2001).

63 Singh, T. B., Marjanovic, N., Sariciftci, N. S. & Menon, R. Correlation between morphology and ambipolar transport in organic field-effect transistors. *J. Appl. Phys.* **97**, 114508 (2005).

64 Martijn M. Wienk, J. M. K., Wiljan J. H. Verhees, Joop Knol, Jan C. Hummelen, Paul A. van Hal, René A. J. Janssen,. Efficient Methano[70]fullerene/MDMO-PPV Bulk Heterojunction Photovoltaic Cells13. *Angew. Chem., Int. Ed.* **42**, 3371-3375 (2003).

65 Haddon, R. C. C-70 thin film transistors. *Journal of the American Chemical Society* **118**, 3041-3042 (1996).

66 Haddock, J. N., Zhang, X. H., Domercq, B. & Kippelen, B. Fullerene based n-type organic thin-film transistors. *Organic electronics* **6**, 182-187 (2005).

67 Pavel A. Troshin *et al.* Material Solubility-Photovoltaic Performance Relationship in the Design of Novel Fullerene Derivatives for Bulk Heterojunction Solar Cells. *Adv. Funct. Mater.* **19**, 779-788 (2009).

68 Peet, J. *et al.* Efficiency enhancement in low-bandgap polymer solar cells by processing with alkane dithiols. *Nat Mater* **6**, 497-500 (2007).

69 Kim, J. Y. *et al.* Efficient Tandem Polymer Solar Cells Fabricated by All-Solution Processing. *Science* **317**, 222-225 (2007).

70 Wöbkenberg, P. H. *et al.* Fluorine containing C-60 derivatives for high-performance electron transporting field-effect transistors and integrated circuits. *Appl. Phys. Lett.* **92**, 143310-143313 (2008).

71 Anthopoulos, T. D., Anyfantis, G. C., Papavassiliou, G. C. & de Leeuw, D. M. Air-stable ambipolar organic transistors. *Appl. Phys. Lett.* **90**, 122105 (2007).

72 Katz, H. E. *et al.* A soluble and air-stable organic semiconductor with high electron mobility. *Nature* **404**, 478-481 (2000).

73 Cantatore, E. & Meijer, E. J. *Proceedings of the 29th European Solid-State Circuits Conference, Estoril, Portugal* (2003).

Chapter 5: Ambipolar organic field-effect transistors for opto/electronic applications

Most organic semiconductors are known for transporting predominantly one type of charge carrier, i.e. electrons or holes, and they are referenced as either n-type or p-type materials, respectively. The ability of some organic semiconductors to transport both, holes and electrons, can be exploited to fabricate ambipolar organic field-effect transistors. These devices could play an important role in advancing organic complementary-like logic to large scale fabrication, as well as in some optoelectronic applications. Squaraine molecules and a polymer:fullerene blend are investigated as ambipolar semiconductors and are shown to bear significant potential for (UV - Infrared) light sensing field-effect transistors as well as complementary-like integrated circuits.

5.1. Introduction

The vast majority of organic semiconductors known to date are classified as either hole (p-type) or electron (n-type) transporters. Ambipolar organic semiconductors, i.e. compounds that are able to conduct both holes and electrons, are a relatively new addition to the family of organic semiconductors. They are currently attracting increasing attention due to their interesting electronic properties. In the area of organic microelectronics, for example, the sequential deposition and patterning of p-type and n-type semiconductors has proven to be a major hurdle for the implementation of organic complementary logic, which is considered a key enabling technology for the development of high-performance organic integrated circuits (ICs).[1] The availability of soluble ambipolar materials could enable the fabrication of complementary-like circuits through the use of a single semiconductor that behaves both as p-type or n-type depending on the biasing conditions across the device, hence eliminating the need of sequential deposition and patterning of the different semiconductors. Further applications of ambipolar organic semiconductors include the recent demonstration of bifunctional organic transistors such as light-sensing (LS-OFETs)[2,3] and light-emitting organic field-effect transistors (LE-OFETs).[4] These transistors combine electrical switching with additional functionalities such as light-sensing or light-emission, in a single device structure, making them attractive for various optoelectronic applications including nanoscale light sources and large area image sensor arrays.[2,3,5]

In collaboration with the group of Jean-Pierre Djukic at the University of Strasbourg we have studied a promising family of ambipolar organic molecules, namely the squaraines. The molecules were synthesized and characterized in Strasbourg, while the focus of my work lay on the fabrication of transistor devices and their characterization.[6] We demonstrated solution processed ambipolar field-effect transistors with balanced hole and electron mobilities by injection from symmetric gold source-drain (S-D) electrodes. Furthermore it has been demonstrated that squaraine based devices are suitable for integration into complementary-like logic circuits, as well as for utilisation in light sensing applications in the near-infrared (600 - 1000 nm) spectrum. Infrared (IR) sensors are particularly desirable as most other organic sensor systems reported to date are limited to the visible and ultra violet (UV) spectrum.[7-11] Light sensing ambipolar transistors were also fabricated from a two

component blend comprising a hole transporting donor polymer and an electron transporting acceptor fullerene derivative. Thanks to the different absorption spectra of these material systems, the fabrication of colour-sensitive light sensing arrays can be envisioned.

5.2. Chemical characterization of Squarylium dye

The chemistry of squaraines is well known. They are the main product of the condensation of electron-rich aromatics with squaric acid, a reaction that obeys the rules of aromatic electrophilic substitution. A detailed description of the synthesis of the molecules prepared by Djukic *et al.* is given elsewhere.[6] Squaraines belong to the class of polymethyne dyes with resonance-stabilized zwitterionic structures. They are structurally flat, highly conjugated organic molecules, which are expected to stack very closely in crystals. Squaraine molecules typically consist of an electron deficient central four membered ring and two electron-donating groups in a donor-acceptor-donor (D-A-D) formation. This configuration is expected to enable the transport of holes via the acceptor and electrons via the donor groups. The chemical structure of the molecule investigated in this study (2,4-di-3-guaiazulenyl-1,3-dihydroxy-cyclobutenediyliumdixydroxide-bis-zwitterion (SQ1)) is displayed in Fig. 5.1(a).

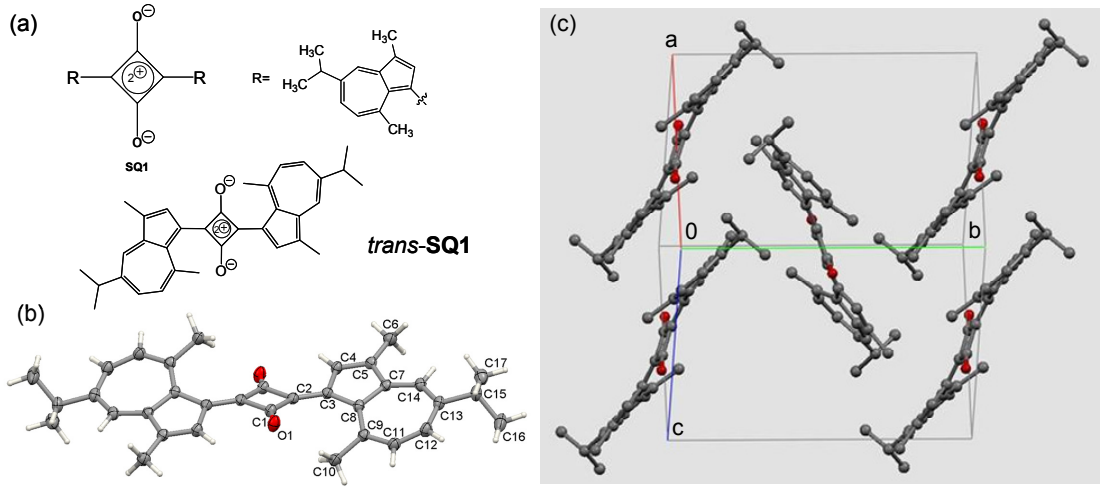


Fig. 5.1: (a) Molecular formula of SQ1. (b) CSD Mercury ellipsoid diagram and numbering scheme of the structure of *trans*-SQ1: ellipsoids are drawn at 50 % probability level. (c) view of the packing scheme in the crystal lattice.

The exact geometry of the pure compound obtained after chromatographic purification was sought by means of structural X-ray diffraction analysis of a single

crystal that was obtained by the slow evaporation of the solvent from a solution of SQ1 in a 1:1 mixture of methanol and chloroform. The crystal lattice presents the typical herringbone packing [Fig. 2.16] of independent layers of squaraines [Fig. 5.1(c)]. The shortest distance between two molecules of SQ1 was measured between two consecutive cyclopentadienyl rings and amounts to ≈ 3.83 Å. The π stacking is not optimal and the SQ1 molecules appear to be distorted. The torsion between the mean plane of the 4-membered ring and, for instance, the mean plane defined by the fused 5- and 7-membered rings of the guaiazulenyl moiety amounts to ≈ 27°. Quite consistently it is noticed that the mean planes of two guaiazulenyls that belong to the same molecule are parallel to each other.

Table 5.1: Electrochemical data measured by cyclic voltammetry (CV) at a scan rate of v = 0.1 V/s and rotating disk voltammetry (RDV) in CH_2Cl_2 + 0.1M Bu4NPF6. All potentials are given versus ferrocene, used as internal standard.

species	CV			RDV	
	$E°$ [a] ($V_{Fc+/Fc}$)	ΔE_p [b] (mV)	E_p [c] ($V_{Fc+/Fc}$)	$E_{1/2}$ ($V_{Fc+/Fc}$)	slope [d] (mV)
SQ1	0.56	65	-2.03	0.59	60
	0.11	65		0.12	60
	-1.23	60		-1.24	60
				-2.06	60

[a] $E° = (E_{pc} + E_{pa})/2$, where E_{pc} and E_{pa} correspond to the cathodic and anodic peak potentials, respectively. [b] $\Delta E_p = E_{pa} - E_{pc}$. [c] E_p = irreversible peak potential. [d] Logarithmic analysis of the wave obtained by plotting E versus $\log[I/(I_{lim}-I)]$.

Electrochemical investigations were carried out in dichloromethane (Table 5.1). Rotating disk voltammetry gave four waves of equal amplitude, namely two oxidations and two reductions. Cyclic voltammetry gave well resolved voltammograms. The SQ1 compound gave two reversible one-electron oxidation steps at +0.11 and at +0.56 V vs. Fc^+/Fc, a reversible one-electron reduction at –1.23 V, as well as an irreversible one electron step at E_p = –2.03 V [Fig. 5.2]. The latter remained irreversible for scan rates of up to 10 V/s. The potential difference between the first oxidation and the first reduction is equal to 1.34 V. The highest occupied molecular orbital (HOMO) and the lowest unoccupied molecular orbital (LUMO) were estimated to be $E_{HOMO,CV}$ ≈ -4.9 eV and $E_{LUMO,CV}$ ≈ -3.6 eV, using $E_{Fc+/Fc}$ = -4.8 V as the reference potential to the vacuum level.

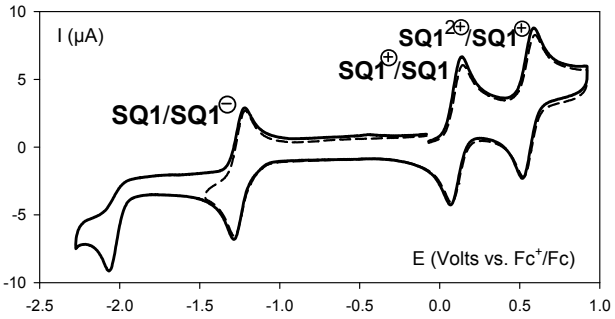


Fig. 5.2: Cyclic voltammetry of SQ1 in CH_2Cl_2 + 0.1M Bu4NPF6 at a scan rate of 0.1V/s.

Furthermore, quantum calculations were performed by applying density functional theory (DFT). Details of this analysis and the software packages used to perform the calculations can be found elsewhere.[6] The theoretically computed LUMO and HOMO of singlet ground-state SQ1 lie at –3.3 and –4.4 eV, respectively, which corresponds to a theoretical energy gap of 1.1 eV in vacuum [Fig. 5.3]. This approximation is close to the values estimated from cyclic voltammetry, taking into account that absolute energy values are often underestimated in DFT analysis.[12] It is worth noting that this value is smaller than the average energy gaps determined by Bhanuprakash, Rao *et al.*[13] for a series of symmetric and asymmetric squaraines. Das *et al.*[14] attained similar values of HOMO-LUMO gaps with squaraines derived from N,N-dialkylaminoanthracene.

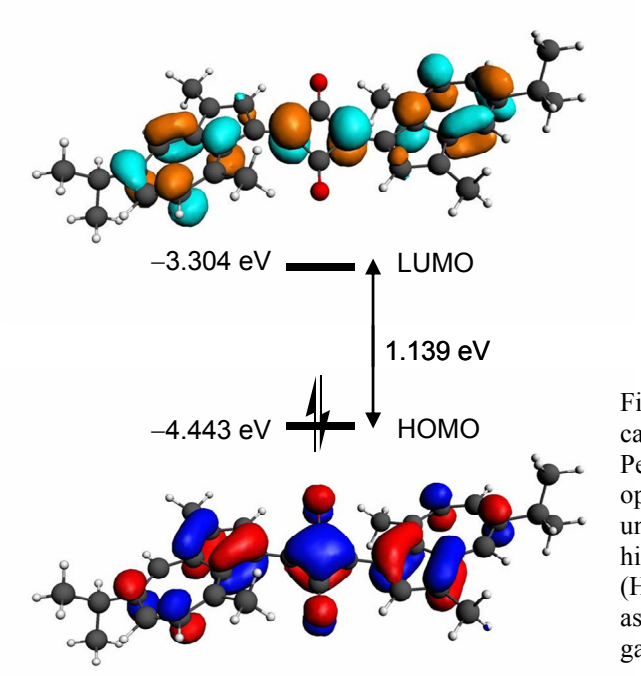


Fig. 5.3: Density functional theory calculations carried out at the Becke-Perdew/TZ2P level with geometry-optimized SQ1: plot of the lowest unoccupied molecular orbital (LUMO) and highest occupied molecular orbital (HOMO) of the singlet ground-state associated with the corresponding energy gap.

Another interesting observation is that the two frontier orbitals are highly delocalized with a rather balanced contribution of the *p* orbitals of the central 4-

membered ring and other π-type orbitals located at the guaiazulenyl fragments [Fig. 5.3].

The zwitterionic character of neutral SQ1 was confirmed by the natural population analysis carried out with the results of the previously obtained geometry optimization from the DFT calculation (data not shown). The natural population analysis using GENNBO[15] indicates that the natural charge at the two oxygen atoms is –0.61 and that the highest natural positive charge of +0.43 is located at the carbonyl's carbon, the rest of the molecule being only moderately charged with compensated slight positive and negative biases.

5.3. Ambipolar organic field-effect transistors

The ambipolar nature of organic semiconductors is investigated in field-effect transistors, which can operate either in the hole- and/or in the electron accumulation regime. We fabricated bottom gate - bottom contact (BG-BC) OFETs using SQ1 that was synthesized in the University of Strasbourg, as well as using a two component semiconductor blend of poly(2-methoxy 5-(3'-7' dimethyloctyloxy)-1-4 phenylenevinylene) (OC_1C_{10}-PPV) and [6,6]-phenyl-C61-butyric acid ester ([60]PCBM).

5.3.1. Squarylium as organic semiconductor

The BG-BC FETs were fabricated on a highly doped silicon wafer with a thermally grown 200 nm layer of SiO_2 dielectric [Fig. 5.4(c)]. The S-D gold electrodes were patterned by a standard photo-lithography process, and the SiO_2 dielectric surface was passivated using a monolayer of hexamethyldisilazane (HMDS). The squaraine dye was deposited as organic semiconductor by spin coating from a 10 mg/ml solution in chlorobenzene. The films generally appeared to be of a highly crystalline nature. Examination of the film by optical polarized reflection microscopy [Fig. 5.4(a) and (b)] revealed a large number of adjacent domains in the crystalline films, separated by clearly defined grain boundaries. The size of the spheralitic type grains often extended to over several tens of μm, thereby easily covering the length of a transistor channel.

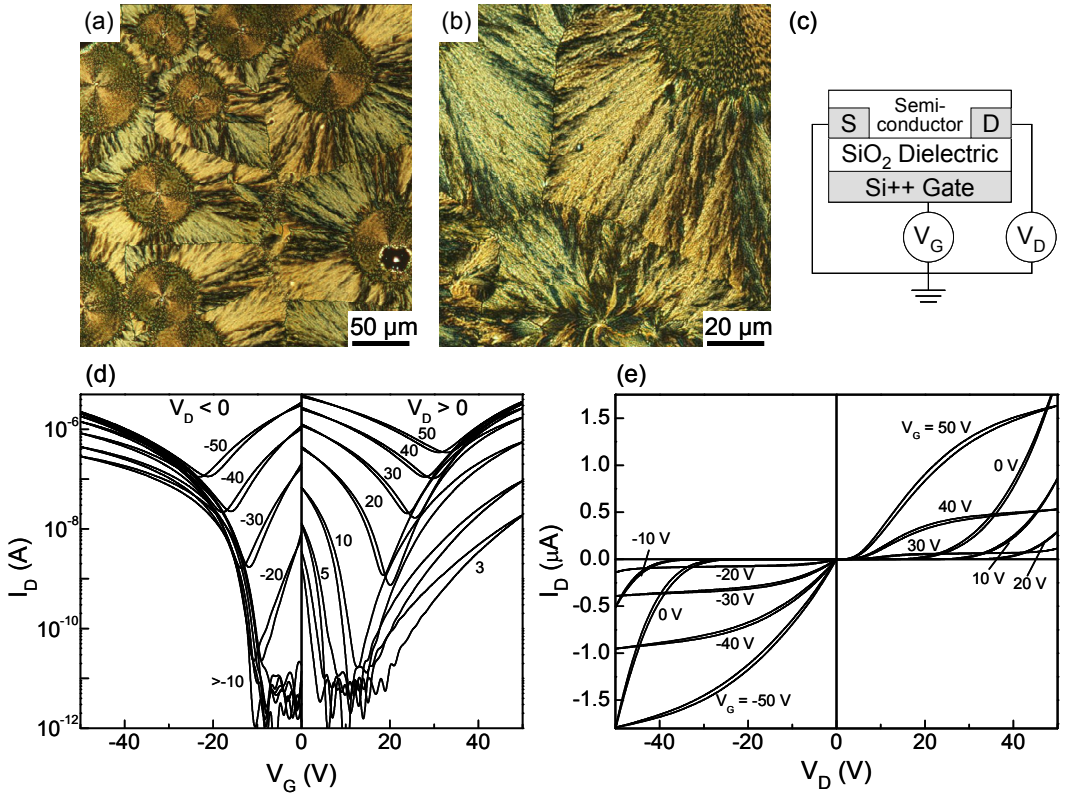


Fig. 5.4: (a-b) Polarized optical reflection microscopy of crystalline SQ1 films. (c) Schematic representation of transistor bottom gate-bottom contact architecture employed. (d) Transfer and (e) output characteristics of ambipolar SQ1 transistor. L = 2.5 µm, W = 10 mm, C_i = 17 nF/cm^2.

Typical output and transfer characteristics of SQ1 based transistors are shown in Fig. 5.4(d) and (e). The transistors exhibit clear ambipolar behaviour with balanced hole and electron mobilities of the order of 10^{-4} cm^2/Vs in saturation. The hysteresis between forward and backward scans was found to be negligible. The output characteristics at positive gate bias show non-linear features at low drain voltages, which are a signature of injection limited transport. This phenomenon is not observed in the output curves during p-channel operation, e.g. at negative gate bias. This is likely to be due to the large injection barrier for electrons ($\phi_e \approx$ 1.5 - 1.8 eV) from the work function of gold (≈ 5.1 eV) into the LUMO level of the SQ1 molecules (≈ 3.3 - 3.6 eV), which is smaller for hole injection ($\phi_h \approx$ 0.2 - 0.6 eV) into the HOMO level (≈ 4.5 – 4.9 eV) [Fig. 5.5(a)].

The charge carrier mobility was found to decrease in devices with larger channel length of up to 40 µm. This was attributed to a grain boundary effect, which typically arises in films that consist of many crystalline domains. The interface between two crystalline domains gives rise to a potential barrier or trapping states, which inhibit the movement of charges.[16] In longer channel devices charges are likely

to encounter more domain boundaries, which adversely affect the measured charge carrier mobility.

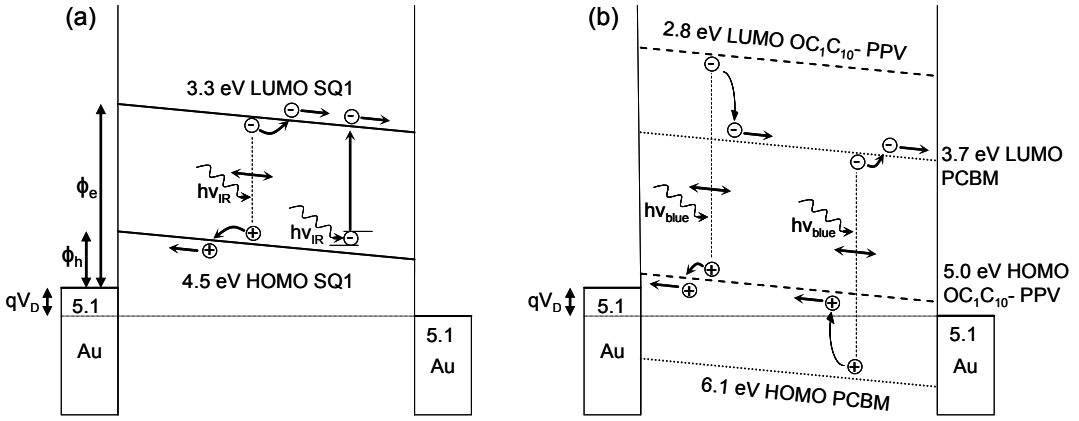


Fig. 5.5: Schematic representation of LUMO and HOMO energies in (a) SQ1 and (b) PCBM:OC_1C_{10}-PPV blend with respect to the work function of gold electrodes under an applied S-D voltage V_D. Band bending is ignored. Photo-generation processes of mobile charges via exciton formation and via de-trapping of localized charges are also represented.

5.3.2. [60]PCBM – OC_1C_{10}-PPV blend as organic ambipolar semiconductor

The alternative to using a single molecule that is intrinsically capable of both, electron and hole transport, is to blend an electron transporting material and a hole transporting material to create a heterogeneous two-component film. Here I employed OC_1C_{10}-PPV as hole transporting polymer and [60]PCBM as electron transporting molecule (see Fig. 5.6(a) for molecular structures). Parent solutions were prepared in Chlorobenzene at concentrations of ≈ 20 mg/ml ([60]PCBM) and ≈ 3 mg/ml (OC_1C_{10}-PPV) and then blended at a ratio of 6:1 ([60]PCBM:OC_1C_{10}-PPV) by volume. Hence the weight ratio in the final solution was approximately 40:1 ([60]PCBM:OC_1C_{10}-PPV). The solution was spin coated onto BG-BC transistor structures [Fig. 5.4(c)], employing a highly doped silicon substrate as gate electrode, with 200 nm of SiO_2 as dielectric and photolithographically patterned gold S-D contacts. The dielectric surface was passivated with HMDS. Fig. 5.6 shows (b) transfer and (c) output curves of the ambipolar transistor. The asymmetry of the transfer curves expresses the imbalance of hole and electron mobility. The saturation hole mobility was found to be of the order of 10^{-4} cm^2/Vs and the electron mobility approximately 10^{-2} cm^2/Vs. Meijer *et al.*[17] found that the electron mobility in the blend films decreased drastically by two orders of magnitude with respect to pristine [60]PCBM films. This effect may be attributed to the significantly smaller ratio of [60]PCBM:OC_1C_{10}-PPV employed in

their study (4:1). A lower [60]PCBM content in the film is expected to lead to greater distances between the molecules (i.e. below percolation threshold) and hence lead to less efficient electron transport.[18,19] It is unclear, however, whether this effect can account for a mobility decrease by several orders of magnitude. Meijer *et al.* explained their observation and the increased electron injection difficulties in the blend films with the wetting behaviour of the semiconductor blend solution on the gold surface of the S-D electrodes.[17] Phase segregation is likely to occur in the [60]PCBM:OC_1C_{10}-PPV solution during spin coating due to a different wettability of gold by the polymer compared to the small molecule semiconductor. However, a clear effect of this segregation on the electron mobility was not observed here. Furthermore, non-linear features in the output curves indicating problematic injection at low V_D are present in both, ambipolar blend [Fig. 5.6(c)] and unipolar [60]PCBM devices, as shown in chapter 4.2. They are explained by the large energy offset between the work function of Au and the LUMO level of [60]PCBM [Fig. 5.5(b)].

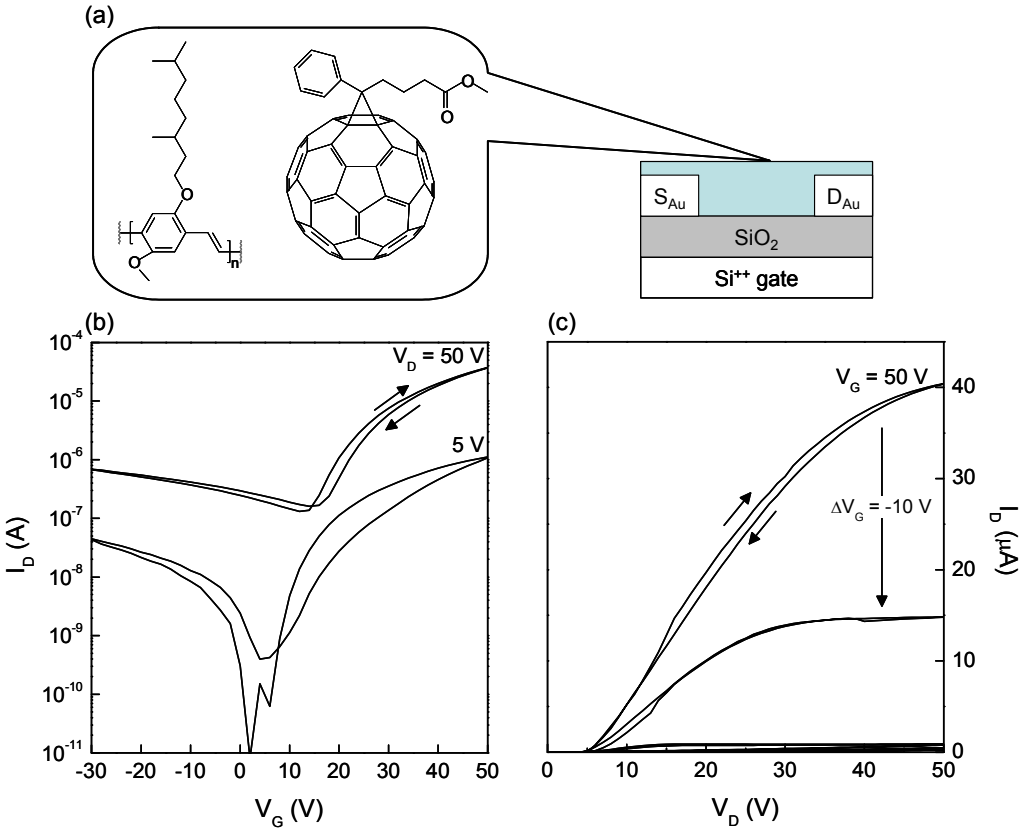


Fig. 5.6: (a) Molecular structures of poly(2-methoxy 5-(3'-7' dimethyloctyloxy)-1-4 phenylenevinylene) (OC_1C_{10}-PPV) and [6,6]-phenyl-C61-butyric acid ester ([60]PCBM). Architecture of bottom gate-bottom contact ambipolar OFET employing blend of OC_1C_{10}-PPV and [60]PCBM as semiconductor. (b) Transfer and (c) output characteristics of the ambipolar blend transistor, L = 40 µm, W = 10 mm, C_i = 17 nF/cm^2.

5.4. Ambipolar transistor applications

The transport characteristics of the ambipolar organic transistors based on SQ1 and on the [60]PCBM:OC_1C_{10}-PPV semiconductor blend were found to be dependent on fluorescent light in proximity to the measurement setup. This led us to closely investigate the absorption properties of these materials and their application in light sensing transistors.

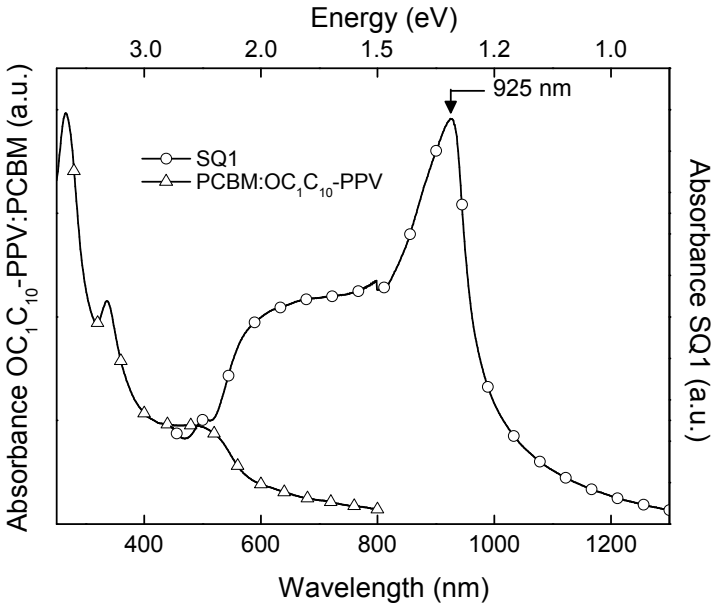


Fig. 5.7: Absorbance characteristics of thin films of SQ1 and PCBM:OC_1C_{10}-PPV blend on different scales.

5.4.1. UV-Vis and near-IR absorption measurements

The absorption characteristics of solid thin films of the SQ1 compound and of the [60]PCBM:OC_1C_{10}-PPV blend on quartz substrates were measured from the UV to IR spectrum [Fig. 5.7]. The SQ1 film absorbs strongest in the near-IR spectrum and weakest in the region between 400-500 nm. The increasing absorption in the UV is omitted for the SQ1 compound. The absorption peaks at 925 nm, with an onset close to 1000 nm. This corresponds to an approximate energy gap between electronic HOMO and LUMO of 1.2 eV, which is in good agreement with the energy gap estimated from electrochemical measurements (≈ 1.3 eV) and the theoretical DFT analysis (≈ 1.1 eV) in section 5.2. In the case of the [60]PCBM:OC_1C_{10}-PPV blend absorption begins to rise at wavelengths below 600 nm, remains at a plateau between 500 nm and 400 nm and then increases steeply for smaller wavelengths in the UV

region. The absorption onset around 2.2-2.4 eV corresponds approximately to the HOMO-LUMO energy gap of OC_1C_{10}-PPV (2.2 eV) and [60]PCBM (2.4 eV) [Fig. 5.5(b)].

5.4.2. Light-sensing OFETs

The strong absorption in different spectral ranges of these ambipolar material systems makes them interesting candidates for application in LS-OFETs. In the case of the squaraine transistors, we employed an IR light emitting diode (LED) (λ_{max} = 880 nm) to illuminate the devices during operation. Light-dependent modulation of the drain current by several orders of magnitude was observed [Fig. 5.8(a)]. We note that the hole and electron mobility extracted from the transfer characteristic did not change upon illumination. The threshold voltage was extracted from plots of I_D and $I_D^{1/2}$ vs. V_G in the linear and saturation regime, respectively. It was found to shift by $\Delta V_{T,h} \approx 4$ V towards smaller $\left| V_G \right|$ for hole accumulation, but remained approximately constant for electron accumulation. The shift of threshold voltage in unipolar phototransistors under illumination is typically associated with the trapping of photo-generated less mobile minority carriers, e.g. electrons in p-type transistors, near the source contact.[20-22] The presence of electrons in that region effectively reduces the threshold voltage for hole injection from the source electrode.[23] From the threshold voltage shift the change in trapped electron density is calculated using equation 5.1:[24]

$$\Delta n_{photo,e} = \frac{C_i \cdot \Delta V_{T,h}}{e} \approx 4 \cdot 10^{10} cm^{-2} \qquad (5.1)$$

where C_i is the geometric capacitance of the gate dielectric and e is the elementary charge. This change in trap density is at least one order of magnitude lower than that reported for unipolar pentacene phototransistors.[24] This is expected, since our transistors exhibit balanced ambipolar characteristics, i.e. also electron transport. Hence we do not distinguish majority and minority carrier types and expect that both types of charge carriers are extracted from the device. Nevertheless electron trapping could explain the asymmetric threshold voltage shift upon illumination, i.e. $\Delta V_{T,h} \approx 4$ V and $\Delta V_{T,e} \approx 0$ V. Furthermore it is consistent with the observation that the SiO_2 dielectric layer is a source for electron traps in the n-type systems discussed in chapter 4. In the literature it has been shown that the threshold voltage shift in phototransistors

can be tuned by controlling the electron trapping ability of the dielectric layer.[24] Yet the exact origin of the trap density increase is unclear.

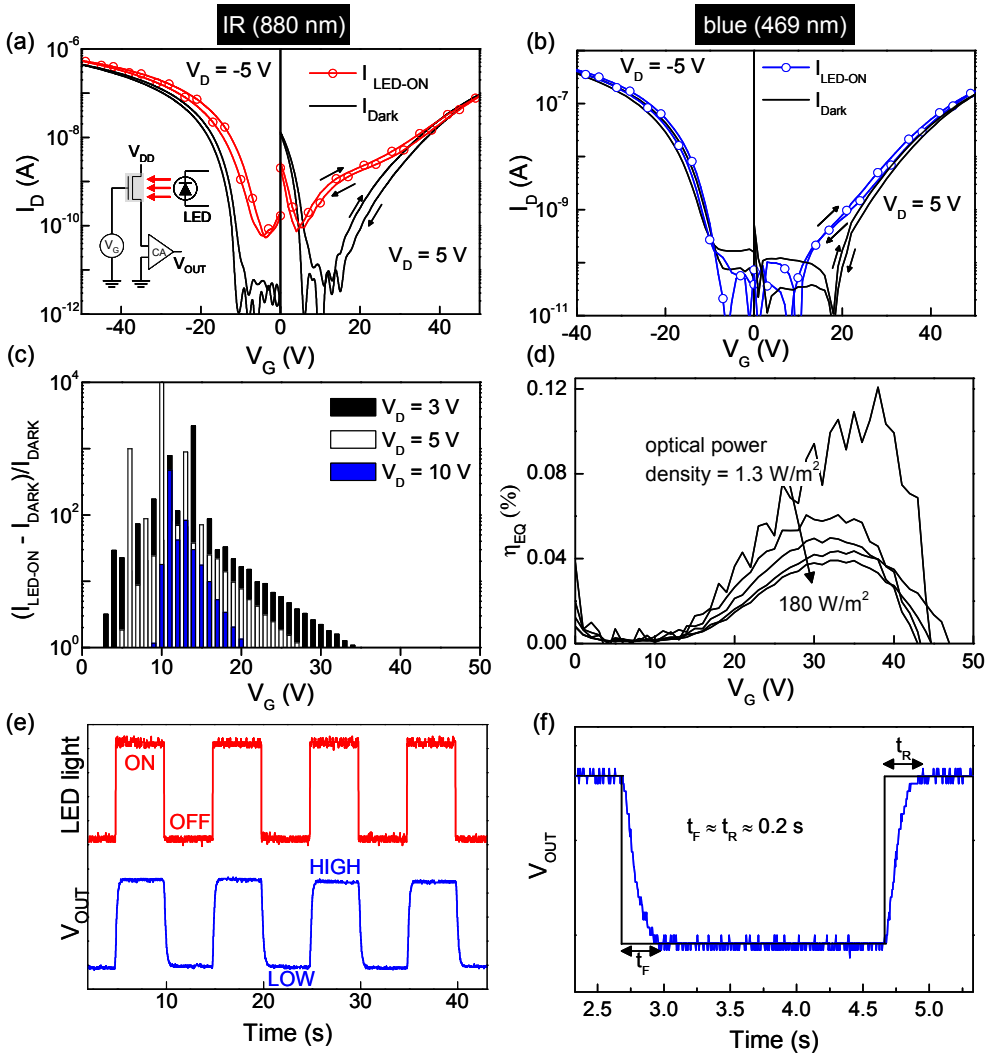


Fig. 5.8: Ambipolar SQ1 transistor measured in dark and under illumination with (a) IR-LED (λ_{peak} = 880 nm) and (b) blue LED (λ_{peak} = 469 nm). (c) Photosensitivity dependence on drain and gate bias at maximum near-IR-irradiance (180 W/m^2). (d) Dependence of external quantum efficiency on gate bias and irradiance, measured at V_D = 5 V. (e) Dynamic photo-modulation of current in ambipolar transistor biased at V_G = 12 V and V_D = 5 V. The IR-LED was pulsed at a frequency of 0.1 Hz. (f) Analysis of rise and fall times of photo-modulated transistor current.

The pinch-off current in the dark is very low (≈10^{-11} A) and close to the detection limit of the measurement setup. Under illumination we see that the off current increases by approximately one order of magnitude. The mechanism responsible for the photocurrent is likely to be the photon induced formation of excitonic electron-hole pairs, which can dissociate and give rise to an ambipolar photocurrent. The dissociation is facilitated by the externally applied source-drain electric field and by inbuilt potentials at impurity sites.[25] Recombination of excitons

before dissociation reduces the photocurrent. In the electron accumulation regime, at gate biases below the threshold voltage ($V_{T,e} \approx 37$ V), we observe an additional doping-like[26] current increase which seems to be superimposed to the exciton photocurrent. This could be explained by photon-induced direct transitions of electrons from localized tail states or in-gap states (traps) into delocalized states.[27] In the subthreshold regime some localized tail states and traps are filled with injected electrons, which are then easily excited to delocalized higher energy states by the absorption of low energy infrared photons. As a result we observe an enhanced electron photocurrent in the subthreshold regime.

The pinch-off point and saturation behaviour in the output curves, as measured in the dark [Fig. 5.4(e)], are preserved upon illumination. This means that the devices are not significantly affected by gate bias independent space charge limited currents due to photo-generation of mobile charges in the bulk semiconductor film. Fig. 5.8(c) shows the photosensitivity of I_D in the electron accumulation regime to illumination at different drain voltage biases. The effect of illumination is the largest at low drain (3-5 V) and gate (7-15 V) bias.

The maximum irradiance received by the transistor was measured using an inorganic photodiode and an optical power meter to be approximately 180 W/m^2. The active area was calculated using the width (W = 10 mm) and length (L = 2.5 μm) of the transistor channel (i.e. $A = L \cdot W$). The incident optical power to the transistor channel region was $P_{opt} \approx 4.5$ μW. Hence the maximum photoresponsivity R of the light sensing transistor at a photo-induced current increase of $I_{ph}=I_{ill} - I_{dark} \approx$ 1-3 nA is estimated to be approximately[25]

$$R_{IR} = \frac{I_{ph}}{P_{opt}} = 0.2 - 0.7 \text{ mA/W} \qquad (2.35)$$

The responsivity value is rather low when compared with other ambipolar LS-OFETs.[9] However, we do note that our calculation takes into account the total incident optical power and not the absorbed photons, hence it is an underestimation of R. Furthermore, one defines the external quantum efficiency η_{EQE} as the ratio of the number of photo-generated charge carriers N_e that contribute to I_D per unit time t to the number of photons N_γ incident on the transistor channel area per unit time t, given by equation 2.38:[11]

$$\eta_{EQE} = \frac{N_e}{N_\gamma} = \frac{I_{ph} \cdot h \cdot c}{e \cdot P_{opt} \cdot \lambda} \tag{2.38}$$

where h is Planck's constant, c is the speed of light in vacuum, e is the elementary charge and λ is the wavelength of the incident light. Fig. 5.8(d) shows the calculated η_{EQE} vs. V_G for different illumination intensities. The highest η_{EQE} of ≈ 0.1 % is achieved at low illumination intensity of ≈ 1.3 W/m^2 at V_G ≈ 30 V. External quantum efficiencies of the order of 10^{-4}-10^{-5} and a decreasing efficiency with increasing light intensity were also observed by Singh *et al*.[28] The latter trend can be attributed to saturation of photo-generated charge carriers in the LS-OFETs, as explained by Wasapinyokul *et al.*.[29] They attribute the lower responsivity at high light intensities to effects of space-charge-limited conduction in the channel, as well as polaron-polaron annihilation. Again, the calculation ignores photon absorption in the bulk film away from the channel. The result can therefore only be considered as a lower limit for the actual efficiency of this device. Moreover it is important to emphasize that the efficiency of the LS-OFET depends on the gate voltage. The highest efficiency is obtained at large positive gate voltages around the threshold voltage, at which most trap states in the channel are filled and a conductive region is formed at the semiconductor-dielectric interface. Under these circumstances photo-generated charges are likely to remain mobile and to be extracted through the S-D electrodes.

In the case of two-terminal diodes, a large portion of photo-generated charges remain immobilized in local trap states in the bulk semiconductor. These charges are not detected as photo-current and hence the effective sensitivity is reduced. It has been suggested that this is the reason for the superior sensitivity of LS-OFETs at low illumination intensity compared to simple 2-terminal photodiodes.[22] The gate voltage control over the photocurrent could also allow for internal amplification, hence making LS-OFETs a good alternative to photodiodes for light sensing technology.[30]

Upon exposure to light of a shorter wavelength of 469 nm the current modulation was very small [Fig. 5.8(b)]. The irradiance received by the transistor was in this case ≈ 173 W/m^2. The responsivity to the blue light is approximately one order of magnitude lower compared to the infrared LED, i.e. R_{blue} ≈ 0.05 mA/W. The weak response is due to the low optical absorption of SQ1 films at these wavelengths [Fig. 5.7].

The hysteresis between forward and backward scans is negligible, both for characteristics measured in the dark and under illumination. We also observed that the photo-induced current disappeared when the light was switched off. This led us to study the dynamic light response of SQ1 LS-OFETs using a pulsed IR-LED. In the ON-state (i.e. light on) the irradiance received by the transistor was approximately 30 W/m^2. The transistor current modulation in pulsed mode is shown in Fig. 5.8(e). The transistor current clearly follows the LED pulsing signal at frequencies below 1 Hz. The rise (t_R) and fall (t_F) times of the transistor output signal were extracted as shown in Fig. 5.8(f). The total response time measured was

$$t_T = t_F + t_R \approx 0.4s \tag{5.2}$$

This value for t_T yields a maximum operational frequency of

$$f = \frac{1}{t_T} \approx 2.5Hz\,. \tag{5.3}$$

These time constants are many orders of magnitude longer than the characteristic times for the recombination of photo-generated excitons in other organic semiconductors,[31] but they are consistent with trap emission rates of 0.1-10 Hz observed in deep level transient spectroscopy experiments[32] and the electrically driven filling and emptying of traps in organic transistors.[33] This observation is in agreement with the hypothesis stated above that some component of the photocurrent originates from the release of trapped charges. While the response time of the light sensing transistor is admittedly slow, the potential for future application in the area of cheap, possibly disposable infrared light sensors is very significant.

The experiment was repeated with the [60]PCBM:OC_1C_{10}-PPV blend based ambipolar transistors, employing a white fluorescent light source for illumination. Again, the pinch-off current in the dark was low ($\approx 10^{-11}$A), but increased drastically upon exposure to light. Fig. 5.9(a) exhibits transfer curves recorded at constant $V_D = 5$ V and at different illumination intensities, demonstrating the photomodulation of the drain-source current. As illustrated in the energy diagram in Fig. 5.5(b), absorption of blue light (hv > 2.2 eV) is expected to generate electron-hole pairs in the blend components, which diffuse to a fullerene/polymer interface and dissociate into mobile holes and electrons.[17] Due to the good intermixing of the two blend components the excitons typically reach a heterojunction before recombination. At the heterojunction

electrons are transferred to the [60]PCBM molecules and holes to the polymer [Fig. 5.5(b)]. An applied source-drain bias (V_D) causes the electrons to migrate towards the anode via the fullerene network and holes towards the cathode via the polymer network. The mechanisms responsible for exciton creation, diffusion to the heterojunction, charge separation and extraction are under intense investigation in the field of organic photovoltaics.[34] Fig. 5.9(b) represents the dependence of the light response on V_D. The data show that the pinch-off current increases by close to five orders of magnitude upon illumination and that the sensitivity is largest for low drain voltages (< 5 V) and gate biases of 5 to 15 V.

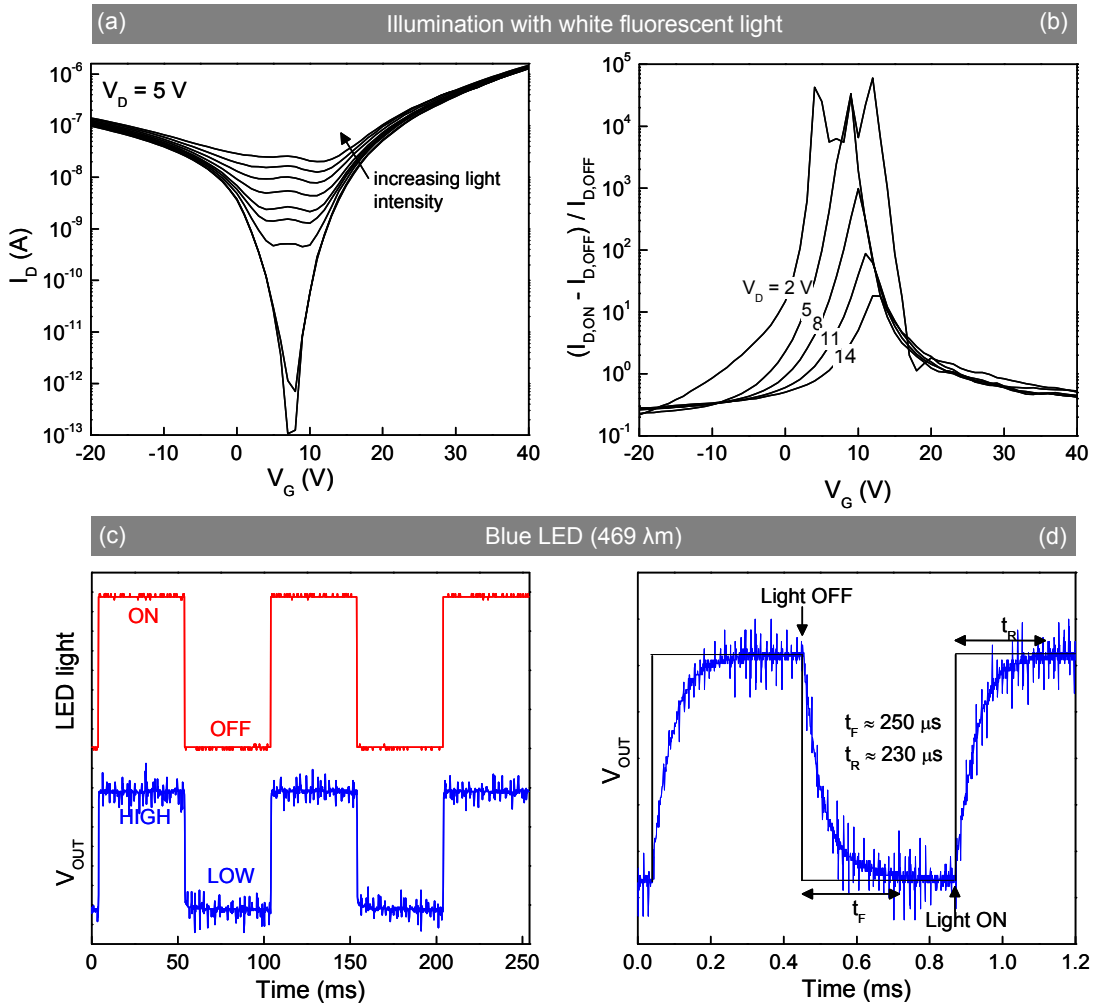


Fig. 5.9: (a) Photo-modulation of ambipolar transfer characteristics of [60]PCBM:OC_1C_{10}-PPV blend transistor by fluorescent white light. (b) Sensitivity dependence on V_D and V_G. (c) Dynamic modulation of photocurrent by a pulsed blue LED (λ_{peak} = 469 nm) at frequency 10 Hz. (d) Analysis of rise and fall times of transistor current modulated at 1.2 kHz.

Modulation of the drain current was observed also when illuminating the transistor with blue light of an LED (λ_{peak} = 469 nm). Driving the LED with a pulse generator allowed measuring the response of the LS-OFET to dynamic illumination.

Fig. 5.9(c) and (d) show the modulation of I_D vs. time at different pulsing frequencies of the light source. It is observed that the current modulation follows the light signal at frequencies up to several hundred Hz, but for frequencies above 1 kHz [Fig. 5.9(d)], the rise (t_R) and fall (t_F) times of I_D become comparable to half of the period of the modulating signal. The combined rise and fall time t_T was found to be $t_T \approx 480\mu s$, which corresponds to an operating frequency of $f \approx 2kHz$. Slightly faster operating speeds of LS-OFETs based on the same semiconductor components have been reported previously.[2]

The reason for the much faster optical response time of the blend-based ambipolar transistors compared to the SQ1 based transistors has not yet been clarified. A possible explanation is a higher density of shallow trap states in the SQ1 material. We observe that the threshold voltage in the blend transistors shifts towards smaller $|V_G|$ by approximately 3 V in the hole and 1.5 V in the electron accumulation regime. The density of trapped photo-generated electrons and holes are calculated using equation 5.1: $\Delta n_{photo,e} \approx 3 \cdot 10^{10} cm^{-2}$ and $\Delta n_{photo,h} \approx 1.5 \cdot 10^{10} cm^{-2}$. These photo-generated charges are trapped before additional charges contribute to the transistor current and a delay (t_R) of the current increase is observed. When the light is switched off, the trapped charges are slowly released, causing a prolongation (t_F) of the observed photocurrent. However the differences in trap densities and related threshold voltage shifts between the two material systems seem too small to explain such significant frequency limitations in the SQ1 devices. The difference between the two material systems could also be related to the higher charge carrier mobility and a shorter exciton diffusion path until charge separation occurs at the heterojunction in the blend transistors.

In conclusion, it is worth emphasizing that ambipolar LS-OFETs generally suffer much less from the slow photovoltaic-type light response, which is typically observed in unipolar LS-OFETs.[21,22] For example, in p-type unipolar devices photo-generated electrons are trapped near the source electrode when the transistor is turned on.[21] The resulting threshold voltage shift for majority carrier accumulation facilitates an additional photocurrent, but with long response times due to the slow charging and discharging of the trap states.[30] In ambipolar devices however, both holes and electrons are transported to and extracted through the electrodes, and thus contribute

to the photocurrent. These devices are less affected by charge carrier trapping and can therefore operate at higher modulation frequencies.

It is also interesting to note that light sensing material systems like the ones discussed here could enable facile fabrication of colour sensing arrays based solely on LS-OFETs. The characteristic absorption of different materials would also be a useful asset to the utilization of various frequency bands in optoelectronic circuits, where the sensing and switching functionality is combined in a single type of device, i.e. LS-OFETs.

5.4.2. Complementary-like integrated circuits

In order to demonstrate the potential of ambipolar semiconductors for application in organic electronics, we fabricated complementary-like inverters comprising two SQ1 based transistors [Fig. 5.10(b) inset]. Due to the well balanced hole and electron currents in the transistors, the inverter's output characteristics [Fig. 5.10(a)] exhibit insufficient "pull-up" and "pull-down" in the low and the high input state, respectively. This dependence of V_{OUT} for small and large values of V_{IN} is not observed in complementary inverters.[35] It is a direct consequence of the fact that an ambipolar transistor operates like a parallel circuit of an n- and a p-type transistor. Hence there is always leakage current flowing through the inverter, as neither transistor is ever fully switched off.[17,36] Despite this effect we observe symmetric output curves with high gain (15) and wide noise margins, approximately 50 % of the maximum theoretical value. The gain value compares favourably with values reported for other complementary-like inverters based on ambipolar organic semiconductors.[36] It is to be noted that the semiconductor was applied without patterning to the whole substrate and no post-treatment was performed on the films following deposition from solution. The inverter's gain and noise margins are significantly better than results obtained typically from unipolar inverters based on materials of superior charge carrier mobility.[37]

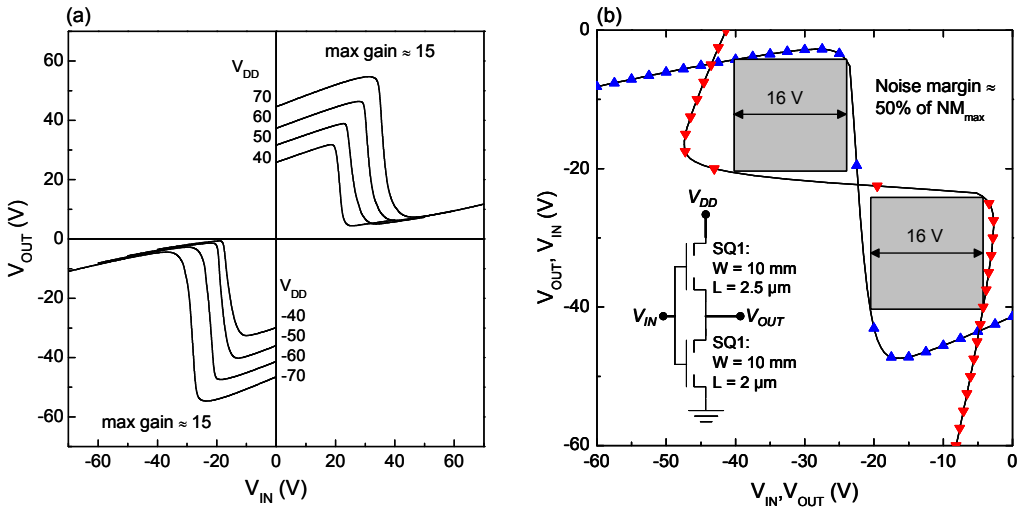


Fig. 5.10: (a) Output curves of a complementary-like voltage inverter based on two ambipolar SQ1 transistors connected according to the schematic shown in the inset in (b). The inverter was measured in the 1st and the 3rd quadrant. (b) Graphical representation of noise margins.

5.5. Outlook

In this part of my work two ambipolar organic semiconductor systems (Squaraines and OC_1C_{10}-PPV:[60]PCBM) have been shown to be great candidates for application in light sensing organic field-effect transistors. Under certain biasing conditions illumination can be used as a fourth "terminal" to control the transistor current, besides source, drain and gate electrodes. In fact this "dual gate" (response to light and/or electric input signal) functionality of LS-OFETs enables the fabrication of optoelectronic logic gates in a single device structure. Moreover, the possible combination of light sensing with internal amplification makes light sensing transistors an attractive alternative to conventional photodiodes. Their potential advantages include, in principle, higher sensitivity and lower dark currents. LS-OFETs with ambipolar characteristics offer an additional advantage over unipolar phototransistors. Their ability to transport both, holes and electrons, reduces charge trapping inside the semiconductor that could cause slow charging and discharging of the film. Hence ambipolar light-sensing OFETs are expected to exhibit a faster photoresponse than unipolar devices. Furthermore, thanks to the individual absorption spectra of different organic material systems investigated here, the fabrication of colour-sensitive light sensing arrays can be envisioned. Although the performance in terms of sensitivity and response time are yet to be optimized, the novel infrared light-sensing ability of the SQ1 based LS-OFETs is particularly interesting for application in low-cost organic optical sensors.

Furthermore, the solution processed ambipolar OFETs are employed in voltage inverters to demonstrate the superior properties of complementary-like logic compared to unipolar logic, in terms of noise margin, power consumption and signal gain. These findings encourage the use of ambipolar organic semiconductors for the facile implementation of power saving and low cost complementary-like organic logic.

Reference list:

1 Crone, B. *et al.* Large-scale complementary integrated circuits based on organic transistors. *Nature* **403**, 521-523 (2000).

2 Anthopoulos, T. D. Electro-optical circuits based on light-sensing ambipolar organic field-effect transistors. *Appl. Phys. Lett.* **91**, 113513-113513 (2007).

3 Anthopoulos, T. D., Wöbkenberg, P. H. & Bradley, D. D. C. Light-sensing ambipolar organic transistors for optoelectronic applications. *Organic Optoelectronics and Photonics III* **6999**, 69990-69997 (2008).

4 F. Cicoira & C. Santato. Organic Light Emitting Field Effect Transistors: Advances and Perspectives. *Adv. Funct. Mater.* **17**, 3421-3434 (2007).

5 Smits, E. C. P. *et al.* Near-infrared light-emitting ambipolar organic field-effect transistors. *Adv. Mater.* **19**, 734-738 (2007).

6 Wöbkenberg, P. H. *et al.* Ambipolar organic transistors and near-infrared phototransistors based on a solution processable squarylium dye. (submitted).

7 Inganäs, O. *et al.* Recent progress in thin film organic photodiodes. *Synthetic Metals* **121**, 1525-1528 (2001).

8 Gang Yu, Jian Wang, Jon McElvain & Alan J. Heeger. Large-Area, Full-Color Image Sensors Made with Semiconducting Polymers. *Adv. Mater.* **10**, 1431-1434 (1998).

9 Saragi, T. P. I., Onken, K., Suske, I., Fuhrmann-Lieker, T. & Salbeck, J. Ambipolar organic phototransistor. *Optical Materials* **29**, 1332-1337 (2007).

10 Mi Yeon Cho *et al.* Highly Sensitive, Photocontrolled, Organic Thin-Film Transistors Using Soluble Star-shaped Conjugated Molecules. *Adv. Funct. Mater.* **18**, 2905-2912 (2008).

11 Rauch, T. *et al.* Near-infrared imaging with quantum-dot-sensitized organic photodiodes. *Nat Photon* **3**, 332-336 (2009).

12 Wodrich, M. D., Corminboeuf, C. & Schleyer, P. v. R. Systematic Errors in Computed Alkane Energies Using B3LYP and Other Popular DFT Functionals. *Org. Lett.* **8**, 3631-3634 (2006).

13 Srinivas, K. *et al.* Enhanced Diradical Nature in Oxyallyl Derivatives Leads to Near Infra Red Absorption: A Comparative Study of the Squaraine and Croconate Dyes Using Computational Techniques. *J. Phys. Chem. A* **111**, 3378-3386 (2007).

14 Basheer, M. C. *et al.* Design and synthesis of squaraine based near infrared fluorescent probes. *Tetrahedron* **63**, 1617-1623 (2007).

15 v. 5.0 (Theoretical Chemistry Institute, University of Wisconsin, Madison, 2001).

16 Horowitz, G., Hajlaoui, M. E. & Hajlaoui, R. Temperature and gate voltage dependence of hole mobility in polycrystalline oligothiophene thin film transistors. *J. Appl. Phys.* **87**, 4456-4463 (2000).

17 Meijer, E. J. *et al.* Solution-processed ambipolar organic field-effect transistors and inverters. *Nat.Mater.* **2**, 678-682 (2003).

18 J. K. J. van Duren *et al.* Relating the Morphology of Poly(p-phenylene vinylene)/Methanofullerene Blends to Solar-Cell Performance. *Adv. Funct. Mater.* **14**, 425-434 (2004).

19 Hoppe, H. & Sariciftci, N. S. Morphology of polymer/fullerene bulk heterojunction solar cells. *Journal of materials chemistry* **16**, 45-61 (2006).

20 Kang, S. J. *et al.* Ambipolar organic thin-film transistors using C60/pentacene structure: Characterization of electronic structure and device property. *Appl. Phys. Lett.* **87**, 233502 (2005).

21 Noh, Y.-Y. *et al.* Effect of light irradiation on the characteristics of organic field-effect transistors. *J. Appl. Phys.* **100**, 094501 (2006).

22 Noh, Y.-Y., Kim, D.-Y. & Yase, K. Highly sensitive thin-film organic phototransistors: Effect of wavelength of light source on device performance. *J. Appl. Phys.* **98**, 074505 (2005).

23 Noh, Y.-Y. & Kim, D.-Y. Organic phototransistor based on pentacene as an efficient red light sensor. *Solid-State Electronics* **51**, 1052-1055 (2007).

24 Hu, Y., Dong, G., Liu, C., Wang, L. & Qiu, Y. Dependency of organic phototransistor properties on the dielectric layers. *Appl. Phys. Lett.* **89**, 072108 (2006).

25 Hamilton, M. C., Martin, S. & Kanicki, J. Thin-film organic polymer phototransistors. *Electron Devices, IEEE Transactions on* **51**, 877-885 (2004).

26 Cantatore, E. & Meijer, E. J. in *Solid-State Circuits Conference, 2003. ESSCIRC '03. Proceedings of the 29th European.* 29-36.

27 Chaji, G., Nathan, A. & Pankhurst, Q. Merged phototransistor pixel with enhanced near infrared response and flicker noise reduction for biomolecular imaging. *Appl. Phys. Lett.* **93**, 203504 (2008).

28 Thokchom Birendra Singh, Robert Koeppe, Niyazi Serdar Sariciftci, Mauro Morana & Christoph J. Brabec. Monitoring the Channel Formation in Organic Field-Effect Transistors via Photoinduced Charge Transfer. *Adv. Funct. Mater.* **19**, 789-795 (2009).

29 Wasapinyokul, K., Milne, W. I. & Chu, D. P. Photoresponse and saturation behavior of organic thin film transistors. *J. Appl. Phys.* **105**, 024509 (2009).

30 Kang, H.-S., Choi, C.-S., Choi, W.-Y., Kim, D.-H. & Seo, K.-S. Characterization of phototransistor internal gain in metamorphic high-electron-mobility transistors. *Appl. Phys. Lett.* **84**, 3780-3782 (2004).

31 Marciniak, H. *et al.* Ultrafast Exciton Relaxation in Microcrystalline Pentacene Films. *Phys. Rev. Lett.* **99**, 176402 (2007).

32 Yang, Y. S. *et al.* Deep-level defect characteristics in pentacene organic thin films. *Appl. Phys. Lett.* **80**, 1595-1597 (2002).

33 Gu, G., Kane, M. G., Doty, J. E. & Firester, A. H. Electron traps and hysteresis in pentacene-based organic thin-film transistors. *Appl. Phys. Lett.* **87**, 243512 (2005).

34 P. W. M. Blom, V. D. Mihailetchi, L. J. A. Koster & D. E. Markov. Device Physics of Polymer:Fullerene Bulk Heterojunction Solar Cells. *Adv. Mater.* **19**, 1551-1566 (2007).

35 Gundlach, D. J. *et al.* High mobility n-channel organic thin-film transistors and complementary inverters. *J. Appl. Phys.* **98**, 064502-064508 (2005).

36 Singh, T. B. Organic inverter circuits employing ambipolar pentacene field-effect transistors. *Appl. Phys. Lett.* **89**, 033512- (2006).

37 Smith, J. *et al.* High-performance organic integrated circuits based on solution processable polymer-small molecule blends. *Appl. Phys. Lett.* **93**, 253301-253303 (2008).

Chapter 6: Fabrication of Organic Transistors by Interlayer Lithography

The patterning of organic materials into layers of electroactive and passive components remains a major hurdle for their large scale implementation into electronic applications. The industry requires methodologies that provide high throughput, high manufacturing yield and which employ low cost equipment. Interlayer lithography is proposed for the patterning of organic conducting electrodes (PEDOT:PSS) in organic field-effect transistors. It builds on the existing expertise and equipment of photolithography, and presents a simplified method that does not significantly affect the optoelectronic properties of the patterned organic material. High performance p-channel and ambipolar OFETs are demonstrated employing diF-TESADT and [60]PCBM as organic semiconductors, respectively.

6.1. Introduction

Crucial to the advancement of organic electronics to an industrial production scale is the availability of adequate technologies for patterning the various device components in 3-D integrated structures. For high throughput, high manufacturing yield and low cost fabrication of organic electronic devices the industry requires techniques that will enable the fast realization of high resolution patterns over large areas, on various types of substrates including rigid glass and flexible plastics. Such technologies should require minimal equipment expenditure and cause negligible impact on the optoelectronic properties of the electroactive materials.

Printing based patterning methods such as inkjet printing,[1] offset printing,[2] and spray printing[3] are very attractive because of their simplicity and good compatibility with soluble organic materials, but resolution limitations (~10 μm) still remain a main technology bottleneck. Enhanced pattern resolutions have been achieved by soft lithography[4-6] and stamping methods[7] down to several micrometers or submicrometer scales, but the prepatterning of Si mold and the consequent polydimethylsiloxane (PDMS) transfer often need to be assisted by conventional photolithography or e-beam lithography. Conventional photolithography,[8-11] originally designed for patterning of inorganic materials, has also been demonstrated for the patterning of organic electrodes with sub-micrometer resolution.[8] Relatively many process steps and solvent-induced damage to the organic electrodes have been reported as some drawbacks of this technique.[8] In the meantime, orthogonal solvents, which do not dissolve the organic materials, have been developed,[8] rendering photolithography suitable for organic patterning. Recently, Huang *et al.* have proposed a further simplified photolithographic method for patterning organic PEDOT:PSS (poly(3,4-ethylendioxythiophene):poly(styrenesulfonate)) electrodes, namely interlayer lithography.[12] Thus, the photolithographic tool still possesses a great potential for patterning of organic materials, in particular with regard to its high-throughput parallel nature, its scalability to large area substrates and its use of established equipment and expertise.

In addition to organic semiconductors, flexible electrodes are also of great technological importance for the realisation of high performance plastic electronics.[13] Various materials such as poly(3,4-ethylendioxythiophene)-based conducting

polymers,[13,14] carbon nanotubes,[15] graphenes,[16] and amorphous metal oxides[17] have been widely investigated in order to find a replacement for the conventional indium tin oxide (ITO) electrodes, which generally suffer from bending cracks and bear increasing material cost.[13] Among them, poly(3,4-ethylendioxythiophene):poly(styrenesulfonate) (PEDOT:PSS) has been recognized as one of the most promising alternative electrodes owing to its high flexibility, good compatibility with other organic materials, competitive electrical and optical properties, and cost-efficient solution processibility[18-20] and thus, many attempts have been made to implement high performance organic devices on plastic substrates with PEDOT:PSS electrodes.[12,18-21]

Here the method developed by Huang *et al.*[12] is employed to photolithographically pattern the recently released high conductivity PEDOT:PSS (Clevios PH500). In the previous work, patterning of PEDOT:PSS with feature size resolution down to 2–5 μm has been accomplished and has been applied in polymer light-emitting diodes, with millimetre scale PEDOT:PSS anode patterns.[12] In this study organic field-effect transistors (OFETs) with PEDOT:PSS electrodes patterned by interlayer photolithography are investigated.

This chapter discusses results of my work in collaboration with Leem Dong Seok, who is currently a Post-Doctoral researcher in the group of John de Mello in the Department of Chemistry at Imperial College London. While his part of the work focused on the optimization and characterization of the patterning method to achieve highest resolution and high conductivities of the PEDOT:PSS films, my work focused on the fabrication of field-effect transistors, circuits and their characterization.

6.2. Electrode patterning by Interlayer Lithography

Fig. 6.1 shows a schematic illustration of the interlayer lithography patterning processes. First, a conventional negative tone SU 8-2 photoresist (PR) is spin-coated on the substrate [Fig. 6.1(a)]. Second, the PR is exposed through either a photo mask or a metal mask by a UV light source [Fig. 6.1(b)], causing a subsequent cross-linking reaction in the UV exposed PR regions [Fig. 6.1(c)]. Third, PEDOT:PSS is spin-coated on top of the UV exposed PR [Fig. 6.1(c)]. Finally, the PEDOT:PSS coated

substrate is transferred to a developer solution, which dissolves the uncross-linked PR region and simultaneously removes the PEDOT:PSS above, leaving the patterned PEDOT:PSS layer on the cross-linked PR [Fig. 6.1(d)].

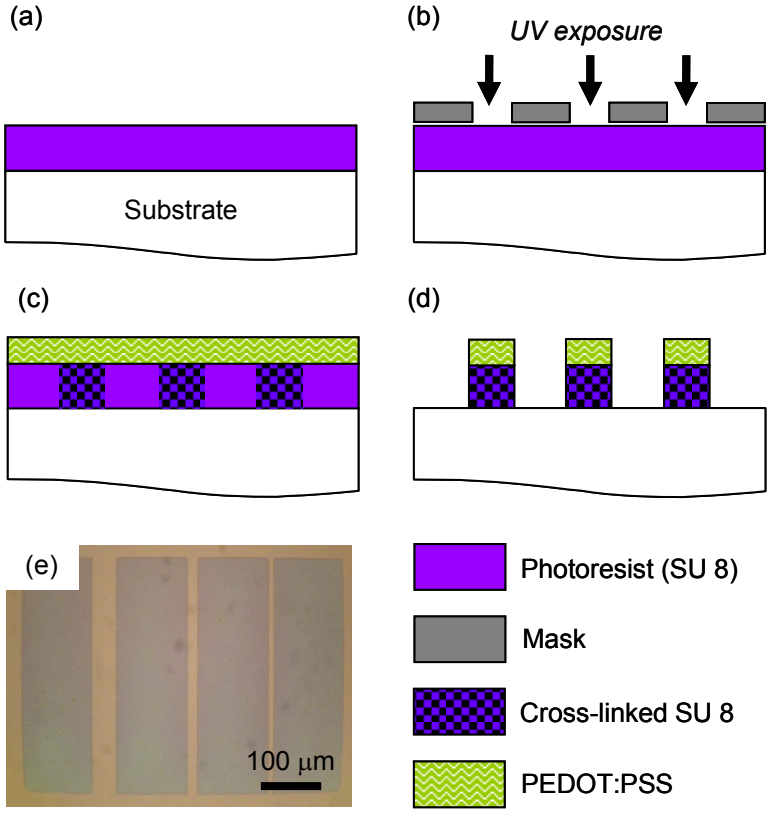


Fig. 6.1 Interlayer lithography process: (a) SU 8-2 photoresist is spin coated on substrate (glass or PET). (b) PR is exposed to UV through photomask, cross linking of PR in exposed regions occurs. (c) Target material (here PEDOT:PSS) is spin coated. (d) Sample is immersed in developer solution to remove uncross-linked PR, leaving the pattern of PEDOT:PSS behind. (e) Photograph of patterned PEDOT:PSS fields on glass, minimum gap width is 10 μm.

Unlike in conventional photolithography, the final structure patterned by this technique still possesses an intermediate PR layer between PEDOT:PSS and the substrate (hence the name 'interlayer lithography'). The technique eliminates the conventional pre-development step of the PR and thereby simplifies the lithography process. It is known that the SU 8-2 PR itself has good thermal, chemical and mechanical stability.[22] The optical microscopy image in Fig. 6.1(e) exhibits an example of the patterned PEDOT:PSS on a glass substrate with 150 μm width and 50, 20, and 10 μm gaps, but it does not reflect the minimum feature sizes achieved by this method. A further reduced pattern gap of 4 μm has been achieved in PEDOT:PSS films[23] and line widths of 2-5 μm were demonstrated in the previous report.[12] The typical thickness of SU 8-2 PR (1.4 μm) was reduced to 230 ± 20 nm by adding a SU 8 thinner, in order to minimize the impact of the profile on the formation of

subsequently spin coated films. The total heights of the patterned PEDOT:PSS fields on the PR interlayer were measured to be 350 ± 20 nm including the 120 nm-thick PEDOT:PSS film.[23]

To investigate possible physical property changes of the PEDOT:PSS during the patterning process, the conductivities of films made on glass and poly(ethylene terephthalate) (PET) substrates are measured and compared for each step (data not shown). The PEDOT:PSS films directly coated on either glass or PET substrate without SU 8-2 PR interlayer exhibit typically high conductivities of 415–421 S/cm. We observed that the patterned PEDOT:PSS films by interlayer lithography still maintain high conductivities of ca. 360 S/cm, which is higher than recently reported values for the same PEDOT:PSS (PH500) formula.[20,24-26]

6.3. OFETs and their integrated circuits

We fabricated PEDOT:PSS array patterns on glass and PET substrates by interlayer lithography for use as source and drain electrodes in OFETs, as shown in Fig. 6.2(a) and (b), respectively. The patterned PEDOT:PSS electrodes feature five different channel lengths in the range of 20 μm to 100 μm and three different channel widths of 500, 1000, and 2000 μm.

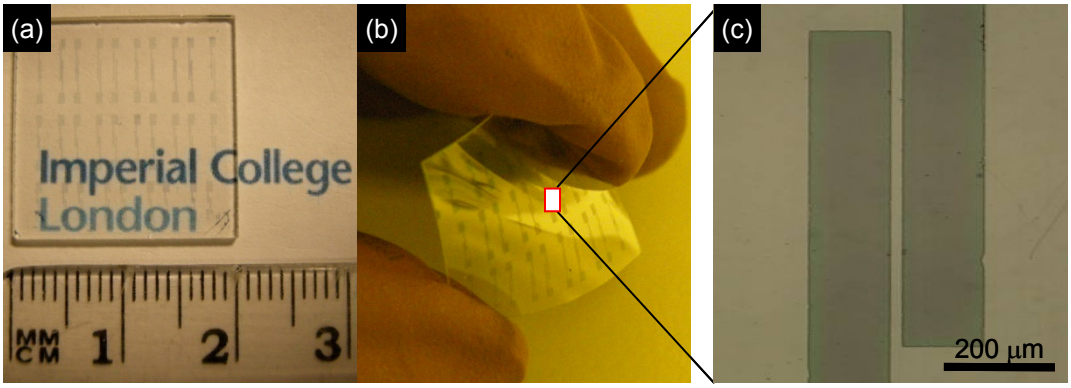


Fig. 6.2 Array of PEDOT:PSS source and drain electrodes patterned on (a) glass and on (b) PET. (c) Optical micrograph of patterned source-drain contacts with L = 20 μm on glass.

The enlarged image [Fig. 6.2(c)] clearly shows a well defined source and drain pattern with a channel length of 20 μm and a width of 500 μm. We note that the PEDOT:PSS patterning for OFET demonstration was carried out by UV exposure

through an existing metal mask rather than a photo mask. A complete OFET structure is schematically depicted in Fig. 6.3(a). OFETs were fabricated with the p- and n-type organic semiconductors 8-difluoro-5,11-bis(triethylsilylethynyl)anthradithiophene (diF-TESADT)[27] (blended at a ratio 2:1 with poly(triarylamine) (PTAA)) and methanofullerene [6,6]-phenyl-C61-butyric acid methylester ([60]PCBM)[28], respectively. The molecular structures of these materials are shown in Fig. 6.4. For instance, Fig. 6.3(b) exhibits a polarized microscopy image of a diF-TESADT:PTAA film on a patterned PEDOT:PSS electrode on glass, showing large crystal grains on both PEDOT:PSS contact and glass substrate.

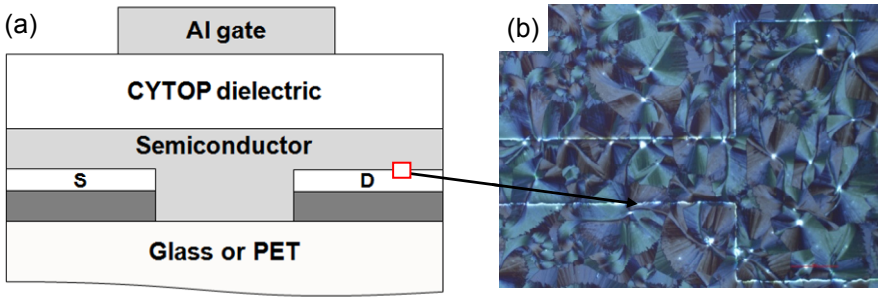


Fig. 6.3: (a) Schematic representation of transistor architecture and (b) optical micrograph of crystalline diF-TESADT:PTAA film on PEDOT:PSS contact and glass substrate.

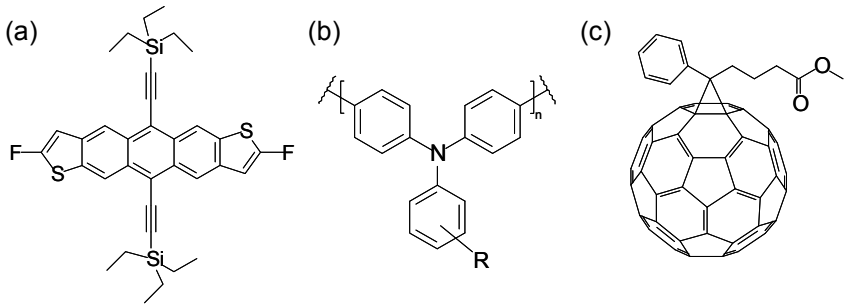


Fig. 6.4: Chemical structures of (a) diF-TESADT, (b) PTAA and (c) [60]PCBM semiconductors.

Device fabrication was completed by deposition of a dielectric layer of Cytop and the thermal evaporation of a top Al gate electrode. Ultimately, this last step is expected to be replaced by a second lithography process to pattern the gate electrode. Typical transfer and output characteristics are shown in Fig. 6.5 for transistors with PEDOT:PSS contacts patterned by interlayer lithography on glass, based on diF-TESADT:PTAA [Fig. 6.5(a-b)] and [60]PCBM [Fig. 6.5(c-d)]. In the case of the hole transporting device based on diF-TESADT:PTAA we observe negligible hysteresis between forward and backward scans, a current on/off ratio of 10^3 and a high hole

mobility of 0.25 - 1 cm^2/Vs. From the output curves it becomes evident that the device exhibits injection limited characteristics, as indicated by the nonlinear current increase in the low drain voltage (V_D) regime. This feature is attributed to a non-ohmic resistance at the contact between injecting electrode and organic semiconductor, the origin of which is most likely the energy barrier for hole injection from the Fermi level of the PEDOT:PSS electrode ($E_{F(PEDOT:PSS)} \approx 5.1$ eV) into the highest occupied molecular orbital (HOMO) of diF-TESADT (5.35 eV)[29]. A similar problem occurs for the injection of electrons in [60]PCBM devices, as evident from the output curves in Fig. 6.5(d). The lowest unoccupied molecular orbital (LUMO) of [60]PCBM is 3.7 eV resulting in a significant energy barrier for electrons of approximately 1.4 eV.

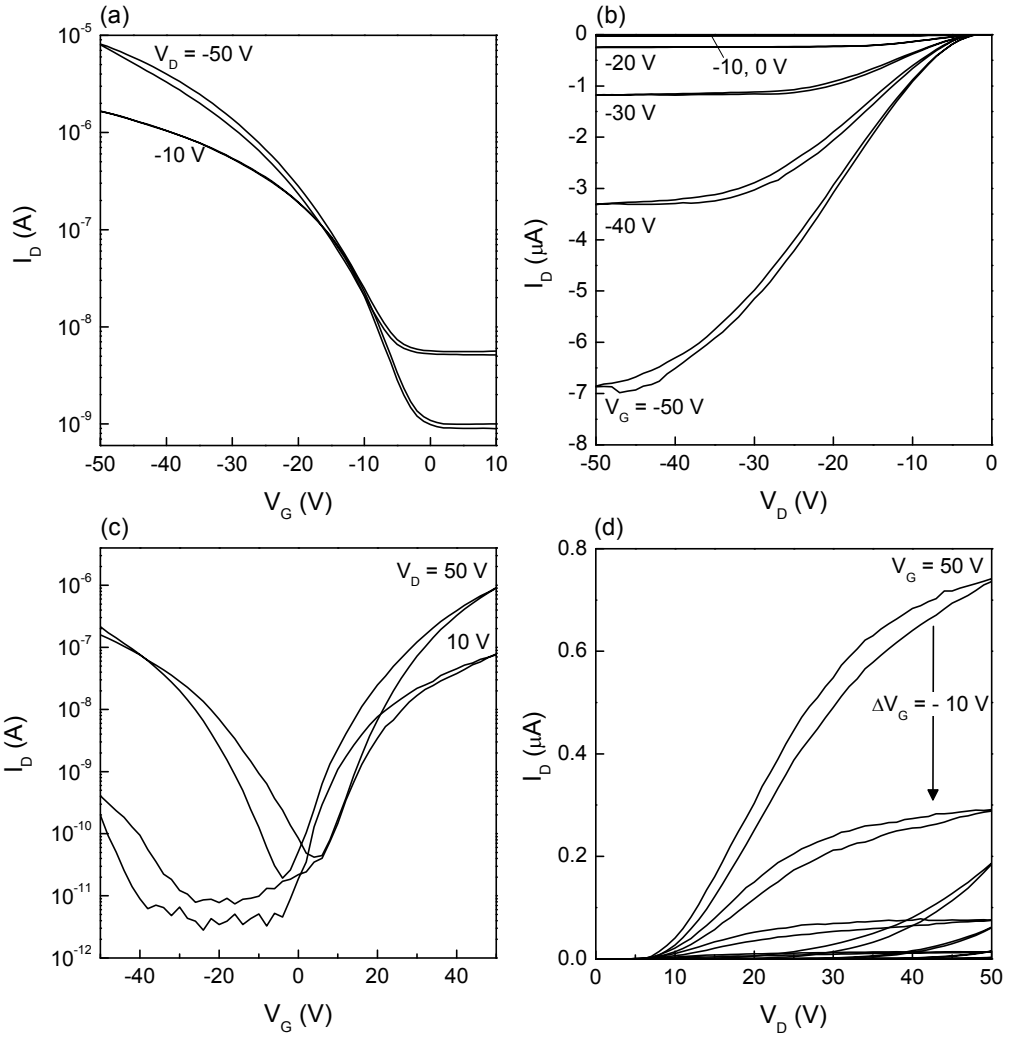


Fig. 6.5: Transfer and output characteristics of field-effect transistors with PEDOT:PSS source-drain electrodes patterned on glass by interlayer lithography, employing (a-b) diF-TESADT:PTAA (L = 30 µm, W = 1 mm, C_i = 2 nF/cm^2) and (c-d) [60]PCBM (L = 50 µm, W = 1 mm, C_i = 2 nF/cm^2) as semiconductors, respectively.

However, the position of the Fermi-level of the conducting PEDOT:PSS electrodes also allows the injection of holes into the HOMO level of [60]PCBM (6.1 eV). Hence the device exhibits ambipolar characteristics and can be operated in the hole ($V_G << 0$ V) and/or the electron ($V_G >> 0$ V) accumulation regime, as demonstrated in the transfer curve of Fig. 6.5(c). Hole injection into [60]PCBM is limited by an energy barrier of approximately 1 eV, and is therefore only observed at large $|V_G - V_D|$. The observation that hole injection is more difficult than electron injection despite a smaller energy offset was explained by Veenstra *et al.*[30] and van Duren *et al.*[31] for the case of gold electrodes. They demonstrated a shift of the metal workfunction towards the LUMO level due to the presence of dipoles at the [60]PCBM-Au interface. This explanation could also be valid in the case of PEDOT:PSS contacts, although no experimental proof can be given at this point. Although the hole field-effect mobility (0.005 cm^2/Vs) is lower by one order of magnitude compared to the electron mobility (0.05 cm^2/Vs), the observations made here are in good agreement with previous reports on ambipolar charge transport in [60]PCBM.[28] To our knowledge, this is the first demonstration of ambipolar charge transport in [60]PCBM based transistors employing solution processed, transparent PEDOT:PSS source and drain electrodes. A summary of the performance parameters of [60]PCBM and diF-TESADT:PTAA based transistors on glass substrates is given in Table 6.1.

Table 6.1: Summary of performance parameters of [60]PCBM and diF-TESADT:PTAA based transistors

	PCBM		diF-TESADT:PTAA
	electrons	holes	holes
V_T (V)	16	-10	- 10
μ_{sat} (cm^2/Vs)	0.05	0.005	0.25
S (V/dec)	5.5	6.5	8
on/off	10^4	10^3	10^3

Similar transistor characteristics were obtained with patterned electrodes on PET substrates, although in some cases with lower mobility, in agreement with previous reports.[27] We note that the characteristics of devices employing PEDOT:PSS electrodes that were patterned by interlayer lithography are comparable to results reported on diF-TESADT:PTAA[32] and [60]PCBM[28] based transistors with gold electrodes. The work function of gold is very similar to that of PEDOT:PSS (≈ 5.1

eV). Hence the results demonstrate the suitability of the interlayer lithography technique for patterning of solution processable PEDOT:PSS electrodes and their successful use in transistor devices. The large profile height (≈ 350 nm) of the suspended electrodes due to the underlying photoresist interlayer does not seem to significantly affect the transistor operation (i.e. carrier injection and transport). Moreover, the high transparency of the patterned PEDOT:PSS electrodes is of great significance for the development of transparent flexible electronics.

In an attempt to demonstrate the applicability of our transistors to more complex electronic circuits we fabricated complementary voltage inverters comprising a hole transporting and an electron transporting transistor. The circuit schematic is illustrated in Fig. 6.6(a) and the transfer characteristics of the circuit in quasi-static operation at various supply voltages (V_{DD}) are shown in Fig. 6.6(b). The inverter displays the correct logic function with maximum signal gain ≈ 16. The noise margin was approximately 50 % of the maximum theoretical value ($NM_{max} = V_{DD}/2$), and is comparable to noise margins reported previously for solution processed complementary inverters.[33]

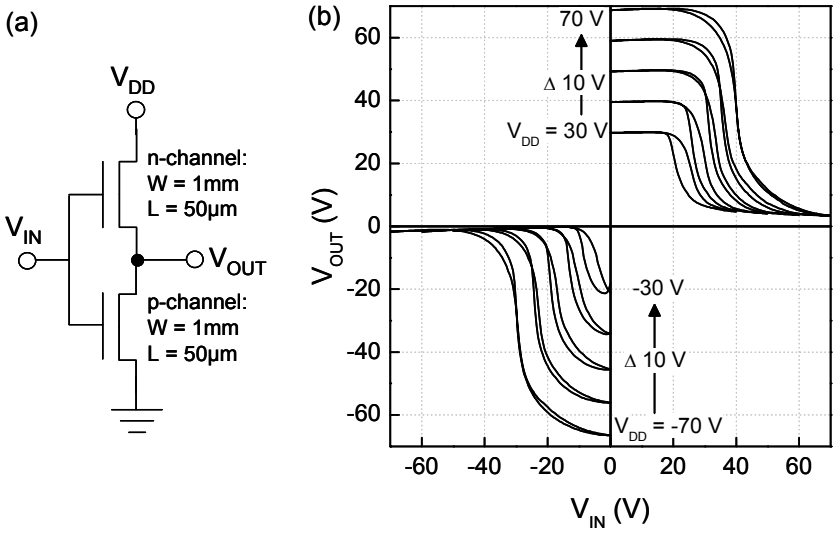


Fig. 6.6: (a) Schematic representation of complementary inverter circuit and (b) its output characteristics in quasi-static operation in the first and the third quadrant.

6.4. Outlook

The issue of materials patterning (i.e. conductors, insulators, semiconductors) imposes significant challenges for their large scale implementation into organic electronics. More precisely the issues of patterning speed, resolution and degradation

of the material properties have to be addressed. In this context interlayer lithography is considered a useful technique that benefits from the high resolution patterning of conventional photolithography in a simplified process. We employed it successfully to pattern organic conducting PEDOT:PSS source-drain electrodes for the use in organic field-effect transistors, which exhibit the same level of performance as analogue devices with thermally deposited gold electrodes. Furthermore, ambipolar transport is observed for the first time in [60]PCBM based transistors with polymeric source-drain electrodes. It is anticipated that the patterning technique could easily be scaled up and applied to the fabrication of large scale integrated circuits. The method could also be used for patterning of organic semiconductors and for the fabrication of transparent, flexible organic electronics.

Reference list:

1 Sirringhaus, H. *et al.* High-Resolution Inkjet Printing of All-Polymer Transistor Circuits. *Science* **290**, 2123-2126 (2000).

2 Zielke, D. *et al.* Polymer-based organic field-effect transistor using offset printed source/drain structures. *Appl. Phys. Lett.* **87**, 123508 (2005).

3 Jang, Y. *et al.* Patterning the organic electrodes of all-organic thin film transistors with a simple spray printing technique. *Appl. Phys. Lett.* **89**, 183501 (2006).

4 R. Parashkov, E. Becker, T. Riedl, H.-H. Johannes & W. Kowalsky. Microcontact Printing as a Versatile Tool for Patterning Organic Field-Effect Transistors. *Adv. Mater.* **17**, 1523-1527 (2005).

5 Cosseddu, P. & Bonfiglio, A. Soft lithography fabrication of all-organic bottom-contact and top-contact field effect transistors. *Appl. Phys. Lett.* **88**, 023506 (2006).

6 Takakuwa, A., Ikawa, M., Fujita, M. & Yase, K. Micropatterning of Electrodes by Microcontact Printing Method and Application to Thin Film Transistor Devices. *Japanese Journal of Applied Physics* **46**, 5960-5963 (2007).

7 Li, D. & Guo, L. J. Organic thin film transistors and polymer light-emitting diodes patterned by polymer inking and stamping. *Journal of Physics D: Applied Physics*, 105115 (2008).

8 Priscilla G. Taylor *et al.* Orthogonal Patterning of PEDOT:PSS for Organic Electronics using Hydrofluoroether Solvents. *Adv. Mater.* **21**, 2314-2317 (2009).

9 M. Halik *et al.* Polymer Gate Dielectrics and Conducting-Polymer Contactsfor High-Performance Organic Thin-Film Transistors. *Adv. Mater.* **14**, 1717-1722 (2002).

10 Chan, J. R., Huang, X. Q. & Song, A. M. Nondestructive photolithography of conducting polymer structures. *J. Appl. Phys.* **99**, 023710 (2006).

11 DeFranco, J. A., Schmidt, B. S., Lipson, M. & Malliaras, G. G. Photolithographic patterning of organic electronic materials. *Organic electronics* **7**, 22-28 (2006).

12 Huang, J. *et al.* Patterning of organic devices by interlayer lithography. *Journal of materials chemistry* **17**, 1043-1049 (2007).

13 P. A. Levermore, L. Chen, X. Wang, R. Das & D. D. C. Bradley. Fabrication of Highly Conductive Poly(3,4-ethylenedioxythiophene) Films by Vapor Phase Polymerization and Their Application in Efficient Organic Light-Emitting Diodes. *Adv. Mater.* **19**, 2379-2385 (2007).

14 L. Groenendaal, F. Jonas, D. Freitag, H. Pielartzik & J. R. Reynolds. Poly(3,4-ethylenedioxythiophene) and Its Derivatives: Past, Present, and Future. *Adv. Mater.* **12**, 481-494 (2000).

15 Qing Cao & John A. Rogers. Ultrathin Films of Single-Walled Carbon Nanotubes for Electronics and Sensors: A Review of Fundamental and Applied Aspects. *Adv. Mater.* **21**, 29-53 (2009).

16 Kim, K. S. *et al.* Large-scale pattern growth of graphene films for stretchable transparent electrodes. *Nature* **457**, 706-710 (2009).

17 Nomura, K. *et al.* Room-temperature fabrication of transparent flexible thin-film transistors using amorphous oxide semiconductors. *Nature* **432**, 488-492 (2004).

18 Huang, J., Wang, X., deMello, A. J., deMello, J. C. & Bradley, D. D. C. Efficient flexible polymer light emitting diodes with conducting polymer anodes. *Journal of materials chemistry* **17**, 3551-3554 (2007).

19 Seok-In Na, Seok-Soon Kim, Jang Jo & Dong-Yu Kim. Efficient and Flexible ITO-Free Organic Solar Cells Using Highly Conductive Polymer Anodes. *Adv. Mater.* **20**, 4061-4067 (2008).

20 Zhou, Y. *et al.* Investigation on polymer anode design for flexible polymer solar cells. *Appl. Phys. Lett.* **92**, 233308 (2008).

21 D. Hohnholz, H. Okuzaki & A. G. MacDiarmid. Plastic Electronic Devices Through Line Patterning of Conducting Polymers. *Adv. Funct. Mater.* **15**, 51-56 (2005).

22 Agirregabiria, M. *et al.* Fabrication of SU-8 multilayer microstructures based on successive CMOS compatible adhesive bonding and releasing steps. *Lab on a Chip* **5**, 545-552 (2005).

23 Dong-Seok, L. *et al.* Interlayer lithographic patterning of high conductivity PEDOT:PSS for organic field-effect transistors. (in preparation).

24 Colsmann, A., Stenzel, F., Balthasar, G., Do, H. & Lemmer, U. Plasma patterning of Poly(3,4-ethylenedioxythiophene):Poly(styrenesulfonate) anodes for efficient polymer solar cells. *Thin Solid Films* **517**, 1750-1752 (2009).

25 Ahlswede, E., Muhleisen, W., Wahi, M. W. b. M., Hanisch, J. & Powalla, M. Highly efficient organic solar cells with printable low-cost transparent contacts. *Appl. Phys. Lett.* **92**, 143307 (2008).

26 Piliego, C., Mazzeo, M., Cortese, B., Cingolani, R. & Gigli, G. Organic light emitting diodes with highly conductive micropatterned polymer anodes. *Organic electronics* **9**, 401-406 (2008).

27 Hamilton, R. *et al.* High-Performance Polymer-Small Molecule Blend Organic Transistors. *Adv. Mater.* **21**, 1166-1171 (2009).

28 Anthopoulos, T. D. *et al.* Ambipolar Organic Field-Effect Transistors Based on a Solution-Processed Methanofullerene. *Adv. Mater.* **16**, 2174-2179 (2004).

29 Day, J., Platt, A. D., Ostroverkhova, O., Subramanian, S. & Anthony, J. E. Organic semiconductor composites: Influence of additives on the transient photocurrent. *Appl. Phys. Lett.* **94**, 013306 (2009).

30 Veenstra, S. C., Heeres, A., Hadziioannou, G., Sawatzky, G. A. & Jonkman, H. T. On interface dipole layers between C60 and Ag or Au. *Appl. Phys. A: Mater. Sci. Process.* **75**, 661-666 (2002).

31 Duren, J. K. J. v. *et al.* Injection-limited electron current in a methanofullerene. *J. Appl. Phys.* **94**, 4477-4479 (2003).

32 Park, S. K., Mourey, D. A., Subramanian, S., Anthony, J. E. & Jackson, T. N. High-mobility spin-cast organic thin film transistors. *Appl. Phys. Lett.* **93**, 043301 (2008).

33 Wöbkenberg, P. H. *et al.* High mobility n-channel organic field-effect transistors based on soluble C60 and C70 fullerene derivatives. *Synthetic Metals* **158**, 468-472 (2008).

Chapter 7: Low-Voltage Organic Transistors and Circuits based on Self-Assembled Monolayer dielectrics

One of the main hurdles for the large scale implementation of organic field-effect transistors is their large operating voltages and the associated high power consumption. Both make them incompatible with battery powered, light weight applications, in which organic electronics are anticipated to be most competitive. Reducing the thickness of the gate dielectric with the help of (phosphonic acid) self-assembled monolayer dielectrics enables transistor operation at few volts. By means of this approach, high performance solution processed fullerene-based n-channel transistors and complementary inverter circuits are demonstrated, which operate at less than 2 Volts and exhibit low power consumption.

7.1. Introduction

A major drawback associated with most organic transistors and circuits reported to date is the high operating voltages, i.e. > 20 V.[1,2] In order to make organic electronics compatible with portable, i.e. battery powered applications the devices have to operate at much reduced voltages and preferably at < 5 V.

A possible approach to surmounting this problem has consisted of reducing the thickness of the gate dielectric. In theory, the amount of charge induced in the transistor channel is proportional to the geometrical capacitance of the gate dielectric (C_i), which in turn is inversely proportional to the dielectric thickness d as expressed by equation 7.1:[3]

$$C_i = \frac{\varepsilon \cdot \varepsilon_r}{d} \tag{7.1}$$

where ε is the dielectric constant and ε_r is the relative permittivity of the dielectric material. Successful demonstrations have involved the use of solution processable self-assembled monolayers (SAMs) as gate dielectrics. Ultra-thin SAM layers, in comparison to conventional dielectrics such as grown oxides or polymer films, yield increased geometrical capacitance (C_i) enabling the accumulation of high charge carrier densities at reduced gate bias. Reports commonly employ alkyltrichlorosilanes, as used by Collet *et al.*,[4] or alkylphosphonic acids, as used by Klauk *et al.*,[5] as part of the gate insulation layer. In the latter report, octadecylphosphonic acid (ODPA) was functionalized on oxidized aluminium gate electrodes. The majority of examples of low-voltage OFETs based on SAM dielectrics utilize evaporated organic semiconductors for the active layer. Demonstrations of solution processed semiconductors on SAM dielectrics are scarce.[6-8] This is mainly attributed to the difficulty in processing solutions of high mobility small molecule semiconductors onto methyl terminated monolayers (such as ODPA) due to the characteristically low and dispersive surface energy that prevents the formation of continuous thin films.[7] Low-voltage transistors on a self-assembled monolayer of docosyltrichlorosilane (DCTS) have been demonstrated with a solution processed polymer, poly(3-hexylthiophene) (P3HT), but with lower mobilities.[6]

In this chapter the problems related to solution processing of high mobility small molecule semiconductors on energetically unfavourable surfaces will be

investigated and results on solution processed low-operating voltage n-channel transistors will be presented. Fabrication of a solution processed low-voltage complementary inverter circuit is also demonstrated.

7.2. SAM based gate dielectrics

Self-assembled molecular gate dielectrics of ODPA (see Fig. 7.1(a) for molecular structure) were fabricated on 30 nm thick Aluminium gate electrodes, which were evaporated onto glass substrates employing shadow masks. The gate electrodes were first oxidised in oxygen plasma and then submerged in a 5 mM solution of ODPA in ethanol. Contact angle measurements were performed on Al-AlO_x surfaces before and after treatment. Fig. 7.1(b) displays images of a water droplet on the oxidized aluminium surface. It is evident that upon treatment with ODPA [Fig. 7.1(c)] the water contact angle (θ_C) changes from <40° to >105° degrees, clearly indicating the presence of the hydrophobic ODPA layer. Water contact angles in excess of 100° are typical for methyl-terminated SAMs.[5,9]

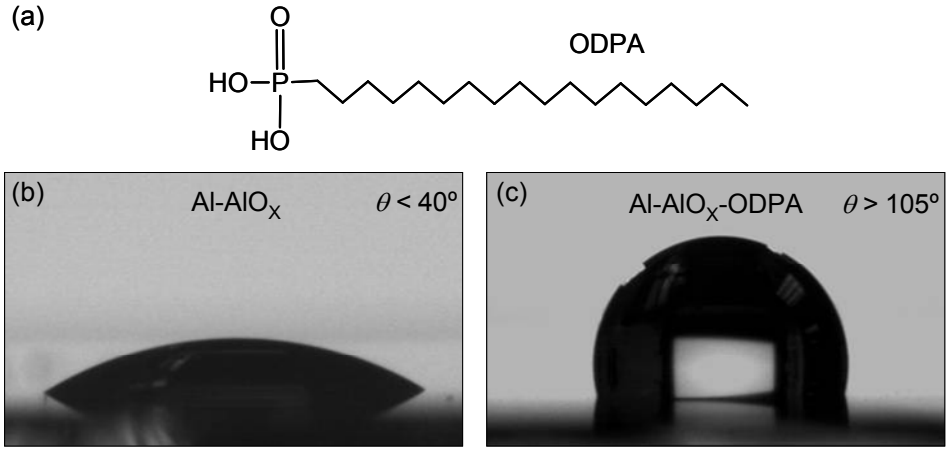


Fig. 7.1: (a) Molecular structure of octadecylphosphonic acid (ODPA). Water contact angle on Al-AlO_X electrode (b) before and (c) after treatment with ODPA.

Metal-insulator-metal diode structures [Fig. 7.2(a)] were fabricated for determining the leakage current and geometric capacitance (C_i) of the insulating layer before and after treatment. Fig. 7.2(b) shows the current density-voltage (*J-V*) characteristics measured for three diodes at different stages of the fabrication process. A striking observation is the drastic reduction in the leakage current upon treatment with ODPA. The current density through the SAM dielectric is typically 10^{-7} A/cm^2 at

an applied voltage of 1 V. At a dielectric thickness of < 10 nm, this corresponds to a field strength of > 1 MV/cm. Similar leakage current densities were reported at this field strength for 50 nm thin polymer dielectrics[10] and 100 nm of thermally grown SiO_2 on Si.[11] The measured geometric capacitance of the dielectric between the two metal electrodes was found to be in the range of 500-700 nF/cm^2 (obtained between 0.01 and 1 kHz). These results are in good agreement with data reported in the literature.[5,6] The capacitance increase by several orders of magnitude as compared to BCB (≈ 1.2 nF/cm^2) and SiO_2 (≈ 17 nF/cm^2) dielectrics is expected to yield a significant decrease in the operating voltage of the transistors.

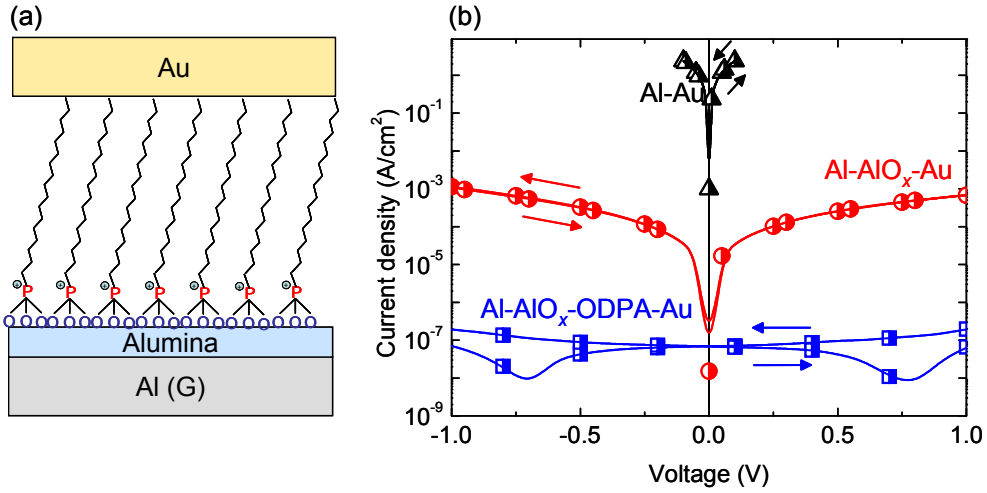


Fig. 7.2: (a) Schematic representation of metal-insulator-metal structures employed to measure the leakage currents at different stages of Al-AlO_X-SAM dielectric fabrication (b).

7.3. Surface energy and solution processing

Having established the suitability of AlO_X-ODPA structures as dielectrics, we have attempted to fabricate OFETs employing a number of soluble organic semiconductors [Fig. 7.5(a)]. Unfortunately, wetting of the Al-AlO_x-ODPA surface by several different semiconductor solutions proved to be very problematic, with only few exceptions. In order to study and understand the interplay between the surface properties of the dielectric and the semiconductor solutions a series of surface energy measurements were carried out employing a Krüss Drop Shape Analysis system.

7.3.1. Surface energy of hybrid dielectric

The dispersive and polar solid surface energy components of the Al-AlO_x-ODPA surface were calculated by measuring the contact angles of three different liquids (whose polar and dispersive components were known) on the solid surface. Here distilled water (γ^P = 46.4 mN/m, γ^D = 26.4 mN/m), diiodomethane (γ^P = 0 mN/m, γ^D = 50.8 mN/m) and ethylene glycol (γ^P = 21.3 mN/m, γ^D = 26.4 mN/m) were used, which formed contact angles of 107°, 68° and 85°, respectively [Fig. 7.3].[12]



Fig. 7.3: Contact angles of (a) water, (b) diiodomethane and (c) ethylene glycol on Al-AlO_X-ODPA.

Following the Owens-Wendt-Kaelble method, solid surface energy components can be extracted from a linear fit to equation 3.3, derived from the Owens-Wendt-Kaelble and Young's equations (sections 2.8.2 and 3.1.5).[13,14]

$$\frac{\gamma_L(\cos\theta+1)}{2\left(\gamma_L^D\right)^{1/2}} = \left(\gamma_S^P\right)^{1/2}\left(\frac{\gamma_L^P}{\gamma_L^D}\right)^{1/2} + \left(\gamma_S^D\right)^{1/2} \qquad (3.3)$$

where θ is the equilibrium contact angle made by each liquid on the solid surface; γ is the surface energy where superscripts D and P refer to the dispersive part and the polar part respectively. The subscripts L and S refer to the liquid and solid. The polar part and dispersive part of the surface energy of Al-AlO_x-ODPA were obtained to be 0.24 mN/m and 22.9 mN/m, respectively. This low and highly dispersive surface energy is attributed to the methyl-terminated alkyl chains of ODPA, which are expected to be incapable of polar interactions. Hence Van der Waals forces are assumed to dominate the interaction between this dielectric surface and the semiconductor solution. The slight polar contribution may be a result of the close proximity to the AlO_X surface, which features a high density of polar hydroxyl groups.

7.3.2. Liquid surface energy of organic semiconductor solutions

The polar and dispersive components of the liquid surface tension of the organic semiconductor solutions were calculated from contact angles of the solutions on two different solid surfaces (whose polar and dispersive surface energy components were known) using equations 3.7 and 7.2 also derived from the Owens-Wendt-Kaelble and Young's equations.

$$\gamma_L^D = \left(\frac{\gamma_L(\cos\theta_1 + 1)\left(\gamma_{S2}^P\right)^{1/2} - \gamma_L(\cos\theta_2 + 1)\left(\gamma_{S1}^P\right)^{1/2}}{2\left(\gamma_{S1}^D\gamma_{S2}^P\right)^{1/2} - 2\left(\gamma_{S2}^D\gamma_{S1}^P\right)^{1/2}} \right)^2 \tag{3.7}$$

$$\gamma_L^P = \gamma_L - \gamma_L^D \tag{7.2}$$

Here, the subscripts 1 and 2 refer to solids 1 and 2, respectively. The total surface energy of each liquid (γ_L), was measured from analysis of pendant drops of solutions. For example, Fig. 7.4 shows the images of pendant drops of 10 mg/ml F17-DOPF and [60]PCBM solutions in chlorobenzene. The drop shape was fitted by the Krüss Drop Shape Analysis system to calculate their volume and extract the total liquid surface tensions (see section 2.8.1).

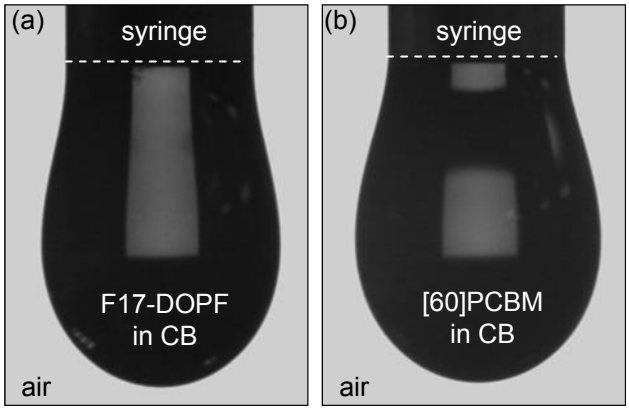


Fig. 7.4: Pendant drops of (a) F17-DOPF and (b) [60]PCBM in chlorobenzene solutions used to measure liquid surface tension.

As mentioned in 2.8.2 and 3.1.5 the two solid surfaces have to be chosen with care because large experimental error is observed when the liquid and solid surfaces are very different in terms of the type of interaction they are able to engage in.[13] However, if they exhibit very similar surface energy components, this yields low contact angles ($\theta < 10°$) that are difficult to measure accurately. The balance is therefore left to the experimenter to determine. In this work contact angles between 20° and 50° were considered acceptable. Most organic semiconductor solutions

formed contact angles within this range on HMDS treated Si/SiO_2 wafers with a homogeneous and reproducible surface energy of $\gamma_{SiO2\text{-}HMDS}$ = 34.2 mN/m (γ_S^P = 16.2 mN/m and γ_S^D = 18 mN/m) (see section 4.7.2.) and on the ODPA treated Al/AlO_X surface $\gamma_{AlOx\text{-}ODPA}$ = 23.1 mN/m (γ_S^P = 0.2 mN/m and γ_S^D = 22.9 mN/m). Using equation 3.7 and 7.2 the surface tension components of a variety of liquid semiconductor solutions (molecular structures shown in Fig. 7.5(a)) were calculated, as shown in Table 7.1.

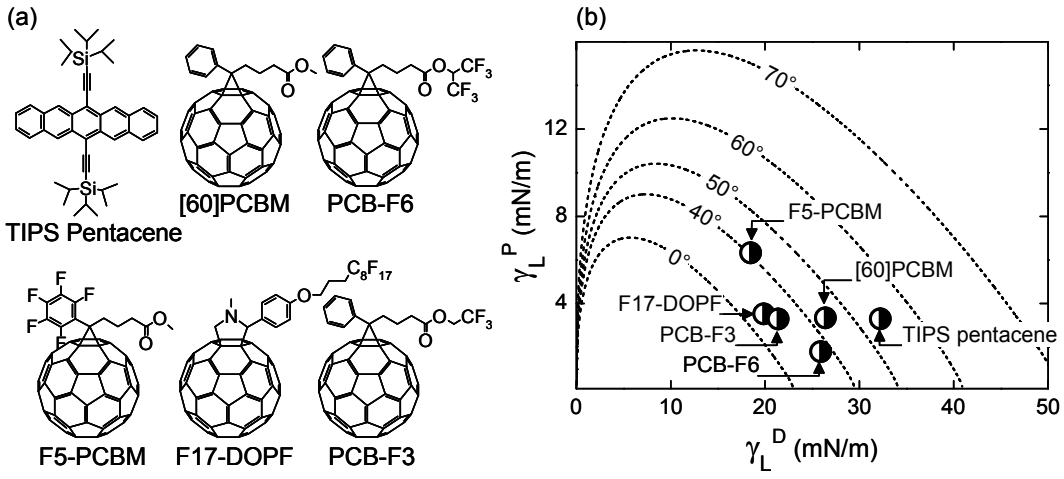


Fig. 7.5: (a) Chemical structure of the molecules studied. (b) Wetting envelopes for the AlOx-ODPA surface with coordinates of liquid surface energy components of semiconductor solutions plotted (symbols).

Table 7.1: Summary of material properties and transistor characteristics. All measurements were performed using 10 mg/ml chlorobenzene solutions.

Molecule	Parameter							
	γ^P (mN/m)	γ^D (mN/m)	θ (°)	ΔW (mN/m)	μ (cm^2/Vs)	V_T (V)	S (mV/dec)	I_{ON}/I_{OFF}
F17-DOPF	3.5	19.9	25.0	-2.2	0.04	0.3	110	10^4
PCB-F3	3.3	21.4	33.3	-4.1	0.01	0.13	200	10^3
PCB-F6	1.8	25.9	37.5	-5.7	-	-	-	-
F5-PCBM	6.3	18.5	40.1	-5.8	-	-	-	-
[60]PCBM	3.4	26.4	42.8	-7.9	-	-	-	-
TIPS-pentacene	3.3	32.2	51.7	-13.5	-	-	-	-

To quantify the wettability of each solution on the SAM surface it is useful to compute the spreading parameter (ΔW) given as $\Delta W = \gamma_L(\cos\theta - 1)$ (equation 2.53).[15] The latter represents the difference between the work of adhesion ($W_{SL} = \gamma_L(\cos\theta + 1)$, i.e. the work required to separate a unit area of the solid-liquid

interface) and the work of cohesion ($W_{LL} = 2\gamma_L$, i.e. the work required to separate a unit area of liquid-liquid interface).[16] ΔW shows the extent to which the liquid will adhere to the surface relative to itself and hence indicates the ability of a liquid drop to stick to the solid surface during solution-processing. At $\theta = 0°$, $\Delta W = 0$, indicating that the liquid can adhere equally well to the surface of the solid as it does to itself and hence complete wetting is observed.

Another useful illustration of the wetting behaviour of liquids on the Al-AlO_x-ODPA surface can be gained from determining the wetting envelopes. These are contour lines of constant equilibrium contact angle in a plot of γ_L^P vs. γ_L^D, determined by suitable manipulation of the Owens-Wendt-Kaelble equation 2.51:

$$\gamma_L^P = \left(\frac{\left(\gamma_S^P\right)^{1/2} + \sqrt{\gamma_S^P - (\cos\theta + 1)(\gamma_L^D(\cos\theta + 1) - 2\left(\gamma_L^D\gamma_S^D\right)^{1/2})}}{(\cos\theta + 1)} \right)^2 \qquad (3.4)$$

The plot, shown in Fig. 7.5(b), gives an indication of the degree to which various liquids will wet the surface, if knowledge of the γ_L^P and γ_L^D is available. It also illustrates the surface properties of ideal liquids for solution processing on the dielectric. It is implicit from $\Delta W = \gamma_L(\cos\theta - 1)$ that smaller contact angles will generally be associated with increased wettability. Any liquids whose surface energy components plotted on the graph lie below the line of $\theta = 0°$ are expected to completely wet the surface. In the experiment, liquids whose surface energy components lie above the line of $\theta = 40°$ do not demonstrate particularly good wetting and good film formation from solution processing becomes less likely. Hence, for use with ODPA, the most practical candidate semiconductor solutions should possess low surface energies dominated by dispersive rather than polar forces (i.e. $\gamma_L^P \approx 0$ and ideally $\gamma_L^D \leq \gamma_S^D$). Fig. 7.5(b) also displays plots of the coordinates of the organic semiconductor solutions calculated above. The experimentally determined contact angles and surface energy components for each material are summarised in Table 7.1. It can be observed that those solutions with $|\Delta W| > 5$ mN/m and whose surface energy components lie to the right of the $\theta = 40°$ wetting envelope did not demonstrate transistor operation. Upon spin coating, these solutions formed inhomogeneous films or no film at all. Interestingly, two solutions, F17-DOPF and

PCB-F3, are seen to approach the surface energy characteristics required for wetting the Al-AlO_X-ODPA surface. Indeed, upon spin coating, these solutions are found to form continuous films that are suitable for use in OFETs.

In conclusion, surface energy analysis is found to provide a powerful tool to examine the wettability of liquid solutions on dielectric thin films and to explain/predict the film forming behaviour of those. However, it is noted that other factors controlling the dynamics of film formation such as solute adsorption, surface roughness, liquid viscosity and solvent evaporation rate will also play a role in the spin coating process.[17-20] It can be assumed that these parameters were constant throughout the experiment, since spin coating was always performed in the glovebox under N_2 atmosphere, at similar spinning speeds and from solutions in the same solvent at similar concentrations.

7.4. Low-voltage, high mobility n-type OFETs

To test the applicability of ODPA dielectrics in devices we have fabricated transistors employing a self-assembled layer of ODPA functionalized onto oxidized Al gate electrodes using F17-DOPF/PCB-F3 as the semiconductors [Fig. 7.6(b) inset]. The transistor parameters calculated for the best devices are summarised in Table 7.1. Fig. 7.6 displays the transfer [Fig. 7.6(a)] and output [Fig. 7.6(b)] characteristics of a F17-DOPF OFET. The field-effect mobility μ and threshold voltage V_T were calculated from a linear fit to a plot of $\sqrt{I_D}$, measured in saturation, vs. V_G. Electron mobility values in the range of μ = 0.01 - 0.04 cm^2/Vs and threshold voltages of V_T = 0 – 0.3 V are obtained. The current on/off ratio and subthreshold slope ($S = \partial V_G / \partial \log_{10} I_D$) were also estimated yielding $\approx 10^4$ and ≈130 mV/decade, respectively. The subthreshold slope obtained here is comparable to the best values reported previously for evaporated small-molecule semiconductors on ODPA gate dielectrics.[21] Furthermore it is similar to state of the art silicon MOS-FETs[22] and close to the theoretical room temperature limit of 60 mV/dec.[23,24] The gate leakage currents were always at least one to two orders of magnitude lower than the drain current.

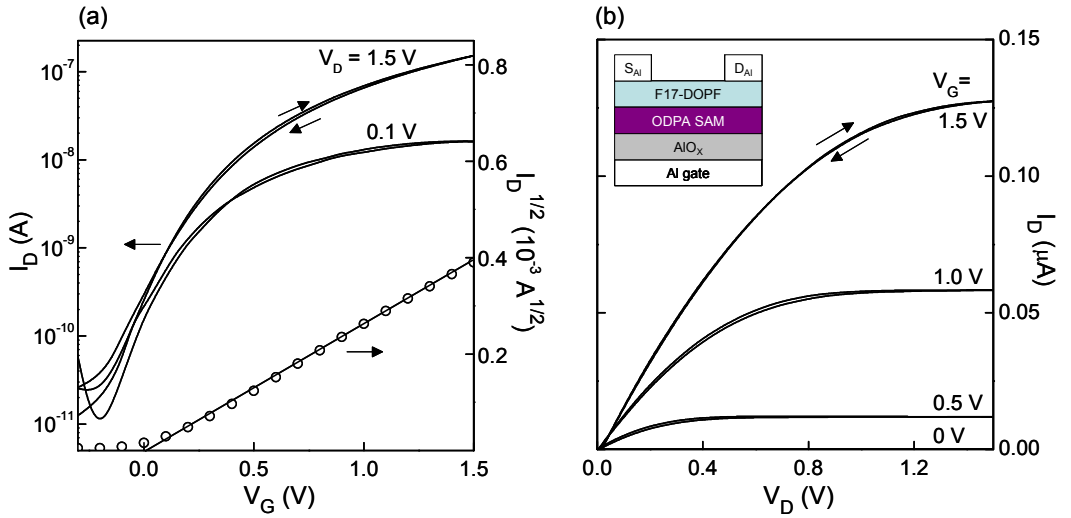


Fig. 7.6: (a) Transfer and (b) output characteristics of F17-DOPF based n-channel transistor fabricated on SAM dielectric (inset b). L = 60 μm, W = 1.5 mm, C_i = 600 nF/cm^2.

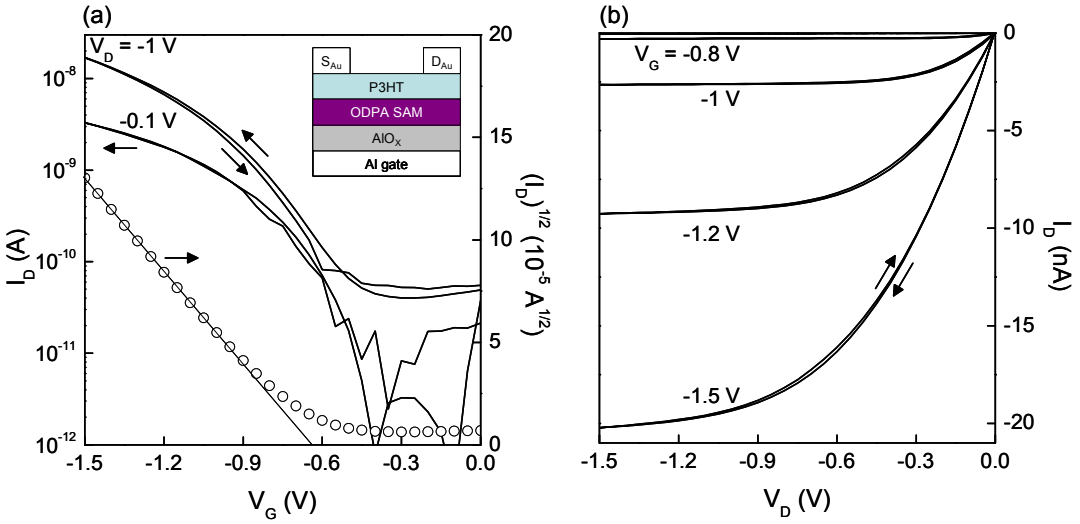


Fig. 7.7: (a) Transfer and (b) output characteristics of P3HT based p-channel transistor fabricated on SAM dielectric (inset a). L = 60 μm, W = 1 mm, C_i = 600 nF/cm^2.

Low-voltage transistors were also fabricated using poly(3-hexylthiophene) (P3HT) as hole conducting semiconductor. In this case substrate wetting was less problematic, since the deposition of polymer solutions is less affected by the surface tension of the solid. This is attributed to a larger viscosity of the solution,[19] due to the larger molecular weight of the P3HT polymer used. A representative set of the p-channel operation characteristics obtained from an OFET based on an AlO_X-ODPA dielectric and P3HT as semiconductor is shown in Fig. 7.7. The transistor operates with low hysteresis and exhibits a current on/off ratio of $\approx 10^2$. The hole mobility in saturation and the threshold voltage were obtained from a linear fit to the $(I_D)^{1/2}$ vs. V_G plot to be $\mu \approx 0.006$ cm^2/Vs and V_T = -0.6 V, respectively. The subthreshold slope is

250 mV/dec. These characteristics are very similar to a low-voltage P3HT based transistor fabricated on a DCTS monolayer dielectric, reported by Park *et al.*; except for the subthreshold slope, which they found to be 630 mV/dec.[6]

The threshold voltage and subthreshold slope of the p-channel transistors are higher compared to the n-channel fullerene based transistors. From the threshold voltages and the subthreshold slopes the density of charge carrier traps in the channel region, i.e. at the dielectric/semiconductor interface, are estimated using equations 2.22 and 2.25:

$$n_{trap} = \frac{V_T \cdot C_i}{e} \tag{2.22}$$

$$n_{trap}^{\max} \approx C_i \left(\frac{S}{k_B T \ln 10} - \frac{1}{e} \right) \tag{2.25}$$

Using $C_i \approx 600$ nF/cm^2 and $T = 293$ K electron and hole trap densities are obtained in the range of $n_e \approx 1 - 4 \cdot 10^{12} cm^{-2}$ and $n_h \approx 3 - 12 \cdot 10^{12} cm^{-2}$, respectively. Similar trap densities were determined using the same methods in other organic transistors.[25-27] Klauk *et al.* also measured a larger threshold in devices based on evaporated films of hole conducting (pentacene) than in electron conducting (hexadecafluorocopperphthalocyanine (F_{16}CuPc)) semiconductors on ODPA dielectrics.[5] These observations suggest that trapping of holes at the ODPA surface is more pronounced than trapping of electrons and that an applied gate bias forms a conductive n-channel more efficiently than a p-channel on this type of dielectric.

The transistor performance is generally comparable to the performance observed in high voltage transistors based on polymer or oxide dielectrics using the same set of semiconductors and injection electrodes. However, operation at drastically reduced voltages, typically less than 2 Volts, is achieved. These results could pave the path towards low-voltage, solution processed field-effect transistors for use in low-power, large-area organic electronics.

7.5. Low-voltage complementary inverters

Solution processed low-voltage p- and n-channel SAM based transistors were integrated to produce complementary inverters employing the circuitry shown

schematically in the inset of Fig. 7.8(a). As can be seen the inverter operates at less than 1.5 V and exhibits a relatively high gain of the order of >10 [Fig. 7.8(a, c)]. The noise margin was about 60% of the maximum theoretical value, i.e. $V_{DD}/2$ [Fig. 7.8(b)]. As expected from complementary logic, the circuit current during quasistatic operation of the inverter was low (≈ 1 nA) resulting in a static power dissipation below 5 nW per logic gate. The circuit current is attributed to current leakage via the semiconductor material, and is therefore expected to depend on the charge carrier mobility of the semiconductor. The power consumption here is slightly higher than the value reported by Klauk *et al.* (< 1 nW per logic gate), even though the mobility of our devices is lower by at least one order of magnitude.[21] Improvement of the power consumption characteristics is expected upon patterning of the organic semiconductors, i.e. reducing the off current of the OFETs. Finally, it is to be taken into account that the overall inverter performance is limited by the operating characteristics of the p-channel device and could be improved by implementing superior hole transporting materials.

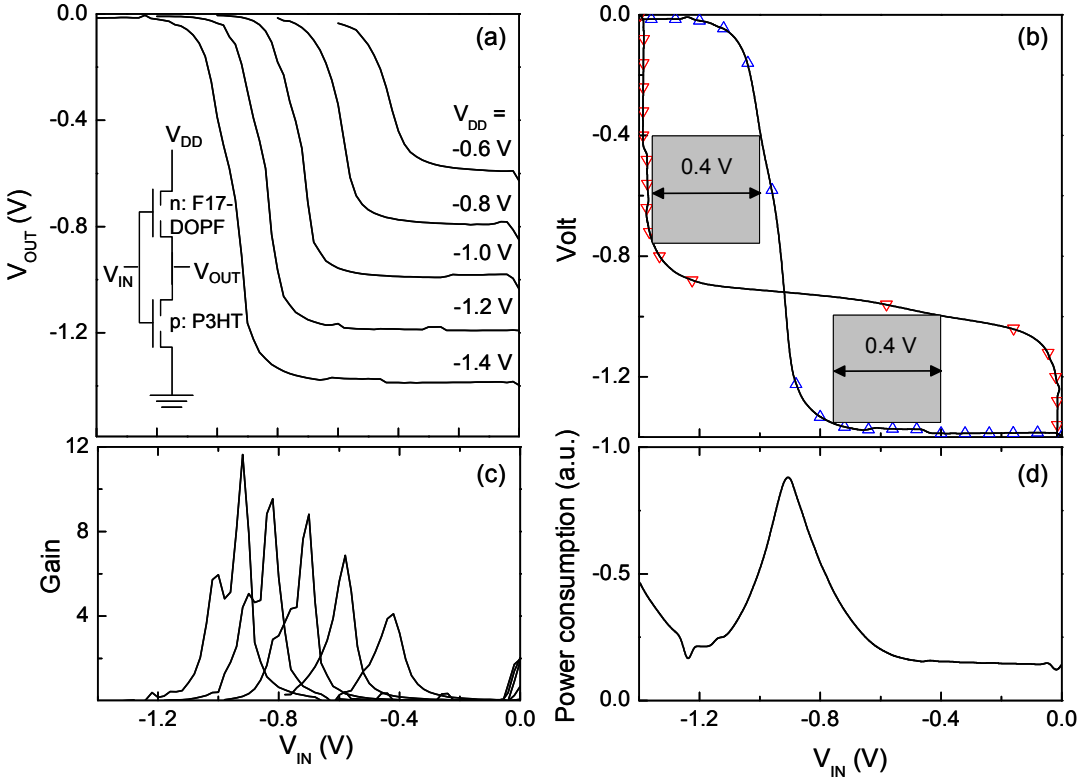


Fig. 7.8: (a) Output characteristics of complementary voltage inverter (inset, design rule: L = 60 µm) based on low voltage n-channel (W = 1 mm, F17-DOPF) and p-channel (W = 2 mm, P3HT) transistors. Representation of (b) noise margin, (c) gain and (d) power consumption of the inverter in quasi-static operation.

7.6. Outlook

In summary, by studying the surface energy interactions between the AlO_x-ODPA dielectric and a number of soluble organic semiconductors the fabrication of SAM based low-voltage n-channel and p-channel OFETs from solution was enabled. This method of surface analysis to determine the suitability of soluble organic semiconductors for processing on a given solid surface is generic and should be applicable to a wide range of SAM dielectric/organic semiconductor systems. The low temperature fabrication of the ultra thin hybrid dielectrics from solution is in principle compatible with a wide range of processing methodologies, including inkjet-, contact- and gravure printing and spray pyrolysis. Hence this work could have significant implications for the development of large area, low-power solution processed organic electronics. This work is the first demonstration of a low power complementary voltage inverter that is based on solution processed organic semiconductors and SAM gate dielectrics and which operates at less than 2 Volts.

Reference list:

1 Crone, B. *et al.* Large-scale complementary integrated circuits based on organic transistors. *Nature* **403**, 521-523 (2000).

2 Zhou, L. *et al.* All-organic active matrix flexible display. *Appl. Phys. Lett.* **88**, 083502 (2006).

3 Sze, S. M. *Physics of Semiconductor Devices*. (Wiley, 1981).

4 J. Collet, O. Tharaud, A. Chapoton & D. Vuillaume. Low-voltage, 30 nm channel length, organic transistors with a self-assembled monolayer as gate insulating films. *Applied Physics Letters* **76**, 1941-1943 (2000).

5 Klauk, H., Zschieschang, U., Pflaum, J. & Halik, M. Ultralow-power organic complementary circuits. *Nature* **445**, 745-748 (2007).

6 Park, Y. D. *et al.* Low-voltage polymer thin-film transistors with a self-assembled monolayer as the gate dielectric. *Appl. Phys. Lett.* **87**, 243509 (2005).

7 P. H. Wöbkenberg *et al.* Low-voltage organic transistors based on solution processed semiconductors and self-assembled monolayer gate dielectrics. *Applied Physics Letters* **93**, 013303 (2008).

8 Ball, J. M. *et al.* Complementary circuits based on solution processed low-voltage organic field-effect transistors. (submitted).

9 Lee, D. H., Kim, D., Oh, T. & Cho, K. Phase State Effect on Adhesion Behavior of Self-Assembled Monolayers. *Langmuir* **20**, 8124-8130 (2004).

10 Chua, L. L., Ho, P. K., Sirringhaus, H. & Friend, R. H. High-stability ultrathin spin-on benzocyclobutene gate dielectric for polymer field-effect transistors. *Appl. Phys. Lett.* **84**, 3400-3402 (2004).

11 Klauk, H. *et al.* High-mobility polymer gate dielectric pentacene thin film transistors. *J. Appl. Phys.* **92**, 5259-5263 (2002).

12 Kruss. *Selected literature values for surface tension of liquids*, http://www.kruss.de/en/theory/substance-properties/liquids.html (2009).

13 Kwok, D. Y. & Neumann, A. W. Contact angle measurement and contact angle interpretation. *Adv. Colloid Interface Sci.* **81**, 167-249 (1999).

14 D. K. Owens, R. C. W. Estimation of the surface free energy of polymers. *Journal of Applied Polymer Science* **13**, 1741-1747 (1969).

15 de Gennes, P. G. Wetting: statics and dynamics. *Reviews of modern physics* **57**, 827 (1985).

16 Zhang, J. & Kwok, D. Y. Calculation of Solid-Liquid Work of Adhesion Patterns from Combining Rules for Intermolecular Potentials. *The Journal of Physical Chemistry B* **106**, 12594-12599 (2002).

17 Ramos, S. & Tanguy, A. Pinning-depinning of the contact line on nanorough surfaces. *The European physical journal. E, Soft matter* **19**, 433-440 (2006).

18 Chang, J.-F. *et al.* Enhanced Mobility of Poly(3-hexylthiophene) Transistors by Spin-Coating from High-Boiling-Point Solvents. *Chemistry of materials* **16**, 4772-4776 (2004).

19 Schwartz, L. W. & Roy, R. V. Theoretical and numerical results for spin coating of viscous liquids. *Physics of Fluids* **16**, 569-584 (2004).

20 Deegan, R. D. *et al.* Capillary flow as the cause of ring stains from dried liquid drops. *Nature* **389**, 827-829 (1997).

21 H. Klauk, U. Zschieschang, J. Pflaum & M. Halik. Ultralow-power organic complementary circuits. *Nature* **445**, 745-748 (2007).

22 Thompson, S. *et al.* in *Electron Devices Meeting, 2002. IEDM '02. Digest. International.* 61-64.

23 Halik, M. *et al.* Low-voltage organic transistors with an amorphous molecular gate dielectric. *Nature* **431**, 963-966 (2004).

24 Brews, J. R. Subthreshold behavior of uniformly and nonuniformly doped long-channel MOSFET. *Electron Devices, IEEE Transactions on* **26**, 1282-1291 (1979).

25 McDowell, M., Hill, I. G., McDermott, J. E., Bernasek, S. L. & Schwartz, J. Improved organic thin-film transistor performance using novel self-assembled monolayers. *Appl. Phys. Lett.* **88**, 073505 (2006).

26 Zan, H.-W. *et al.* Low-voltage organic thin film transistors with hydrophobic aluminum nitride film as gate insulator. *Organic electronics* **8**, 450-454 (2007).

27 Klauk, H., Zschieschang, U. & Halik, M. Low-voltage organic thin-film transistors with large transconductance. *J. Appl. Phys.* **102**, 074514 (2007).

Chapter 8: Thin-Film Transistors based on Transparent Oxide Semiconductors deposited by Spray Pyrolysis

Metal oxides have been used for decades in a wide range of applications, as optical and protective coatings and as electroactive materials. Recently they have received a lot of interest as transparent semiconductors for use in opto-electronics. Their many advantages, such as high charge carrier mobility, air stability, optical transparency, mechanical robustness and compatibility with a wide range of processing methodologies, including from solution, make them very promising candidates for electronic applications. Here a very simple solution deposition method, namely spray pyrolysis, is used to fabricate thin-film transistors employing TiO_2 and ZnO as transparent semiconductors. The best devices exhibit air-stable electron transport and operation at <2 V, with charge carrier mobility of the order of 10 cm^2/Vs.

8.1. Introduction

Organic materials offer the prospect of low manufacturing cost combined with some desirable physical characteristics such as ease of processing and mechanical flexibility. But while research in the area of organic materials and devices has been intensifying, a different class of semiconducting materials, namely transparent oxide semiconductors (TOS), has emerged as possible alternative technology.[1] Metal oxides incorporate important qualities that are currently absent from organic-based semiconductors. For instance, they generally exhibit higher charge carrier mobility that is already sufficient for use in optical displays, such as current-driven organic light-emitting diode (OLED) based displays.[2,3] An additional advantage of TOS relevant to many electronic applications is the superb optical transparency resulting from their wide bandgap. The latter makes oxide semiconductors particularly interesting for use in transparent electronics[4] as well as in backplanes for the next generation of current-driven displays.[2,5]

Here, the use of a simple deposition technique, namely spray pyrolysis, is demonstrated for the fabrication of high-performance low-voltage metal oxide electronics. The method is compatible with large area deposition onto ultra-thin self-assembled monolayer gate dielectrics and could potentially address both the issue of manufacturing cost and high operating voltages.

8.2. Air-stable TFTs based on transparent oxide semiconductors

A wide variety of TOS systems have been studied for a range of different purposes (see section 2.9.1). Few examples include materials deposited using solution processing techniques. In this work I focused on two non-toxic TOS, for which solution processable precursor materials were commercially available at very low cost.

On the one hand, titanium dioxide (TiO_2) is a well known member of the TOS family and one of the most promising materials for application in hybrid photovoltaics i.e. dye-sensitized solar cells (DSCs).[6,7] On the other hand, very high electron mobilities have recently been reported in devices based on zinc oxide (ZnO).[8,9] Here

the application of both materials as semiconductors in thin-film transistors by solution processing is explored.

8.2.1. TiO_2 semiconductor layers

Thin films of TiO_2 were deposited from a precursor solution of titanium (IV)iso-propoxide (Ti-iPr), modified with acetylacetone, in absolute ethanol by spray pyrolysis at T_S = 450°C onto quartz substrates [Fig. 8.1(a) inset]. In previous reports this precursor is shown to produce anatase films of TiO_2 at deposition temperatures between 410-550 °C.[10] To study the optical properties of as-deposited films optical absorption measurements in the range 250-750 nm were performed [Fig. 8.1]. From the onset of absorption the optical bandgap (E_G) can be approximated yielding a value of 3.3 eV. This is in agreement with values reported in the literature.[11] Due to its wide bandgap TiO_2 films are highly transparent to the visible part of the electromagnetic spectrum [Fig. 8.1(a) inset]. In particular, measurements yield transparency values in the range 69-92% for wavelengths between 400-750 nm, respectively [Fig. 8.1(b)]. Such superb optical characteristics qualify TiO_2 as a candidate for use in transparent electronics.

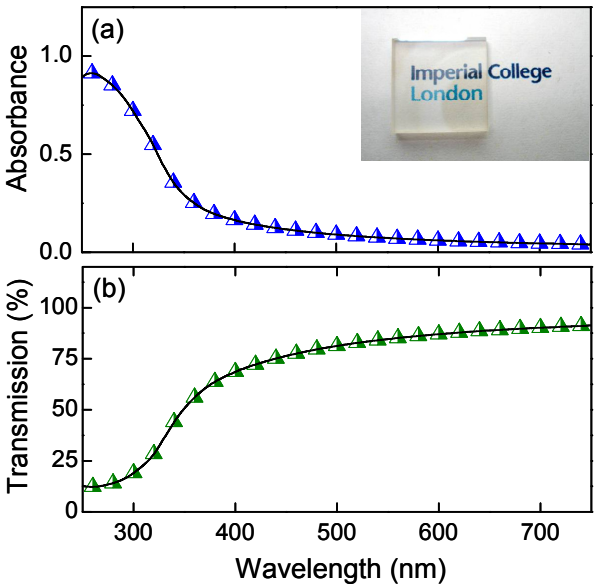


Fig. 8.1: (a) Absorbance and (b) transmission characteristics of TiO_2 films deposited by spray pyrolysis at T_S = 450 °C. Inset: optical photograph of TiO_2 coated quartz substrate.

Next the suitability of TiO_2 films deposited by spray pyrolysis for use in thin-film transistors (TFTs) was examined. Initial tests were carried out in nitrogen

atmosphere in the dark employing a BG-BC type transistors [Fig. 8.2(a) inset] using gold S-D electrodes. Representative sets of the transfer and output characteristics obtained from a TiO_2 BG-BC TFT (L = 5 μm, W = 50 cm) are shown in Fig. 8.2(a) and (b), respectively. The maximum electron mobility derived in saturation from this device was 3×10^{-3} cm^2/Vs (V_D = 80 V) with on/off current ratio and threshold voltage of $\approx 10^5$ and $V_T \approx 33$ V, respectively.

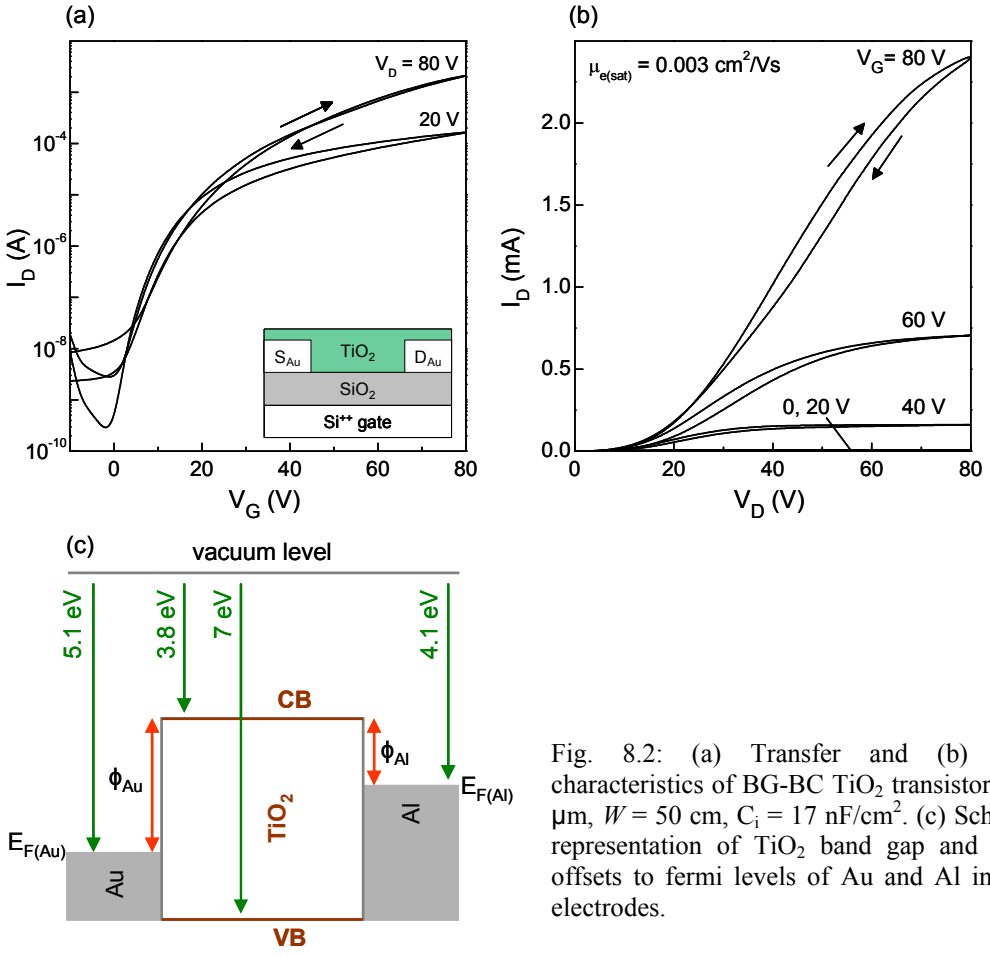


Fig. 8.2: (a) Transfer and (b) output characteristics of BG-BC TiO_2 transistor. L = 5 μm, W = 50 cm, C_i = 17 nF/cm^2. (c) Schematic representation of TiO_2 band gap and energy offsets to fermi levels of Au and Al injecting electrodes.

Strongly injection-limited charge transport is observed as evident from the super-linear behaviour of I_D at low V_D [Fig. 8.2(b)]. This is attributed to the relatively large contact barrier for electrons (ϕ_{Au} = 1.3 eV) present between the Fermi level of Au ($E_{F(Au)}$ = 5.1 eV) and the conduction band of TiO_2 (CB ≈ 3.8 eV).[6] The simplified energy diagram of the contact, neglecting band bending, is shown in Fig. 8.2(c). In an effort to minimise the injection barrier BG-TC TFTs employing low workfunction contact materials were fabricated. The inset in Fig. 8.3(a) shows the BG-TC device architecture employed. Aluminium, with $E_{F(Al)}$ = 4.1 eV, was found to provide an ohmic-like contact with the CB of TiO_2 (ϕ_{Al} = 0.3 eV, Fig. 8.2(c)). The room

temperature transfer and output characteristics obtained from a TiO_2 transistor with Al S-D electrodes are shown in Fig. 8.3. From the transfer curves, in saturation, [Fig. 8.3(a)] a maximum electron mobility of 0.05 cm^2/Vs and a $V_T \approx 32$ V are calculated. Although the electron mobility of TiO_2 is lower than that of other TOS,[1] it compares favourably with values extracted from TFTs based on single crystals of rutile TiO_2.[12]

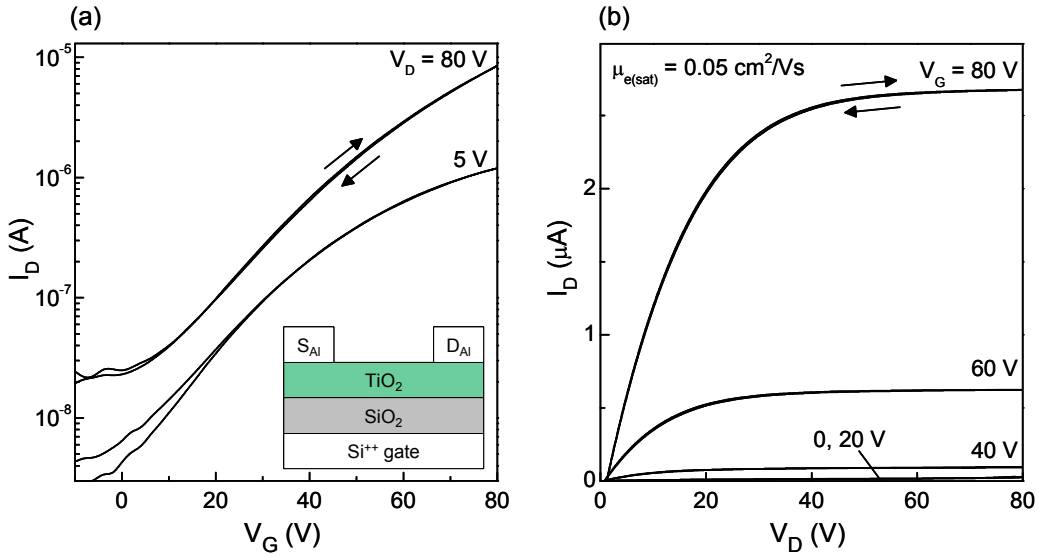


Fig. 8.3: (a) Transfer and (b) output characteristics of BG-TC TiO_2 transistor with Al S-D electrodes. $L = 60$ μm, $W = 1$ mm, $C_i = 17$ nF/cm^2.

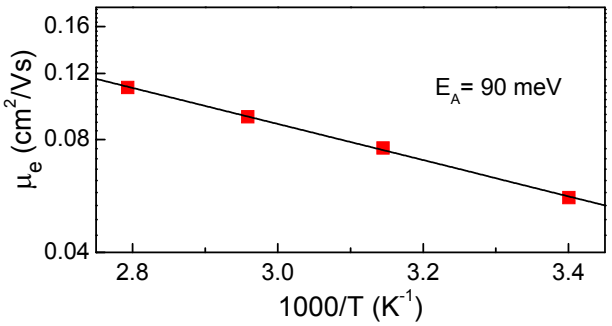


Fig. 8.4: Arrhenius-type dependence of field-effect mobility in saturation on temperature. The activation energy for electron transport is 90 meV.

Fig. 8.4 displays the dependence of electron mobility, measured in saturation, on temperature. A thermally activated electron transport with an associated energy of $E_A \approx 90$ meV is observed, possibly governed by a hopping type conduction mechanism.[13] Interestingly, for temperatures > 350 K the electron mobility exceeds 0.1 cm^2/Vs, a value comparable to that obtained from amorphous silicon (a-Si) based transistors.[14] The mobility is also comparable to the field-effect mobility obtained in transistors based on high quality anatase TiO_2 films, which were produced using an elaborate oxygen modulated pulsed laser deposition method.[15] From these results we

can conclude that SP is a useful method for the deposition of high quality TOS films using very simple processing equipment.

In order to assess their operational stability in air, the TiO_2 transistors were removed from the nitrogen atmosphere and measured in the dark in ambient air at room temperature. Fig. 8.5 demonstrates the air-stable operation of TiO_2 transistors over several days. As evident from Fig. 8.5(a) the electron mobility hardly changes over a period of approximately 6 days. The current on/off ratio decreases slightly towards the end of this period [Fig. 8.5(b)], which is due to a modest increase of the off current. The exact nature of this current increase is subject to further investigation. Overall it is noteworthy that the transistors do not appear to degrade during storage in ambient air, which is a great advantage over most electron transporting organic semiconductors.

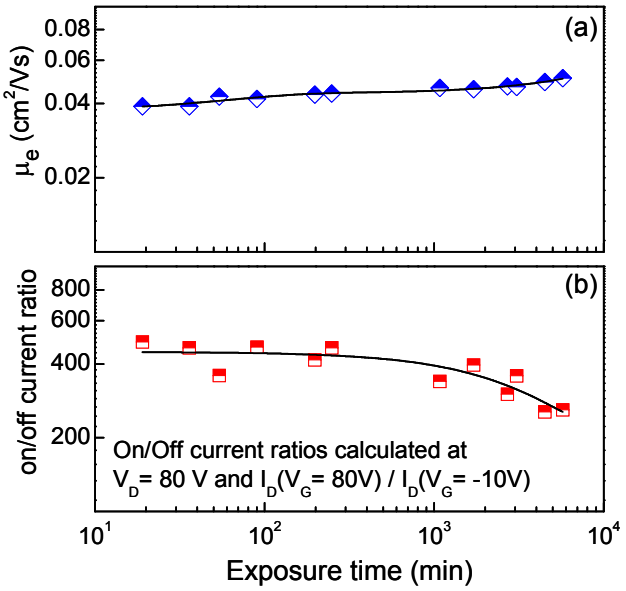


Fig. 8.5: (a) Evolution of electron mobility and (b) current on/off ratio in a TiO_2 transistor stored and operated in air. The solid lines are a guide to the eye.

8.2.2. ZnO semiconductor layers

Encouraged by the excellent results obtained from the TiO_2 TFTs, the suitability of SP for the deposition of other TOS was investigated. The technique was also employed for the deposition of ZnO thin films from a zinc acetate dihydrate ($Zn(CH_3COO) \bullet 2H_2O$) precursor solution [Fig. 8.6(a) inset].[16] The absorption spectrum of a ZnO film deposited at T_S = 400 °C onto a quartz substrate is displayed

in Fig. 8.6(a). The thin film exhibits a clear absorption onset at around 370 nm, corresponding to an optical bandgap energy of approximately 3.35 eV. This is in good agreement with earlier reported values.[1,17,18] The surface morphologies of ZnO films deposited on SiO_2 substrates were studied by close-contact atomic force microscopy (AFM). A representative image is shown in Fig. 8.6(b) of a film deposited at T_S = 400 °C. The surface root mean square roughness is found to be ≈ 1.6 nm.

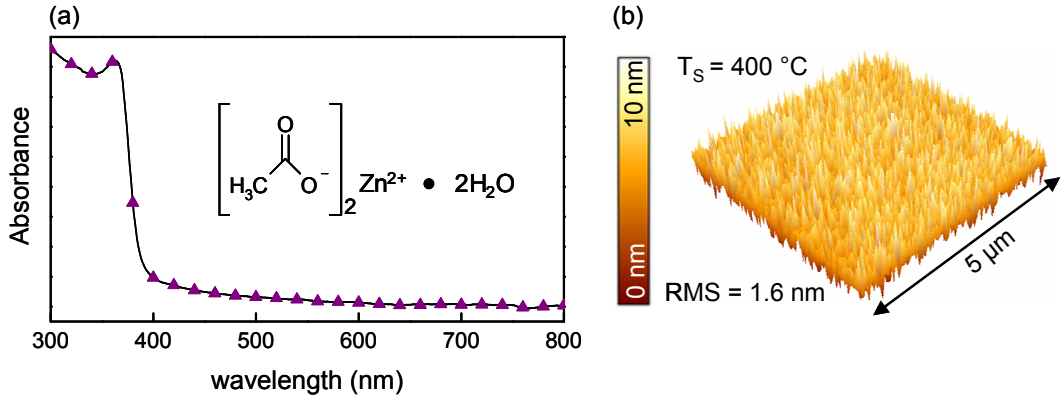


Fig. 8.6 (a) inset: Chemical structure of Zn acetate dihydrate precursor material. (a) Absorbance characteristics and (c) close contact AFM images of ZnO films deposited by spray pyrolysis at T_S = 400°C.

To investigate the suitability of the SP-deposited ZnO films for the fabrication of functional devices a number of ZnO TFTs were constructed. Fig. 8.7(a-b) displays the transfer and output characteristics measured in the dark from a BG-TC ZnO transistor fabricated at 400 °C employing Al S-D electrodes. A schematic diagram of the device architecture is shown in the inset of Fig. 8.7(a). Excellent transport characteristics are obtained with maximum electron mobility of the order of 15-20 cm^2/Vs.[16,19] This value is amongst the highest electron mobilities reported to date for transistors based on solution processed TOS films.[18,20,21]

BG-BC transistors based on ZnO were also fabricated employing Au S-D electrodes. These devices generally exhibited lower mobility (i.e. < 2 cm^2/Vs) values compared to the ZnO transistors with Al S-D TC electrodes. As for the TiO_2 transistors, this effect is attributed, partly, to the significant energy offset present between the Fermi level of the gold S-D electrodes ($E_{F(Au)}$ = 5.1 eV) and the conduction band of ZnO (≈ 4.4 eV) (the offset is much less pronounced in BG-TC devices where aluminium electrodes with a work function of 4.1 eV are employed). In addition to the energy offset, Göpel *et al*. also demonstrated that the Schottky barrier at the non-reactive Au-ZnO interface is qualitatively different from that of the rather

reactive Al-ZnO interface.[22] This may also explain the differences in charge transport across the interface. Finally, the difference in performance could also be related to the different geometrical configuration of the injecting electrodes and the order of deposition, as mentioned in section 2.3.1. The films formed on the smooth SiO_2 surface are likely to be more homogeneous in their morphology and thickness than the films deposited on the pre-patterned Au electrodes, and should therefore be more suitable for the formation of a conducting channel.

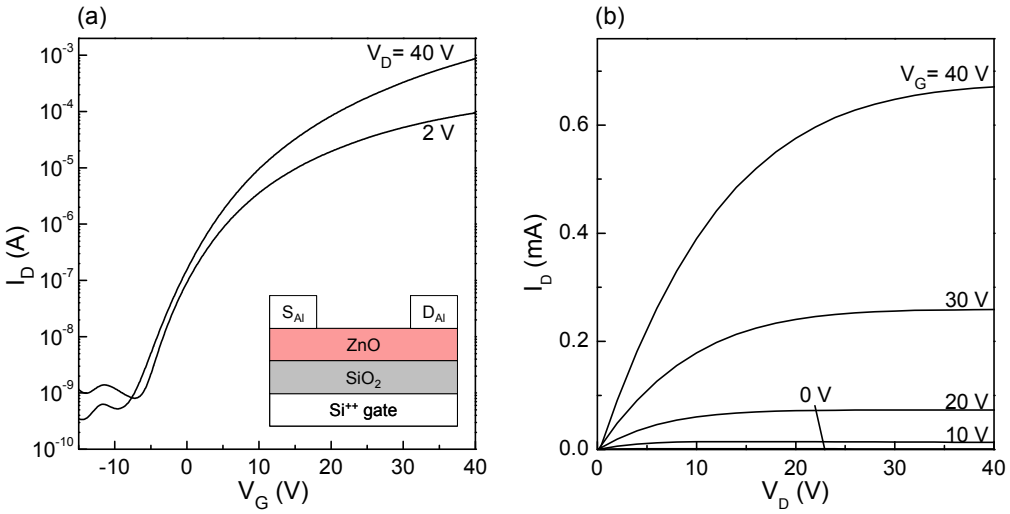


Fig. 8.7: (a) Transfer and (b) output characteristics obtained from a BG-TC (Al, L = 60 μm, W = 1.5 mm, C_i = 17 nF/cm^2) TFT employing semiconducting ZnO films deposited by spray pyrolysis at T_S = 400°C.

8.3. Spray Pyrolysis on Self-Assembled Monolayer gate dielectrics

The implementation of high-performance TOS based integrated circuits not only requires TFTs with high charge carrier mobilities, but also low operating voltages. In an effort to reduce the operating voltage of the high mobility ZnO transistors the SP deposition technique was used to fabricate transistors utilising self-assembled monolayer (SAM) gate dielectrics. The SAM gate dielectrics used here are the same type of molecules as the ones discussed in chapter 7.

8.3.1. Low-voltage, high mobility ZnO transistors

Ultra-thin gate dielectrics based on self-assembled layers of octadecylphosphonic acid molecules were fabricated on oxidized Al gate electrodes, as described in chapter 7.[16,23] The molecular structure of the n-octadecylphosphonic

acid (ODPA) employed is shown in Fig. 8.8(a). Fig. 8.8(b) shows pictures of water droplets on the Al-AlO_x surface before and after treatment with ODPA. The significant changes in the water contact angle from $\theta_{AlO_x} = (40 \pm 2)°$ to $\theta_{ODPA} = (105 \pm 2)°$ confirm the presence of the hydrophobic monolayer. Interestingly, it is found that high contact angles are preserved even after heat treatment of the samples at 400-450°C in N_2. Detailed surface energy measurements reveal that the surface characteristics of Al-AlO_x-ODPA electrodes do not change significantly for annealing periods of up to 10 minutes. Hence, it can be concluded that phosphonic acid groups bond very strongly to AlO_x and the insulating alkyl chains are not removed during annealing. An important observation made previously in chapter 7 is that SAM functionalisation is found to drastically reduce the leakage current between the Al-AlO_X electrode and an evaporated top gold electrode. Impedance measurements carried out on the same devices yield a geometric capacitance in the range 500-700 nF/cm^2.[23,24]

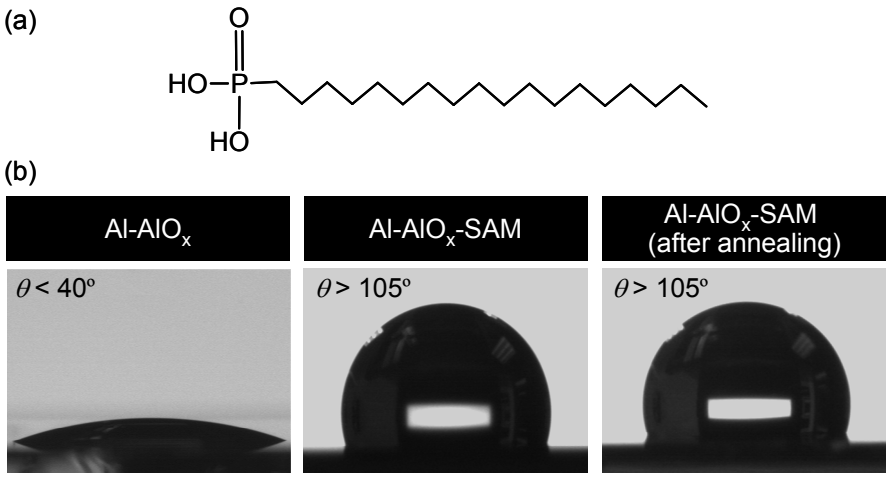


Fig. 8.8: (a) Chemical structure of the n-octadecylphosphonic acid molecule employed in the SAM gate dielectric. (b) Images of water droplets on the surfaces of Al-AlOx, Al-AlOx-SAM and Al-AlOx-SAM after annealing at 400°C in N_2. The high contact angles of >105° measured for Al-AlOx-SAM surfaces after thermal annealing clearly demonstrate the thermal stability of ODPA monolayers.

In order to prepare low-voltage oxide transistors and integrated circuits employing SAM dielectrics ZnO was deposited on Al-AlO_x-ODPA gate electrodes by SP followed by the evaporation of Al S-D top contacts. Fig. 8.9(a-b) show the transfer and output characteristics of a SAM-based ZnO TFT (T_S = 400°C). The transistor exhibits excellent operating characteristics with minimum hysteresis. The device structure is shown in the inset of Fig. 8.9(a). As-prepared n-channel transistors operate

at less than 1.5 V. Table 8.1 summarises the performance parameters of SAM-based ZnO TFTs fabricated at different T_S between 200 °C and 500 °C. The extracted electron mobilities are comparable to values obtained from BG-TC transistors employing an SiO_2 gate dielectric. The upper limit for the electron trap density in the channel region is determined using equation 2.25:

$$n_{trap}^{\max} \approx C_i\left(\frac{S}{k_B T \ln 10} - \frac{1}{e}\right) \tag{2.25}$$

The trap densities of the order 10^{13} cm^{-2} obtained here are higher compared to the trap densities previously observed in amorphous organic materials (see section 7.4). This finding is attributed to the polycrystalline nature of the TOS material and the effect of grain boundary trapping.[25,26] A clear trend with deposition temperature could not be determined.

Table 8.1: Performance parameters of low-voltage BG-TC ZnO transistors based on AlOx-SAM dielectrics. The channel length of the TFTs was kept constant and equal to 60 μm while the width was varied in the range of 1-2 mm.

T_S [°C]	$\mu_{e(sat)}$ [cm^2/Vs]	V_T [V]	S [mV/dec]	n_{trap}^{max} [10^{12} cm^{-2}]	I_{ON}/I_{OFF}
200	0.27	0.6	270	14	10^3
400	7.6	0	320	17	10^3
500	8.3	0.3	290	15	10^3

To prove that the ODPA SAM layer plays a key role in reducing the leakage current to the gate electrode, I also fabricated ZnO TFTs employing bare Al-AlO_x gates. Surprisingly, operational transistors can be obtained even when functionalisation of the Al-AlO_x gate with ODPA is omitted [Fig. 8.9(c)]. This is due to the simultaneous occurrence of two important chemical processes during SP: (i) conversion of the zinc acetate dihydrate solution to ZnO, and (ii) further oxidisation of the surface of the aluminium gate electrode to AlO_x. However, it is observed that low-voltage ZnO transistors without ODPA exhibit significantly higher gate leakage current, significantly lower on/off ratios ($<10^2$) and reduced electron mobilities as compared to ODPA-based ZnO TFTs. From these results we can conclude that the SAM plays a vital role as part of the gate dielectric and for the significantly improved TFT performance.

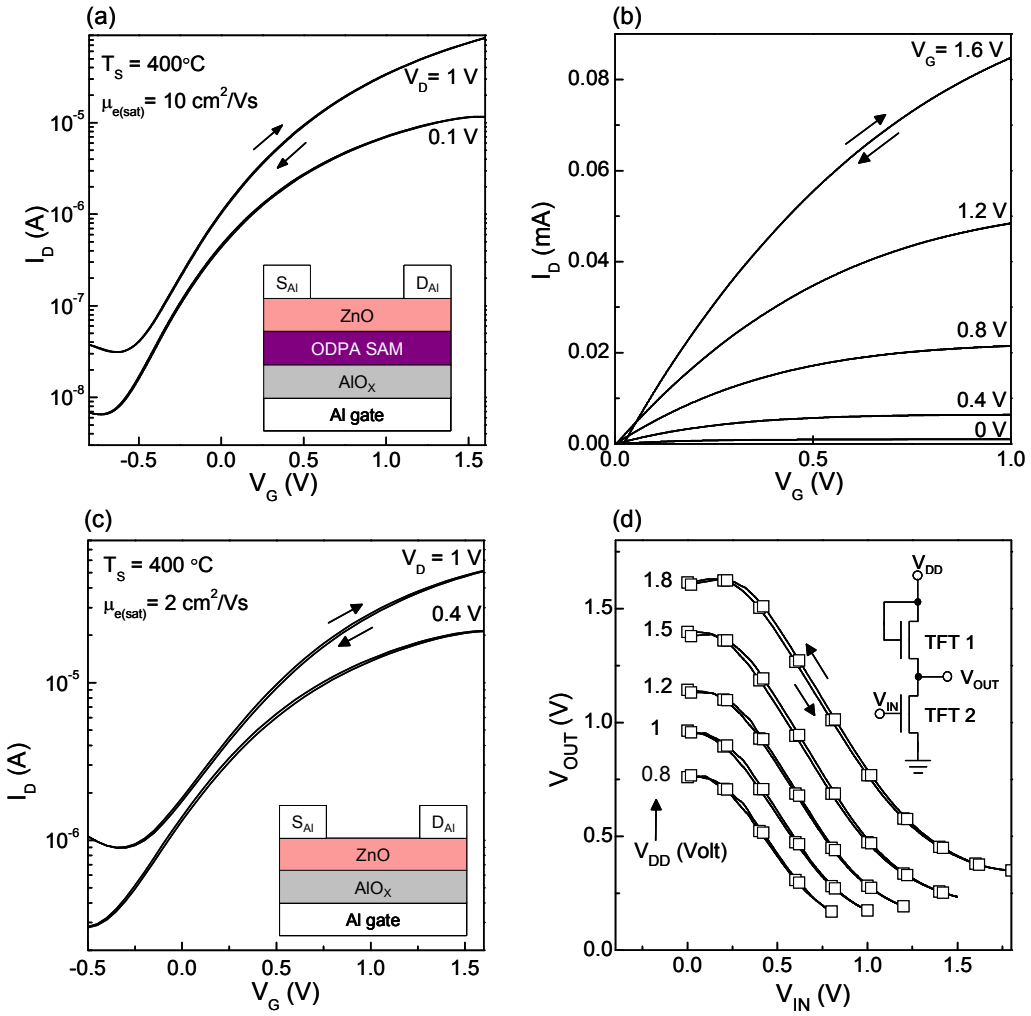


Fig. 8.9: (a) Transfer characteristics and (b) output characteristics measured from a low-voltage ODPA-based ZnO transistor. Inset in (a) shows the BG-TC transistor architecture employed (L = 60 μm, W = 1 mm). ZnO was deposited by spray pyrolysis in air at T_S = 400°C. (c) Transfer characteristics of low voltage ZnO transistor without ODPA SAM in dielectric (architecture see inset, L = 60 μm, W = 2 mm). (d) Output characteristics of a unipolar voltage inverter comprising two low-voltage ODPA-based ZnO transistors measured at different V_{DD}. Inverter characterisation was performed in ambient atmosphere. Inset in (d) shows the circuitry of the unipolar inverter (using L = 60 μm design rule).

8.3.2. Low-voltage ZnO based unipolar inverters

N-channel SAM-based ZnO transistors were used to fabricate low-voltage unipolar logic gates. The output curves of a representative unipolar voltage inverter measured in air are shown in Fig. 8.9(d). The inset figure displays the circuitry of the inverter comprising two low-voltage ZnO transistors (TFT 1 and TFT 2) using 60 μm design rule (i.e. L = 60 μm). The circuit operates at voltages below 2 V and shows the correct logic function with signal gain >1. These results clearly demonstrate the potential of combining simple and low-cost deposition techniques for the fabrication

of high performance transistors and logic circuits. It is also worth noting that the SAM-based ZnO transistors and circuits operate at low voltages comparable to that of state-of-the-art amorphous silicon TFTs and could arguably be considered as an alternative to amorphous and polycrystalline silicon in many electronic applications.

8.4. UV-induced doping in ZnO transistors

During the characterization of the devices made from TiO_2 and from ZnO films deposited by spray pyrolysis, a dependence of the measurements on fluorescent white light was noticed. In order to investigate this phenomenon, current-voltage measurements were performed between two points of a ZnO film deposited on a highly doped Si wafer with a thermally oxidized dielectric layer of SiO_2, before and after illumination by a handheld UV lamp. The resistance between two probes positioned at approximately 1.5 mm from each other decreased from 10^{10} Ω to 10^5 Ω after the film was illuminated for 5 minutes in nitrogen atmosphere. In order to investigate the illumination effect on transistors, transfer curves of low operating voltage ZnO based transistors were recorded in inert nitrogen atmosphere in dark and under illumination by a handheld UV lamp. A strong effect on the drain current was observed [Fig. 8.10(a)]. More precisely, the transfer curves shifted towards more negative gate voltages, causing the threshold voltage to shift from $V_T \approx 0$ V to $V_{T(UV)} \approx$ - 1 V. This observation suggests an increase in the density of mobile charges (i.e. electrons) in the ZnO film upon illumination with UV light. As a result, a negative gate voltage is required to deplete the channel region. Similar findings were reported by Bae *et al.*[27] The light induced doping concentration can be calculated using equation 8.1, which is derived from equation 2.22:

$$n_{doping} = \frac{(V_T - V_{T(UV)}) \cdot C_i}{e} \tag{8.1}$$

Using C_i = 500 nF/cm^2 a doping concentration of $3 \cdot 10^{12}\, cm^{-2}$ is obtained. The effect was not reversible instantaneously, as the high drain currents were sustained after switching the lamp off. Subsequent measurements under vacuum of the drain current vs. time after a short period t_{UV} of illumination with a UV-LED (λ_{peak} = 400 nm, t_{UV} = 10 s) showed that the drain current decayed exponentially with a half-life time of approximately 10 min [Fig. 8.10(b)]. The relaxation was accelerated when a negative

gate bias was applied or when the sample was moved out of the inert atmosphere into ambient air. This dependence of the photoresponse time on the ambient conditions was already observed early on by Collins and Thomas for ZnO crystals[28], by Kind *et al.* in the case ZnO nanowires[29] and by Takahashi *et al.* in sol-gel deposited ZnO films.[30] They argued that in the presence of air, O_2 molecules adsorb into the ZnO film and trap mobile electrons. Upon illumination with UV light these O_2^- ions are discharged by holes, which are photogenerated in the ZnO bulk. The photogenerated electrons remain mobile and contribute to the increased conductivity, until the illumination is stopped and trapping by adsorbed oxygen molecules occurs. This optical gating effect also operates under quasi vacuum (10^{-4} mbar), however less electrons are trapped by fewer adsorbing O_2 molecules and hence the conductivity decays more slowly when the light is switched off. This phenomenon and the potential exploitation of the UV light sensing capability of ZnO films in photodetectors are subject to further investigation.

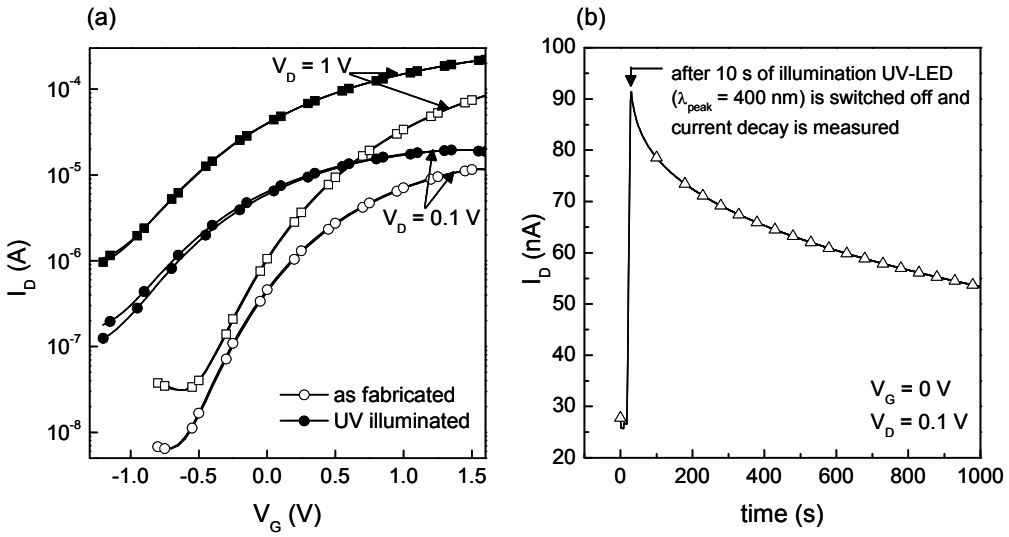


Fig. 8.10: (a) UV-induced shift of transfer characteristics of low voltage ZnO transistor (L = 60 μm, W = 1 mm). (b) Slow decay of photocurrent after brief illumination with UV (λ_{peak} = 400 nm) of a ZnO TFT of same dimensions measured in vacuum.

8.5. Outlook

In conclusion, the present results demonstrate the possibility of combining two very simple deposition techniques, namely spin/drop casting of SAM-dielectrics and spray pyrolysis of TOS, for the fabrication of high performance transistors and

integrated circuits. Electron mobility of the order of 10 cm^2/Vs was achieved in transistors operating at less than 2 Volts in air. Semiconductor deposition by spray pyrolysis is performed entirely in ambient atmosphere without any special precautions. It is established that the as-deposited TOS films are of high quality and uniformity. Further investigations are under way to better control the morphology and the conductivity level of the films deposited by SP. Doping the TOS precursor solution and tuning the chemical composition of the precursor material in order to reduce the conversion temperature are anticipated to make the SP technique suitable for low temperature fabrication processes. Moreover, the novel combination of solution-processable SAM-dielectrics with large-area compatible spray pyrolysis deposition should be applicable to other metal oxides and could potentially enable the low-cost fabrication of high-performance transparent electronics.

Reference list:

1 Nomura, K. *et al.* Room-temperature fabrication of transparent flexible thin-film transistors using amorphous oxide semiconductors. *Nature* **432**, 488-492 (2004).

2 Wager, J. F., Keszler, D. A. & Presley, R. E. *Transparent Electronics*. (Springer, 2008).

3 Sony. *First commercial organic light-emitting diode TV: Sony XEL-1*, http://www.sony.co.uk/product/tvp-oled-tv/xel-1 (2008).

4 Fortunato, E. M. C. *et al.* Wide-bandgap high-mobility ZnO thin-film transistors produced at room temperature. *Appl. Phys. Lett.* **85**, 2541-2543 (2004).

5 Ito, M. *et al.* "Front Drive" Display Structure for Color Electronic Paper Using Fully Transparent Amorphous Oxide TFT Array. *IEICE Transactions on Electronics* **90**, 2105 (2007).

6 Grätzel, M. Photoelectrochemical cells. *Nature* **414**, 338-344 (2001).

7 O'Regan, B. & Grätzel, M. A low-cost, high-efficiency solar cell based on dye-sensitized colloidal TiO2 films. *Nature* **353**, 737-740 (1991).

8 Fortunato, E. *et al.* Recent advances in ZnO transparent thin film transistors. *Thin Solid Films* **487**, 205-211 (2005).

9 Navamathavan, R. *et al.* Fabrication and characterizations of ZnO thin film transistors prepared by using radio frequency magnetron sputtering. *Solid-State Electronics* **52**, 813-816 (2008).

10 Krunks, M. *et al.* Thermoanalytical study of acetylacetonate-modified titanium(IV) isopropoxide as a precursor for TiO2 films. *J. Therm. Anal. Calorim.* **80**, 483-488 (2005).

11 Conde-Gallardo, A. *et al.* TiO_2 anatase thin films deposited by spray pyrolysis of an aerosol of titanium diisopropoxide. *Thin Solid Films* **473**, 68-73 (2005).

12 Katayama, M. *et al.* Field-effect transistor based on atomically flat rutile TiO[sub 2]. *Appl. Phys. Lett.* **89**, 242103 (2006).

13 H. Bässler, P. M. B., R. J. Perry,. Charge transport in poly(methylphenylsilane): The case for superimposed disorder and polaron effects. *Journal of Polymer Science Part B: Polymer Physics* **32**, 1677-1685 (1994).

14 Wagner, S., Gleskova, H., Cheng, I. C. & Wu, M. Silicon for thin-film transistors. *Thin Solid Films* **430**, 15-19 (2003).

15 Katayama, M., Ikesaka, S., Kuwano, J., Koinuma, H. & Matsumoto, Y. High quality anatase TiO_2 film: Field-effect transistor based on anatase TiO_2. *Appl. Phys. Lett.* **92**, 132107 (2008).

16 Aneeqa Bashir, P. H. W., Jeremy Smith, James M. Ball, George Adamopoulos, Donal D. C. Bradley, Thomas D. Anthopoulos,. High-Performance Zinc Oxide Transistors and Circuits Fabricated by Spray Pyrolysis in Ambient Atmosphere. *Adv. Mater.* **9999**, NA (2009).

17 Paraguay, D., Estrada, L., Acosta, N., Andrade, E. & Miki-Yoshida, M. Growth, structure and optical characterization of high quality ZnO thin films obtained by spray pyrolysis. *Thin Solid Films* **350**, 192-202 (1999).

18 Studenikin, S. A., Golego, N. & Cocivera, M. Optical and electrical properties of undoped ZnO films grown by spray pyrolysis of zinc nitrate solution. *J. Appl. Phys.* **83**, 2104-2111 (1998).

19 Adamopoulos, G., Bashir, A., Wöbkenberg, P. H., Bradley, D. D. C. & Anthopoulos, T. D. Electronic properties of ZnO field-effect transistors fabricated by spray pyrolysis in ambient air. *Appl. Phys. Lett.* (accepted for publication).

20 Perednis, D. & Gauckler, L. J. Thin film deposition using spray pyrolysis. *Journal of electroceramics* **14**, 103-111 (2005).

21 Lee, S., Jeong, S., Kim, D., Park, B. K. & Moon, J. Fabrication of a solution-processed thin-film transistor using zinc oxide nanoparticles and zinc acetate. *Superlattices and Microstructures* **42**, 361-368 (2007).

22 Göpel, W., Brillson, L. J. & Brucker, C. F. Surface point defects and Schottky barrier formation on ZnO(1010). *Journal of Vacuum Science and Technology* **17**, 894-898 (1980).

23 Klauk, H., Zschieschang, U., Pflaum, J. & Halik, M. Ultralow-power organic complementary circuits. *Nature* **445**, 745-748 (2007).

24 Wöbkenberg, P. H. *et al.* Low-voltage organic transistors based on solution processed semiconductors and self-assembled monolayer gate dielectrics. *Appl. Phys. Lett.* **93**, 013303-013303 (2008).

25 Verlaak, S., Arkhipov, V. & Heremans, P. Modeling of transport in polycrystalline organic semiconductor films. *Appl. Phys. Lett.* **82**, 745-747 (2003).

26 Levinson, J. *et al.* Conductivity behavior in polycrystalline semiconductor thin film transistors. *J. Appl. Phys.* **53**, 1193-1202 (1982).

27 Bae, H. S., Yoon, M. H., Kim, J. H. & Im, S. Photodetecting properties of ZnO-based thin-film transistors. *Appl. Phys. Lett.* **83**, 5313-5315 (2003).

28 Collins, R. J. & Thomas, D. G. Photoconduction and Surface Effects with Zinc Oxide Crystals. *Physical review* **112**, 388 (1958).

29 H. Kind, H. Yan, B. Messer, M. Law & P. Yang. Nanowire Ultraviolet Photodetectors and Optical Switches. *Adv. Mater.* **14**, 158-160 (2002).

30 Takahashi, Y., Kanamori, M., Kondoh, A., Minoura, H. & Ohya, Y. Photoconductivity of Ultrathin Zinc Oxide Films. *Japanese Journal of Applied Physics* **33**, 6611-6615 (1994).

Chapter 9: Conclusion

After an introduction to the theory and literature on organic electronics it becomes clear to the reader that the issues of charge carrier injection, carrier trapping by impurities and defects in the semiconductor or at the interface to the dielectric, the film morphology and the role of surface energy at the interfaces are crucial aspects to the development of any organic semiconductor-based device. Furthermore, the performance of a particular organic semiconductor material can be strongly dependent on the specific device architecture used, the nature of other device components (i.e. dielectric, contact materials etc.) and the type of processing methodologies employed. It is this point where organic chemistry meets device physics. It is expected that the synergy of research efforts in both fields is required to improve the current level of performance of organic devices and develop organic electronics into a widely applicable technology.

In the first part of my research work a number of aspects related to the fabrication and performance of n-channel organic transistors for use in complementary integrated circuits were investigated. My work focused on soluble fullerene derivatives, a very promising class of small-molecule electron transporting organic semiconductors. The devices were developed in several steps by choosing an adequate polymer gate dielectric and improving electron injection through low work function source-drain top contact electrodes. The best devices exhibited a maximum electron mobility of 0.2 cm^2/Vs. This value is amongst the highest reported electron mobilities in organic field-effect transistors (OFETs) based on solution processed organic semiconductors and brings organic solution processed n-channel OFETs

closer to the performance level of analogue state-of-the-art p-channel devices. Complementary circuits fabricated using p- and n-channel transistors are found to exhibit lower power consumption, higher signal gain and better noise margins than unipolar circuits based on hole- or electron-only OFETs. Another important finding was that the electron mobility in solution processed [70]PCBM- based devices is comparable to that in [60]PCBM. This result is expected to further nourish the interest in [70]PCBM for use in organic solar cells, where its broader absorption spectrum can be of great benefit.

Part of my research has also focused on the development of ambipolar OFETs and circuits. Ambipolar OFETs are interesting for a number of reasons, particularly for their use in complementary-like logic and optoelectronic devices, such as light sensors. The analysis of their operating characteristics provides valuable information on the physical processes that occur in the organic materials during electrical conduction, light absorption and photoconductivity. Furthermore, ambipolar OFETs have a significant potential for use as low-cost light sensors. Particularly noteworthy is the infra-red light sensing capability of the squaraine-based ambipolar transistors discussed in the fifth chapter, as most other light sensing organic systems reported to date are limited to the visible and ultra-violet spectrum.

Although ambipolar materials might be able to eliminate the problem of processing discrete electron and hole transporting OFETs, the development of efficient patterning methods for organic components is of critical importance for the implementation in large scale organic integrated circuits. While printing methods are often considered the best option for soluble organic materials, it is suggested here that well known photolithography techniques could also be adapted for the patterning of solvent-sensitive and mechanically soft materials, such as organic conductors and semiconductors. The interlayer lithography method discussed in chapter 6 allows pattern resolutions of less than 10 μm and could be applied to organic conducting, insulating and semiconducting components.

A main topic discussed and addressed in this work is the prevailing high power consumption and high operating voltages of state of the art OFETs. A very promising approach is adopted for reducing the operating voltages. The latter is based on the introduction of very thin self-assembled monolayer gate dielectrics and solution processed organic semiconductors. The method enables OFET operation at 1-2 V.

These low-voltage devices exhibit similar charge carrier mobility as OFETs based on conventional oxide or polymer gate dielectrics and the same semiconductor systems, which typically operate at 10-80 V. By employing solution processed n- and p-channel low-voltage OFETs a complementary voltage inverter is demonstrated, which operates at less than $\left|2\right|$ V. This achievement is considered an important step in the development of low power solution processed organic integrated circuits.

While the advancements in organic electronics have been driven by the research on new low cost and high performance alternatives to amorphous and polycrystalline silicon for use in integrated circuits for several decades, another family of materials, namely transparent oxide semiconductors (TOS), has sparked strong interest in recent years. Here TiO_2 and ZnO are shown to encompass excellent electron transport characteristics with high optical transparency. The materials are deposited from a soluble precursor material employing the spray pyrolysis method. The latter is compatible with large area, low cost deposition and patterning. The highest electron mobility found in transistors based on ZnO as the semiconductor and self-assembled monolayer gate dielectrics was of the order of 10 cm^2/Vs at operating voltages below 2 V. This performance qualifies the devices for many applications in which amorphous or polycrystalline silicon is currently employed, and in particular the backplane circuitry of active matrix light emitting diode displays. Furthermore, the optical transparency of oxide electronics is expected to be a great advantage in the design of new display and optical/chemical sensor architectures. ZnO, for example, is shown to be suitable for UV-light sensing.

Based on the results obtained in this work, it is anticipated that organic and transparent oxide semiconductors will each soon be found in applications where their specific competitive advantages make them most attractive. This may be low-end portable, flexible and/or disposable light weight printed electronics, in the case of organic materials, and transparent sensors or active matrix OLED displays in the case of metal oxide semiconductors. However, several important issues remain to be solved before the advantageous properties of these materials overweigh the difficulties of implementing them into large scale production facilities. These are especially the limited air-stability and low charge carrier mobility in the case of organics and the high temperature processing in the case of oxide semiconductors processed by spray pyrolysis. Furthermore, the implementation of organic and oxide

materials will strongly depend on the simultaneous development of adequate processing technologies to enable their inexpensive deposition and patterning. These could be roll-to-roll printing or stamping methods or deposition by spraying or from the vapour phase with the support of masking or lithographic methods. A large number of research groups worldwide work on these issues and the impressive progress that has been achieved over the past few decades is ongoing. Revolutionary developments towards flexible, low cost, printed and transparent microelectronics are therefore to be expected.

Appendix A: List of patents and publications

A1. Patents

07/2008 GB patent Application No: P44897GB/JEP. "Low-Voltage Thin-Film Transistors". Thomas D. Anthopoulos, Paul H. Wöbkenberg, Donal D.C. Bradley.

A2. Journal Publications

A2.1. Articles in preparation or submitted

2009 *"Ambipolar organic transistors and near-infrared phototransistors based on a solution processable squarylium dye"*
In preparation. Paul H. Wöbkenberg, John G. Labram, Jean-Marie, Swiecicki, Ksenia Parkhomenko, Dusan Sredojevic, Jean-Paul Gisselbrecht, Dago de Leeuw, Donal D. C. Bradley, Jean-Pierre Djukic, Thomas D. Anthopoulos

2009 *"Low-voltage ambipolar organic transistors for microelectronics and light-sensor applications"*
In preparation. John G. Labram, Paul H. Wöbkenberg, Donal D. C. Bradley, Thomas D. Anthopoulos

2009 *"Ink-jet printed p-type polymer electronics based on liquid-crystalline polymer semiconductors"*
In preparation. Mohammed A. Baklar, Paul H. Wöbkenberg, David Sparrow, Magda Goncalves, Iain McCulloch, Martin Heeney, Thomas Anthopoulos, Natalie Stingelin

2009 *"Interlayer Lithographic Patterning of High Conductivity Poly(3,4-ethylendioxythiophene):Poly(styrenesulfonate) for Organic Field-Effect Transistors"*
In preparation. Dong-Seok Leem, Paul H. Wöbkenberg, Jingsong Huang, Thomas D. Anthopoulos, John C. de Mello and Donal D. C. Bradley

2009 *"Solid-State Processing of Virgin Poly(3-hexylthiophene)into High-Mobility Structures"*
Submitted. Mohammed A. Baklar, Avinesh Kumar, Felix Koch, Paul H. Wöbkenberg, Thomas Anthopoulos, Martin Heeney, Theo Kreouzis, Iain McCulloch, Paul Smith, Natalie Stingelin

A2.2. Published Articles

2009 *"Electronic properties of ZnO field-effect transistors fabricated by spray pyrolysis in ambient air"*
Appl. Phys. Lett. **95**, 133507 (2009) George Adamopoulos, Aneeqa Bashir, Paul H. Wöbkenberg, Donal D. C. Bradley, Thomas D. Anthopoulos

2009 *"Solution processed low-voltage organic transistors and complementary inverters"*
Appl. Phys. Lett. **95**, 103310 (2009) James M. Ball, Paul H. Wöbkenberg, Florian Colléaux, Martin Heeney, John E. Anthony, Iain McCulloch, Donal D. C. Bradley and Thomas D. Anthopoulos

2009 *"High-performance zinc oxide transistors and circuits fabricated by spray pyrolysis in ambient atmosphere"*
Adv. Mater. **21**, 2226 (2009) Aneeqa Bashir, Paul H. Wöbkenberg, Jeremy Smith, James Ball, George Adamopoulos, Donal D. C. Bradley and Thomas D. Anthopoulos

2008 *"Low-voltage organic transistors based on solution processed semiconductors and self-assembled monolayer gate dielectrics"*
Appl. Phys. Lett. **93**, 013303 (2008) Paul H. Wöbkenberg, James Ball, Floris B. Kooistra, Jan C. Hummelen, Dago M. de Leeuw, Donal D. C. Bradley and Thomas D. Anthopoulos
This paper was amongst the 5th most downloaded articles from the website of Applied Physics Letters in the month of its publication, July 2008.

2008 *"Fluorine containing C_{60} derivatives for use in high-performance electron transporting field-effect transistors and integrated circuits"*
Appl. Phys. Lett. **92**, 143310 (2008) Paul H. Wöbkenberg, James Ball, Floris B. Kooistra, Donal D. C. Bradley, Jan C. Hummelen, Dago M. de Leeuw and Thomas D. Anthopoulos

2008 "*High mobility n-channel organic field-effect transistors based on soluble C_{60} and C_{70} fullerene derivatives"*
Synth. Metals **158**, 468 (2008) Paul H. Wöbkenberg, Donal D. C. Bradley, David Kronholm, Jan C. Hummelen, Dago M. de Leeuw, Michael Cölle and Thomas D. Anthopoulos

2006 *"Megahertz operation of organic field-effect transistors based on poly(3-hexylthiopene)"*
Appl. Phys. Lett. **89**, 243515 (2006) Veit Wagner, Paul H. Wöbkenberg, Arne Hoppe and Jörg Seekamp

A2.3. Conference Proceedings

2009 "*Complementary circuits based on solution processed low-voltage organic field-effect transistors"*
Accepted for publication in Synth. Metals, Special Issue ICSM 2008. James M. Ball, Paul H. Wöbkenberg, Floris B. Kooistra, Jan C. Hummelen, Dago M. de Leeuw, Donal D. C. Bradley and Thomas D. Anthopoulos

2009 *"Solution processed low-voltage organic transistors based on self-assembled monolayer gate dielectrics"*
Proceedings of the society of photo-optical instrumentation engineers (SPIE), Conference on Organic Field-Effect Transistors VIII in San Diego, United States *(2009)* James M. Ball, Paul H. Wöbkenberg, Florian Colléaux, Jeremy Smith, Donal D. C. Bradley, Thomas D. Anthopoulos

2008 "*Light-sensing ambipolar organic transistors for optoelectronic applications"*
Proceedings of the society of photo-optical instrumentation engineers (SPIE), Conference on Organic Optoelectronics and Photonics III in Strasbourg, France *(2008)* Thomas D. Anthopoulos, Paul H. Wöbkenberg, Donal D. C. Bradley

2008 *"Solution Processed Self-Assembled Monolayer Gate Dielectrics for Low-Voltage Organic Transistors"*
Proceedings of the MRS Fall meeting in Boston *(2008)* James Ball, Paul H. Wöbkenberg, Florian Colléaux, Floris B. Kooistra, Jan C. Hummelen, Donal D. C. Bradley, Thomas D. Anthopoulos

Appendix B: Abbreviations, symbols and constants

Abbreviations:

[60]PCBM	[6,6]-phenyl-C61-butyric acid ester
AFM	atomic force microscopy
a-Si	amorphous silicon
BC	bottom contact
BCB	divinyltetramethyldisiloxanebis (benzocyclobutene)
BG	bottom gate
CB	conduction band
CB	chlorobenzene
CDM	correlated disorder model
C_i	geometrical capacitance
CV	cyclic voltammetry
DFT	density functional theory
diF-TESADT	8-difluoro-5,11-bis(triethylsilylethynyl)anthradithiophene
DOS	density of states
EA	electron affinity
HMDS	hexamethyldisilazane
HOMO	highest occupied molecular orbital

IC	integrated circuit
IR	infrared
LED	light emitting diode
LUMO	lowest unoccupied molecular orbital
MIM	metal-insulator-metal
MOSFET	metal-oxide semiconductor field-effect transistor
MTR	multiple trapping and release
NM	noise margin
OC1C10-PPV	poly(2-methoxy 5-(3',7' dimethyloctyloxy)-1-4 phenylene-vinylene)
ODPA	octadecylphosphonic acid
OFET	organic field-effect transistor
OPV	organic photovoltaics
PDMS	polydimethylsiloxane
PEDOT:PSS	poly(3,4-ethylendioxythiophene):poly(styrenesulfonate)
PET	poly(ethylene terephthalate)
PR	photoresist
PTAA	polytriarylamines
PTFE	polytetrafluoroethylene (Teflon)
PVP	polyvinylphenol
RDV	rotating disc voltammetry
rms	root mean square
SAM	self-assembled monolayer
S-D	source-drain
SP	spray pyrolysis
SU 8-2 PR	cross linkable epoxy photoresist
TC	top contact
TG	top gate
TFT	thin film transistor
TOS	transparent oxide semiconductor
UV	ultra violet
VB	valence band

Symbols:

E_F	fermi energy level
E_G	optical band gap energy
E_{gap}	energy gap between HOMO and LUMO
I_D	drain current
I_G	gate current
I_{OFF}	transistor off-current
I_{ON}	transistor on-current
$L_{e(h)}$	length of electron (hole) accumulation layer
n_{trap}	charge carrier trap density
$t_{F/R}$	fall/rise time
T_S	substrate temperature
V_D	drain voltage
V_{DD}	inverter supply voltage
V_G	gate voltage
V_{IN}	inverter input voltage
V_{OUT}	inverter output voltage
ΔI_{photo}	photo-induced current increase
θ_C	contact angle
τ_d	inverter stage delay

Constants:

c	speed of light in vacuum	2.998×10^{8} ms^{-1}
e	elementary charge	1.602×10^{-19} C
h	Plancks constant	6.626×10^{-34} Js
k_B	Boltzmann constant	1.381×10^{-23} $m^2kgs^{-2}K^{-1}$
ε_0	Permittivity constant	8.854×10^{-12} Fm^{-1}